UNIVERSIDADE FEDERAL DO RIO GRANDE DO SUL
INSTITUTO DE MATEMÁTICA
PROGRAMA DE PÓS-GRADUAÇÃO EM MATEMÁTICA APLICADA

Numerical methods for regularization models of geophysical flows

por

Igor Oliveira Monteiro

Tese submetida como requisito parcial
para a obtenção do grau de

Doutor em Matemática Aplicada

Prof. Dra. Carolina Cardoso Manica
Orientadora

Porto Alegre, Julho de 2015.

CIP - CATALOGAÇÃO NA PUBLICAÇÃO

Monteiro, Igor Oliveira

Numerical methods for regularization models of geophysical flows / Igor Oliveira Monteiro.—Porto Alegre: PPGMAp da UFRGS, 2015.

163 p.: il.

Tese (doutorado) —Universidade Federal do Rio Grande do Sul, Programa de Pós-Graduação em Matemática Aplicada, Porto Alegre, 2015.
Orientadora: Manica, Carolina Cardoso

Tese: Matemática Aplicada,
geophysical flows, finite element, regularization models, barotropic vorticity model, boussinesq model

Numerical methods for regularization models of geophysical flows

por

Igor Oliveira Monteiro

Tese submetida ao Programa de Pós-Graduação em Matemática Aplicada do Instituto de Matemática da Universidade Federal do Rio Grande do Sul, como requisito parcial para a obtenção do grau de

Doutor em Matemática Aplicada

Linha de Pesquisa: Dinâmica dos Fluidos

Orientadora: Prof. Dra. Carolina Cardoso Manica

Banca examinadora:

Prof. Dr. Dagoberto Adriano Rizzotto Justo
PPGMAp-UFRGS

Prof. Dr. Wiliam Correa Marques
IMEF-FURG

Prof. Dr. Leo Gregory Rebholz
Clemson University

Tese apresentada e aprovada em
Agosto de 2015.

Prof. Dr. Carlos Hoppen
Coordenador

Esta tese é dedicada a minha esposa, Sandra, a minha mãe, Maria do Carmo, e a minha sogra, Zélia.

AGRADECIMENTO

Gostaria de agradecer a todas as pessoas e instituições que de alguma forma ajudaram na minha formação acadêmica e na elaboração desta tese. Começo agradecendo à minha orientadora, Professora Carolina Manica, a confiança, os ensinamentos, o tempo despendido e o esforço para que o trabalho tivesse seguimento diante das adversidades ocorridas no percurso. Agradeço também por me ajudar a desenvolver o olhar matemático e por me introduzir no estudo da turbulência! I am very grateful to Professor Leo Rebholz for his support, patience and good ideas which were crucial to this thesis and to my academic development. Aos professores do PPGMAp os ensinamentos, em especial, ao Professor Mark Thompson os ensinamentos, as conversas e o incentivo. Aos professores João Carvalho, Dagoberto Justo e Leonardo Guidi, responsáveis pelo LICC, o apoio computacional, determinante para a elaboração desta tese. Aos meus professores na FURG, onde obtive minha formação inicial. À equipe do FreeFem++ a disponibilidade do modelo e a ajuda nas simulações. Aos colegas do PPGMAp os momentos que compartilhamos nas disciplinas e a amizade. À banca a participação e as contribuições. Ao PPGMAp a oportunidade e o suporte durante o curso. Ao PRH-PB216 e à Petrobrás a bolsa e o auxílio no desenvolvimento do trabalho. Aos professores Maria Cristina Varriale e Renato Brito as conversas e o suporte como bolsista.

Gostaria de agradecer também ao Instituto Federal do Rio Grande do Sul e aos colegas do câmpus Rio Grande o apoio e incentivo.

Por fim, eu gostaria de agradecer à minha querida família. Aos meus dindos, Zeca e Mariluce. Aos meus saudosos avós. Aos meus sogros, à saudosa Zélia e o seu Octaviano. Aos meus pais Maria do Carmo e Paulo Roberto os ensinamentos, o incentivo, o suporte e a paciência ao longo desta longa jornada. À minha amada esposa Sandra, sem o teu amor, incentivo e apoio este trabalho não seria possível! Finalmente, gostaria de agradecer ao bondoso Pai por esta experiência enriquecedora em minha vida.

Contents

List of Figures

List of Tables

LIST OF ABBREVIATIONS AND SYMBOLS

List of Abbreviation

BV	Barotropic Vorticity
CNLE	Crank-Nicolson Linearly Extrapolated
DNS	Direct Numerical Simulation
FEM	Finite Element Method
GFD	Geophysical Fluid Dynamics
LES	Large Eddy Simulation
NSE	Navier Stokes Equations
RHS	Right hand side
NS	Navier Stokes
URANS	Unsteady Reynolds Averaged Navier Stokes

List of Symbols

D_N	van Cittert deconvolution operator
D_N^h	discrete van Cittert deconvolution operator
F	Continuous filtering operator
F_h	Discrete filtering operator
H^k	Sobolev space W_2^k
H_0^1	H_0^1 is the subspace of H^1 with zero boundary condition
$J(f,g)$	Jacobian $\frac{\partial f}{\partial x}\frac{\partial g}{\partial y} - \frac{\partial f}{\partial y}\frac{\partial g}{\partial x}$

L	Length scale
p	Pressure field
P	L^2 orthogonal projection in the space X_h
Pr	Prandtl number
Re	Reynolds number
Ri	Richardson number
Ro	Rossby number
T	Endtime, Temperature field
u	Velocity vector field
X	X is the space H_0^1
Y_h	continuous FE space with kth degree polynomial on each element of the triangulation
X_h	subspace of Y_h with zero boundary condition
α	Filter cut-off length
δ_M	Munk scale
Δ_h	Discrete Laplacian
Π	Eliptic orthogonal projection in X_h
τ_h	Regular, conforming triangulation
ψ	Streamfunction field
ω	Vorticity field
$\overline{\omega}$	Filtered vorticity
Ω	Physical domain

RESUMO

Escoamentos geofísicos são aqueles escoamentos que são afetados pela rotação da Terra. Simulações computacionais envolvendo este tipo de escoamento tem diversas aplicações como, por exemplo, em estudos sobre mudanças climáticas e em previsões de tempo e do escoamento oceânico, imprescindíveis para o bem-estar da sociedade moderna. Em especial no caso do Brasil, a importância destas simulações é ainda maior devido à sua ampla aplicação na indústria do petróleo.

Porém, devido ao imenso número de Reynolds conferido à estes escoamentos, os recursos computacionais disponíveis atualmente (e decerto no futuro próximo) não são suficientes para simulá-los integralmente. Modelos regularizados são modelos simplificados concebidos para lidar com este problema, pois permitem a redução dos graus de liberdade em virtude de alterações nas equações originais que encurtam a cascata de energia e propiciam o uso de malhas menos refinadas.

Nesta tese, foram estudados dois modelos com extenso uso em escoamentos geofísicos: o Modelo da Vorticidade Barotrópica (modelo BV) e o Modelo de Boussinesq. Para o modelo BV três tipos de regularizações foram consideradas: a regularização alfa com deconvolução modificada de Tikhonov-Lavrentiev, a regularização Bardina e a regularização alfa com deconvolução aproximada de van Cittert. Algoritmos com discretização temporal de Crank-Nicolson e espacial em elementos finitos foram propostos para estas regularizações e demonstrados incondicionalmente estáveis e otimamente convergentes. Também, simulações computacionais foram feitas, tanto para validar a teoria desenvolvida, como para avaliar o desempenho destes modelos em malhas com pouco refinamento, em situações mais próximas àquelas que ocorrem em aplicações reais.

No caso do modelo de Boussinesq foram estudadas quatro tipo de regularizações: alfa, omega, Leray e Leray modificada, todas com deconvolução aproximada de van Cittert. Para estas regularizações, algoritmos do tipo Crank-Nicolson/elementos finitos, junto com algumas técnicas bem sucedidas quando aplicadas às equações de Navier-Stokes, foram propostos e analisados numericamente. É mostrado que os algoritmos conservam energia e são incondicionalmente estáveis e otimamente convergentes. Em complemento, simulações computacionais são apresentadas, tanto para validar a teoria de convergência, como também para avaliar o desempenho de cada regularização em situações mais realistas. Nestas simulações, é mostrado que a regularização de Leray, além de ter grandes vantagens do ponto de vista computacional, pois permite controlar a ordem do erro de consistência do modelo sem alterar significativamente o tempo computacional, produziu, em malhas com pouco refinamento, as melhores soluções em comparação às soluções esperadas para os experimentos.

ABSTRACT

Geophysical flows are the flows influenced by the Earth's rotation. Computational simulations involving this kind of flow have several applications, such as climate changes studies and weather and ocean forecasts which are essential for the welfare in modern society. In particular for Brazil, the importance of geophysical simulations is even greater due to applications in the oil industry.

However, due to the extremely large Reynolds numbers associated with geophysical flows, the current available computational resources (and certainly in the near future) are not enough to simulate it entirely. Regularized models are simplified models designed to deal with this kind of problem, because they reduce the degrees of freedom in simulations by virtue of small changing the original equations, which shorten the energy cascade and enable to the the use of less refined meshes.

In this work, two models with extensive application in geophysical flow are studied: the Barotropic Vorticity model (BV model) and the Boussinesq model. First, in the case of the BV model, three different regularization techniques are studied, namely, the alpha regularization with modified Tikhonov-Lavrentiev deconvolution, the Bardina regularization and the alpha regularization with van Cittert approximate deconvolution. Crank-Nicolson in time, finite element in space algorithms for these models are proposed and rigorously proven to be unconditionally stable and optimally convergent. Also, computational simulations are performed that validate the developed theory for the proposed regularized models, and shows their effectiveness on coarse meshes in situations similar to real applications.

In the Boussinesq model case, four regularizations are studied, namely, alpha, omega, Leray and modified Leray, all of them with van Cittert approximate deconvolution and some techniques which have enjoyed success when applied to the Navier-Stokes equations. Crank-Nicolson/finite element algorithms, are developed and numerically analysed. They are proven to be unconditionally stable and optimally convergent. Moreover, computational simulations are performed to validate the convergence theory and to evaluate the performance of each regularization in more realistic situations. In these simulations, the Leray regularization, in addition of presenting substantial computational advantages because it enables controlling the model consistency error order with no significant increase in computations, produced the best solutions in coarse meshes when compared to the expected solutions.

1 INTRODUCTION

1.1 Problem statement

Geophysical fluid dynamics (GFD) is the study of flows influenced by Earth's rotation. It is the foundation for understanding atmospheric and oceanic flows. Its difference from traditional engineering flows is due to the presence of fictitious forces caused by the description of the flow in a non-inertial rotating reference system: the Earth's surface.

Presently, GFD is related to at least two important scientific subjects: weather forecasting and climate modeling. It is also important to other scientific fields such as meso and large scale studies in oceanography and meteorology, planktonic migration in marine biology, waves, tides and sedimentology studies and pollutant dispersion in atmosphere and ocean. Moreover, it has important commercial and social applications such as navigation, agriculture, coastal engineering, natural disasters prediction and mitigation and, especially in the Brazil case, oil exploration.

As in engineering flows, modeling geophysical flows is a challenging task, the reason being that geophysical flows are described by the Navier-Stokes equations (NSE). NSE are well known by mathematicians because of their complexity. Even after centuries of effort, fundamental theoretical aspects such as existence of strong solutions in the three-dimensional case remains unsolved. In the year 2000, the Clay Mathematics Institute offered a one million dollar prize to anyone who makes substantial progress presenting a proof or a counterexample. To the best of our knowledge, until this moment the problem remains unsolved!

As in other fields of fluid dynamics, analytical solutions for geophysical flows may be achieved only in a very limited number of cases, so instead one needs to employ advanced numerical methods and computational simulations. Geophysical flows simulations was one of the first applications of general-purposes computers to numerical simulations. In 1950, Jule Charney, Ragnar Fjörtoft and John von Neumann in their seminal work entitled "Numerical integration of the barotropic vorticity equation" [17] accomplished the first computational weather forecast using the legendary ENIAC world's first computer (see [72, 71] and references therein for a historical survey). Since that time, several mathematical models and numerical methods have been devised in order to, along with the computer advances, simulate oceans and atmosphere. Among the available methods, the Finite Element Method (FEM) is one of the most powerful method ever conceived in order to approximate solutions of boundary-value problems, such as NSE. It has gained importance due to its relative ease to deal with non-structured meshes and arbitrary geometries, as those often necessary in geophysical applications.

Associated with the difficulty of solving NSE it is the phenomenon of turbulence. In particular, the correct representation of geophysical flows, due to high Reynolds number, depends on the development of advanced techniques to deal with turbulence. High Reynolds number flows have a wideband spectrum. A simple estimation based on the Kolmogorov theory [92] shows that a typical geophysical flow with horizontal length scale of 100 km and a Reynolds number of 10^{10} will dissipate energy in a length scale of centimeters. Therefore, simulations resolving all the necessary scales involved in geophysical flows (Direct Numerical Simulation - DNS) are far beyond the reach of current computers.

Among the different techniques to deal with this problem, Large Eddy Simulation (LES) and Regularization Models are two of the most promising methods. LES consists of calculating the large structures of a flow by modeling the effect of small scale structures on the large structures. This is accomplished by filtering the Navier-Stokes equations and resolving the filtered equations, whereas the resulting subfilter stress, which represents the interaction between the resolved and unresolved scales, is modeled. This approach is valid because, according to the

Kolmogorov theory, the large structures, which are related with external forces and boundary conditions, are specific for each flow, whereas the small structures have a universal behavior [92, 5]. On the other hand, regularization models were initially created for theoretical purposes. For example, the Leray-α model is a well-posed earlier regularization proposed by Jean Leray in 1934 in order to analyse the Navier-Stokes equations [64]. A common feature for regularization models is that they are well-posed and regular from the mathematical point of view. The regularization meaning the disappearance of supposed existing singularities in the original Navier-Stokes equations [97]. Recently, a considerable interest has arisen for regularization models as simpler models to deal with turbulence in numerical simulations. In this approach, the regularization model is obtained from the direct regularization of the convective flux [34]. Thus, the computed solution is a regularized approximation of the NSE solution, rather than a local, spacial average of the fluid velocity (as in LES models [66]). However, some studies have shown that regularization models can be interpreted as LES models using the so-called regularization principle [32, 33, 34]. The main advantage of these approaches in relation to DNS modeling is that the number of degrees of freedom in numerical simulations are significant fewer in LES and regularization models. More recently, some LES models such as the Approximate Deconvolution Models [100] and regularization models such as alpha models started to be tested in the geophysical framework [47, 112, 22, 41, 42].

Despite computational simulations being widely applied in geophysical flows, studies involving new numerical schemes and their mathematical analysis are uncommon, possibly due to the wide range of numerical schemes available and the difficulty to perform a mathematical analysis in realistic conditions. Nevertheless, this kind of study, even in non-realistic situations, are useful to produce more accurate results with less computational cost.

In light of the above, this thesis focuses on application and mathematical analysis of regularization modeling techniques to geophysical flows. Thus, new algorithms using FEM discretizations were developed, analysed, and computational tests were performed in a geophysical context in order to understand and evaluate their performance in simulations.

1.2 Relevance

The subject of this thesis is closely related with some current issues, such as oil exploration in the pre-salt layer, climate change, and weather and ocean forecasting. Apart from being motivated by interesting fluid dynamics and numerical analysis open problems like those described in the previous section, it is also encouraged by its substantial applications of social interest.

From the point of view of fluid dynamics and numerical analysis, this thesis deals with subjects such as the development of stable and robust algorithms in order to apply regularization models in geophysical fluid dynamics. There is strong evidence, such as that presented in the next section, to believe it would be fruitful in this application, and provide more accurate results with less computational cost.

On the other hand, from the point of view of applications, the following three issues guided the development of this thesis:

1. Brazil has become an important oil producer. With the recent discovery of the vast oil reserve in the pre-salt layer, Brazil can become one of the largest oil producers in the world. However, oil exploration in the pre-salt layer is very challenging. An important tool to assist oil exploration in the sea is the use of reliable ocean models. They are necessary both for logistics in oil exploration and to mitigate the environmental impact caused by oil spills. Moreover, ocean and atmosphere forecasting also helps in navigation. For logistics, ocean simulations can supply the velocity field, which is essential to design oil platforms. From the environmental point of view, ocean forecasting is very helpful in cases of oil

spills because it provides information about the fate of the oil slick. It is very important, especially in the case of Brazil, where there exists natural sanctuaries such as the Abrolhos bank, for instance.

2. Climate modeling allows a better understanting in man's role in climate change. With a huge heat capacity, oceans are particularly important because they absorb and store heat, damping temperature fluctuations. However, oceanic simulations can only be performed on coarse meshes in order to be computationally viable. Moreover, most of them employ URANS (unsteady Reynolds averaged Navier-Stokes) and the eddy viscosity hypothesis. Thus, they are likely to provided limited results, affecting large scale features [41, 54]. Therefore, it is necessary to develop more appropriate techniques to deal with subgrid scale motion.

3. In addition, regularization models can have a positive impact on atmospheric and oceanic forecasts. Geophysical flow forecasts depend heavily on the initial conditions, resulting in a very small prediction time [57]. Thus, Control Theory has to be applied to guarantee accurate predictions. Most of these techniques assumes a perfect model, that is, a model without bias whose only source of error is the uncertainty in initial conditions. Therefore, the more accurate the model is, the more suitable the Control Theory will be for this kind of problem.

Computational fluid dynamics has also been used increasingly in environmental applications and social welfare. At present, in order to build new industries, harbours and oil platforms, governments, in several contries including Brazil require environmental impact studies involving ocean and/or atmospheric modeling. In addition, computational simulations are extensively used to help assess and control damage in environmental accidents, such as the 2010 British Petroleum oil spill in the Gulf of Mexico, the 2011 Puyehue volcano plume in Chile and the 2011 tsunami in Japan. All these applications may be immensely benefit by more accurate techniques to simulate the ocean and atmosphere.

1.3 Theoretical background and objectives

Geophysical flows present some differences compared to traditional engineering flows. The main differences are: the motion is thin (small aspect ratio) and is influenced by Earth's rotation.

The small aspect ratio results from the problem asymmetry due to differences between vertical and horizontal scales in the Earth's surface. Large scale geophysical flows have an aspect ratio similar to a sheet of paper. Typical horizontal scale is 10^6 meters and depth scale is 10^3 meters. As a result, the vertical velocity component is much smaller than horizontal velocity. Thus, some approximations following from the small aspect ratio are often assumed in order to derive mathematical models for geophysical flows.

In addition, Newton's second law is formulated for inertial frames. However, Earth's surface is not an inertial frame because of Earth's rotation. Thus apparent forces must be considered in order to mathematically represent the flow in coordinate systems in the Earth's surface: the Coriolis and centrifugal forces. A scale analysis shows that the centrifugal force and vertical component of Coriolis force are negligible in comparison to other terms, but the horizontal component of the Coriolis force can be comparable to the other terms in the horizontal momentum equations depending on the length scale of the flow [91]. The relative importance of Earth's rotation effect is estimated by the nondimensional Rossby number (Ro) defined as:

$$Ro = \frac{U}{2\Omega_E \sin(\phi) L}$$

where U and L are respectively characteristic horizontal velocity and length scales, Ω_E is the planetary angular velocity and ϕ is the latitude of the flow.

The Rossby number describes the ratio of inertial and Coriolis accelerations. When $Ro << 1$ the flow is said to be **geophysical**.

Geophysical flows can be studied by mathematical models resulting from different levels of aproximations, which, despite their simplifications, can still represent several important physical phenomena. The main geophysical models are:

- Primitive Equations
- Boussinesq
- Shallow Water
- Quasi-geostrophic

The most complete mathematical model used to simulate geophysical flows is the **Primitive Equations Model**, which describes flows with small aspect ratio subject to the Coriolis, gravitational and external forces and with pressure field determined by density and free surface fields. It is often used in atmospheric and oceanic forecast systems, and in climate modeling. The system of equations:

$$
\begin{aligned}
\frac{\partial \mathbf{u}_H}{\partial t} + \mathbf{u}_H \cdot \nabla_H \mathbf{u}_H + w\frac{\partial \mathbf{u}_H}{\partial z} + 2\Omega_E \times \mathbf{u}_H + \frac{1}{\rho_0}\nabla_H p - \nu_H \Delta_H \mathbf{u}_H - \nu_V \frac{\partial^2 \mathbf{u}_H}{\partial z^2} &= \mathbf{f}, \\
\frac{\partial p}{\partial z} + \rho g &= 0, \\
\nabla_H \cdot \mathbf{u}_H + \frac{\partial w}{\partial z} &= 0, \\
\rho &= F(p, \phi_i), \\
\frac{\partial \phi_i}{\partial t} + \mathbf{u}_H \cdot \nabla_H \phi_i + w\frac{\partial \phi_i}{\partial z} + \nu_{H,\phi_i}\Delta_H \phi_i + \nu_{V,\phi_i}\frac{\partial}{\partial z}\phi_i &= 0,
\end{aligned}
$$

describes the primitive equations model [41, 14], where $\mathbf{u}_H$ is the horizontal velocity vector (u, v), w is the vertical velocity component, $\nabla_H = (\frac{\partial}{\partial x}, \frac{\partial}{\partial y})$ is the horizontal gradient operator, Ω_E is the angular planetary velocity, ρ_0 is the fluid reference density (constant), ρ is the density, p is the pressure, ν_H is the horizontal kinematic viscosity, ν_V is the vertical kinematic viscosity, $\mathbf{f}$ is the resultant external force, F is a functional for the thermodynamic state equation, ϕ_i are the thermodynamic state scalars (temperature, humidity or salinity), ν_{H,ϕ_i} is the horizontal diffusivity of the scalar ϕ_i and ν_{V,ϕ_i} is the vertical diffusivity of the scalar ϕ_i.

Another important model is the **Boussinesq Model**. The Boussinesq Model allows us to represent flows in the presence of density stratification in which the Buoyancy force is important. The Boussinesq model is given by

$$\begin{aligned}\frac{\partial \mathbf{u}}{\partial t} + \mathbf{u}\cdot\nabla\mathbf{u} + 2\Omega\times\mathbf{u} + \frac{1}{\rho_0}\nabla p - \nu\Delta\mathbf{u} + \rho' g\mathbf{k} &= \mathbf{f},\\ \nabla\cdot\mathbf{u} &= 0,\\ \frac{\partial \rho'}{\partial t} + \mathbf{u}\cdot\nabla\rho' - \nu_{\rho'}\Delta\rho' &= 0,\end{aligned}$$

where $\mathbf{u}$ is the velocity vector, p is the pressure, ρ_0 is the reference density (constant), ρ' is an active tracer (temperature or salinity, for example), g is the gravitational acceleration, ν is the kinematic viscosity, $\mathbf{f}$ is the external force and $\nu_{\rho'}$ is the ρ' diffusivity. Note that momentum and tracer equations are constrained by the buoyancy term in the Boussinesq Model, therefore flow is forced by spatial differences in the density field.

In addition to Primitive equations and Boussinesq Model, the two-dimensional **Shallow Water Model** describes a flow with a small aspect ratio and under the action of pressure gradients caused by gradients in the fluid free surface field. In the geophysical case this kind of flow is described by [91]:

$$\begin{aligned}\frac{\partial \mathbf{u}_H}{\partial t} + \mathbf{u}_H\cdot\nabla\mathbf{u}_H - f\mathbf{k}\times\mathbf{u}_H - \nu\Delta\mathbf{u}_H + g\nabla h &= \mathbf{f},\\ \frac{\partial h}{\partial t} + \nabla\cdot(h\mathbf{u}_H) &= 0,\end{aligned}$$

where $f = 2\Omega\sin(\phi)$ is the Coriolis parameter and h is the water depth.

Finally, one of the simplest models is the **Quasi-geostrophic Model**. The geostrophic equilibrium is the fundamental state (or mean state) of a geophysical flow, in which the pressure gradients and Coriolis force are in balance, i.e.,

$$f\mathbf{k}\times\mathbf{u}_h = -\frac{1}{\rho}\nabla p.$$

The Quasi-geostrophic model results from an assymptotic expansion of the velocity field in the Rossby number Ro, that is,

$$u\left(x,y,t,Ro\right)=u_0\left(x,y,t\right)+u_1\left(x,y,t\right)Ro+u_2\left(x,y,t\right)Ro^2+....$$

Using this expansion, a closed set of equations is obtained from the shallow water model representing the balance of the first order terms around the zeroth order geostrophic balance (mean state). The balance of the first order terms is the quasi-geostropic model [91, 47, 100], also known as Barotropic Vorticity model, given by

$$\begin{aligned} Ro\frac{\partial\omega}{\partial t}+RoJ(\psi,\omega)-\frac{\partial\psi}{\partial x}-\left(\tfrac{\delta_M}{L}\right)^3\Delta\omega &= \mathcal{F}, \\ \Delta\psi &= -\,\omega. \end{aligned}$$

which ω is the vorticity, ψ is the streamfunction, $J(\cdot,\cdot)$ is the Jacobian, Ro is the Rossby number, δ_M is the Munk scale, L is the length scale and $\mathcal{F}$ is the forcing.

The four models above mentioned can describe a vast variety of geophysical phenomena such as the general ocean and atmosphere circulation, mesoscale processes (vortices and cyclones) and also planetary (Rossby), plane, Kelvin and Poincaré waves [91].

Due to the high Reynolds number associated with geophysical flows direct numerical simulations (DNS) are unfeasible. Therefore, computational simulations are carried out in meshes which cannot resolve all necessary scales anticipated by the Kolmogorov Theory of energy cascade, and some methods are necessary to deal with the small scales which are not resolvable. Traditionally, small scale modeling in geophysical flow simulations is made using the Reynolds Stress tensor and the Boussinesq eddy viscosity hypothesis, which is a fundamentally dissipative technique [47, 100]. This approach has been used because it provides the correct rate of energy dissipation [100] and improves numerical stability [47, 54]. However, according to [47], increased values of viscosity reduce the flow variability in large scales causing meaningful differences between coarse resolution meshes and DNS. The effects of high eddy viscosity values on climate simulations are studied in [54], and they observed several places in the ocean where computed solutions were severely affected by this problem. They also noted that reducing eddy viscosity leads to a generally improved ocean circulation at the expense of increased numerical noise. Thus, decreasing eddy viscosity values is not enough to solve this problem, and the solution is probably related to a better representation of small scale flow.

Besides, the small aspect ratio in geophysical flows results in a quasi-two-dimensional flow and, hence, a possible coexistence between the enstrophy cascade and the inverse energy cascade [103, 102, 28]. Thus, an approach consistent with phenomenology is imperative.

LES and regularization models are projected to deal with this kind of problem. Geophysical flows inspired the first LES model through the seminal work of Joseph Smagorinsky [104], but the subsequent development has been made based on engineering applications [100, 28]. Recently, a new interest in LES and regularization models has emerged for geophysical applications with alpha [47, 112, 41, 42] and ADM [6, 100] models.

The Navier-Stokes-α (NS-α) model has received much attention due to its attractive physical and mathematical properties. For example, NS-α admits regular unique solutions [24, 77], is frame invariant [38], conserves energy, helicity and 2D enstrophy [25, 93] and cascades energy at the same rate as Navier-Stokes equations in wavelengths up to α, after which it accelerates energy dissipation [25]. Furthermore, it allows a significant reduction of degrees of freedom in computer simulations. Despite of being presented as a regularization model, NS-α can also be interpreted as a kind of LES model [20, 31, 38].

Based on NS-α model, alpha models has been developed for geophysical flows; for example, the **Quasi-geostrophic-α** model [47, 100], the **shallow water-α**

model [112], the **Boussinesq-α** [22] and the **Primitive equations-α** model [41, 42]. They also present computer simulations which are promising.

In addition to the NS-α model, other alpha-type models has been recently developed for NS equations, such as the NS-ω [61, 65], Leray-α [32, 33], Modified Leray-α [51], Bardina [3, 15] and NS-Voigt [15, 56, 68] models and their deconvolution generalizations [93, 64, 76, 75, 9] which improves accuracy and computational cost. Some of these can also be interpreted as a kind of LES model [32, 33, 34].

In light of the above, there is significant evidence to believe that regularization models can perform better than traditional eddy viscosity models in geophysical flow simulations with a viable computational cost. In the case of engineering flows, FEM algorithms were proposed and analysed to alpha [65, 76], omega [65, 75], Leray-α [64, 9] and zeroth order ADM [74]. Traditionally, algorithms are proposed and analysed for stability, which is related, in the appropriate norm, to the physical intuiton of energy conservation. It is also common to include error analysis showing convergence in appropriate norms. Then, computational simulations are made to determine whether the model can reproduce a known pattern observed in some benchmark test. However, algorithms, mathematical analysis and computational tests are still necessary for geophysical analogues of these regularization models.

In GFD, flows are routinely studied separately as barotropic and baroclinic flows[1] (see, e.g. [91]), the reason being the difference in terms of temporal and spatial scales between these two kind of flows. In this thesis we addressed GFD considering these two points of view:

1. Can state-of-art regularization models improve coarse mesh large-scale geophysical barotropic simulations? The first part of the thesis investigates this question, performing a numerical analysis of the Quasi-Geostrophic model for three

different regularization techniques, namely, alpha with Tikhonov approximate deconvolution, Bardina and alpha with Van Cittert approximated deconvolution.

2. How can state-of-art regularization models affect numerical solutions obtained in the case of computational expensive baroclinic density current simulations? This question is addressed in the last chapter, in which we studied the Boussinesq model through four generalized deconvolved regularizations, namely, alpha, Leray-α, omega and Modified-Leray-α.

Thus, the main objective of this thesis is to propose robust algorithms to apply regularization models in geophysical flows. In addition, we intend to attain the following specific goals:

1. Provide algorithms through FEM discretizations to apply regularization techniques in models used in geophysical fluid dynamics.
2. Study these algorithms from the point of view of numerical analysis.
3. Implement them and carry out simulations in order to evaluate their performance.

All these aspects, with mathematical and scientific motivations, are the object of careful analysis and understanding in this thesis.

In Chapter 2 we study a Crank-Nicolson Finite Element scheme to an alpha regularization with deconvolution of the Barotropic Vorticity (BV) model of geophysical flows, called the BV-Tikhonov model. The BV-Tikhonov model is a deconvolved version of the BV-α model where the Tikhonov regularization is modified to give an approximate deconvolution of the Helmholtz filter. We prove the scheme is unconditionally stable and second order accurate. We also test the

---

[1] Barotropic flows are those which the density is only a function of pressure. Otherwise, the flow is called baroclinic [110].

BV-Tikhonov model in the traditional double-gyre wind forcing benchmark. We show, when the coarse mesh BV model solution degenerates, the BV-α model can retrieve the high resolution pattern, but solutions are dramatically improved by the choice of the deconvolution parameter in the BV-Tikhonov model. We believe this behaviour is related to the second order consistency error term shown in the convergence analysis, which could affect the model solution in coarse meshes, but could be handled by a careful choice of the deconvolution parameter.

In Chapter 3[2] we study a Crank-Nicolson in time and Finite Element in space numerical scheme for a Bardina regularization of the barotropic vorticity model. We derive the regularized model from the simplified Bardina model in primitive variables, present a numerical algorithm for it, and prove the algorithm is unconditionally stable with respect to the timestep size, and optimally convergent in both space and time. Numerical experiments are provided that verify the theoretical convergence rates, and also that test the model/scheme on a benchmark double-gyre wind forcing experiment. For the latter test, we find the proposed model/scheme gives a good coarse mesh approximation to the highly resolved direct numerical simulation of the barotropic vorticity model, and compares favorably to related regularization model results.

In Chapter 4[3] we study the BV-α-Deconvolution model. It is a family of regularizations of the Barotropic Vorticity model that generalizes the BV-α model and improves its accuracy. An unconditionally stable and optimally convergent scheme for the BV-α-Deconvolution model is proposed and we show that it is $O(\alpha^{2N+2})$, where N is the deconvolution order, whereas the BV-α model is at most second order accurate. We perform numerical simulations to confirm the predicted convergence rates and test the model in the traditional double gyre wind experiment. For the latter test, we show that the BV-α-Deconvolution model can retrieve the expected high resolution pattern, being more accurate for larger values of deconvolution order.

In Chapter 5 we study numerically four regularization models with deconvolution for density currents, namely, Boussinesq-α, Boussinesq-ω, Boussinesq-Leray and Modified-Boussinesq-Leray. A Crank-Nicolson in time and Finite Element in space algorithm is proposed and proved to be unconditionally stable and optimally convergent, which is verified through convergence rates in computational simulations. Finally, the regularization models are compared through the Marsigli's flow benchmark for $Re = 2000$ and $Re = 5000$. We found that Boussinesq-α and Boussinesq-Leray models produced the most accurate solutions for low Reynolds number. Moreover, as expected, all regularized models had their solutions improved when deconvolution order was increased. On the other hand, the Boussinesq-Leray provided the best solution for high Reynolds number. Besides, from the computational point of view the Boussinesq-Leray model presents great advantages due to its decoupling between momentum and filter equations which permits to increase the deconvolution order with no significant increase in the computational cost.

Finally, in Chapter 6 we present the main conclusions and suggestions for future works.

---

[2] The content of this chapter is coauthored by Professor Carolina C. Manica and Professor Leo G. Rebholz, being accepted in 1 December, 2014, for publication in the journal Numerical Methods for Partial Differential Equations with the title *Numerical study of a Regularized Barotropic Vorticity Model of Geophysical Flow.*

[3] The content of this chapter is coauthored by Professor Carolina C. Manica and was published in Volume 5, Number 4, Pages 317-338 (2014) of the International Journal of Numerical Analysis and Modelling, Series B, with the title *Improving numerical accuracy in a regularized Barotropic Vorticity model of geophysical flow.*

2 BAROTROPIC VORTICITY MODEL WITH TIKHONOV-LAVRENTIEV DECONVOLUTION

2.1 Introduction

Nowadays, numerical simulations of geophysical flows have several applications, such as climate change studies, weather and oceanic forecast, biological transport in the ocean, pollutants dispersion and oil exploration. The Barotropic Vorticity Model (BV model) is one of the simplest models used to represent geophysical flows. It is defined in dimensionless form by [47, 100]

$$\begin{aligned} Ro\tfrac{\partial \omega}{\partial t} + RoJ(\psi,\omega) - \tfrac{\partial \psi}{\partial x} - \left(\tfrac{\delta_M}{L}\right)^3 \Delta\omega =& \mathcal{F}, \\ \Delta\psi =& -\omega, \end{aligned}$$

where ω is the vorticity, ψ is the streamfunction, $J(\psi,\omega) = \frac{\partial \psi}{\partial x}\frac{\partial \omega}{\partial y} - \frac{\partial \psi}{\partial y}\frac{\partial \omega}{\partial x}$ is the Jacobian, Ro is the Rossby number, δ_M is the Munk scale, L is the length scale and $\mathcal{F}$ is the forcing term. The BV model can be used to represent the meso and large scale flow in the atmosphere and oceans. It is commonly used in oceanography to study the midlatitude oceanic circulation. Furthermore, it can also be extended to multilayer to describe the vertical motions in the ocean [78, 99]. Presently, it has been used in studies involving data assimilation [113, 21], climate [95, 73, 36] and oceanic processes [12, 108].

Despite the fact that the BV model is a simplified model in comparison with the full primitive equations of geophysical flows, solving it numerically is still challenging when long-time integration is necessary, as in climate modeling [100]. Traditionally, essentially dissipative methods such as eddy viscosity parametrization have been used to represent the under-resolved part of the flow. However, according to [47] artificial viscosity tends to reduce variability and nonlinear structures are often destroyed by excessive dissipation [37, 47]. Thus some methods such as Approximate Deconvolution Models [100, 99], BV-α [82, 81, 47] and BV-Bardina [59] have been developed with success to improve accuracy and reduce the degrees of freedom in computational simulations.

The BV-α model [47] is a regularization of the BV model in which the alpha terms modify the fluid nonlinearity without introducing additional dissipative terms or increasing the viscosity coefficient in the BV equations. In the BV-α model the nonlinearity is altered so that the flow at length scales that are smaller than the alpha length scale are nonlinearly removed by motions at the larger scales. The Barotropic Vorticity-α model (BV-α) is given by

$$Ro\tfrac{\partial \omega}{\partial t} + RoJ(\psi, \omega) - \tfrac{\partial \psi}{\partial x} - \left(\tfrac{\delta_M}{L}\right)^3 \Delta\omega = \mathcal{F}, \tag{2.2a}$$

$$\Delta\psi = -\,\overline{\omega}, \tag{2.2b}$$

$$-\alpha^2 \Delta\overline{\omega} + \overline{\omega} = \omega, \tag{2.2c}$$

where $\overline{\omega}$ is the filtered vorticity and α is the filter length scale. A more complete description of BV-α is presented in [47].

However, from the equation (2.2c) we can see that the BV-α, as well as its analogue counterpart for the Navier-Stokes equations, has an $O(\alpha^2)$ consistency error. Experiments have shown in the Navier-Stokes equations case (see [105] and references therein) that alpha models can have large error growth and that this error growth can be attenuated when accuracy is increased by replacing the filtered field by some higher order aproximation of the original field. Deconvolution regularization is a kind of regularization in which the filtered velocity $\overline{u}$ (or vorticity in the BV model case) is substituted in the regularized model by $D\overline{u}$ where D is a proper deconvolution operator. The Tikhonov-Lavrentiev regularization is a general approach to deal with ill-posed problems which allows to select desirable solutions in the least square method. It can also be employed to produce a suitable approximate solution to the deconvolution problem. In [105] the filtered velocity $\overline{u}$ is replaced by $D_\mu \overline{u}$ where the deconvolution operator $D_\mu = [F + \mu(I - F)]^{-1}$ is the modified Tikhonov-Lavrentiev regularization of the formal filter inverse F^{-1} and $0 < \mu \leq 1$ is a regularization parameter. Following the study presented in [105] on the application of the Tikhonov-Lavrentiev deconvolution in the Navier-Stokes context, in this chapter we study a family of Tikhonov-Lavrentiev regularizations of the BV model, hereafter called BV-Tikhonov model, that results by replacing $\overline{\omega}$ by $D_\mu \overline{\omega}$ in (2.2b). We note that in this framework the original BV-α model results from the BV-Tikhonov family in the case in which $\mu = 1$.

In order to apply the Tikhonov-Lavrentiev deconvolution in the BV-α model, we propose and study a Crank-Nicolson in time, finite element (FE) in space algorithm to approximate solution for the BV-Tikhonov model. We believe the advantage of BV-Tikhonov model over other techniques to deal with turbulence is in its simplicity, as there is only one filtering procedure that needs to be performed and in its direct control over the regularization intensity through the μ parameter. Moreover, although a significant amount of work has been done on the related vorticity-streamfunction formulation of the Navier-Stokes equations (see [4] and references therein) and for steady state analysis of numerical schemes for BV model [26, 27], a numerical analysis for the BV-α model has not been performed. Thus, the main objective of this chapter is to provide a FE algorithm for the BV-Tikhonov model and study it from the numerical analysis point of the view. To the best of our knowledge, this is the first time that the FE method is applied to obtain approximated solutions for the BV-Tikhonov model.

The chapter is organized as follows: Section 2 introduces some notation and mathematical prelimimaries. The BV-Tikhonov algorithm and its stability are presented in Section 3. Convergence analysis is presented in Section 4. In Section 5 simulations are performed in order to estimate model convergence rates and to test the BV-Tikhonov model in the more realistic double gyre wind forcing experiment. Finally, the main conclusions and final remarks are summarized in Section 6.

2.2 Preliminaries

Let $\Omega \subset \mathbb{R}^2$ be a polygonal domain and τ_h be a regular discretization of Ω. Let H^1 be the Sobolev space $W_2^1(\Omega)$ and H_0^1 its subspace with zero boundary condition. Let Y_h be the continuous finite element (FE) with kth degree polynomial on each element of the triangulation τ_h [18] and X_h be the subspace of Y_h with zero boundary values. Denote by $\langle \cdot, \cdot \rangle$ and $\| \cdot \|$ the inner product and norm in $L^2(\Omega)$ and $\| \cdot \|_k$ for the norm in the space H^k.

For continuous in time functions we denote for $1 \leq m < \infty$

$$\|f\|_{\infty,k} := \operatorname*{ess\,sup}_{t\in(0,T)} \|f(t,\cdot)\|_k \text{ and } \|f\|_{m,k} := \Big\{ \int_0^T \|f(t,\cdot)\|_k^m dt \Big\}^{\frac{1}{m}}.$$

For the discrete case we denote

$$|||f|||_{\infty,k} := \operatorname*{ess\,sup}_{0\leq n\leq M} \|f^n\|_k, \ |||f^{1/2}|||_{m,k} := \Big\{ \sum_{n=0}^{M} \|f^{n+\frac{1}{2}}\|_k^m dt \Big\}^{\frac{1}{m}}.$$

As in [100], we consider slip boundary conditions for the velocity which translate into homogeneous Dirichlet condition $\omega|_{\partial\Omega} = 0$ and the impermeability condition $\psi|_{\partial\Omega} = 0$. Multiplying (2.1) by appropriate test functions and integrating by parts, the BV model reads in its variational formulation: find $(\omega, \psi) \in H_0^1 \times H_0^1$ such that

$$\big\langle \tfrac{\partial \omega}{\partial t}, \lambda \big\rangle + b\big(\psi, \omega, \lambda\big) - \big\langle \tfrac{\partial \psi}{\partial x}, \lambda \big\rangle + \big(\tfrac{\delta_M}{L}\big)^3 \langle \nabla\omega, \nabla\lambda \rangle = \big\langle F, \lambda \big\rangle \ \forall \lambda \in H_0^1, \tag{2.3a}$$

$$\big\langle \nabla\psi, \nabla\chi \big\rangle = \big\langle \omega, \chi \big\rangle \ \forall \chi \in H_0^1. \tag{2.3b}$$

where $b\big(\cdot,\cdot,\cdot\big) := \big\langle J\big(\cdot,\cdot\big), \cdot \big\rangle$ represents the trilinear form.

Now we present some definitions and lemmas which are helpful in the subsequent analysis.

Lemma 2.1 (Skew-symmetry of the trilinear form)**.** *For ψ, $\xi \in X_h$ and $\chi \in Y_h$,*

$$b\big(\psi, \chi, \xi\big) = -b\big(\psi, \xi, \chi\big).$$

Proof. We start from the vector identity

$$\big[(\nabla\psi \times \mathbf{k})\cdot\nabla\chi\big]\xi = \big[\nabla\cdot(\nabla\psi\times\mathbf{k})\big]\chi\xi - \big[(\nabla\psi\times\mathbf{k})\cdot\nabla\xi\big]\chi - \nabla\cdot\big[(\nabla\psi\times\mathbf{k})\chi\xi\big].$$

Integrating and using the divergence theorem, the result follows because of the cyclic continuity inside elements and since $\xi \in X_h$. □

We also make use of the following estimate for the non-linear term

Lemma 2.2. *Let $\zeta, \phi \in H_0^1$ and $\xi \in H^2 \cap H_0^1$ we have*

$$|b\big(\xi,\phi,\zeta\big)| \le C(\Omega)\|\nabla\xi\|_1\|\nabla\phi\|\|\zeta\|_1.$$

Proof. The result follows using Holder's inequality with $p, q = 4$ and $r = 2$ and the embedding $H^1 \hookrightarrow L^4$. □

Given $\xi \in H_0^1$, let $P\xi \in X^h$ be the standard L^2 projection of ξ onto X^h such that

$$\big\langle \xi - P\xi, \phi\big\rangle = 0 \ \forall\phi \in X^h,$$

and $\Pi\xi \in X^h$ be the Elliptic projection of ξ onto X^h such that

$$\big\langle \nabla(\xi - \Pi\xi), \nabla\phi\big\rangle = 0 \ \forall\phi \in X^h.$$

Lemma 2.3. *Given $\xi \in H^k$ we have the following estimates [109]*

$$\begin{aligned} &i)\ \|\xi - P\xi\| \le Ch^{k+1}\|\xi\|_{k+1},\\ &ii)\ \|\nabla(\xi - P\xi)\| \le Ch^{k}\|\xi\|_{k+1},\\ &iii)\ \|\nabla(\xi - \Pi\xi)\| \le Ch^{k}\|\xi\|_{k+1}.\end{aligned}$$

Taylor expansion with integral remainder [60] gives

Lemma 2.4. *Assume $f \in C^0(t^n, t^{n+1}; L^2(\Omega))$. If f is twice differentiable in time and $f_{tt} \in L^2((t^n, t^{n+1}) \times \Omega)$ then*

$$\big\|f^{n+\frac{1}{2}} - f(t^{n+\frac{1}{2}})\big\|^2 \le \tfrac{\Delta t^3}{48}\int_{t^n}^{t^{n+1}} \big\|f_{tt}\big\|^2 dt.$$

If $f_t \in C^0(t^n, t^{n+1}; L^2(\Omega))$ *and* $f_{ttt} \in L^2((t^n, t^{n+1}) \times \Omega)$ *then*

$$\left\| \tfrac{f^{n+1}-f^n}{\Delta t} - f_t(t^{n+\frac{1}{2}}) \right\|^2 \leq \tfrac{\Delta t^3}{1280} \int_{t^n}^{t^{n+1}} \|f_{ttt}\|^2 dt.$$

If $\nabla f \in C^0(t^n, t^{n+1}; L^2(\Omega))$ *and* $\nabla f_{tt} \in L^2((t^n, t^{n+1}) \times \Omega)$ *then*

$$\left\| \nabla\big(f^{n+\frac{1}{2}} - f(t^{n+\frac{1}{2}})\big) \right\|^2 \leq \tfrac{\Delta t^3}{48} \int_{t^n}^{t^{n+1}} \|\nabla f_{tt}\|^2 dt.$$

The convergence analysis relies in the following discrete Gronwall inequality [45]:

Lemma 2.5. *Let* $\Delta t \in \mathbb{R}_{>0}$ *and* $H, a_n, b_n, c_n, d_n \in \mathbb{R}_{\geq 0}$ $(n \in \mathbb{Z}_{\geq 0})$ *such that*

$$a_l + \Delta t \sum_{n=0}^{l} b_n \leq \Delta t \sum_{n=0}^{l} d_n a_n + \Delta t \sum_{n=0}^{l} c_n + H \text{ for } l \geq 0.$$

Suppose that $d_n \Delta t \leq 1\ \forall n$*. Then,*

$$a_l + \Delta t \sum_{n=0}^{l} b_n \leq \exp\Big(\Delta t \sum_{n=0}^{l} \tfrac{d_n}{1-\Delta t d_n}\Big)\Big(\Delta t \sum_{n=0}^{l} c_n + H\Big) \text{ for } l \geq 0.$$

We also make use of the Young inequality given by

Lemma 2.6.

$$ab \leq \tfrac{\epsilon}{2}a^2 + \tfrac{1}{2\epsilon}b^2 \text{ for } \epsilon > 0.$$

2.2.1 Discrete filtering and the modified Tikhonov deconvolution

The discrete Laplacian operator $\Delta_h : H_0^1 \to X^h$ is defined in the usual way by

$$\langle \Delta_h \psi, \chi \rangle = -\langle \nabla\psi, \nabla\chi \rangle,\ \forall \chi \in X^h.$$

As [66], given $\phi \in L^2$, the continuous and discrete filters are defined respectively as the unique solution $\overline{\phi} = F\phi$ in X and $\overline{\phi}^h = F_h\phi$ in X^h of

$$\alpha^2 \langle \nabla\overline{\phi}, \nabla\xi \rangle + \langle \overline{\phi}, \xi \rangle = \langle \phi, \xi \rangle\ \forall \xi \in X,$$
$$\alpha^2 \langle \nabla\overline{\phi}^h, \nabla\xi \rangle + \langle \overline{\phi}^h, \xi \rangle = \langle \phi, \xi \rangle\ \forall \xi \in X^h.$$

We also define the continuous and the discrete modified Tikhonov Deconvolution operator by: given the filter radius $\alpha > 0$ and $0 < \mu \le 1$, the continuous D_μ and its discrete counterpart, denoted by D_μ^h, are defined to be

$$\begin{aligned} D_\mu &= \big[(1-\mu)F + \mu I\big]^{-1} = \big[F + \mu(I-F)\big]^{-1}, \\ D_\mu^h &= \big[(1-\mu)F_h + \mu I\big]^{-1} = \big[F_h + \mu(I-F_h)\big]^{-1}. \end{aligned}$$

From the D_μ and D_μ^h definitions, we can see that the modified Tikhonov-Lavrentiev deconvolution can be interpreted as a Tikhonov-Lavrentiev deconvolution with the "Tikhonov matrix" being the high pass filters $I - F$ and $I - F_h$. Clearly from the D_μ^h definition, $D_\mu^h F_h \phi$ can be determined by

$$\mu\alpha^2\big\langle \nabla D_\mu^h F_h\phi, \nabla\xi\big\rangle + \big\langle D_\mu^h F_h\phi, \xi\big\rangle = \big\langle \phi, \xi\big\rangle \ \forall \xi \in X^h.$$

The following lemma regarding D_μ^h is presented in [105]

Lemma 2.7. *The operator D_μ^h is bounded, self-adjoint and positive definite on X^h. For $\phi \in X$, the following bounds holds*

$$\begin{aligned} \|D_\mu^h\overline{\phi}^h\| &\le \|\phi\|. \\ \|\nabla D_\mu^h\overline{\phi}^h\| &\le sC(\Omega)\|\nabla\phi\|. \end{aligned}$$

The following estimate for $\phi - D_\mu^h\overline{\phi}^h$ is also presented in [105]

Lemma 2.8. *For all $\phi \in X$ with $\Delta\phi \in L^2(\Omega)$, we have*

$$\|\phi - D_\mu^h\overline{\phi}^h\| \le \mu\alpha^2\|\phi\|_2 + \big(\alpha h^k + h^{k+1}\big)\|\overline{\phi}\|_{k+1} + \big(\mu^{1/2}\alpha h^k + h^{k+1}\big)\|D_\mu\overline{\phi}\|_{k+1}.$$

2.3 The Finite Element algorithm and its stability

Our motivation for studying the BV-Tikhonov model is the search for efficient, unconditionally stable and accurate methods in order to simulate geophysical flows. We propose now a finite element discretization in space, together with a Crank-Nicolson in time discretization. As is common in such discretizations, we denote the half timestep by $v^{n+\frac{1}{2}} := \frac{v^n+v^{n+1}}{2}$ and $t^{n+\frac{1}{2}} := \frac{t^n+t^{n+1}}{2}$.

Algorithm 2.1 (Crank-Nicolson - BV-Tikhonov model)**.** *Let ω_h^0 and ψ_h^0 be the $L^2(\Omega)$ projections into X_h of $\omega_0 \in X$ and $\psi_0 \in X$, endtime T, $F \in L^\infty(0,T;L^2(\Omega))$, and timestep $\Delta t > 0$. Set $M = \frac{T}{\Delta t}$ and for n=0,...,M-1, find $(\omega^n, \psi^n, D_\mu^h \overline{\omega^n}^h) \in X_h \times X_h \times X_h$ satisfying:*

$$
\begin{aligned}
Ro\big\langle \tfrac{\omega_h^{n+1}-\omega_h^n}{\Delta t}, \lambda\big\rangle + Ro\; b\big(\psi_h^{n+\frac{1}{2}}, \omega_h^{n+\frac{1}{2}}, \lambda\big) - \big\langle \tfrac{\partial \psi_h^{n+\frac{1}{2}}}{\partial x}, \lambda\big\rangle &\\
+\big(\tfrac{\delta_M}{L}\big)^3 \big\langle \nabla \omega_h^{n+\frac{1}{2}}, \nabla\lambda\big\rangle = \big\langle \mathcal{F}^{n+\frac{1}{2}}, \lambda\big\rangle \;\forall \lambda \in X^h, &\qquad (2.5a)\\
\big\langle \nabla \psi_h^{n+1}, \nabla\chi\big\rangle = \big\langle D_\mu^h \overline{\omega_h^{n+1}}^h, \chi\big\rangle \;\forall \chi \in X^h, &\qquad (2.5b)\\
\mu\alpha^2 \big\langle \nabla D_\mu^h \overline{\omega_h^{n+1}}^h, \nabla\xi\big\rangle + \big\langle D_\mu^h \overline{\omega_h^{n+1}}^h, \xi\big\rangle = \big\langle \omega_h^{n+1}, \xi\big\rangle \;\forall \xi \in X^h. &\qquad (2.5c)
\end{aligned}
$$

We are going to show that Algorithm 2.1 is unconditionally stable. The first step is to demonstrate that Algorithm 2.1 conserves enstrophy and kinetic energy. We start defining the Modified Kinetic Energy, the Modified Dissipation and the Enstrophy in the BV-Tikhonov model respectively by

$$
\begin{aligned}
E_\alpha^\mu(\psi,\omega) &:= \tfrac{1}{2}\|\nabla\psi\|^2 + \tfrac{1}{2}\mu\alpha^2 \|D_\mu^h \overline{\omega}^h\|^2,\\
\epsilon_\alpha^\mu(\psi,\omega) &:= \big(\tfrac{\delta_M}{L}\big)^3 \mu\alpha^2 \|\nabla D_\mu^h \overline{\omega}^h\|^2 + \big(\tfrac{\delta_M}{L}\big)^3 \|D_\mu^h \overline{\omega}^h\|^2,\\
\mathcal{E}(\omega) &:= \tfrac{1}{2}\|\omega\|^2.
\end{aligned}
$$

We obtain the following lemma:

Lemma 2.9 (Conservation of kinetic energy)**.** *The solution of (2.5a) satisfies*

$$
E_\alpha^\mu(\psi_h^M, \omega_h^M) + \tfrac{\Delta t}{Ro} \sum_{n=0}^{M-1} \epsilon_\alpha^\mu\big(\psi_h^{n+\frac{1}{2}}, \omega_h^{n+\frac{1}{2}}\big) = E_\alpha^\mu(\psi_h^0, \omega_h^0) + \tfrac{\Delta t}{Ro} \sum_{n=0}^{M-1} \big\langle \mathcal{F}^{n+\frac{1}{2}}, \psi_h^{n+\frac{1}{2}}\big\rangle.
$$

In particular, if $\delta_M = 0$ and $\mathcal{F} = 0$ we have $E_\alpha^\mu(\psi_h^M, \omega_h^M) = E_\alpha^\mu(\psi_h^0, \omega_h^0)$.

Proof. Rewriting the non-linear term in (2.5a) as $b(\psi_h^{n+\frac{1}{2}}, Ro\omega_h^{n+\frac{1}{2}} + y, \lambda)$, choosing $\lambda = \psi_h^{n+\frac{1}{2}}$ and using Lemma 2.1, we obtain after we multiply by $\frac{\Delta t}{Ro}$

$$
\big\langle \omega_h^{n+1} - \omega_h^n, \psi_h^{n+\frac{1}{2}}\big\rangle + \tfrac{\Delta t}{Ro}\big(\tfrac{\delta_M}{L}\big)^3 \big\langle \nabla\omega_h^{n+\frac{1}{2}}, \nabla\psi_h^{n+\frac{1}{2}}\big\rangle = \tfrac{\Delta t}{Ro}\big\langle \mathcal{F}^{n+\frac{1}{2}}, \psi_h^{n+\frac{1}{2}}\big\rangle. \qquad (2.6)
$$

Now, we analyze the two terms on the LHS. For the first, subtracting (2.5b) in time step n from (2.5b) in time step $n+1$ and choosing $\chi = \psi_h^{n+\frac{1}{2}}$ gives

$$\big\langle D_\mu^h\big(\overline{\omega_h^{n+1}}^h - \overline{\omega_h^n}^h\big), \psi_h^{n+\frac{1}{2}}\big\rangle = \big\langle \nabla\psi_h^{n+1} - \nabla\psi_h^n, \nabla\psi_h^{n+\frac{1}{2}}\big\rangle = \tfrac{\|\nabla\psi_h^{n+1}\|^2 - \|\nabla\psi_h^n\|^2}{2}. \tag{2.7}$$

Averaging in (2.5b) and choosing $\chi = D_\mu^h\big(\overline{\omega}_h^{n+1} - \overline{\omega}_h^n\big)$, we obtain

$$\big\langle \nabla\psi_h^{n+\frac{1}{2}}, \nabla D_\mu^h\big(\overline{\omega_h^{n+1}}^h - \overline{\omega_h^n}^h\big)\big\rangle = \big\langle D_\mu^h\overline{\omega_h^{n+\frac{1}{2}}}^h, D_\mu^h\big(\overline{\omega_h^{n+1}}^h - \overline{\omega_h^n}^h\big)\big\rangle = \tfrac{\|D_\mu^h\overline{\omega_h^{n+1}}^h\|^2 - \|D_\mu^h\overline{\omega_h^n}^h\|^2}{2}. \tag{2.8}$$

Subtracting (2.5c) in time step n from (2.5c) in time step $n+1$ and choosing $\xi = \psi_h^{n+\frac{1}{2}}$, we have

$$\mu\alpha^2\big\langle \nabla D_\mu^h\big(\overline{\omega_h^{n+1}}^h - \overline{\omega_h^n}^h\big), \nabla\psi_h^{n+\frac{1}{2}}\big\rangle + \big\langle D_\mu^h\big(\overline{\omega_h^{n+1}}^h - \overline{\omega_h^n}^h\big), \psi_h^{n+\frac{1}{2}}\big\rangle = \big\langle \omega_h^{n+1} - \omega_h^n, \psi_h^{n+\frac{1}{2}}\big\rangle \tag{2.9}$$

Combining (2.7) and (2.8) in (2.9) we obtain, after we use the definition of $E_\alpha^\mu(\psi, \omega)$,

$$E_\alpha^\mu(\psi_h^{n+1}, \omega^{n+1}) - E_\alpha^\mu(\psi_h^n, \omega^n) = \big\langle \omega_h^{n+1} - \omega_h^n, \psi_h^{n+\frac{1}{2}}\big\rangle. \tag{2.10}$$

For the second term in (2.6), averaging in (2.5b) and (2.5c) and choosing respectively $\chi = \omega_h^{n+\frac{1}{2}}$ and $\xi = D_\mu^h\overline{\omega}_h^{n+\frac{1}{2}}$,

$$\big\langle \nabla\psi_h^{n+\frac{1}{2}}, \nabla\omega_h^{n+\frac{1}{2}}\big\rangle = \big\langle D_\mu^h\overline{\omega_h^{n+\frac{1}{2}}}^h, \omega_h^{n+\frac{1}{2}}\big\rangle, \tag{2.11}$$

$$\mu\alpha^2\|\nabla D_\mu^h\overline{\omega_h^{n+\frac{1}{2}}}^h\|^2 + \|D_\mu^h\overline{\omega_h^{n+\frac{1}{2}}}^h\|^2 = \big\langle \omega_h^{n+\frac{1}{2}}, D_\mu^h\overline{\omega_h^{n+\frac{1}{2}}}^h\big\rangle. \tag{2.12}$$

Combining (2.11) and (2.12) we have

$$\mu\alpha^2\|\nabla D_\mu^h\overline{\omega_h^{n+\frac{1}{2}}}^h\|^2 + \|D_\mu^h\overline{\omega_h^{n+\frac{1}{2}}}^h\|^2 = \big\langle \nabla\psi_h^{n+\frac{1}{2}}, \nabla\omega_h^{n+\frac{1}{2}}\big\rangle. \tag{2.13}$$

Using (2.10) and (2.13) in (2.6)

$$\begin{aligned} &E_\alpha^\mu(\psi_h^{n+1}, \omega^{n+1}) - E_\alpha^\mu(\psi_h^n, \omega^n) \\ &\qquad + \tfrac{\Delta t}{Ro}\big(\tfrac{\delta_M}{L}\big)^3\big(\mu\alpha^2\|\nabla D_\mu^h\overline{\omega_h^{n+\frac{1}{2}}}^h\|^2 + \|D_\mu^h\overline{\omega_h^{n+\frac{1}{2}}}^h\|^2\big) = \tfrac{\Delta t}{Ro}\big\langle \mathcal{F}^{n+\frac{1}{2}}, \psi_h^{n+\frac{1}{2}}\big\rangle. \end{aligned} \tag{2.14}$$

The result follows summing from $n = 0, 1, ..., M-1$. □

We also have

Lemma 2.10 (Conservation of enstrophy)**.**

$$\mathcal{E}(\omega_h^M) + \tfrac{\Delta t}{Ro}\big(\tfrac{\delta_M}{L}\big)^3 \sum_{n=0}^{M} \|\nabla \omega_h^{n+\frac{1}{2}}\|^2 = \\ \mathcal{E}(\omega_h^0) + \tfrac{\Delta t}{Ro} \sum_{n=0}^{M} \big\langle \tfrac{\partial \psi_h^{n+\frac{1}{2}}}{\partial x}, \omega_h^{n+\frac{1}{2}} \big\rangle + \tfrac{\Delta t}{Ro} \sum_{n=0}^{M} \big\langle \mathcal{F}^{n+\frac{1}{2}}, \omega_h^{n+\frac{1}{2}} \big\rangle. \tag{2.15}$$

In particular, if $\delta_M = \mathcal{F} = 0$ *and* Ro *is sufficiently large* $\mathcal{E}(\omega_h^M) = \mathcal{E}(\omega_h^0)$.

Proof. Choosing $\lambda = \omega_h^{n+\frac{1}{2}}$ in (2.5a), using Lemma 2.1, multiplying by $\frac{\Delta t}{Ro}$ we obtain

$$\|\omega_h^{n+1}\|^2 + \tfrac{\Delta t}{Ro}\big(\tfrac{\delta_M}{L}\big)^3 \|\nabla \omega_h^{n+\frac{1}{2}}\|^2 = \|\omega_h^n\|^2 + \tfrac{\Delta t}{Ro}\big\langle \tfrac{\partial \psi_h^{n+\frac{1}{2}}}{\partial x}, \omega_h^{n+\frac{1}{2}} \big\rangle + \tfrac{\Delta t}{Ro}\big\langle \mathcal{F}^{n+\frac{1}{2}}, \omega_h^{n+\frac{1}{2}} \big\rangle. \tag{2.16}$$

Summing from $n = 0, 1, ..., M-1$, the result follows, after we use the $\mathcal{E}(\omega)$ definition.

$\square$

Lemma 2.11 (Stability)**.** *Algorithm 2.1 is unconditionally stable. Its solutions satisfy*

$$\mu\alpha^2 \|D_\mu^h \overline{\omega_h^M}^h\|^2 + \|\nabla \psi_h^M\|^2 + \tfrac{\Delta t}{Ro}\big(\tfrac{\delta_M}{L}\big)^3 \sum_{n=0}^{M} \big(\mu\alpha^2 \|\nabla D_\mu^h \overline{\omega_h^{n+\frac{1}{2}}}^h\|^2 + \tfrac{1}{2}\|\Delta_h \psi_h^{n+\frac{1}{2}}\|^2\big) \leq C(data)$$

$$\|\omega_h^M\|^2 + \tfrac{\Delta t}{Ro}\big(\tfrac{\delta_M}{L}\big)^3 \sum_{n=0}^{M} \|\nabla \omega_h^{n+\frac{1}{2}}\|^2 \leq C(data)$$

Remark 2.1. *The bounds in Lemma 2.11 are sufficient for the Leray-Schauder fixed point theorem to be applied, in order to prove existence of a solution at each timestep (as in [60]). Uniqueness can be proven in the standard way, and will hold provided a timestep restriction.*

Proof. First we bound the streamfunction in the first inequality in the lemma above. Using (2.14) and the Cauchy-Schwarz inequality we have

$$E_\alpha^\mu(\psi_h^{n+1}, \omega_h^{n+1}) - E_\alpha^\mu(\psi_h^n, \omega_h^n) \\ + \tfrac{\Delta t}{Ro}\big(\tfrac{\delta_M}{L}\big)^3 \big(\mu\alpha^2 \|\nabla D_\mu^h \overline{\omega_h^{n+\frac{1}{2}}}^h\|^2 + \|D_\mu^h \overline{\omega_h^{n+\frac{1}{2}}}^h\|^2\big) \leq \tfrac{\Delta t}{Ro} \|\mathcal{F}^{n+\frac{1}{2}}\|_{-1} \|\nabla \psi_h^{n+\frac{1}{2}}\|.$$

Averaging in (2.5b), choosing $\chi = \psi_h^{n+\frac{1}{2}}$ and using Cauchy-Schwarz and Poincaré inequalities we have $\|\nabla \psi_h^{n+\frac{1}{2}}\| \leq C_{PF}\|\overline{D_\mu^h \omega_h^{n+\frac{1}{2}}}^h\|$. Thus, using Young's inequality with $\epsilon = \left(\frac{\delta_M}{L}\right)^3$

$$
\begin{aligned}
E_\alpha^\mu(\psi_h^{n+1}, \omega^{n+1}) - E_\alpha^\mu(\psi_h^n, \omega^n) + \tfrac{\Delta t}{Ro}\left(\tfrac{\delta_M}{L}\right)^3 \left(\mu\alpha^2 \|\nabla \overline{D_\mu^h \omega_h^{n+\frac{1}{2}}}^h\|^2 + \tfrac{1}{2}\|\overline{D_\mu^h \omega_h^{n+\frac{1}{2}}}^h\|^2\right) \\
\leq \left(\tfrac{L}{\delta_M}\right)^3 \tfrac{C_{PF}^2}{Ro} \Delta t \|\mathcal{F}^{n+\frac{1}{2}}\|_{-1}^2.
\end{aligned}
$$

from which the result follows summing from $n = 0, 1, ..., M-1$ and using the $E_\alpha(\psi, \omega)$ definition.

Now we bound the vorticity ω. Using (2.16) and Cauchy-Schwarz and Poincaré inequalities

$$
\begin{aligned}
\mathcal{E}(\omega_h^{n+1}) - \mathcal{E}(\omega_h^n) + \tfrac{\Delta t}{Ro}\left(\tfrac{\delta_M}{L}\right)^3 \|\nabla \omega_h^{n+\frac{1}{2}}\|^2 \\
\leq \tfrac{\Delta t}{Ro}\|F(t^{n+\frac{1}{2}})\|_{-1}\|\nabla \omega_h^{n+\frac{1}{2}}\| + \tfrac{\Delta t}{Ro} C_{PF} \big\|\nabla \psi_h^{n+\frac{1}{2}}\big\| \big\|\nabla \omega_h^{n+\frac{1}{2}}\big\|.
\end{aligned}
$$

The result follows using Young's inequality with $\epsilon = \frac{1}{2}\left(\frac{\delta_M}{L}\right)^3$, the $\mathcal{E}(\omega)$ definition and summing from $n = 0, 1, ..., M-1$. $\square$

2.4 Convergence analysis

Now we present our main convergence result for the discrete BV-Tikhonov model

Theorem 2.1 (Convergence)**.** *Consider the discrete BV-Tikhonov model. Let $(\omega(t), \psi(t))$ be a smooth strong solution of the BV model satisfying free slip boundary conditions such that the norms of $(\omega(t), \psi(t))$ on the right hand side of (2.17) and (2.18) are finite. Suppose $\omega_h, \psi_h \in X^h \times X^h$ solves the Crank-Nicolson approximation (2.5a)-(2.5c) of the BV-Tikhonov model with $X_h = (P_k)^2 \cap X$. Then for Δt small enough* *(in order to apply the discrete Gronwall inequality), we have*

$$\big\||\omega-\omega_h|\big\|_{\infty,0} \le F\big(\Delta t,h,\mu,\alpha\big) + Ch^{k+1}\big\||\omega|\big\|_{\infty,k+1}, \tag{2.17}$$

$$\Big(\big(\tfrac{\delta_M}{L}\big)^3\sum_{n=0}^{M-1}\tfrac{\Delta t}{Ro}\big\|\nabla\big(\omega(t^{n+\frac{1}{2}})-\omega_h^{n+\frac{1}{2}}\big)\big\|^2\Big)^{1/2} \le F\big(\Delta t,h,\mu,\alpha\big) + C\Delta t^2\big(\tfrac{\delta_M}{L}\big)^{3/2}\big\|\omega_{tt}\big\|_{2,0} + C\big(\tfrac{\delta_M}{L}\big)^{3/2}h^k\big\||\omega|\big\|_{2,k+1} \tag{2.18}$$

where

$$\begin{aligned}F\big(\Delta t,h,\alpha\big) := C^*\Big\{&h^k\big(\tfrac{L}{\delta_M}\big)^{3/2}\Big[C\big(\tfrac{\delta_M}{L}\big)^3\||\omega^{1/2}|\|_{2,k+1} + C\||\psi^{1/2}|\|_{2,k+1} + hC\||\omega^{1/2}|\|_{2,k+1}\\
&+\big(\alpha+h\big)C\||\overline{\omega^{1/2}}|\|_{2,k+1} + \big(\mu^{1/2}\alpha+h\big)C\||D_\mu\overline{\omega^{1/2}}|\|_{2,k+1} + hCRo\||\omega^{1/2}|\|_{4,k+1}^2 + CRo\||\nabla\omega^{1/2}|\|_{4,1}^2\\
&+CRo\||\psi^{1/2}|\|_{4,k+1}^2 + \big(\alpha+h\big)CRo\||\overline{\omega^{1/2}}\|_{4,k+1}^2 + \big(\mu^{1/2}\alpha+h\big)CRo\||D_\mu\overline{\omega^{1/2}}|\|_{4,k+1}^2\\
&+\big(\alpha+2h+\mu^{1/2}\alpha\big)CRo\||\nabla\omega^{1/2}|\|_{4,1}^2 + hCRo\||\psi^{1/2}|\|_{4,k+1}^2 + hCRo\||\omega^{1/2}|\|_{4,k+1}^2 + CRo\||\omega^{1/2}|\|_{4,1}^2\\
&+\big(\alpha+h\big)CRo\|\overline{\omega^{1/2}}\|_{4,k+1}^2 + \big(\alpha+h+\mu^{1/2}\alpha\big)CRo\||\omega^{1/2}|\|_{4,k+1}^2 + \big(\mu^{1/2}\alpha+h\big)CRo\||D_\mu\overline{\omega^{1/2}}|\|_{4,k+1}^2\Big]\\
&+\mu\alpha^2\big(\tfrac{L}{\delta_M}\big)^{3/2}C\Big[\||\omega^{1/2}|\|_{2,2} + CRo\||\omega^{1/2}|\|_{4,2}^2 + Ro\||\nabla\omega^{1/2}|\|_{4,1}^2 + Ro\||\omega^{1/2}|\|_{4,k+1}^2 + Ro\||\omega^{1/2}|\|_{4,2}^2\Big]\\
&+\Delta t^2\big(\tfrac{L}{\delta_M}\big)^{3/2}CRo\Big[\|\omega_{ttt}\|_{2,0} + C\|\nabla\omega_{tt}\|_{2,0} + C\|\psi_{tt}\|_{2,0} + C\big\||\nabla\psi^{1/2}|\big\|_{4,1}^2 + C\|\omega_{tt}\|_{4,1}^2\\
&+C\big\||\nabla\omega^{1/2}|\big\|_{4,1}^2 + C\|\psi_{tt}\|_{4,1}^2\Big]\Big\}.\end{aligned}$$

k is the polynomial degree in the vorticity and streamfunction finite element space.

Remark 2.2. *The smallness assumption on the time step Δt above mentioned is given by $\Delta t < \big({}^{\delta_M}/_L\big)^3\big(C + CRo^2\|\nabla\omega^{n+\frac{1}{2}}\|_1^2 + CRo^2\|\omega^{n+\frac{1}{2}}\|_{k+1}^2\big)^{-1}$. The constant C^* depends on $\big({}^{\delta_M}/_L\big)^3$ like $\exp\big(\big({}^{\delta_M}/_L\big)^{-3}T\big)$.*

Corollary 2.1. *Suppose that the indicated norms on the right hand side of (2.17)-(2.18) are finite. Then the error in the Crank-Nicolson finite element scheme for the BV-Tikhonov is of the order*

$$\begin{aligned}\big\||\omega-\omega_h|\big\|_{\infty,0} + \Big(\big(\tfrac{\delta_M}{L}\big)^3\sum_{n=0}^{M-1}\Delta t\big\|\nabla\big(\omega(t^{n+\frac{1}{2}})-\omega_h^{n+\frac{1}{2}}\big)\big\|^2\Big)^{1/2}&\\
= O\big(h^k+\Delta t^2+\mu\alpha^2\big).&\end{aligned}$$

Moreover,

$$|||\psi - \psi_h|||_{2,1} \leq O\big(h^k + \Delta t^2 + \mu\alpha^2\big).$$

Proof of Theorem 2.1. The solution ω of the BV model (2.3a) satisfies

$$Ro\Big\langle \tfrac{\omega^{n+1}-\omega^n}{\Delta t}, v_h\Big\rangle + Ro\; b\big(\psi^{n+\frac{1}{2}}, \omega^{n+\frac{1}{2}}, v_h\big) - \big\langle \tfrac{\partial \psi^{n+\frac{1}{2}}}{\partial x}, v_h\big\rangle + \big(\tfrac{\delta_M}{L}\big)^3\big\langle \nabla\omega^{n+\frac{1}{2}}, \nabla v_h\big\rangle$$
$$= \big\langle \mathcal{F}^{n+\frac{1}{2}}, v_h\big\rangle + Intp(\omega^n, \psi^n; v_h)\ \forall v_h \in X^h \qquad (2.19)$$

where

$$Intp(\omega^n, \psi^n; v_h) := Ro\big\langle \tfrac{\omega^{n+1}-\omega^n}{\Delta t} - \omega_t(t^{n+\frac{1}{2}}), v_h\big\rangle + \big(\tfrac{\delta_M}{L}\big)^3\big\langle \nabla\omega^{n+\frac{1}{2}} - \nabla\omega(t^{n+\frac{1}{2}}), \nabla v_h\big\rangle \qquad (2.20)$$
$$-\big\langle \tfrac{\partial \psi^{n+\frac{1}{2}}}{\partial x} - \tfrac{\partial \psi(t^{n+\frac{1}{2}})}{\partial x}, v_h\big\rangle + Ro\big[b\big(\psi^{n+\frac{1}{2}}, \omega^{n+\frac{1}{2}}, v_h\big) - b\big(\psi(t^{n+\frac{1}{2}}), \omega(t^{n+\frac{1}{2}}), v_h\big)\big]. \qquad (2.21)$$

Now we define

$$e := \omega - \omega_h = \big(\omega - P\omega\big) - \big(\omega_h - P\omega\big) = e_\perp - e_h,$$
$$E := \psi - \psi_h = \big(\psi - \Pi\psi\big) - \big(\psi_h - \Pi\psi\big) = E_\perp - E_h.$$

Subtracting (2.5a) from (2.19), adding and subtracting $b\big(\psi_h^{n+\frac{1}{2}}, \omega^{n+\frac{1}{2}}, v_h\big)$ and choosing $v_h = e_h^{n+\frac{1}{2}}$ we obtain

$$Ro(\|e_h^{n+1}\|^2 - \|e_h^n\|^2) + 2\Delta t\big(\tfrac{\delta_M}{L}\big)^3\|\nabla e_h^{n+\frac{1}{2}}\|^2 = 2\Delta t\big(\tfrac{\delta_M}{L}\big)^3\big\langle \nabla e_\perp^{n+\frac{1}{2}}, \nabla e_h^{n+\frac{1}{2}}\big\rangle$$
$$-2\Delta t\big\langle \tfrac{\partial E^{n+\frac{1}{2}}}{\partial x}, e_h^{n+\frac{1}{2}}\big\rangle + 2Ro\Delta t\big[b\big(\psi_h^{n+\frac{1}{2}}, e_\perp^{n+\frac{1}{2}}, e_h^{n+\frac{1}{2}}\big) + b\big(E^{n+\frac{1}{2}}, \omega^{n+\frac{1}{2}}, e_h^{n+\frac{1}{2}}\big)\big]$$
$$- 2\Delta t Intp(\omega^n, \psi^n; e_h^{n+\frac{1}{2}}). \qquad (2.23)$$

because $\big\langle e_\perp^{n+1} - e_\perp^n, e_h^{n+\frac{1}{2}}\big\rangle = 0$ and $b\big(\psi_h^{n+\frac{1}{2}}, e_h^{n+\frac{1}{2}}, e_h^{n+\frac{1}{2}}\big) = 0$.

Now, we bound the terms on the RHS of (2.23). Using Cauchy-Schwarz and Young inequalities with $\epsilon = \frac{1}{8}$ and Lemma 2.3 we obtain

$$\big|\big(\tfrac{\delta_M}{L}\big)^3\big\langle \nabla e_\perp^{n+\frac{1}{2}}, \nabla e_h^{n+\frac{1}{2}}\big\rangle\big| \leq \tfrac{1}{16}\big(\tfrac{\delta_M}{L}\big)^3\|\nabla e_h^{n+\frac{1}{2}}\|^2 + h^{2k}C\big(\tfrac{\delta_M}{L}\big)^3\|\omega^{n+\frac{1}{2}}\|_{k+1}^2. \qquad (2.24)$$

Integrating by parts, using Cauchy-Schwarz, Poincaré and Young inequalities with $\epsilon = \frac{1}{8}\big(\frac{\delta_M}{L}\big)^3$ and $\big\|\frac{\partial e_h^{n+\frac{1}{2}}}{\partial x}\big\| \leq \big\|\nabla e_h^{n+\frac{1}{2}}\big\|$, we obtain

$$\big|\big\langle \tfrac{\partial E^{n+\frac{1}{2}}}{\partial x}, e_h^{n+\frac{1}{2}} \big\rangle\big| \leq \tfrac{1}{16}\big(\tfrac{\delta_M}{L}\big)^3 \|\nabla e_h^{n+\frac{1}{2}}\|^2 + C\big(\tfrac{L}{\delta_M}\big)^3 \|\nabla E^{n+\frac{1}{2}}\|^2. \tag{2.25}$$

We have to estimate $\|\nabla E^{n+\frac{1}{2}}\|$. Averaging and subtracting (2.3b) from (2.5b), choosing $v_h = E_h^{n+\frac{1}{2}}$ and using Cauchy-Schwarz and Poincaré inequalities, we obtain

$$\big\|\nabla E_h^{n+\frac{1}{2}}\big\|^2 \leq C\big\|D_\mu^h\big(\overline{\omega_h^{n+\frac{1}{2}} - \omega^{n+\frac{1}{2}}}^h\big)\big\|\big\|\nabla E_h^{n+\frac{1}{2}}\big\| + C\big\|D_\mu^h\overline{\omega^{n+\frac{1}{2}}}^h - \omega^{n+\frac{1}{2}}\big\|\big\|\nabla E_h^{n+\frac{1}{2}}\big\|. \tag{2.26}$$

Using (2.26) and Lemma 2.7 we obtain

$$\|\nabla E^{n+\frac{1}{2}}\|^2 \leq \|\nabla E_\perp^{n+\frac{1}{2}}\|^2 + C\big\|e_h^{n+\frac{1}{2}}\big\|^2 + C\big\|e_\perp^{n+\frac{1}{2}}\big\|^2 + C\big\|D_\mu^h\overline{\omega^{n+\frac{1}{2}}}^h - \omega^{n+\frac{1}{2}}\big\|^2. \tag{2.27}$$

Using (2.27), Lemma 2.8 and Lemma 2.3 in (2.25) we obtain

$$\begin{aligned}
&\big|\big\langle \tfrac{\partial E^{n+\frac{1}{2}}}{\partial x}, e_h^{n+\frac{1}{2}} \big\rangle\big| \leq \tfrac{1}{16}\big(\tfrac{\delta_M}{L}\big)^3 \|\nabla e_h^{n+\frac{1}{2}}\|^2 \\
&+ C\big(\tfrac{L}{\delta_M}\big)^3\big(C\|\nabla E_\perp^{n+\frac{1}{2}}\|^2 + C\|e_\perp^{n+\frac{1}{2}}\|^2 + C\|e_h^{n+\frac{1}{2}}\|^2 + C\big\|D_\mu^h\overline{\omega^{n+\frac{1}{2}}}^h - \omega^{n+\frac{1}{2}}\big\|^2\big) \\
&\leq \tfrac{1}{16}\big(\tfrac{\delta_M}{L}\big)^3 \|\nabla e_h^{n+\frac{1}{2}}\|^2 + C\big(\tfrac{L}{\delta_M}\big)^3 \|e_h^{n+\frac{1}{2}}\|^2 + \big(\tfrac{L}{\delta_M}\big)^3\big[h^{2k}C\|\psi^{n+\frac{1}{2}}\|_{k+1}^2 + h^{2k+2}C\|\omega^{n+\frac{1}{2}}\|_{k+1}^2 \\
&+ \mu^2\alpha^4\|\omega^{n+\frac{1}{2}}\|_2^2 + \big(\alpha^2 h^{2k} + h^{2k+2}\big)\|\overline{\omega^{n+\frac{1}{2}}}\|_{k+1}^2 + \big(\mu\alpha^2 h^{2k} + h^{2k+2}\big)\|D_\mu\overline{\omega^{n+\frac{1}{2}}}\|_{k+1}^2\big].
\end{aligned} \tag{2.28}$$

Using Lemma 2.2, Young inequality with $\epsilon = \frac{1}{8Ro}\big(\frac{\delta_M}{L}\big)^3$, Poincaré inequality, (2.27) and Lemma 2.8 and for $k \geq 1$ we have

$$\begin{aligned}
&\big|Ro\ b\big(E^{n+\frac{1}{2}}, \omega^{n+\frac{1}{2}}, e_h^{n+\frac{1}{2}}\big)\big| \leq \tfrac{1}{16}\big(\tfrac{\delta_M}{L}\big)^3 \|\nabla e_h^{n+\frac{1}{2}}\|^2 + CRo^2\big(\tfrac{L}{\delta_M}\big)^3 \|\nabla \omega^{n+\frac{1}{2}}\|_1^2 \|\nabla E^{n+\frac{1}{2}}\|^2 \\
&\leq \tfrac{1}{16}\big(\tfrac{\delta_M}{L}\big)^3 \|\nabla e_h^{n+\frac{1}{2}}\|^2 + CRo^2\big(\tfrac{L}{\delta_M}\big)^3 \|\nabla \omega^{n+\frac{1}{2}}\|_1^2 \|e_h^{n+\frac{1}{2}}\|^2 \\
&+ Ro^2\big(\tfrac{L}{\delta_M}\big)^3 \|\nabla \omega^{n+\frac{1}{2}}\|_1^2 \big(h^{2k} C \|\psi^{n+\frac{1}{2}}\|_{k+1}^2 + h^{2k+2} C \|\omega^{n+\frac{1}{2}}\|_{k+1}^2 + C\big\|D_\mu^h \overline{\omega^{n+\frac{1}{2}}}^h - \omega^{n+\frac{1}{2}}\big\|^2\big) \\
&\leq \tfrac{1}{16}\big(\tfrac{\delta_M}{L}\big)^3 \|\nabla e_h^{n+\frac{1}{2}}\|^2 + CRo^2\big(\tfrac{L}{\delta_M}\big)^3 \|\nabla \omega^{n+\frac{1}{2}}\|_1^2 \|e_h^{n+\frac{1}{2}}\|^2 + CRo^2\big(\tfrac{L}{\delta_M}\big)^3 \Big[h^{2k+2} \|\omega^{n+\frac{1}{2}}\|_{k+1}^4 \\
&+ h^{2k} \|\nabla \omega^{n+\frac{1}{2}}\|_1^4 + h^{2k} \|\psi^{n+\frac{1}{2}}\|_{k+1}^4 + \mu^2 \alpha^4 \|\omega^{n+\frac{1}{2}}\|_2^4 + \big(\alpha^2 h^{2k} + h^{2k+2}\big) \|\overline{\omega^{n+\frac{1}{2}}}\|_{k+1}^4 \\
&+ \big(\mu\alpha^2 h^{2k} + h^{2k+2}\big) \|D_\mu \overline{\omega^{n+\frac{1}{2}}}\|_{k+1} + \big(\mu^2\alpha^4 + \alpha^2 h^{2k} + 2h^{2k+2} + \mu\alpha^2 h^{2k}\big) \|\nabla \omega^{n+\frac{1}{2}}\|_1^4\Big].
\end{aligned} \tag{2.29}$$

Using Holder's inequality with $p = \infty$ and $q = r = 2$,

$$\big|b\big(\psi_h^{n+\frac{1}{2}}, e_\perp^{n+\frac{1}{2}}, e_h^{n+\frac{1}{2}}\big)\big| \leq \|\nabla \psi_h^{n+\frac{1}{2}}\|_\infty \|e_\perp^{n+\frac{1}{2}}\|^2 \|\nabla e_h^{n+\frac{1}{2}}\|^2.$$

From $\|\nabla\psi_h^{n+\frac{1}{2}} - \nabla\psi^{n+\frac{1}{2}}\|_\infty = \|\nabla E^{n+\frac{1}{2}}\|_\infty$ and using Agmon's inequality and the regularity estimate $\|\psi\|_{m+2} \leq C\|\omega\|_m$ for ψ satisfying (2.5b)

$$\begin{aligned}
\|\nabla\psi_h^{n+\frac{1}{2}}\|_\infty &\leq \|\nabla E^{n+\frac{1}{2}}\|_\infty + \|\nabla\psi^{n+\frac{1}{2}}\|_\infty \leq \|\nabla E^{n+\frac{1}{2}}\|_\infty + C\|\psi^{n+\frac{1}{2}}\|_3 \\
&\leq \|\nabla E^{n+\frac{1}{2}}\|_\infty + C\|\omega^{n+\frac{1}{2}}\|_1
\end{aligned} \tag{2.30}$$

We have to estimate the term $\|\nabla E^{n+\frac{1}{2}}\|_\infty$. Let I^h be a global Langrangian interpolator, we have $\|\nabla E^{n+\frac{1}{2}}\|_\infty \leq \|\nabla(I^h\psi^{n+\frac{1}{2}} - \psi_h^{n+\frac{1}{2}})\|_\infty + \|\nabla(\psi^{n+\frac{1}{2}} - I^h\psi^{n+\frac{1}{2}})\|_\infty$. Using an inverse inequality for $\|\nabla(I^h\psi^{n+\frac{1}{2}} - \psi_h^{n+\frac{1}{2}})\|_\infty$ (Theorem 4.5.11 in [11]) and a standard estimate for $\|\nabla(\psi^{n+\frac{1}{2}} - I^h\psi^{n+\frac{1}{2}})\|_\infty$ (Theorem 4.4.20 in [11]) we have

$$\begin{aligned}
\|\nabla E^{n+\frac{1}{2}}\|_\infty &\leq Ch^{-1}\|\nabla(I^h\psi^{n+\frac{1}{2}} - \psi_h^{n+\frac{1}{2}})\| + Ch^{k-1}\|\psi^{n+\frac{1}{2}}\|_{k+1} \\
&\leq Ch^{-1}\|\nabla(I^h\psi^{n+\frac{1}{2}} - \psi^{n+\frac{1}{2}} - E^{n+\frac{1}{2}})\| + Ch^{k-1}\|\psi^{n+\frac{1}{2}}\|_{k+1} \\
&\leq Ch^{-1}\|\nabla E_h^{n+\frac{1}{2}}\| + Ch^{k-1}\|\psi^{n+\frac{1}{2}}\|_{k+1}
\end{aligned} \tag{2.31}$$

Thus, for $0 < h \leq 1$ and for $k \geq 1$ we have

$$\|\nabla \psi_h^{n+\frac{1}{2}}\|_\infty \leq Ch^{-1}\|\nabla E_h^{n+\frac{1}{2}}\| + C\|\omega^{n+\frac{1}{2}}\|_1 + C\|\psi^{n+\frac{1}{2}}\|_{k+1}$$

Therefore, for $h \leq 1$ and $k \geq 1$ and using Lemma 2.3

$$\begin{aligned}
&\big|b\big(\psi_h^{n+\frac{1}{2}}, e_\perp^{n+\frac{1}{2}}, e_h^{n+\frac{1}{2}}\big)\big| \leq \big(Ch^{-1}\|\nabla E_h^{n+\frac{1}{2}}\| + \|\omega^{n+\frac{1}{2}}\|_1 + \|\psi^{n+\frac{1}{2}}\|_{k+1}\big)\|e_\perp^{n+\frac{1}{2}}\|\|\nabla e_h^{n+\frac{1}{2}}\| \\
&\leq C\|\omega^{n+\frac{1}{2}}\|_{k+1}\|\nabla E_h^{n+\frac{1}{2}}\|\|\nabla e_h^{n+\frac{1}{2}}\| + C\big(\|\omega^{n+\frac{1}{2}}\|_1 + \|\psi^{n+\frac{1}{2}}\|_{k+1}\big)\|e_\perp^{n+\frac{1}{2}}\|\|\nabla e_h^{n+\frac{1}{2}}\|.
\end{aligned}$$

Using Young inequality in both terms with $\epsilon = \frac{1}{16CRo}\big(\frac{\delta_M}{L}\big)^3$, (2.26), Lemma 2.3 and for $k \geq 1$

$$\begin{aligned}
&\big|Ro\ b\big(\psi_h^{n+\frac{1}{2}}, e_\perp^{n+\frac{1}{2}}, e_h^{n+\frac{1}{2}}\big)\big| \leq \tfrac{1}{16}\big(\tfrac{\delta_M}{L}\big)^3\|\nabla e_h^{n+\frac{1}{2}}\|^2 + 8Ro^2\big(\tfrac{L}{\delta_M}\big)^3\|\psi^{n+\frac{1}{2}}\|_{k+1}^2\|e_\perp^{n+\frac{1}{2}}\|^2 \\
&+ 8Ro^2\big(\tfrac{L}{\delta_M}\big)^3\|\omega^{n+\frac{1}{2}}\|_{k+1}^2\big(\|e_h^{n+\frac{1}{2}}\|^2 + \|e_\perp^{n+\frac{1}{2}}\|^2 + \big\|D_\mu^h\overline{\omega^{n+\frac{1}{2}}}^h - \omega^{n+\frac{1}{2}}\big\|^2 + h^{2k}C\|\omega^{n+\frac{1}{2}}\|_1^2\big) \\
&\leq \tfrac{1}{16}\big(\tfrac{\delta_M}{L}\big)^3\|\nabla e_h^{n+\frac{1}{2}}\|^2 + CRo^2\big(\tfrac{L}{\delta_M}\big)^3\|\omega^{n+\frac{1}{2}}\|_{k+1}^2\|e_h^{n+\frac{1}{2}}\|^2 + CRo^2\big(\tfrac{L}{\delta_M}\big)^3\Big[h^{2k+2}\|\psi^{n+\frac{1}{2}}\|_{k+1}^4 \\
&+ h^{2k+2}\|\omega^{n+\frac{1}{2}}\|_{k+1}^4 + h^{2k}\|\omega^{n+\frac{1}{2}}\|_1^4 + \big(\mu^2\alpha^4 + \alpha h^{2k} + h^{2k+2} + \mu\alpha^2h^{2k}\big)\|\omega^{n+\frac{1}{2}}\|_{k+1}^4 \\
&+ \mu^2\alpha^4\|\omega^{n+\frac{1}{2}}\|_2^4 + \big(\alpha^2h^{2k} + h^{2k+2}\big)\|\overline{\omega^{n+\frac{1}{2}}}\|_{k+1}^4 + \big(\mu\alpha^2h^{2k} + h^{2k+2}\big)\|D_\mu\overline{\omega^{n+\frac{1}{2}}}\|_{k+1}^4\Big]
\end{aligned} \tag{2.32}$$

It remains to bound $Intp(\omega^n, \psi^n; e_h^{n+\frac{1}{2}})$. Using Cauchy-Schwarz, Poincaré and Young inequalities with $\epsilon = \frac{1}{8}\big(\frac{\delta_M}{L}\big)^3$ and Lemma 2.4 in (2.20), we obtain

$$Ro\big|\big\langle \tfrac{\omega^{n+1}-\omega^n}{\Delta t} - \omega_t(t^{n+\frac{1}{2}}), e_h^{n+\frac{1}{2}}\big\rangle\big| \leq \tfrac{1}{16}\big(\tfrac{\delta_M}{L}\big)^3\|\nabla e_h^{n+\frac{1}{2}}\|^2 + \Delta t^3 CRo^2\big(\tfrac{L}{\delta_M}\big)^3\int_{t^n}^{t^{n+1}}\|\omega_{ttt}\|^2dt. \tag{2.33}$$

Using Cauchy-Schwarz and Young inequalities ($\epsilon = \frac{1}{8}$) and Lemma 2.4

$$\big|\big(\tfrac{\delta_M}{L}\big)^3\big\langle\nabla\omega^{n+\frac{1}{2}} - \nabla\omega(t^{n+\frac{1}{2}}), \nabla e_h^{n+\frac{1}{2}}\big\rangle\big| \leq \tfrac{1}{16}\big(\tfrac{\delta_M}{L}\big)^3\|\nabla e_h^{n+\frac{1}{2}}\|^2 + \Delta t^3 C\big(\tfrac{\delta_M}{L}\big)^3\int_{t^n}^{t^{n+1}}\|\nabla\omega_{tt}\|^2dt. \tag{2.34}$$

Integrating by parts, using Cauchy-Schwarz and Young inequalities with $\epsilon = \frac{1}{8}\big(\frac{\delta_M}{L}\big)^3$ we obtain, after we use Lemma 2.4,

$$\Big|\Big\langle \frac{\partial\big(\psi^{n+\frac{1}{2}} - \psi(t^{n+\frac{1}{2}})\big)}{\partial x}, e_h^{n+\frac{1}{2}} \Big\rangle\Big| = \Big| - \int_\Omega \big(\psi^{n+\frac{1}{2}} - \psi(t^{n+\frac{1}{2}})\big) \frac{\partial e_h^{n+\frac{1}{2}}}{\partial x} \Big|$$
$$\leq \tfrac{1}{16}\big(\tfrac{\delta_M}{L}\big)^3 \|\nabla e_h^{n+\frac{1}{2}}\|^2 + \Delta t^3 C \big(\tfrac{L}{\delta_M}\big)^3 \int_{t^n}^{t^{n+1}} \|\psi_{tt}\|^2 dt. \tag{2.35}$$

Adding and subtracting $b\big(\psi(t^{n+\frac{1}{2}}), \omega^{n+\frac{1}{2}}, e_h^{n+\frac{1}{2}}\big)$ in the nonlinear term and using Lemma 2.2, Young inequality with $\epsilon = \frac{1}{16}\big(\frac{\delta_M}{L}\big)^3$ and Lemma 2.4 we obtain

$$\big|b\big(\psi^{n+\frac{1}{2}}, \omega^{n+\frac{1}{2}}, e_h^{n+\frac{1}{2}}\big) - b\big(\psi(t^{n+\frac{1}{2}}), \omega(t^{n+\frac{1}{2}}), e_h^{n+\frac{1}{2}}\big)\big| =$$
$$\leq C\big\|\psi^{n+\frac{1}{2}} - \psi(t^{n+\frac{1}{2}})\big\|_1 \big\|\nabla e_h^{n+\frac{1}{2}}\big\| \big\|\nabla \omega^{n+\frac{1}{2}}\big\|_1 + C\big\|\nabla\psi(t^{n+\frac{1}{2}})\big\|_1 \big\|\nabla e_h^{n+\frac{1}{2}}\big\| \big\|\omega^{n+\frac{1}{2}} - \omega(t^{n+\frac{1}{2}})\big\|_1$$
$$\leq \tfrac{1}{16}\big(\tfrac{\delta_M}{L}\big)^3 \|\nabla e_h^{n+\frac{1}{2}}\|^2 + C\Delta t^3 \big(\tfrac{\delta_M}{L}\big)^3 \big\|\nabla\omega^{n+\frac{1}{2}}\big\|_1^2 \int_{t^n}^{t^{n+1}} \|\psi_{tt}\|_1^2 dt$$
$$+ C\Delta t^3 \big(\tfrac{L}{\delta_M}\big)^3 \big\|\nabla\psi(t^{n+\frac{1}{2}})\big\|_1^2 \int_{t^n}^{t^{n+1}} \|\omega_{tt}\|_1^2 dt$$
$$\leq \tfrac{1}{16}\big(\tfrac{\delta_M}{L}\big)^3 \|\nabla e_h^{n+\frac{1}{2}}\|^2 + \Delta t^4 C \big(\tfrac{L}{\delta_M}\big)^3 \big\|\nabla\omega^{n+\frac{1}{2}}\big\|_1^4 + \Delta t^3 C \big(\tfrac{L}{\delta_M}\big)^3 \int_{t^n}^{t^{n+1}} \|\psi_{tt}\|_1^4 dt$$
$$+ \Delta t^4 C \big(\tfrac{L}{\delta_M}\big)^3 \big\|\nabla\psi(t^{n+\frac{1}{2}})\big\|_1^4 + \Delta t^3 C \big(\tfrac{L}{\delta_M}\big)^3 \int_{t^n}^{t^{n+1}} \|\omega_{tt}\|_1^4 dt. \tag{2.36}$$

Summing in (3.35) from $n = 0$ to $n = M - 1$ and using (2.33), (2.34), (2.35) and (2.36) we obtain

$$\sum_{n=0}^{M-1} \Delta t \big| Intp(\omega^n, \overline{\psi^n}^h; e_h^{n+\frac{1}{2}}) \big| \leq \sum_{n=0}^{M-1} \tfrac{\Delta t}{4}\big(\tfrac{\delta_M}{L}\big)^3 \big\|\nabla e_h^{n+\frac{1}{2}}\big\|^2 + \Delta t^4 C Ro^2 \big(\tfrac{L}{\delta_M}\big)^3 \|\omega_{ttt}\|_{2,0}^2$$
$$+ \Delta t^4 C \big(\tfrac{\delta_M}{L}\big)^3 \|\nabla\omega_{tt}\|_{2,0}^2 + \Delta t^4 C \big(\tfrac{L}{\delta_M}\big)^3 \|\psi_{tt}\|_{2,0}^2 + \Delta t^4 C \big(\tfrac{L}{\delta_M}\big)^3 \big\|\big|\nabla\psi^{1/2}\big|\big\|_{4,1}^4$$
$$+ \Delta t^4 C \big(\tfrac{L}{\delta_M}\big)^3 \|\omega_{tt}\|_{4,1}^4 + \Delta t^4 C \big(\tfrac{L}{\delta_M}\big)^3 \big\|\big|\nabla\omega^{1/2}\big|\big\|_{4,1}^4 + \Delta t^4 C \big(\tfrac{L}{\delta_M}\big)^3 \|\psi_{tt}\|_{4,1}^4. \tag{2.37}$$

Now, using (2.24), (2.28), (2.29), (2.32) and (2.37) in (2.23) and summing from $n = 0$ to $n = M - 1$ we obtain

$$
\begin{aligned}
&Ro(\|e_h^M\|^2 - \|e_h^0\|^2) + \Delta t\big(\tfrac{\delta_M}{L}\big)^3 \sum_{n=0}^{M-1} \|\nabla e_h^{n+\frac{1}{2}}\|^2 \leq h^{2k} C\big(\tfrac{\delta_M}{L}\big)^3 |||\omega^{1/2}|||_{2,k+1}^2 \\
&+ h^{2k} C\big(\tfrac{L}{\delta_M}\big)^3 |||\psi^{1/2}|||_{2,k+1}^2 + h^{2k+2} C\big(\tfrac{L}{\delta_M}\big)^3 |||\omega^{1/2}|||_{2,k+1}^2 + C\big(\tfrac{L}{\delta_M}\big)^3 \Big[\mu^2\alpha^4 |||\omega^{1/2}|||_{2,2}^2 \\
&+ \big(\alpha^2 h^{2k} + h^{2k+2}\big) |||\overline{\omega^{1/2}}|||_{2,k+1}^2 + \big(\mu\alpha^2 h^{2k} + h^{2k+2}\big) |||D_\mu \overline{\omega^{1/2}}|||_{2,k+1}^2\Big] \\
&+ CRo^2\big(\tfrac{L}{\delta_M}\big)^3 \Big[h^{2k+2} |||\omega^{1/2}|||_{4,k+1}^4 + h^{2k} |||\nabla\omega^{1/2}|||_{4,1}^4 + h^{2k} |||\psi^{1/2}|||_{4,k+1}^4 + \mu^2\alpha^4 |||\omega^{1/2}|||_{4,2}^4 \\
&+ \big(\alpha^2 h^{2k} + h^{2k+2}\big) |||\overline{\omega^{1/2}}\|_{4,k+1}^4 + \big(\mu\alpha^2 h^{2k} + h^{2k+2}\big) |||D_\mu \overline{\omega^{1/2}}|||_{4,k+1}^4\Big] \\
&+ \big(\mu^2\alpha^4 + \alpha^2 h^{2k} + 2h^{2k+2} + \mu\alpha^2 h^{2k}\big) |||\nabla\omega^{1/2}|||_{4,1}^4 + CRo^2\big(\tfrac{L}{\delta_M}\big)^3 \Big[h^{2k+2} |||\psi^{1/2}|||_{4,k+1}^4 \\
&+ h^{2k+2} |||\omega^{1/2}|||_{4,k+1}^4 + h^{2k} |||\omega^{1/2}|||_{4,1}^4 + \mu^2\alpha^4 |||\omega^{1/2}|||_{4,2}^4 + \big(\alpha h^{2k} + h^{2k+2}\big) \|\overline{\omega^{1/2}}\|_{4,k+1}^4 \\
&+ \big(\mu\alpha^2 h^{2k} + h^{2k+2}\big) |||D_\mu \overline{\omega^{1/2}}\|_{4,k+1}^4 + \big(\mu^2\alpha^4 + \alpha^2 h^{2k} + h^{2k+2} + \mu\alpha^2 h^{2k}\big) |||\omega^{1/2}|||_{4,k+1}^4\Big] \\
&+ \Delta t^4 CRo^2\big(\tfrac{L}{\delta_M}\big)^3 \|\omega_{ttt}\|_{2,0}^2 + \Delta t^4 C\big(\tfrac{\delta_M}{L}\big)^3 \|\nabla\omega_{tt}\|_{2,0}^2 + \Delta t^4 C\big(\tfrac{L}{\delta_M}\big)^3 \|\psi_{tt}\|_{2,0}^2 \\
&+ \Delta t^4 C\big(\tfrac{L}{\delta_M}\big)^3 \big|||\nabla\psi^{1/2}|||\big|_{4,1}^4 + \Delta t^4 C\big(\tfrac{L}{\delta_M}\big)^3 \|\omega_{tt}\|_{4,1}^4 + \Delta t^4 C\big(\tfrac{L}{\delta_M}\big)^3 \big|||\nabla\omega^{1/2}|||\big|_{4,1}^4 \\
&+ \Delta t^4 C\big(\tfrac{L}{\delta_M}\big)^3 \|\psi_{tt}\|_{4,1}^4 + \sum_{n=0}^{M-1} \Delta t\big(\tfrac{L}{\delta_M}\big)^3 \big(C + CRo^2 \|\nabla\omega^{n+\frac{1}{2}}\|_1^2 + CRo^2 \|\omega^{n+\frac{1}{2}}\|_{k+1}^2\big) \|e_h^{n+\frac{1}{2}}\|^2.
\end{aligned}
$$

If $\Delta t < \dfrac{\big({}^{\delta_M}/_L\big)^3}{C + CRo^2\|\nabla\omega^{n+\frac{1}{2}}\|_1^2 + CRo^2\|\omega^{n+\frac{1}{2}}\|_{k+1}^2}$ using Gronwall Lemma, we have

$$
\begin{aligned}
&Ro(\|e_h^M\|^2 - \|e_h^0\|^2) + \Delta t\big(\tfrac{\delta_M}{L}\big)^3 \sum_{n=0}^{M-1} \|\nabla e_h^{n+\frac{1}{2}}\|^2 \leq C^* \Big\{h^{2k} C\big(\tfrac{\delta_M}{L}\big)^3 |||\omega^{1/2}|||_{2,k+1}^2 \\
&+ h^{2k} C\big(\tfrac{L}{\delta_M}\big)^3 |||\psi^{1/2}|||_{2,k+1}^2 + h^{2k+2} C\big(\tfrac{L}{\delta_M}\big)^3 |||\omega^{1/2}|||_{2,k+1}^2 + C\big(\tfrac{L}{\delta_M}\big)^3 \Big[\mu^2\alpha^4 |||\omega^{1/2}|||_{2,2}^2 \\
&+ \big(\alpha^2 h^{2k} + h^{2k+2}\big) |||\overline{\omega^{1/2}}|||_{2,k+1}^2 + \big(\mu\alpha^2 h^{2k} + h^{2k+2}\big) |||D_\mu \overline{\omega^{1/2}}|||_{2,k+1}^2\Big] \\
&+ CRo^2\big(\tfrac{L}{\delta_M}\big)^3 \Big[h^{2k+2} |||\omega^{1/2}|||_{4,k+1}^4 + h^{2k} |||\nabla\omega^{1/2}|||_{4,1}^4 + h^{2k} |||\psi^{1/2}|||_{4,k+1}^4 + \mu^2\alpha^4 |||\omega^{1/2}|||_{4,2}^4 \\
&+ \big(\alpha^2 h^{2k} + h^{2k+2}\big) |||\overline{\omega^{1/2}}\|_{4,k+1}^4 + \big(\mu\alpha^2 h^{2k} + h^{2k+2}\big) |||D_\mu \overline{\omega^{1/2}}|||_{4,k+1}^4\Big] \\
&+ \big(\mu^2\alpha^4 + \alpha^2 h^{2k} + 2h^{2k+2} + \mu\alpha^2 h^{2k}\big) |||\nabla\omega^{1/2}|||_{4,1}^4 + CRo^2\big(\tfrac{L}{\delta_M}\big)^3 \Big[h^{2k+2} |||\psi^{1/2}|||_{4,k+1}^4 \\
&+ h^{2k+2} |||\omega^{1/2}|||_{4,k+1}^4 + h^{2k} |||\omega^{1/2}|||_{4,1}^4 + \mu^2\alpha^4 |||\omega^{1/2}|||_{4,2}^4 + \big(\alpha h^{2k} + h^{2k+2}\big) \|\overline{\omega^{1/2}}\|_{4,k+1}^4 \\
&+ \big(\mu\alpha^2 h^{2k} + h^{2k+2}\big) |||D_\mu \overline{\omega^{1/2}}\|_{4,k+1}^4 + \big(\mu^2\alpha^4 + \alpha^2 h^{2k} + h^{2k+2} + \mu\alpha^2 h^{2k}\big) |||\omega^{1/2}|||_{4,k+1}^4\Big] \\
&+ \Delta t^4 CRo^2\big(\tfrac{L}{\delta_M}\big)^3 \|\omega_{ttt}\|_{2,0}^2 + \Delta t^4 C\big(\tfrac{\delta_M}{L}\big)^3 \|\nabla\omega_{tt}\|_{2,0}^2 + \Delta t^4 C\big(\tfrac{L}{\delta_M}\big)^3 \|\psi_{tt}\|_{2,0}^2 + \Delta t^4 C\big(\tfrac{L}{\delta_M}\big)^3 \|\omega_{tt}\|_{4,1}^4 \\
&+ \Delta t^4 C\big(\tfrac{L}{\delta_M}\big)^3 \big|||\nabla\psi^{1/2}|||\big|_{4,1}^4 + \Delta t^4 C\big(\tfrac{L}{\delta_M}\big)^3 \big|||\nabla\omega^{1/2}|||\big|_{4,1}^4 + \Delta t^4 C\big(\tfrac{L}{\delta_M}\big)^3 \|\psi_{tt}\|_{4,1}^4\Big\}. \qquad (2.38)
\end{aligned}
$$

where

$$C^* := \exp\left\{\Delta t \sum_{n=0}^{M-1} \frac{\left(\frac{L}{\delta_M}\right)^3\left(C+CRo^2\|\nabla\omega^{n+\frac{1}{2}}\|_1^2+CRo^2\|\omega^{n+\frac{1}{2}}\|_{k+1}^2\right)}{1-\Delta t\left(\frac{L}{\delta_M}\right)^3\left(C+CRo^2\|\nabla\omega^{n+\frac{1}{2}}\|_1^2+CRo^2\|\omega^{n+\frac{1}{2}}\|_{k+1}^2\right)}\right\}. \tag{2.39}$$

Estimate (2.17) then follows from the triangle inequality and (2.38).

For estimate (2.18), we use (2.38) and

$$\begin{aligned}\left\|\nabla\left(\omega\left(t^{n+\frac{1}{2}}\right)-\omega_h^{n+\frac{1}{2}}\right)\right\|^2 &\leq \left\|\nabla\left(\omega\left(t^{n+\frac{1}{2}}\right)-\omega^{n+\frac{1}{2}}\right)\right\|^2+\left\|\nabla e_\perp^{n+\frac{1}{2}}\right\|^2+\left\|\nabla e_h^{n+\frac{1}{2}}\right\|^2\\ &\leq \tfrac{\Delta t^3}{48}\int_{t^n}^{t^{n+1}}\|\omega_{tt}\|^2dt+Ch^{2k}\left\|\omega^{n+\frac{1}{2}}\right\|_{k+1}^2+\|\nabla e_h^{n+\frac{1}{2}}\|^2.\end{aligned}$$

□

Proof of Corollary 2.1. The result follows directly from

$$\|\nabla(\psi(t^{n+\frac{1}{2}})-\psi_h^{n+\frac{1}{2}})\|^2 \leq \|\nabla\left(\psi(t^{n+\frac{1}{2}})-\psi^{n+\frac{1}{2}}\right)\|^2+\|\nabla E^{n+\frac{1}{2}}\|^2 \tag{2.40}$$

after we apply inequality (2.27), Lemma 2.8, Lemma 2.3, sum from $n = 0, ..., M-1$ and Theorem 2.1. □

2.5 Numerical experiments

In this section we provide results obtained with the proposed scheme. We start by validating our computational implementation and estimating convergence rates using an analytical solution. Then, we perform simulations of the traditional double-gyre wind forcing experiment. The computational tests were made using the software FreeFem++[40]. The resulting nonlinear system was solved through a newtonian iteration. Moreover, a multi-frontal Gauss LU factorization implemented in the package UMFPACK (provided with FreeFem++ software) was used as our linear solver.

2.5.1 Convergence rates

First, we estimate convergence rates for the BV-Tikhonov model using an analytical solution and results produced in meshes with different spatial resolution. We calculate convergence rates using the error at two successive values of h by postulating that $e(h) = Ch^\beta$ and solving for β with $\beta = \ln(e(h_1)/e(h_2))/\ln(h_1/h_2)$.

Setting $\mathcal{F} = -\pi \exp[-\frac{2\pi^2}{Ro}\big(\frac{\delta_M}{L}\big)^3 t] \cos \pi x \sin \pi y$ and adopting $\Omega = [0,1] \times [-1,1]$, the following time dependent solution for BV (with homogeneous Dirichlet boundary conditions) is obtained

$$\begin{aligned} \psi &= \exp\big[-\frac{2\pi^2}{Ro}\big(\tfrac{\delta_M}{L}\big)^3 t\big] \sin \pi x \sin \pi y, \\ \omega &= 2\pi^2 \exp\big[-\frac{2\pi^2}{Ro}\big(\tfrac{\delta_M}{L}\big)^3 t\big] \sin \pi x \sin \pi y \end{aligned}$$

which we use to estimate convergence rates for BV-Tikhonov model.

We use results obtained in regular rectangular meshes with h equal to $1/4$, $1/8$, $1/16$, $1/32$, $1/64$ and $1/128$ to calculate the convergence rates for $\delta_M/L = 0.02$ and $Ro = 1.0$. In all cases we chose $\alpha = h$ and $\mu = 1$, and the timestep was chosen in terms of h in order to balance the errors sources from the convergence theorem. That is, for P_1 elements and $\alpha = h$, the $L^2(0,T;H^1(\Omega))$ vorticity error and $L^\infty(0,T;H^1(\Omega))$ streamfunction error from the theorem is $O(\Delta t^2 + h)$, and thus we chose $\Delta t = \sqrt{h}$ (but slightly rounded so that Δt evenly divided T), and thus here we expect first order convergence in these norms as $\Delta t,\ h \to 0$. For P_2 elements, we chose $\Delta t = h$, and expect second order convergence of these norms.

Convergence rates for BV-Tikhonov model are presented in Table 2.1. From the table, we observe that convergence rates approach the expected estimates for the given norms in the convergence theorem both for P1 and P2 elements.

Element	h^{-1}	$\|w - w_h\|_{2,1}$	Rate	$\|w - w_h\|_{\infty,0}$	Rate	$\|\psi - \psi_h\|_{2,1}$	Rate
P_1	4	24.189		1.9868		2.1732	
$(\Delta t = \sqrt{h})$	8	12.376	0.97	0.61369	1.69	1.0117	1.10
	16	6.1545	1.01	0.16167	1.92	0.39299	1.36
	32	3.0614	1.01	0.041218	1.97	0.16706	1.23
	64	1.5259	1.00	0.010349	1.99	0.078803	1.08
	128	0.76181	1.00	0.002606	1.99	0.038768	1.02
P_2	4	6.3875		0.79216		1.7969	
$(\Delta t = h)$	8	2.7885	1.20	0.28037	1.50	0.74236	1.23
	16	1.0076	1.47	0.078785	1.83	0.22489	1.72
	32	0.33616	1.58	0.020767	1.92	0.059414	1.92
	64	0.10476	1.68	0.0052803	1.98	0.059414	1.98
	128	0.02967	1.82	0.0013261	1.99	0.015067	1.99

Table 2.1: Convergence rates for BV-Tikhonov model with $\frac{\delta_M}{L} = 0.02$ and $Ro = 1.0$.

2.5.2 Double gyre wind forcing experiment

According to [37, 47], when BV equations are forced by a double gyre wind forcing in a rectangular basin and dissipation is weak, the instantaneous vorticity and streamfunction fields are highly variable but their mean fields present a well defined four gyre pattern in which the two central gyres are driven by the wind and the northern and southern ends of the basin are driven by the eddy flux of potential vorticity. Moreover, the outer gyres are not a linear effect, instead it results from a mean balance between eddy flux of potential vorticity and wind forcing which is susceptible to destruction by excessive dissipation [47].

The double gyre wind forcing experiment has been used in several studies as a model of more realistic ocean dynamics. Besides, it has been used as an interesting benchmark test in order to analyze new techniques to deal with turbulence in geophysical flows, e.g. [81, 47, 100]. In order to accomplish the double gyre wind forcing experiment, $\mathcal{F}$ is set to $\mathcal{F}_0 \sin(\pi y)$ where $\mathcal{F}_0 = 1$.

Here we follow [100] and adopt the standard LES methodology: first we run the double gyre wind forcing experiment in a high resolution simulation with BV model (no treatment of turbulence). After we run several experiments in a coarse resolution mesh with BV model and BV-Tikhonov model and compare them with the high resolution BV model solution as reference.

Following [37, 81, 47, 100], we run simulations in different regular triangular meshes in the dimensionless rectangular domain $[0,1] \times [-1,1]$ considering $h = 1/4$ (which corresponds to a grid with 4 × 8 squares), $1/8$ (8×16), $1/16$ (16×32), $1/32$ (32×64) and $1/64$ (64×128) where h is the mesh-width. Figure 2.1 presents the coarsest mesh used in experiments.

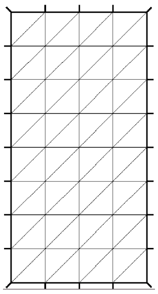

Figure 2.1: Mesh with $h = 1/4$ which corresponds to a grid with 4 × 8 squares.

Experiments were made starting from $t = 0$ up until $t = 100$ (corresponding to 56.6 years in dimensional units) as in [100]. In this and in the next section we present figures of the average fields of streamfunction (ψ) and potential vorticity (given by $q = Ro\omega + y$) calculated using results from $t = 20$ until 100 as in [100]. Moreover, we considered two interesting cases: i) $\delta_M/L = 0.02$ and $Ro = 0.0016$ (which is presented in [100]) and ii) $\delta_M/L = 0.01$ and $Ro = 0.0002$.

Firstly, we present the results obtained in the experiment using $\delta_M/L = 0.02$ and $Ro = 0.0016$. In this case, the high spatial resolution experiment with the BV model was made in a regular rectangular mesh with 16,384 triangular elements (33,153 degrees of freedom) corresponding to a grid with spatial resolution of 64 × 128 squares. Thus, the mean length of the triangle edge is about 0.015 which permits to resolve the Munk scale (δ_M). Solutions for the high resolution experiment using $\Delta t = 0.001$ are presented in

Figures 2.2(a) and 2.3(a). We observe that the high resolution solution produced by our FE scheme can reproduce the four gyre pattern found by [100] in their DNS experiment.

Now, we evaluate the results produced with BV model in the coarse 4×8 mesh using the timestep $\Delta t = 0.001$. In Figures 2.2(b) and 2.3(b) we can see, when mesh resolution is reduced (h is increased), the BV model streamfunction solution become more diffusive causing the degeneration of the four gyres pattern in two gyres, as is also observed in [81, 47, 100]. According to [47], in this case the grid resolution is too coarse to resolve the viscous boundary layer (Munk scale of 0.02).

Next, we present the solutions obtained with the BV-Tikhonov model ($\Delta t = 0.001$). Figures 2.2(c), 2.2(d), 2.2(e) and 2.2(f) present the streamfunction field and Figures 2.3(c), 2.3(d), 2.3(e) and 2.3(f) the vorticity field produced with the BV-Tikhonov model for $\alpha = h$ and μ equal to 1, $\frac{1}{4}$, $\frac{1}{16}$ and $\frac{1}{64}$, respectively. We can see that the BV-Tikhonov model can recover the four gyre pattern in this experiment for all tested values of the μ parameter. However, the BV-Tikhonov solution can be dramatically different depending on the value of the μ parameter. For example, the BV-Tikhonov provides an accurate solution in the coarse mesh when $\mu = \frac{1}{16}$ and $\mu = \frac{1}{64}$, but for $\mu = 1$ and $\mu = \frac{1}{4}$ some discrepancies are observed in the vorticity field.

Computational times for the BV model in the fine and coarse mesh and for the BV-Tikhonov model in the coarse mesh are presented in Table 2.2. We see that the BV-Tikhonov algorithm is able to recover the four gyre pattern in the coase mesh and it is significant faster than solving the BV model in the fine mesh.

Fine	Coarse	alpha	$\mu = 1/4$	$\mu = 1/16$	$\mu = 1/64$
9.82e5	2.05e3	4.5e3	4.2e3	4.5e3	4.5e3

Table 2.2: Computational time (in seconds) obtained for $Ro = 0.0016$ in the fine (64×128) and coarse (4×8) mesh with the BV model and in the coarse mesh (4×8) with BV-Tikhonov model.

Next, we investigated the effect of different choices of the μ parameter on the solution of the BV-Tikhonov model. Figure 2.4(a) presents the time evolution of the cumulative moving average kinect energy for different values of the μ parameter in the above mentioned experiment. We found for all values of μ parameter, solutions have more energy than the high spatial resolution solution (with BV model). Moreover, in Figure 2.2 we saw that increasing μ produces an intensification of the four gyre pattern. Thus solution can be very sensitive to the value of μ parameter tending to be more energetic when μ is larger. The intensification of the four gyre pattern in the BV-α model was also observed in [47] and according to [82] is attributed to the enhancement of the inverse energy cascade in the model.

We also tested the BV and BV-Tikhonov model in a 16×32 mesh using $\Delta t = 0.001$. Results obtained with the coarse BV model are presented in Figures 2.5(b) and 2.6(b). In this case the BV model solution does not degenerates in two gyres, but instead the gyres are intensified in comparison with the reference solution. In Figures 2.5(c), 2.5(d), 2.5(e) and 2.5(f) we present the streamfunction fields and in Figures 2.6(c), 2.6(d), 2.6(e) and 2.6(f) the vorticity fields obtained with the BV-Tikhonov model for $\alpha = h$ and μ equal to 1, $\frac{1}{4}$, $\frac{1}{16}$ and $\frac{1}{32}$, respectively. In this case, we also observed that the BV-Tikhonov solution can be very sensitive to different values of the μ parameter. For example, when $\mu = 1$ or $\mu = \frac{1}{4}$ the gyres in the BV-Tikhonov solution are intensified in comparison with the high resolution and coarse BV solutions. However, for $\mu = \frac{1}{16}$ and $\mu = \frac{1}{64}$ the BV-Tikhonov model solutions are more similar with the high resolution solution than the coarse BV model solution. Run times for the BV model in the fine and coarse mesh (16×32) and for the BV-Tikhonov model in the coarse mesh (16×32) are presented in Table 2.3. In this experiment we see again that the BV-Tikhonov solution, as well as recovering the expected four gyre pattern, it is significant faster than solving the BV model in the fine mesh.

Fine	Coarse	alpha	$\mu = 1/4$	$\mu = 1/16$	$\mu = 1/64$
9.82e5	3.69e4	9.19e4	9.00e4	8.73e4	8.99e4

Table 2.3: Computational time (in seconds) obtained for $Ro = 0.0016$ in the fine (64×128) and coarse (16×32) mesh with the BV model and in the coarse mesh (16×32) with BV-Tikhonov model. The experiments were made in a Intel® Core™ i7 3.70 GHz.

Finally, we present the results obtained in a experiment using ${}^{\delta_M}/_{L} = 0.01$ and $Ro = 0.0002$. In this test, the high resolution solution is simulated in a 50×100 mesh (8,385 degrees of freedom and 4,096 triangles) using $\Delta t = 0.001$. Figures 2.7(a) and 2.8(a) present the reference solution. Here the streamfunction solution presents a distinct six gyre pattern. This pattern is also very sensitive to the mesh resolution, as we can see in Figures 2.7(b) and 2.8(b) in which the coarse (8×16) BV model solution using the same Δt is presented. That is, in this case the BV model streamfunction solution degenerates in two gyres and the vorticity field becomes very noisy. On the other hand, the coarse mesh BV-Tikhonov streamfunction solutions (also for $\Delta t = 0.001$) for μ equal to 1, $\frac{1}{4}$, $\frac{1}{16}$ and $\frac{1}{64}$ are presented in Figures 2.7(c), 2.7(d), 2.7(e) and 2.7(f), respectively, and their respective vorticity fields in Figures 2.8(c), 2.8(d), 2.8(e) and 2.8(f). We can see that the BV-Tikhonov solution can recover the external gyres for all tested values of the μ parameter. However, like in the previous experiments, the BV-Tikhonov solution is also dramatically dependent on the choice of μ value. For example, when $\mu = 1$ (BV-α model) the gyres are slighly intensified and displaced in relation to the high resolution solution. Nevertheless, when $\mu = \frac{1}{16}$ and $\mu = \frac{1}{64}$ they are in the right place with the correct magnitude. Moreover, the vorticity field is somewhat less noisy than the coarse BV model solution.

To sum up, in this experiment we observed that the BV-Tikhonov model can retrieve the four gyre pattern in all tested cases, but solutions can be dramatically improved by the choice of the μ parameter. We showed that the BV-α model ($\mu = 1$) provides solutions with more kinetic energy in comparison with the reference solution. Consequently, its solutions presents an intensified four gyre pattern. However, this problem can be fixed by choosing $\mu < 1$ in the BV-Tikhonov model. It is in agreement with the convergence analysis presented above, wherein it was shown that the BV-Tikhonov model has a second order consistency error which also depends on μ (see Corollary 2.1). We believe when $\mu = 1$ and the mesh is coarse (the meshwidth h is large and, consequently, the α parameter), the consistency error can affect the BV-Tikhonov solution, probably through the filter effect on the large to moderate scales (the resolved scales), but when $\mu < 1$ this kind of error is partially controlled enabling the model to produce solutions more similar with the reference solution. It is also insightful to analyze the $D_\mu F$ operator in the wave number space given by $\widehat{D_\mu F} = (1 + \mu k^2)^{-1}$ where k is the wave number. In Figure 2.4(b) we present the transfer function of $D_\mu F$ operator for $\alpha = 1$ and μ equal to 1, $\frac{1}{4}$, $\frac{1}{16}$ and $\frac{1}{64}$. In this figure we see that the resolved scale is less affected by the $D_\mu F$ operator when μ is decreased, at the expense of less regularization. We do not investigate an optimal value for the μ parameter, but we observed that values between $\mu = \frac{1}{16}$ and $\mu = \frac{1}{64}$ produce the best results and when μ is smaller than $\frac{1}{64}$ the BV-Tikhonov solution tends to the coarse BV solution. Thus, the BV-α model can retrieve the four gyre pattern in coarse meshes in which the BV model solution degenerates. However, the BV-Tikhonov model improves the BV-α in the sense that more accurate solutions can only be obtained when $\mu < 1$, at the expense of less reguralization, which is related to the consistency error in the regularized model and the undesirable filter effect on the large to moderate scales.

2.6 Conclusions

Geophysical flow simulations, due to their high Reynolds number, are presently unfeasible with the available computational resources. Regularized models are simplified models designed to reduce the degrees of freedom in simulations by virtue of small changes in the original equations, which shorten the energy cascade enabling the use of less refined meshes. In this article we studied the Tikhonov-Lavrentiev regularization applied to the BV model of geophysical flows. Firstly, we proposed a Crank-Nicolson/FEM algorithm for the BV-Tikhonov model and proved it is unconditionally stable and optimally convergent. Then, theoretical convergence rates were confirmed through numerical simulations using an analytical solution. Also, we tested the BV-Tikhonov algorithm in the more realistic double gyre wind forcing experiment. We showed it recovers the expected pattern in the case in which the coarse mesh BV model solution degenerates. Moreover, we showed that a dramatic improve over the BV-α model ($\mu = 1$) can be obtained by a carefull choice of the μ parameter in the BV-Tikhonov model. We believe it is due to the consistency error caused by alpha terms which, despite being second order according to the presented convergence analysis, can be controlled decreasing the μ parameter in the BV-Tikhonov model, at the expense of less regularization.

A natural next step is to investigate the Van Cittert approximate deconvolution technique applied to the BV-α model, which permits to control the order of the consistency error in the regularization model. This technique has been developed and used with success in the case of Navier-Stokes-α model [76, 94]. Application of the Van Cittern approximate deconvolution in the BV-α model is studied in Chapter 4.

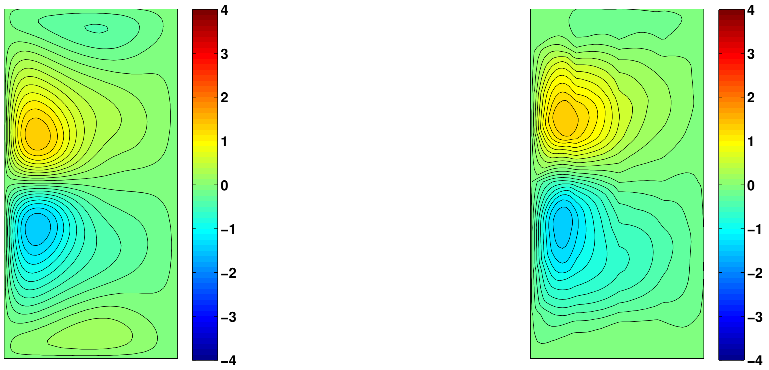

(a) BV (high res.),
$\psi_{min} = -1.40, \psi_{max} = 1.40$

(b) BV (coarse),
$\psi_{min} = -1.39, \psi_{max} = 1.46$

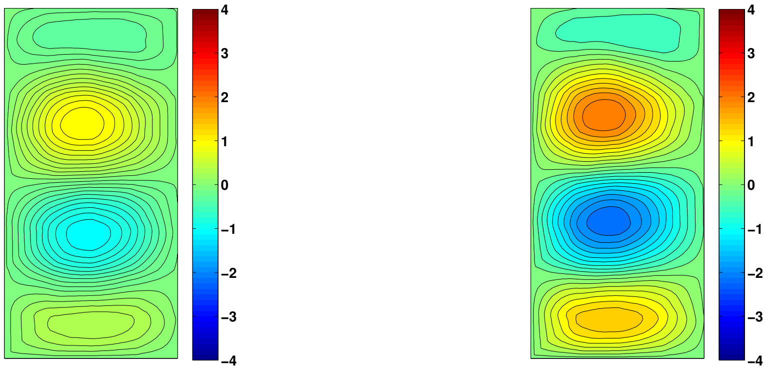

(c) BV-Tikh., $\mu = 1$
$\psi_{min} = -1.06, \psi_{max} = 1.09$

(d) BV-Tikh., $\mu = \frac{1}{4}$
$\psi_{min} = -2.20, \psi_{max} = 2.21$

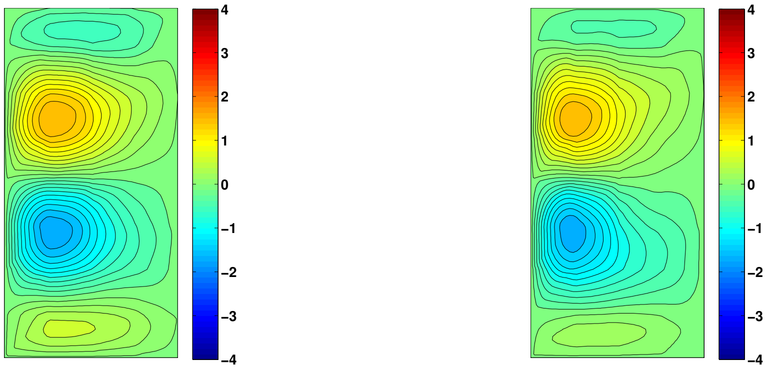

(e) BV-Tikh., $\mu = \frac{1}{16}$
$\psi_{min} = -1.68, \psi_{max} = 1.60$

(f) BV-Tikh., $\mu = \frac{1}{64}$
$\psi_{min} = -1.65, \psi_{max} = 1.59$

Figure 2.2: Streamfunction fields in the experiment with $\delta_M/L = 0.02$ and $Ro = 0.0016$ for (a) the high resolution BV model solution, (b) coarse (4×8) BV model solution and coarse (4×8) BV-Tikhonov solution for (c) $\mu = 1$, (d) $\mu = \frac{1}{4}$, (e) $\mu = \frac{1}{16}$ and (f) $\mu = \frac{1}{64}$.

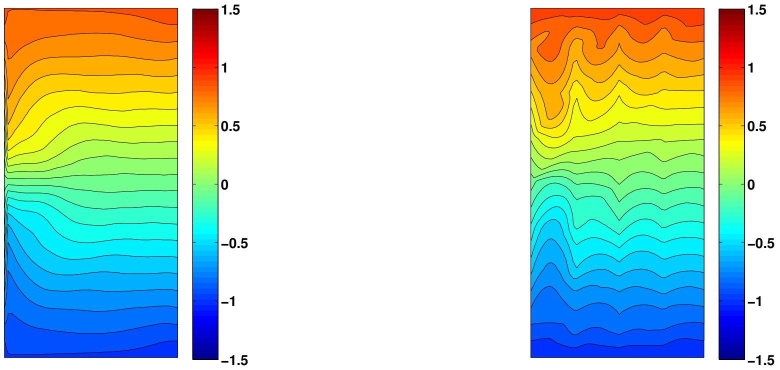

(a) BV (high res.) (b) BV (Coarse)

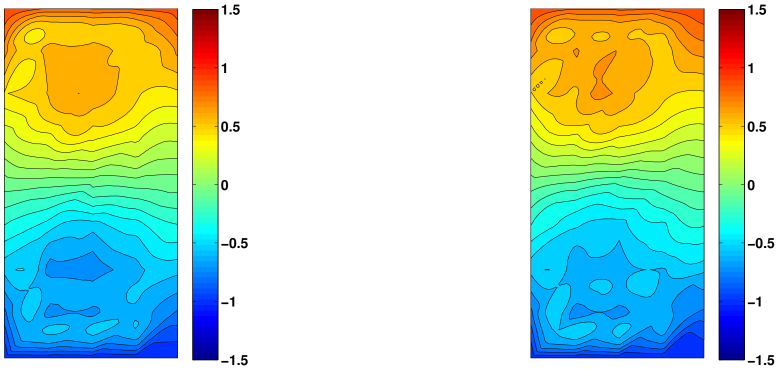

(c) BV-Tikh., $\mu = 1$ (d) BV-Tikh., $\mu = \frac{1}{4}$

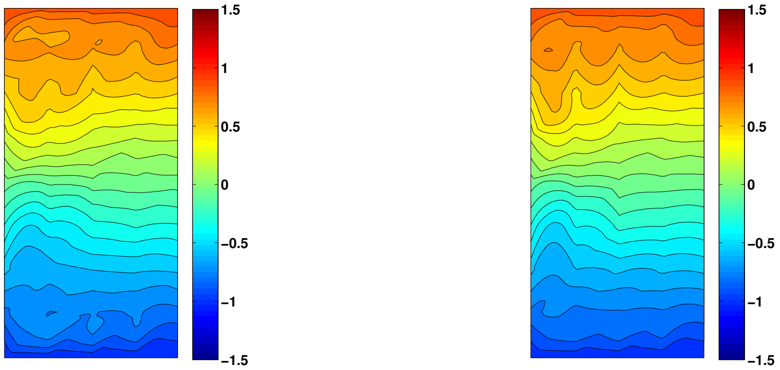

(e) BV-Tikh., $\mu = \frac{1}{16}$ (f) BV-Tikh., $\mu = \frac{1}{64}$

Figure 2.3: Vorticity fields in the experiment with $^{\delta_M}/_{L} = 0.02$ and $Ro = 0.0016$ for (a) the high resolution BV model solution, (b) coarse (4×8) BV model solution and coarse (4×8) BV-Tikhonov solution for (c) $\mu = 1$, (d) $\mu = \frac{1}{4}$, (e) $\mu = \frac{1}{16}$ and (f) $\mu = \frac{1}{64}$.

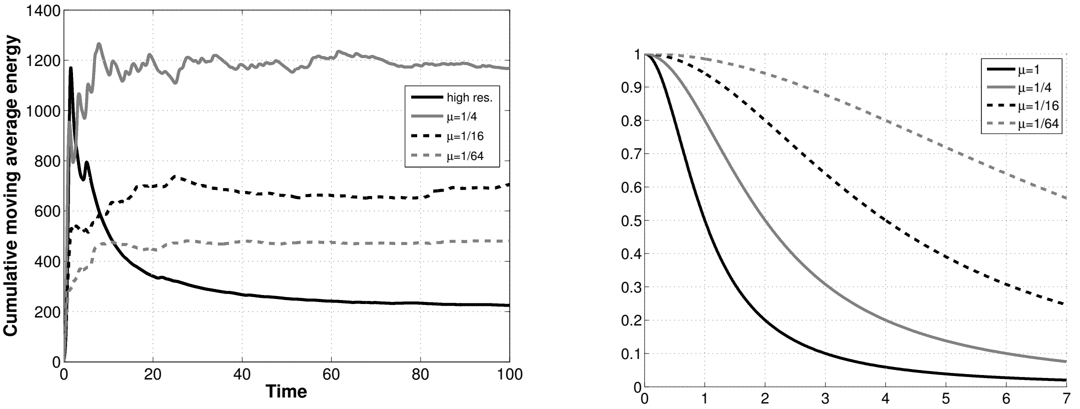

(a) Cumulative moving average (b) $D_\mu F$ transfer function

Figure 2.4: (a) Effect of different values for α on the evolution of kinetic energy in the BV-Tikhonov model. (b) Transfer function of $D_\mu F$ operator.

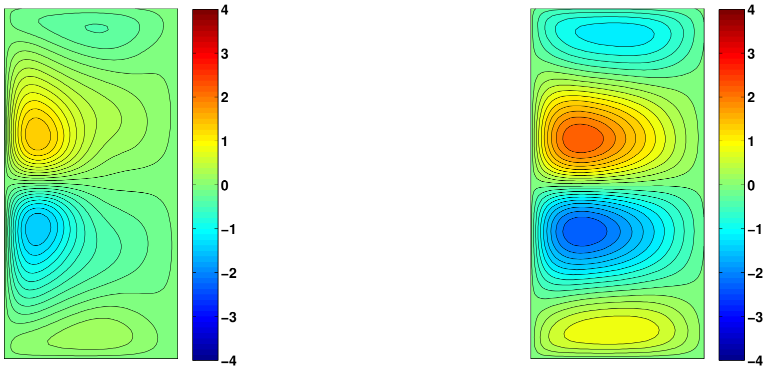

(a) BV (high res.), $\psi_{min} = -1.40, \psi_{max} = 1.40$

(b) BV (Coarse), $\psi_{min} = -2.28, \psi_{max} = 2.36$

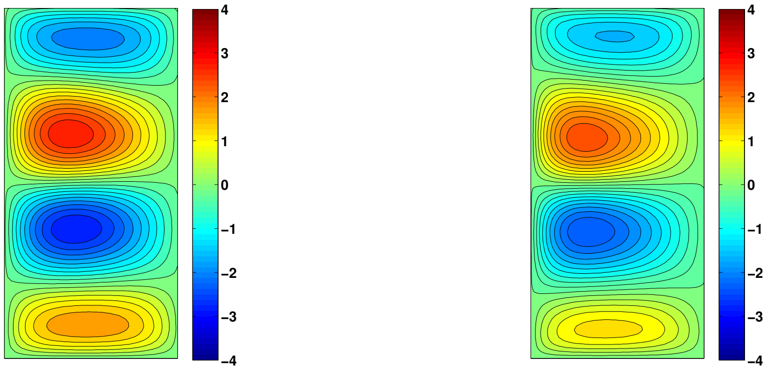

(c) BV-Tikh., $\mu = 1$ $\psi_{min} = -2.85, \psi_{max} = -3.02$

(d) BV-Tikh., $\mu = \frac{1}{4}$ $\psi_{min} = -2.37, \psi_{max} = 2.57$

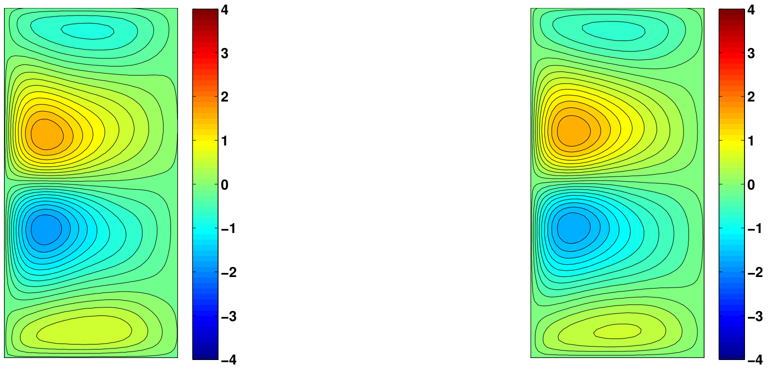

(e) BV-Tikh., $\mu = \frac{1}{16}$ $\psi_{min} = -1.83, \psi_{max} = 1.74$

(f) BV-Tikh., $\mu = \frac{1}{64}$ $\psi_{min} = -1.73, \psi_{max} = 1.78$

Figure 2.5: Streamfunction fields in the experiment with $^{\delta_M}/_L = 0.02$ and $Ro = 0.0016$ for (a) the high resolution BV model solution, (b) coarse (16×32) BV model solution and coarse (16×32) BV-Tikhonov solution for (c) $\mu = 1$, (d) $\mu = \frac{1}{4}$, (e) $\mu = \frac{1}{16}$ and (f) $\mu = \frac{1}{64}$.

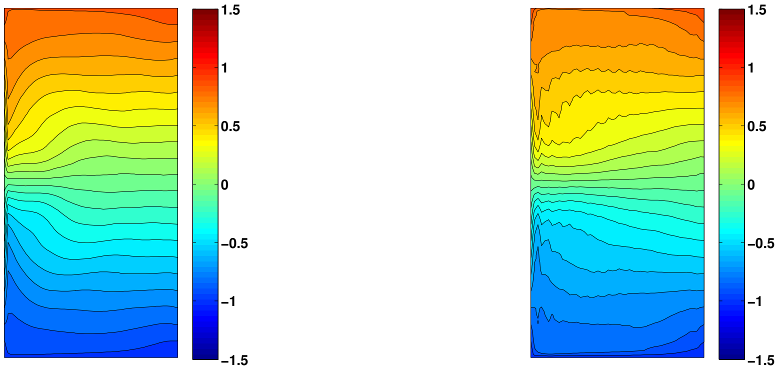

(a) BV (high res.) (b) BV (Coarse)

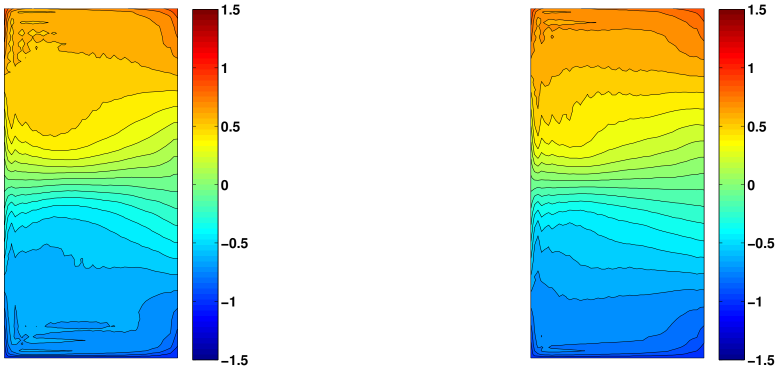

(c) BV-Tikh., $\mu = 1$ (d) BV-Tikh., $\mu = \frac{1}{4}$

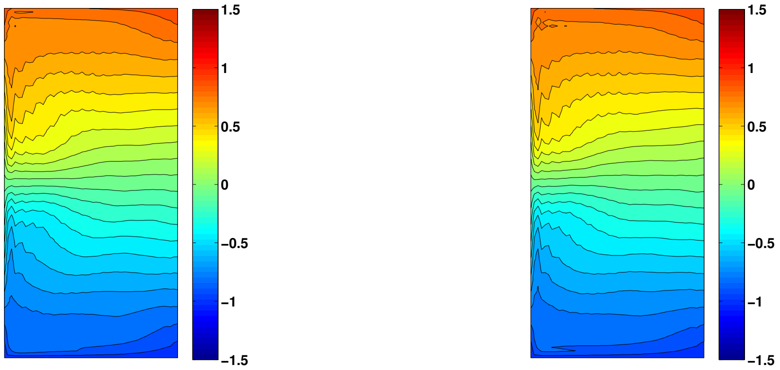

(e) BV-Tikh., $\mu = \frac{1}{16}$ (f) BV-Tikh., $\mu = \frac{1}{64}$

Figure 2.6: Vorticity fields in the experiment with ${}^{\delta_M}\!/_{L} = 0.02$ and $Ro = 0.0016$ for (a) the high resolution BV model solution, (b) coarse (16×32) BV model solution and coarse (16×32) BV-Tikhonov solution for (c) $\mu = 1$, (d) $\mu = \frac{1}{4}$, (e) $\mu = \frac{1}{16}$ and (f) $\mu = \frac{1}{64}$.

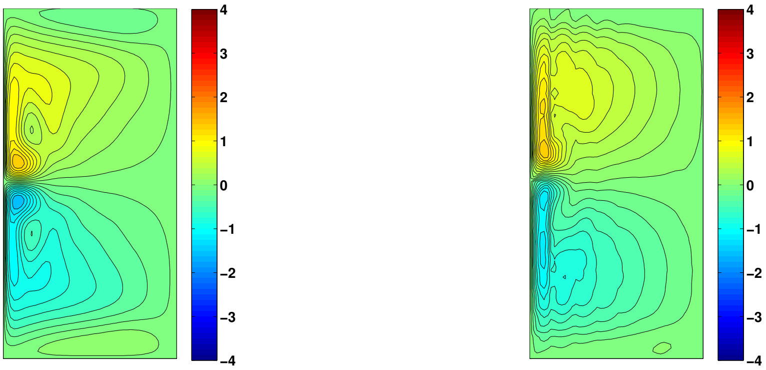

(a) BV (high res.),
$\psi_{min} = -1.51, \psi_{max} = 1.50$

(b) BV (Coarse),
$\psi_{min} = -1.23, \psi_{max} = 1.41$

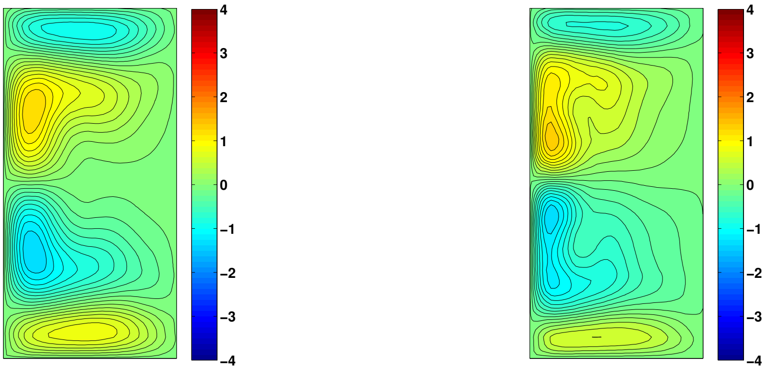

(c) BV-Tikh., $\mu = 1$
$\psi_{min} = -3.35, \psi_{max} = 3.40$

(d) BV-Tikh., $\mu = \frac{1}{4}$
$\psi_{min} = -2.25, \psi_{max} = 2.33$

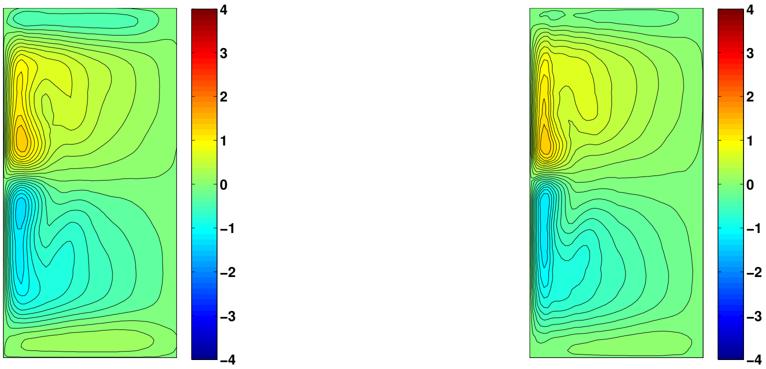

(e) BV-Tikh., $\mu = \frac{1}{16}$
$\psi_{min} = -1.65, \psi_{max} = 1.79$

(f) BV-Tikh., $\mu = \frac{1}{64}$
$\psi_{min} = -1.35, \psi_{max} = 1.54$

Figure 2.7: Streamfunction fields in the experiment with ${}^{\delta_M}/_{L} = 0.01$ and $Ro = 0.0002$ for (a) the high resolution BV model solution, (b) coarse (8×16) BV model solution and coarse (8×16) BV-Tikhonov solution for (c) $\mu = 1$, (d) $\mu = \frac{1}{4}$, (e) $\mu = \frac{1}{16}$ and (f) $\mu = \frac{1}{64}$.

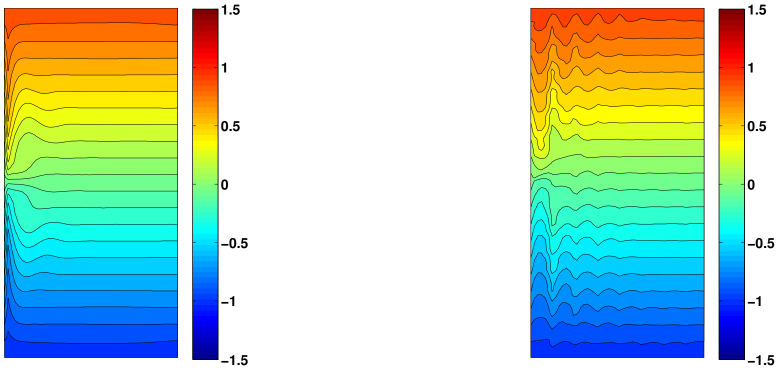

(a) BV (high res.) (b) BV (Coarse)

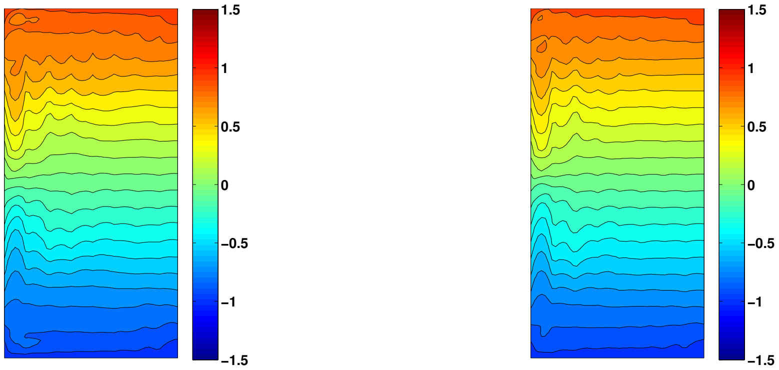

(c) BV-α, $\mu = 1$ (d) BV-Tikh. $\mu = \frac{1}{4}$

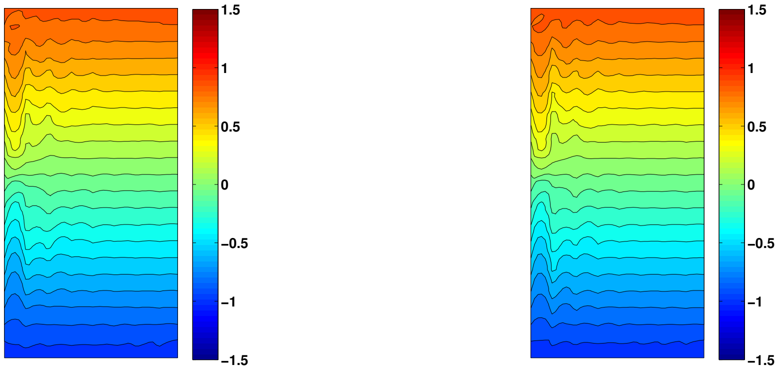

(e) BV-Tikh., $\mu = \frac{1}{16}$ (f) BV-Tikh., - $\mu = \frac{1}{64}$

Figure 2.8: Vorticity fields in the experiment with $^{\delta_M}/_L = 0.01$ and $Ro = 0.0002$ for (a) the high resolution BV model solution, (b) coarse (8×16) BV model solution and coarse (8×16) BV-Tikhonov solution for (c) $\mu = 1$, (d) $\mu = \frac{1}{4}$, (e) $\mu = \frac{1}{16}$ and (f) $\mu = \frac{1}{64}$.

3 BAROTROPIC VORTICITY-BARDINA MODEL[1]

3.1 Introduction

Geophysical flow simulations can assist in the study of climate change, weather and ocean forecasting, biological and pollutant transport in the ocean, oil exploration, and many other applications. One of the simplest models which can be used to represent these meso and large scale flows is the barotropic vorticity (BV) model of geophysical flows, which is given in dimensionless form by [47, 100]

$$\begin{aligned} \mathit{Ro}\,\tfrac{\partial\omega}{\partial t} + \mathit{Ro}\,J(\psi,\omega) - \tfrac{\partial\psi}{\partial x} - \left(\tfrac{\delta_M}{L}\right)^3 \Delta\omega &= F, && (3.1a)\\ \Delta\psi &= -\omega, && (3.1b)\end{aligned}$$

where ω is the vorticity, ψ is the streamfunction, $J(\psi,\omega) = \frac{\partial\psi}{\partial x}\frac{\partial\omega}{\partial y} - \frac{\partial\psi}{\partial y}\frac{\partial\omega}{\partial x}$ is the Jacobian, Ro is the Rossby number, δ_M is the Munk scale, L is the length scale and F is the forcing term. The BV model is commonly used in oceanography to study midlatitude ocean circulation, and it can also be extended to multilayer in order to describe the vertical motions in the ocean [78]. It has recently been used in studies involving data assimilation [113, 21], climate [95, 73, 36] and oceanic processes [12, 108].

Despite its simplified form (compared to, e.g., the primitive equations), the BV system still contains a very large range of active scales, and it is not computationally feasible to perform simulations that resolve them all, particularly when long time integration is necessary (e.g. climate modeling [78]). Traditionally, simulations are done on coarse meshes and essentially dissipative techniques such as eddy viscosity parametrizations have been used to model the under-resolved scales of the flow. However, according to [47], increasing artificial viscosity tends to reduce variability, and nonlinear structures

---

[1] The content of this chapter is coauthored by Professor Carolina C. Manica and Professor Leo G. Rebholz and was accepted in 1 December, 2014, for publication in the journal Numerical Methods for Partial Differential Equations with the title *Numerical study of a Regularized Barotropic Vorticity Model of Geophysical Flow.*

can be destroyed by excess dissipation [37, 47]. We study a regularization / large eddy simulation (LES) approach to this problem, which is to try instead to resolve only the large scales of the flow, and to model the effect of the small scales on the large scales. Even though this is a two dimensional model, it is based on the vorticity equation, which is known to have a forward enstrophy cascade, and thus this approach is valid in this context.

The model we study herein was first proposed by Khouider and Titi in [59], and is a reduction of the well-known (simplified) Bardina model to two dimensions with the beta-plane approximation. We refer to it as BV-Bardina, and it can be written as

$$Ro\frac{\partial \omega}{\partial t} + RoJ\big(\psi, \overline{\omega}\big) - \frac{\partial \psi}{\partial x} - \big(\frac{\delta_M}{L}\big)^3 \Delta\omega = F, \tag{3.2}$$

$$\Delta\psi = -\overline{\omega}, \tag{3.3}$$

$$-\alpha^2 \Delta\overline{\omega} + \overline{\omega} = \omega. \tag{3.4}$$

We will show in section 3.1.1 the derivation of the system (3.2)-(3.4) from the (simplified) Bardina model in velocity-pressure variables.

The main objective of this chapter is to study a Crank-Nicolson-in-time, finite element (FE) in space algorithm for approximating solutions to the BV-Bardina model. After proposing the scheme, we analyze its stability and convergence, and prove it is unconditionally stable with respect to the timestep size, and that it converges optimally in space and time. Moreover, we estimate convergence rates using numerical simulations and perform the benchmark double-gyre wind forcing experiment to evaluate the performance of BV-Bardina on meshes with coarse spatial resolution. To our knowledge, this is the first numerical analysis of a numerical scheme for a regularized/LES BV-type model, although a significant amount of work has been done on the related vorticity-streamfunction formulation of the Navier-Stokes equations (see [4] and references therein). Steady state analysis of numerical schemes for BV and related models has been performed in [26, 27], but of course analysis of the time dependent schemes has more (and somewhat different) complexities. Related models have been studied from a computational point of view using approximate deconvolution modeling [100, 99], and with the NS-α-derived model called BV-α [47], and have enjoyed some computational success. We believe the advantage of

BV-Bardina over approximate deconvolution modeling is in its simplicity, as there is only one filtering procedure that needs performed. BV-α is similar in form to BV-Bardina, and we note that the only difference is in BV-α the Jacobian term has the form $J\big(\psi, \omega\big)$. Hence BV-Bardina can be considered as having more regularization than BV-α. Due to their similarity, we compare solutions produced by the two models in our numerical experiments section, and find that BV-Bardina gives better coarse mesh results on the double-gyre wind forcing benchmark test. Moreover, similar numerical analysis to that performed herein can be extended to BV-α schemes, which to our knowledge has not been studied.

The chapter is organized as follows: Section 3.1.1 presents the BV-Bardina model derivation, and Section 3.2 introduces some mathematical preliminaries. Section 3.3 presents the numerical scheme and its stability analysis. Section 3.4 presents the convergence analysis. Numerical convergence rates tests and the double gyre wind forcing experiment results are given in Section 3.5. Finally, some conclusions and remarks are summarized in Section 3.6.

3.1.1 Barotropic Vorticity-Bardina model

We show here how the BV-Bardina model is obtained from the simplified Bardina model. The Bardina model emerged in 1980 as a particular closure model to approximate the Reynolds stress tensor introduced by Bardina et al. [3]. It was later studied analytically in a simplified form by Layton and Lewandowski [62], and Cao, Lunasin and Titi [15]. Following [15], the simplified Bardina model can be written as

$$\frac{\partial \mathbf{u}}{\partial t} + \overline{\mathbf{u}} \cdot \nabla \overline{\mathbf{u}} - \nu \Delta \mathbf{u} = -\nabla p,$$

$$\nabla \cdot \mathbf{u} = \nabla \cdot \overline{\mathbf{u}} = \mathbf{0},$$

$$-\alpha^2 \Delta \overline{\mathbf{u}} + \overline{\mathbf{u}} = \mathbf{u},$$

where $\alpha > 0$ is the filtering radius. Using the identity $\overline{\mathbf{u}} \cdot \nabla \overline{\mathbf{u}} = \nabla \frac{|\overline{\mathbf{u}}|^2}{2} - \overline{\mathbf{u}} \times \nabla \times \overline{\mathbf{u}}$, we have that

$$\frac{\partial \mathbf{u}}{\partial t} - \overline{\mathbf{u}} \times \nabla \times \overline{\mathbf{u}} - \nu \Delta \mathbf{u} = -\nabla\big(p + \frac{|\overline{\mathbf{u}}|^2}{2}\big). \tag{3.5}$$

Restricting now to two dimensions (0 in the z direction), we note that by a vector identity, since $\overline{\mathbf{u}}$ is divergence free, we have that $\nabla \times \big[\overline{\mathbf{u}} \times \big(\nabla \times \overline{\mathbf{u}}\big)\big] = -\overline{\mathbf{u}} \cdot \nabla\big(\nabla \times \overline{\mathbf{u}}\big)$. Now taking curl of equation (3.5) and the filter equation provides

$$\frac{\partial(\nabla \times \mathbf{u})}{\partial t} - \overline{\mathbf{u}} \cdot \nabla(\nabla \times \overline{\mathbf{u}}) - \nu\Delta(\nabla \times \mathbf{u}) = \mathbf{0}. \tag{3.6}$$

Letting $\omega = \big(\nabla \times \mathbf{u}\big) \cdot \hat{k}$, and ψ be the streamfunction associated with $\overline{\mathbf{u}}$, we have the system (after applying curl on the filter equation),

$$\begin{aligned} \frac{\partial \omega}{\partial t} + J\big(\psi, \overline{\omega}\big) - \nu\Delta\omega = 0 \\ \Delta\psi = -\overline{\omega} \\ -\alpha^2\Delta\overline{\omega} + \overline{\omega} = \omega, \end{aligned}$$

where $\overline{\omega}$ is the filtered vorticity. Now using the beta plane approximation for the Coriolis term and simplifying, we arrive at the BV-Bardina model

$$\begin{aligned} Ro\frac{\partial \omega}{\partial t} + RoJ\big(\psi, \overline{\omega}\big) - \frac{\partial \psi}{\partial x} - \big(\frac{\delta_M}{L}\big)^3\Delta\omega = F, \\ \Delta\psi = -\overline{\omega}, \\ -\alpha^2\Delta\overline{\omega} + \overline{\omega} = \omega. \end{aligned}$$

3.2 Notation and preliminaries

Let $\Omega \subset \mathbb{R}^2$ be a polygonal domain, and τ_h a regular, conforming triangulation of Ω. Define $X = H_0^1(\Omega)$ to be the subspace of $H^1(\Omega)$ with zero boundary condition. Let Y_h be the continuous finite element space with kth degree polynomials on each element of the triangulation τ_h and X_h be the subspace of Y_h with zero boundary values. Denote by $\langle\cdot,\cdot\rangle$ and $\|\cdot\|$ the $L^2(\Omega)$ inner product and norm, and $\|\cdot\|_k$ the $H^k(\Omega)$ norm.

For continuous in time functions, we denote for $1 \le m < \infty$,

$$\|f\|_{\infty,k} := \operatorname*{ess\,sup}_{t\in(0,T)} \|f(t,\cdot)\|_k \text{ and } \|f\|_{m,k} := \Big\{\int_0^T \|f(t,\cdot)\|_k^m dt\Big\}^{\frac{1}{m}}.$$

For discrete in time functions, we use the notation

$$|||f|||_{\infty,k} := \operatorname*{ess\,sup}_{0\le n\le M} \|f^n\|_k, \ |||f^{1/2}|||_{\infty,k} := \operatorname*{ess\,sup}_{0\le n\le M} \|f^{n+\frac{1}{2}}\|_k,$$

$$|||f|||_{m,k} := \big\{ \sum_{n=0}^{M} \|f^n\|_k^m dt \big\}^{\frac{1}{m}},\ |||f^{1/2}|||_{m,k} := \big\{ \sum_{n=0}^{M} \|f^{n+\frac{1}{2}}\|_k^m dt \big\}^{\frac{1}{m}}.$$

Define the trilinear operator $b : X \times X \times X \to \mathbb{R}$ by

$$b(u, v, w) = \langle J(u, v), w \rangle.$$

This trilinear operator has skew-symmetric properties, which seems to be first discovered by Fix in [23]. We state these properties here, and note that the proofs follow by integration by parts, and the divergence theorem.

Lemma 3.1. *For $\psi, \xi \in X_h$ and $\chi \in Y^h$,*

$$i)\ b\big(\psi, \xi, \xi\big) = 0; \qquad ii)\ b\big(\psi, \chi, \psi\big) = 0$$

Proof. See [23]. □

We have the following estimate for the trilinear term.

Lemma 3.2. *Let $\zeta, \phi \in X$ and $\xi \in H^2 \cap X$ we have*

$$|b\big(\xi, \phi, \zeta\big)| \le C(\Omega)\|\nabla\xi\|_1\|\nabla\phi\|\|\nabla\zeta\|.$$

Proof. Using Holder's inequality with $p, q = 4$ and $r = 2$, the result follows from $H^1 \hookrightarrow L^4$ and Poincaré's inequality. □

Given $\xi \in X$, let $P\xi \in X_h$ be the standard L^2 projection of ξ onto X_h such that

$$\big\langle \xi - P\xi, \phi \big\rangle = 0,\ \forall \phi \in X^h, \tag{3.7}$$

and let $\Pi\xi \in X_h$ be the Elliptic projection of ξ onto X_h such that

$$\big\langle \nabla(\xi - \Pi\xi), \nabla\phi \big\rangle = 0,\ \forall \phi \in X_h. \tag{3.8}$$

Lemma 3.3. *Given $\xi \in H^k$ we have the following estimates [11]*

$$i)\ \|\xi - P\xi\| \le Ch^{k+1}\|\xi\|_{k+1}, \tag{3.9a}$$

$$ii)\ \|\nabla(\xi - P\xi)\| \le Ch^{k}\|\xi\|_{k+1}, \tag{3.9b}$$

$$iii)\ \|\nabla(\xi - \Pi\xi)\| \le Ch^{k}\|\xi\|_{k+1}. \tag{3.9c}$$

3.2.1 Discrete filtering

We define the discrete Laplacian operator $\Delta_h : X \to X_h$ in the usual way by

$$\big\langle \Delta_h \psi, \chi \big\rangle = -\big\langle \nabla\psi, \nabla\chi \big\rangle, \, \forall \chi \in X_h. \tag{3.10}$$

Discrete filtering is defined, for $\phi \in L^2(\Omega)$, by

$$\alpha^2 \langle \nabla \overline{\phi}^h, \nabla v_h) \rangle + \langle \overline{\phi}^h, v_h \rangle = \langle \phi, v_h \rangle, \ \forall v_h \in X_h.$$

The following bounds are known to hold for filtered quantities (see [79]): For $\phi \in X$ we have the following upper bounds:

$$\|\overline{\phi}^h\| \le \|\phi\|, \tag{3.11}$$

$$\|\nabla\overline{\phi}^h\| \le C(\Omega)\|\nabla\phi\|, \tag{3.12}$$

$$\|\nabla\overline{\phi}^h\| \le \|\nabla\phi\| \text{ for } \phi \in X_h. \tag{3.13}$$

Lemma 3.4. *For $\phi \in L^2(\Omega)$, the discrete filtering operation satisfies*

$$\|\phi - \overline{\phi}^h\|^2 \le C\alpha^4 \|\Delta\overline{\phi}\|^2 + C\big(\alpha h^k + h^{k+1}\big)^2 |\overline{\phi}|^2_{k+1}, \tag{3.14}$$

and thus for $k \ge 1$,

$$\|\phi - \overline{\phi}^h\|^2 \le \big(C\alpha^4 + C\alpha^2 h^{2k} + h^{2k+2}\big) \|\overline{\phi}\|^2_{k+1}. \tag{3.15}$$

Proof. See [66]. ☐

Define the energy norm $\|\cdot\|_E$ and the energy dissipation norm $\|\cdot\|_\epsilon$ by

$$\|\phi\|_E := \big\langle \phi, \overline{\phi}^h \big\rangle^{1/2} = \big(\|\overline{\phi}^h\|^2 + \alpha^2 \|\nabla\overline{\phi}^h\|^2 \big)^{1/2},$$
$$\|\phi\|_\varepsilon := \big\langle \nabla\phi, \nabla\overline{\phi}^h \big\rangle^{1/2} = \big(\|\nabla\overline{\phi}^h\|^2 + \alpha^2 \|\Delta_h\overline{\phi}^h\|^2 \big)^{1/2}.$$

These norms are natural for the BV-Bardina model we study herein, and it is proven in [79] that this energy norm is equivalent to the $L^2(\Omega)$ norm, and this energy dissipation norm is equivalent to the $H^1(\Omega)$ norm:

Lemma 3.5. *If the filtering radius α is chosen so that $\alpha \leq O\big(h\big)$, the natural energy norm of BV-Bardina, $\|\cdot\|_E$ is equivalent to the usual L^2 norm in X_h: for $\phi \in X_h$, there exists C_E independent of h, ϕ satisfying*

$$\|\phi\|_E \leq \|\phi\| \leq C_E \|\phi\|_E. \tag{3.16}$$

Additionally, the natural energy dissipation norm of BV-Bardina, $\|\cdot\|_\epsilon$, is equivalent to the H^1 norm in X_h: there exists C_ϵ independent of h,ϕ satisfying

$$\|\phi\|_\epsilon \leq \|\nabla\phi\| \leq C_\epsilon \|\phi\|_\epsilon. \tag{3.17}$$

3.3 Numerical Scheme for BV-Bardina

Following [100, 47] we consider the model with slip boundary conditions for velocity, which translates into the homogeneous Dirichlet condition $\omega|_{\partial\Omega} = 0$, and the impermeability condition $\psi|_{\partial\Omega} = 0$. As in [47], we consider the additional homogeneous Dirichlet condition $\overline{\omega}|_{\partial\Omega} = 0$ in the filter equation, which allows inversion to be performed uniquely.

Our motivation for studying the BV and BV-Bardina models is the search for efficient, unconditionally stable and accurate methods for the simulation of geophysical flows. We present now a finite element discretization in space, together with Crank-Nicolson time discretization. As it is common in such discretizations, we denote the half timesteps by $v^{n+\frac{1}{2}} := \frac{v^n+v^{n+1}}{2}$ and $t^{n+\frac{1}{2}} := \frac{t^n+t^{n+1}}{2}$.

Algorithm 3.1 (Crank-Nicolson BV-Bardina model)**.** *Given ω_h^0 and ψ_h^0 as the $L^2(\Omega)$ projections into X_h of $\omega_0 \in X$ and $\psi_0 \in X$, endtime T, $F \in L^\infty(0,T;L^2(\Omega))$, and timestep $\Delta t > 0$, set $M = \frac{T}{\Delta t}$ and for n=0,...,M-1, find $(\omega_h^{n+1}, \psi_h^{n+1}, \overline{\omega_h^{n+1}}^h) \in$*

$X_h \times X_h \times X_h$ satisfying

$$Ro\big\langle \tfrac{\omega_h^{n+1}-\omega_h^n}{\Delta t}, v_h\big\rangle + Ro\ b\big(\psi_h^{n+\frac{1}{2}}, \overline{\omega_h^{n+\frac{1}{2}}}^h, v_h\big) - \big\langle \tfrac{\partial \psi_h^{n+\frac{1}{2}}}{\partial x}, v_h\big\rangle$$

$$+\big(\tfrac{\delta_M}{L}\big)^3\big\langle \nabla\omega_h^{n+\frac{1}{2}}, \nabla v_h\big\rangle = \big\langle F^{n+\frac{1}{2}}, v_h\big\rangle\ \forall v_h \in X_h, \tag{3.18}$$

$$\big\langle \nabla\psi_h^{n+1}, \nabla\chi\big\rangle - \big\langle \overline{\omega_h^{n+1}}^h, \chi\big\rangle = 0\ \forall \chi \in X_h, \tag{3.19}$$

$$\alpha^2\big\langle \nabla\overline{\omega_h^{n+1}}^h, \nabla\xi\big\rangle + \big\langle \overline{\omega_h^{n+1}}^h, \xi\big\rangle - \big\langle \omega_h^{n+1}, \xi\big\rangle = 0\ \forall \xi \in X_h. \tag{3.20}$$

We prove next that Algorithm 3.1 is unconditionally stable with respect to the timestep size.

Lemma 3.6. *Consider Algorithm 3.1. ω_h and ψ_h satisfy the following bounds,*

$$Ro\|\nabla\psi_h^M\|^2 + \Delta t\big(\tfrac{\delta_M}{L}\big)^3 \sum_{n=0}^{M-1} \|\Delta_h \psi_h^{n+\frac{1}{2}}\|^2 \leq C(data). \tag{3.21}$$

and

$$C_E^{-1} Ro\|\omega_h^M\|^2 + \Delta t\big(\tfrac{\delta_M}{L}\big)^3 \sum_{n=0}^{M-1} \tfrac{C_\epsilon^{-1}}{2}\|\nabla\omega_h^{n+\frac{1}{2}}\|^2 \leq C(data). \tag{3.22}$$

Remark 3.1. *The bounds* (3.21)-(3.22) *are sufficient for the Leray-Schauder fixed point theorem to be applied, in order to prove existence of a solution at each timestep (as in [60]). Uniqueness can be proven in the standard way, and will hold provided a timestep restriction.*

Proof. We start proving estimate (3.21). Choosing $v_h = \psi_h^{n+\frac{1}{2}}$, using skew-symmetric properties of b, and that $\big\langle \frac{\partial\psi_h^{n+\frac{1}{2}}}{\partial x}, \psi_h^{n+\frac{1}{2}}\big\rangle = 0$ since $\psi_h^{n+1/2} \in X_h$, we get that

$$Ro\big\langle \frac{\omega_h^{n+1} - \omega_h^n}{\Delta t}, \psi_h^{n+\frac{1}{2}}\big\rangle + \big(\tfrac{\delta_M}{L}\big)^3\big\langle \nabla\omega_h^{n+\frac{1}{2}}, \nabla\psi_h^{n+\frac{1}{2}}\big\rangle = \big\langle F^{n+\frac{1}{2}}, \psi_h^{n+\frac{1}{2}}\big\rangle. \tag{3.23}$$

Rewrite the two terms in the LHS in (3.23). For the first, we average (3.19) at the n and $n+1$ time levels, then choose $\chi = \overline{\omega_h^{n+1}}^h - \overline{\omega_h^n}^h$ to obtain

$$\big\langle \nabla\psi_h^{n+\frac{1}{2}}, \nabla\big(\overline{\omega_h^{n+1}}^h - \overline{\omega_h^n}^h\big)\big\rangle = \big\langle \overline{\omega_h^{n+\frac{1}{2}}}^h, \overline{\omega_h^{n+1}}^h - \overline{\omega_h^n}^h\big\rangle = \tfrac{\|\overline{\omega_h^{n+1}}^h\|^2 - \|\overline{\omega_h^n}^h\|^2}{2}. \tag{3.24}$$

Next, subtracting (3.19) in n from (3.19) in $n+1$ and choosing $\chi = \psi_h^{n+\frac{1}{2}}$

$$\frac{\big\|\nabla\psi_h^{n+1}\big\|^2-\big\|\nabla\psi_h^{n}\big\|^2}{2} = \big\langle \nabla\big(\psi_h^{n+1}-\psi_h^{n}\big), \nabla\psi_h^{n+\frac{1}{2}}\big\rangle = \big\langle \overline{\omega_h^{n+1}}^h - \overline{\omega_h^{n}}^h, \psi_h^{n+\frac{1}{2}}\big\rangle. \tag{3.25}$$

Subtracting (3.20) in the time step n from (3.20) in the time step $n+1$, choosing $\xi = \psi_h^{n+\frac{1}{2}}$ and using (3.24) and (3.25) we get

$$\alpha^2\Big(\frac{\|\overline{\omega_h^{n+1}}^h\|^2-\|\overline{\omega_h^{n}}^h\|^2}{2}\Big) + \frac{\big\|\nabla\psi_h^{n+1}\big\|^2-\big\|\nabla\psi_h^{n}\big\|^2}{2} = \big\langle \omega_h^{n+1}-\omega_h^{n}, \psi_h^{n+\frac{1}{2}}\big\rangle. \tag{3.26}$$

For the second term in (3.23), we average (3.19) and (3.20), choose $\chi = \omega_h^{n+\frac{1}{2}}$ and $\xi = \overline{\omega_h^{n+\frac{1}{2}}}^h$, respectively, and combine the results to obtain

$$\big\langle \nabla\psi_h^{n+\frac{1}{2}}, \nabla\omega_h^{n+\frac{1}{2}}\big\rangle = \alpha^2\|\nabla\overline{\omega_h^{n+\frac{1}{2}}}^h\|^2 + \|\overline{\omega_h^{n+\frac{1}{2}}}^h\|^2. \tag{3.27}$$

Then averaging (3.10), choosing $\chi = \psi_h^{n+\frac{1}{2}}$ and using Poincaré inequality we have

$$\big\|\nabla\psi_h^{n+\frac{1}{2}}\big\| \le C_{PF}\big\|\Delta_h\psi_h^{n+\frac{1}{2}}\big\|. \tag{3.28}$$

Averaging (3.19), combining with (3.10), using Cauchy-Schwarz inequality and choosing $\chi = \Delta_h\psi_h^{n+\frac{1}{2}}$ we obtain

$$\|\Delta_h\psi_h^{n+\frac{1}{2}}\| \le \|\overline{\omega_h^{n+\frac{1}{2}}}^h\|. \tag{3.29}$$

Using (3.26), (3.27), (3.28), (3.29) and Cauchy-Schwarz in (3.23)

$$\begin{aligned}&\tfrac{Ro}{2\Delta t}\big(\big\|\nabla\psi_h^{n+1}\big\|^2 + \alpha^2\|\overline{\omega_h^{n+1}}^h\|^2 - \big\|\nabla\psi_h^{n}\big\|^2 - \alpha^2\|\overline{\omega_h^{n}}^h\|^2\big)\\ &+ \big(\tfrac{\delta_M}{L}\big)^3\big(\alpha^2\|\nabla\overline{\omega_h^{n+\frac{1}{2}}}^h\|^2 + \|\Delta_h\psi_h^{n+\frac{1}{2}}\|^2\big) \le \|F^{n+\frac{1}{2}}\|_{-1}\|\Delta_h\psi_h^{n+\frac{1}{2}}\|.\end{aligned} \tag{3.30}$$

The bound (3.21) follows after we use Young's inequality with $\varepsilon = \big(\frac{\delta_M}{L}\big)^3$ and sum from $n=1$ to $n=M-1$.

It remains to show estimate (3.22). Choosing $v_h = \overline{\omega_h^{n+\frac{1}{2}}}^h$ in (3.18), using that $\big\langle \omega_h^{n+1}, \overline{\omega_h^{n}}^h\big\rangle = \big\langle \overline{\omega_h^{n+1}}^h, \omega_h^{n}\big\rangle$, skew-symmetric properties of b, inequality (3.13) and Cauchy-Schwarz inequality we have

$$\begin{aligned}&\tfrac{Ro}{\Delta t}\big\langle \omega_h^{n+1}, \overline{\omega_h^{n+1}}^h\big\rangle - \tfrac{Ro}{\Delta t}\big\langle \omega_h^{n}, \overline{\omega_h^{n}}^h\big\rangle + \big(\tfrac{\delta_M}{L}\big)^3\big\langle \nabla\omega_h^{n+\frac{1}{2}}, \nabla\overline{\omega_h^{n+\frac{1}{2}}}^h\big\rangle\\ &= \big\langle F^{n+\frac{1}{2}}, \overline{\omega_h^{n+\frac{1}{2}}}^h\big\rangle + \big\langle \tfrac{\partial\psi_h^{n+\frac{1}{2}}}{\partial x}, \overline{\omega_h^{n+\frac{1}{2}}}^h\big\rangle \le \|F^{n+\frac{1}{2}}\|_{-1}\|\nabla\omega_h^{n+\frac{1}{2}}\| + C_{PF}\|\nabla\psi_h^{n+\frac{1}{2}}\|\|\nabla\omega_h^{n+\frac{1}{2}}\|.\end{aligned}$$

Using the norm equivalence in Lemma 3.5 and Young's inequality with $\epsilon = C_\epsilon\big(\frac{L}{\delta_M}\big)^3$, estimate (3.22) follows after we sum from $n = 0$ to $n = M-1$ and use estimate (3.21). $\square$

3.4 Convergence

This section rigorously proves a convergence estimate in space and time for the BV-Bardina algorithm.

Theorem 3.1 (Convergence). *Let $(\omega(t), \psi(t))$ be a smooth strong solution of the BV model such that the norms of $(\omega(t), \psi(t))$ on the right hand side of (3.31) and (3.32) are finite. Suppose $(\omega_h, \psi_h) \in X^h \times X^h$ solves the Crank-Nicolson approximation (3.18)-(3.20) of the BV-Bardina model . Then for Δt small enough (in order to use the discrete Gronwall inequality), we have*

$$Ro\big\||\omega - \omega_h|\big\|_{\infty,0} \leq f\big(\Delta t, h, \alpha\big) + Ch^{k+1}\big\||\omega|\big\|_{\infty,k+1}, \tag{3.31}$$

$$\begin{aligned}\big(C_\epsilon^{-1}\big(\tfrac{\delta_M}{L}\big)^3 \sum_{n=0}^{M-1} \Delta t\big\|\nabla\big(\omega(t^{n+\frac{1}{2}}) - \omega_h^{n+\frac{1}{2}}\big)\big\|^2\big)^{1/2} &\leq f\big(\Delta t, h, \alpha\big) + C\Delta t^2\big(\tfrac{\delta_M}{L}\big)^{3/2}\big\|\omega_{tt}\big\|_{2,0} \\ &\quad + C\big(\tfrac{\delta_M}{L}\big)^{3/2}h^k\big\||\omega|\big\|_{2,k+1},\end{aligned} \tag{3.32}$$

where

$$\begin{aligned}f\big(\Delta t, h, \alpha\big) :=\ & C^*\big\{h^k\big(\tfrac{L}{\delta_M}\big)^{3/2}\big[C|||\psi^{1/2}|||_{2,k+1} + Ch|||\omega^{1/2}|||_{2,k+1} + C\big(\tfrac{\delta_M}{L}\big)^3|||\omega^{1/2}|||_{2,k+1} \\ & + CRoh\big(|||\omega^{1/2}|||^2_{4,k+1} + |||\overline{\omega}^{1/2}|||^2_{4,k+1}\big) + CRo\big(|||\nabla\omega^{1/2}|||^2_{4,1} + |||\psi^{1/2}|||^2_{4,k+1}\big) + CRoh|||\omega^{1/2}|||^2_{4,k+1} \\ & + CRoh\big(|||\omega^{1/2}|||^2_{4,1} + |||\psi^{1/2}|||^2_{4,k+1}\big) + Ro\big(Ch + Ch^k\big)|||\omega^{1/2}|||^2_{4,k+1}\Big] \\ & + \big(\alpha^2 + \alpha^2h^k + h^{k+1}\big)\big(\tfrac{L}{\delta_M}\big)^{3/2}\Big[C|||\overline{\omega}^{1/2}|||_{2,k+1} + Ro\big(|||\nabla\omega^{1/2}|||^2_{4,1} + |||\overline{\omega}^{1/2}|||^2_{4,k+1}\big) \\ & + Ro\big(C|||\overline{\omega}^{1/2}|||^2_{4,k+1} + C|||\omega^{1/2}|||^2_{4,1} + C|||\psi^{1/2}|||^2_{4,k+1}\big)\Big] \\ & + Ro\big(\tfrac{L}{\delta_M}\big)^{3/2}\big(Ch^k\alpha^2 + C\alpha^2h^{k+1} + Ch^{k+2}\big)|||\overline{\omega^{1/2}}|||^2_{4,k+1} + \Delta t^2\big(\tfrac{L}{\delta_M}\big)^{3/2}\Big[C\big(\tfrac{\delta_M}{L}\big)^3\big\||\nabla\omega_{tt}|\big\|_{2,0} \\ & + C\big\||\psi_{tt}|\big\|_{2,0} + C|||\nabla\psi^{1/2}|||^2_{4,1} + C|||\omega_{tt}|||^2_{4,0} + C|||\nabla\omega(t^{1/2})|||^2_{4,1} + C|||\psi_{tt}|||^2_{4,0}\big\}.\end{aligned} \tag{3.33}$$

Remark 3.2. *Suppose that the indicated norms on the right hand side of (3.31)-(3.33) are finite. Then the error in the Crank-Nicolson finite element scheme for* *the BV-Bardina model is of the order*

$$Ro|||\omega - \omega_h|||_{\infty,0} + C_\epsilon^{-1}\big(\big(\tfrac{\delta_M}{L}\big)^3 \sum_{n=0}^{M-1} \Delta t \|\nabla\big(\omega(t^{n+\frac{1}{2}}) - \omega_h^{n+\frac{1}{2}}\big)\|^2\big)^{1/2} \\ \leq O\big(h^k + \Delta t^2 + \alpha^2 |||\overline{\omega}^{1/2}|||^2_{2,k+1}\big).$$

Moreover, using the result above, it is straightforward to show also that

$$|||\psi - \psi_h|||_{\infty,1} \leq O\big(h^k + \Delta t^2 + \alpha^2 |||\overline{\omega}^{1/2}|||^2_{2,k+1}\big).$$

As discussed in [66], the term $|||\overline{\omega}^{1/2}|||_{2,k+1}$ *can depend inversely on* α *if* $k \geq 2$ *and if no assumptions are made either about* ω *being periodic or having normal derivatives vanish at the boundary. Hence for the choice of linear elements (*$k = 1$*) with* $\alpha \leq O(h)$*, optimal spatial convergence can be expected, but not necessarily for* $k = 2$*. However, our numerical experiments with* $k = 2$ *do show optimal convergence.*

Proof. The solution ω of the BV model satisfies

$$Ro\big\langle \tfrac{\omega^{n+1}-\omega^n}{\Delta t}, v_h\big\rangle + Rob\big(\psi^{n+\frac{1}{2}}, \omega^{n+\frac{1}{2}}, v_h\big) - \big\langle \tfrac{\partial\psi^{n+\frac{1}{2}}}{\partial x}, v_h\big\rangle + \big(\tfrac{\delta_M}{L}\big)^3 \big\langle \nabla\omega^{n+\frac{1}{2}}, \nabla v_h\big\rangle \\ = \big\langle F^{n+\frac{1}{2}}, v_h\big\rangle + Intp(\omega^n, \psi^n; v_h) \;\forall v_h \in X^h \tag{3.34}$$

where

$$Intp(\omega^n, \psi^n; v_h) := Ro\big\langle \tfrac{\omega^{n+1}-\omega^n}{\Delta t} - \omega_t(t^{n+\frac{1}{2}}), v_h\big\rangle + \big(\tfrac{\delta_M}{L}\big)^3 \big\langle \nabla\omega^{n+\frac{1}{2}} - \nabla\omega(t^{n+\frac{1}{2}}), \nabla v_h\big\rangle \\ - \big\langle \tfrac{\partial\psi^{n+\frac{1}{2}}}{\partial x} - \tfrac{\partial\psi(t^{n+\frac{1}{2}})}{\partial x}, v_h\big\rangle + Ro\big[b\big(\psi^{n+\frac{1}{2}}, \omega^{n+\frac{1}{2}}, v_h\big) - b\big(\psi(t^{n+\frac{1}{2}}), \omega(t^{n+\frac{1}{2}}), v_h\big)\big]. \tag{3.35}$$

Define

$$e := \omega - \omega_h = \big(\omega - P\omega\big) - \big(\omega_h - P\omega\big) = e_\perp - e_h, \tag{3.36a}$$

$$E := \psi - \psi_h = \big(\psi - \Pi\psi\big) - \big(\psi_h - \Pi\psi\big) = E_\perp - E_h. \tag{3.36b}$$

Subtracting (3.18) from (3.34), choosing $v_h = \overline{e_h^{n+\frac{1}{2}}}^h$, using $\big\langle e_h^{n+1}, \overline{e_h^n}^h\big\rangle = \big\langle \overline{e_h^{n+1}}^h, e_h^n\big\rangle$ and adding and subtracting $b\big(\psi_h^{n+\frac{1}{2}}, \overline{\omega^{n+\frac{1}{2}}}^h, \overline{e_h^{n+\frac{1}{2}}}^h\big)$ and $b\big(\psi_h^{n+\frac{1}{2}}, \omega^{n+\frac{1}{2}}, \overline{e_h^{n+\frac{1}{2}}}^h\big)$, we obtain

$$Ro\big(\langle e_h^{n+1}, \overline{e_h^{n+1}}^h\rangle - \langle e_h^n, \overline{e_h^n}^h\rangle\big) + 2\Delta t\big(\tfrac{\delta_M}{L}\big)^3\langle \nabla e_h^{n+\frac{1}{2}}, \nabla\overline{e_h^{n+\frac{1}{2}}}^h\rangle = -2\Delta t\langle \tfrac{\partial E^{n+\frac{1}{2}}}{\partial x}, \overline{e_h^{n+\frac{1}{2}}}^h\rangle$$
$$-2\Delta t Ro\big[b\big(\psi_h^{n+\frac{1}{2}}, \overline{e_\perp^{n+\frac{1}{2}}}^h, \overline{e_h^{n+\frac{1}{2}}}^h\big) + b\big(\psi_h^{n+\frac{1}{2}}, \overline{\omega^{n+\frac{1}{2}}}^h - \omega^{n+\frac{1}{2}}, \overline{e_h^{n+\frac{1}{2}}}^h\big) + b\big(E^{n+\frac{1}{2}}, \omega^{n+\frac{1}{2}}, \overline{e_h^{n+\frac{1}{2}}}^h\big)\big]$$
$$+2\Delta t\big(\tfrac{\delta_M}{L}\big)^3\langle \nabla e_\perp^{n+\frac{1}{2}}, \nabla\overline{e_h^{n+\frac{1}{2}}}^h\rangle + 2\Delta t Intp(\omega^n, \psi^n; \overline{e_h^{n+\frac{1}{2}}}^h), \tag{3.37}$$

since $\big\langle e_\perp^{n+1} - e_\perp^n, \overline{e_h^{n+\frac{1}{2}}}^h\big\rangle = 0$. We next estimate the terms in the RHS. Using Cauchy-Schwarz and Young inequalities

$$\big|\langle \tfrac{\partial E^{n+\frac{1}{2}}}{\partial x}, \overline{e_h^{n+\frac{1}{2}}}^h\rangle\big| \leq \tfrac{C_\epsilon^{-1}}{16}\big(\tfrac{\delta_M}{L}\big)^3\|\nabla e_h^{n+\frac{1}{2}}\|^2 + C\big(\tfrac{L}{\delta_M}\big)^3\|\nabla E^{n+\frac{1}{2}}\|^2 \tag{3.38}$$

We estimate $\|\nabla E^{n+\frac{1}{2}}\|$ by averaging (3.19) and subtracting $\psi^{n+\frac{1}{2}}$ satisfying the BV model, choosing $v_h = E_h^{n+\frac{1}{2}}$ and using Cauchy-Schwarz and Poincaré inequalities to get

$$\|\nabla E_h^{n+\frac{1}{2}}\|^2 \leq C\|\overline{\omega_h^{n+\frac{1}{2}} - \omega^{n+\frac{1}{2}}}^h\|\|\nabla E_h^{n+\frac{1}{2}}\| + C\|\overline{\omega^{n+\frac{1}{2}}}^h - \omega^{n+\frac{1}{2}}\|\|\nabla E_h^{n+\frac{1}{2}}\|. \tag{3.39}$$

Now, use (3.39) and (3.11) to obtain

$$\|\nabla E^{n+\frac{1}{2}}\|^2 \leq \|\nabla E_\perp^{n+\frac{1}{2}}\|^2 + C\|e_h^{n+\frac{1}{2}}\|^2 + C\|e_\perp^{n+\frac{1}{2}}\|^2 + C\|\overline{\omega^{n+\frac{1}{2}}}^h - \omega^{n+\frac{1}{2}}\|^2. \tag{3.40}$$

Using (3.40), Lemma 3.4 and Lemma 3.3 in (3.38) we get

$$\big|\langle \tfrac{\partial E^{n+\frac{1}{2}}}{\partial x}, \overline{e_h^{n+\frac{1}{2}}}^h\rangle\big| \leq \tfrac{C_\epsilon^{-1}}{16}\big(\tfrac{\delta_M}{L}\big)^3\|\nabla e_h^{n+\frac{1}{2}}\|^2 + C\big(\tfrac{L}{\delta_M}\big)^3\|e_h^{n+\frac{1}{2}}\|^2 + \big(\tfrac{L}{\delta_M}\big)^3\big[Ch^{2k}\|\psi^{n+\frac{1}{2}}\|_{k+1}^2$$
$$+ Ch^{2k+2}\|\omega^{n+\frac{1}{2}}\|_{k+1}^2 + \big(C\alpha^4 + C\alpha^2h^{2k} + h^{2k+2}\big)\|\overline{\omega}^{n+\frac{1}{2}}\|_{k+1}^2\big]. \tag{3.41}$$

Cauchy-Schwarz and Young inequalities, inequality (3.13) and Lemma 3.3 provides

$$\big|\big(\tfrac{\delta_M}{L}\big)^3\langle \nabla e_\perp^{n+\frac{1}{2}}, \nabla\overline{e_h^{n+\frac{1}{2}}}^h\rangle\big| \leq \tfrac{C_\epsilon^{-1}}{16}\big(\tfrac{\delta_M}{L}\big)^3\|\nabla e_h^{n+\frac{1}{2}}\|^2 + C\big(\tfrac{\delta_M}{L}\big)^3h^{2k}\|\omega^{n+\frac{1}{2}}\|_{k+1}^2. \tag{3.42}$$

For the third nonlinear term, we use Lemma 3.2, Young's inequality with $\epsilon = \frac{C_\epsilon^{-1}}{10Ro}\big(\frac{\delta_M}{L}\big)^3$, inequality (3.40), Lemma 3.3, Lemma 3.4, Young's Inequality with $\epsilon = 1$ and for $k \geq 1$, which yields

$$
\begin{aligned}
&\big|Rob\big(E^{n+\frac{1}{2}}, \omega^{n+\frac{1}{2}}, \overline{e_h^{n+\frac{1}{2}}}^h\big)\big| \leq \tfrac{C_\epsilon^{-1}}{20}\big(\tfrac{\delta_M}{L}\big)^3 \|\nabla e_h^{n+\frac{1}{2}}\|^2 + CRo^2\big(\tfrac{L}{\delta_M}\big)^3 \|\nabla \omega^{n+\frac{1}{2}}\|_1^2 \|\nabla E^{n+\frac{1}{2}}\|^2 \\
&\leq \tfrac{C_\epsilon^{-1}}{20}\big(\tfrac{\delta_M}{L}\big)^3 \|\nabla e_h^{n+\frac{1}{2}}\|^2 + CRo^2\big(\tfrac{L}{\delta_M}\big)^3 \|\nabla \omega^{n+\frac{1}{2}}\|_1^2 \|e_h^{n+\frac{1}{2}}\|^2 \\
&+ CRo^2\big(\tfrac{L}{\delta_M}\big)^3 h^{2k}\big(\|\nabla \omega^{n+\frac{1}{2}}\|_1^4 + \|\psi^{n+\frac{1}{2}}\|_{k+1}^4\big) + CRo^2\big(\tfrac{L}{\delta_M}\big)^3 C h^{2k+2} \|\omega^{n+\frac{1}{2}}\|_{k+1}^4 \\
&+ CRo^2\big(\tfrac{L}{\delta_M}\big)^3 \big(C\alpha^4 + C\alpha^2 h^{2k} + h^{2k+2}\big)\big(\|\nabla \omega^{n+\frac{1}{2}}\|_1^4 + \|\overline{\omega}^{n+\frac{1}{2}}\|_{k+1}^4\big). \qquad (3.43)
\end{aligned}
$$

For the second nonlinear term, we use Holder's inequality with $p = \infty$ and $q = r = 2$, and (3.13) to find that

$$
\big|b\big(\psi_h^{n+\frac{1}{2}}, \overline{\omega^{n+\frac{1}{2}}}^h - \omega^{n+\frac{1}{2}}, \overline{e_h^{n+\frac{1}{2}}}^h\big)\big| \leq \|\nabla \psi_h^{n+\frac{1}{2}}\|_\infty \|\overline{\omega^{n+\frac{1}{2}}}^h - \omega^{n+\frac{1}{2}}\| \|\nabla e_h^{n+\frac{1}{2}}\|. \qquad (3.44)
$$

From $\big\|\nabla E\big\|_\infty = \|\nabla(\psi_h^{n+\frac{1}{2}} - \psi^{n+\frac{1}{2}})\|_\infty$, Agmon's inequality and the regularity estimate $\|\psi\|_{m+2} \leq C\|\omega\|_m$ for ψ satisfying a Poisson equation with forcing ω we have

$$
\begin{aligned}
\|\nabla \psi_h^{n+\frac{1}{2}}\|_\infty &\leq \|\nabla E^{n+\frac{1}{2}}\|_\infty + \|\nabla \psi^{n+\frac{1}{2}}\|_\infty \leq \|\nabla E^{n+\frac{1}{2}}\|_\infty + C\|\psi^{n+\frac{1}{2}}\|_3 \\
&\leq \|\nabla E^{n+\frac{1}{2}}\|_\infty + C\|\omega^{n+\frac{1}{2}}\|_1.
\end{aligned}
$$

We next have to estimate the term $\|\nabla E^{n+\frac{1}{2}}\|_\infty$. Let I^h be a global Lagrangian interpolator, we have $\|\nabla E^{n+\frac{1}{2}}\|_\infty \leq \|\nabla(\psi^{n+\frac{1}{2}} - I^h\psi^{n+\frac{1}{2}})\|_\infty + \|\nabla(I^h\psi^{n+\frac{1}{2}} - \psi_h^{n+\frac{1}{2}})\|_\infty$. Using an standard estimate for $\|\nabla(\psi^{n+\frac{1}{2}} - I^h\psi^{n+\frac{1}{2}})\|_\infty$ (Theorem 4.4.20 in [11]) and an inverse inequality for $\|\nabla(I^h\psi^{n+\frac{1}{2}} - \psi_h^{n+\frac{1}{2}})\|_\infty$ (estimate (4.4.22) of Theorem 4.5.11 in [11] with $p = 2$, $n = 2$, $s = 1$ and $m = k+1$) we get that

$$
\begin{aligned}
\|\nabla E^{n+\frac{1}{2}}\|_\infty &\leq Ch^{-1}\|\nabla(I^h\psi^{n+\frac{1}{2}} - \psi_h^{n+\frac{1}{2}})\| + Ch^{k-1}\|\psi^{n+\frac{1}{2}}\|_{k+1} \\
&\leq Ch^{-1}\|\nabla\big(I^h\psi^{n+\frac{1}{2}} - \psi^{n+\frac{1}{2}} - E^{n+\frac{1}{2}}\big)\| + Ch^{k-1}\|\psi^{n+\frac{1}{2}}\|_{k+1} \\
&\leq Ch^{-1}\|\nabla E_h^{n+\frac{1}{2}}\| + Ch^{k-1}\|\psi^{n+\frac{1}{2}}\|_{k+1}.
\end{aligned}
$$

Thus, for $0 < h \leq 1$ and for $k \geq 1$ we have

$$
\|\nabla \psi_h^{n+\frac{1}{2}}\|_\infty \leq Ch^{-1}\|\nabla E_h^{n+\frac{1}{2}}\| + C\|\omega^{n+\frac{1}{2}}\|_1 + C\|\psi^{n+\frac{1}{2}}\|_{k+1}. \qquad (3.45)
$$

Using (3.45) and Lemma 3.4 in (3.44) and for $\alpha = O(h)$, $0 < h \leq 1$ and $k \geq 1$

$$
\begin{aligned}
&\big|b\big(\psi_h^{n+\frac{1}{2}}, \overline{\omega^{n+\frac{1}{2}}}^h - \omega^{n+\frac{1}{2}}, \overline{e_h^{n+\frac{1}{2}}}^h\big)\big| \leq \\
&\big(Ch^{-1}\|\nabla E_h^{n+\frac{1}{2}}\| + C\|\omega^{n+\frac{1}{2}}\|_1 + C\|\psi^{n+\frac{1}{2}}\|_{k+1}\big)\big\|\overline{\omega^{n+\frac{1}{2}}}^h - \omega^{n+\frac{1}{2}}\big\|\|\nabla e_h^{n+\frac{1}{2}}\| \\
&\leq C\|\overline{\omega}^{n+\frac{1}{2}}\|_{k+1}\big\|\nabla E_h^{n+\frac{1}{2}}\big\|\|\nabla e_h^{n+\frac{1}{2}}\| + \big(C\|\omega^{n+\frac{1}{2}}\|_1 + C\|\psi^{n+\frac{1}{2}}\|_{k+1}\big)\big\|\overline{\omega^{n+\frac{1}{2}}}^h - \omega^{n+\frac{1}{2}}\big\|\|\nabla e_h^{n+\frac{1}{2}}\|.
\end{aligned}
$$

We continue bounding the second nonlinear term using Young inequality with $\epsilon = \frac{C_\epsilon^{-1}}{10Ro}\big(\frac{\delta_M}{L}\big)^3$, inequality (3.39) and Lemma 3.4 we have

$$
\begin{aligned}
&\big|Rob\big(\psi_h^{n+\frac{1}{2}}, \overline{\omega^{n+\frac{1}{2}}}^h - \omega^{n+\frac{1}{2}}, \overline{e_h^{n+\frac{1}{2}}}^h\big)\big| \\
&\leq Ro^2\big(\tfrac{L}{\delta_M}\big)^3\big(C\|\overline{\omega}^{n+\frac{1}{2}}\|_{k+1}^2\|e_h^{n+\frac{1}{2}}\|^2 + Ch^{2k+2}\|\omega^{n+\frac{1}{2}}\|_{k+1}^2\|\overline{\omega}^{n+\frac{1}{2}}\|_{k+1}^2 + C\|\overline{\omega}^{n+\frac{1}{2}}\|_{k+1}^2\|\overline{\omega^{n+\frac{1}{2}}}^h - \omega^{n+\frac{1}{2}}\|^2\big) \\
&+ CRo^2\big(\tfrac{L}{\delta_M}\big)^3\big(C\|\omega^{n+\frac{1}{2}}\|_1 + C\|\psi^{n+\frac{1}{2}}\|_{k+1}\big)^2\|\overline{\omega^{n+\frac{1}{2}}}^h - \omega^{n+\frac{1}{2}}\|^2 + \tfrac{C_\epsilon^{-1}}{20}\big(\tfrac{\delta_M}{L}\big)^3\|\nabla e_h^{n+\frac{1}{2}}\|^2 \\
&\leq \big(\tfrac{L}{\delta_M}\big)^3 Ro^2\big(C\|\overline{\omega}^{n+\frac{1}{2}}\|_{k+1}^2\|e_h^{n+\frac{1}{2}}\|^2 + Ch^{2k+2}\|\omega^{n+\frac{1}{2}}\|_{k+1}^2\|\overline{\omega}^{n+\frac{1}{2}}\|_{k+1}^2 + C\big(\alpha^4 + \alpha^2h^{2k} + h^{2k+2}\big)\|\overline{\omega}^{n+\frac{1}{2}}\|_{k+1}^4\big) \\
&+ C\big(\tfrac{L}{\delta_M}\big)^3 Ro^2\big(\alpha^4 + \alpha^2h^{2k} + h^{2k+2}\big)\|\overline{\omega}^{n+\frac{1}{2}}\|_{k+1}^2\big(C\|\omega^{n+\frac{1}{2}}\|_1^2 + C\|\psi^{n+\frac{1}{2}}\|_{k+1}^2\big) + \tfrac{C_\epsilon^{-1}}{20}\big(\tfrac{\delta_M}{L}\big)^3\|\nabla e_h^{n+\frac{1}{2}}\|^2 \\
&\leq CRo^2\big(\tfrac{L}{\delta_M}\big)^3\|\overline{\omega}^{n+\frac{1}{2}}\|_{k+1}^2\|e_h^{n+\frac{1}{2}}\|^2 + Ro^2\big(\tfrac{L}{\delta_M}\big)^3 Ch^{2k+2}\big(\|\omega^{n+\frac{1}{2}}\|_{k+1}^4 + \|\overline{\omega}^{n+\frac{1}{2}}\|_{k+1}^4\big) \\
&+ C\big(\tfrac{L}{\delta_M}\big)^3 Ro^2\big(\alpha^4 + \alpha^2h^{2k} + h^{2k+2}\big)\big(\|\overline{\omega}^{n+\frac{1}{2}}\|_{k+1}^4 + C\|\omega^{n+\frac{1}{2}}\|_1^4 + C\|\psi^{n+\frac{1}{2}}\|_{k+1}^4\big) + \tfrac{C_\epsilon^{-1}}{20}\big(\tfrac{\delta_M}{L}\big)^3\|\nabla e_h^{n+\frac{1}{2}}\|^2.
\end{aligned}
\tag{3.46}
$$

Using Holder's inequality with $p = q = 2$ and $r = \infty$, (3.45), Lemma 3.4 and Young inequality with $\epsilon = \frac{C_\epsilon^{-1}}{10Ro}\big(\frac{\delta_M}{L}\big)^3$, we get for the first nonlinear term,

$$
\begin{aligned}
&\big|b\big(\psi_h^{n+\frac{1}{2}}, \overline{e_\perp^{n+\frac{1}{2}}}^h, \overline{e_h^{n+\frac{1}{2}}}^h\big)\big| \\
&\leq \big(Ch^{-1}\|\nabla E_h^{n+\frac{1}{2}}\| + C\|\omega^{n+\frac{1}{2}}\|_1 + C\|\psi^{n+\frac{1}{2}}\|_{k+1}\big)h^{k+1}\|\omega^{n+\frac{1}{2}}\|_{k+1}\|\nabla e_h^{n+\frac{1}{2}}\| \\
&\leq \tfrac{C_\epsilon^{-1}}{20Ro}\big(\tfrac{\delta_M}{L}\big)^3\|\nabla e_h^{n+\frac{1}{2}}\|^2 + CRo\big(\tfrac{L}{\delta_M}\big)^3h^{2k+2}\big(\|\omega^{n+\frac{1}{2}}\|_{k+1}^4 + \|\omega^{n+\frac{1}{2}}\|_1^4 + \|\psi^{n+\frac{1}{2}}\|_{k+1}^4\big) \\
&\quad + CRo\big(\tfrac{L}{\delta_M}\big)^3h^{2k}\|\omega^{n+\frac{1}{2}}\|_{k+1}^2\|\nabla E_h^{n+\frac{1}{2}}\|^2 \\
&\leq \tfrac{C_\epsilon^{-1}}{20Ro}\big(\tfrac{\delta_M}{L}\big)^3\|\nabla e_h^{n+\frac{1}{2}}\|^2 + CRo\big(\tfrac{L}{\delta_M}\big)^3h^{2k+2}\big(\|\omega^{n+\frac{1}{2}}\|_1^4 + \|\psi^{n+\frac{1}{2}}\|_{k+1}^4\big) \\
&\quad + CRo\big(\tfrac{L}{\delta_M}\big)^3h^{2k}\|\omega^{n+\frac{1}{2}}\|_{k+1}^2\|e_h^{n+\frac{1}{2}}\|^2 + Ro\big(\tfrac{L}{\delta_M}\big)^3\big(Ch^{2k+2} + Ch^{4k}\big)\|\omega^{n+\frac{1}{2}}\|_{k+1}^4 \\
&\quad + Ro\big(\tfrac{L}{\delta_M}\big)^3\big(Ch^{2k}\alpha^4 + C\alpha^2h^{2k+2} + Ch^{2k+4}\big)^2\|\overline{\omega^{n+\frac{1}{2}}}\|_{k+1}^4.
\end{aligned}
\tag{3.47}
$$

It remains to bound the term $Intp$ in (3.35). Standard analysis for the interpolation error (see, e.g., [65] and [76]) provides the bounds

$$\begin{aligned}
&\Delta t \sum_{n=0}^{M-1} |Intp(\omega^n, \psi^n; \overline{e_h^{n+\frac{1}{2}}}^h)| \leq CRo^2\big(\tfrac{L}{\delta_M}\big)^3 \Delta t^4 |||\omega_{ttt}|||_{2,0}^2 + C\big(\tfrac{\delta_M}{L}\big)^3 \Delta t^4 |||\nabla \omega_{tt}|||_{2,0}^2 \\
&+ C\big(\tfrac{L}{\delta_M}\big)^3 \Delta t^4 |||\psi_{tt}|||_{2,0}^2 + CRo^2 \Delta t^4 \big(\tfrac{L}{\delta_M}\big)^3 |||\nabla \psi^{1/2}|||_{4,1}^4 + CRo^2\big(\tfrac{L}{\delta_M}\big)^3 \Delta t^4 |||\omega_{tt}|||_{4,0}^4 \\
&+ CRo^2\big(\tfrac{L}{\delta_M}\big)^3 \Delta t^4 |||\nabla \omega(t^{1/2})|||_{4,1}^4 + CRo^2\big(\tfrac{L}{\delta_M}\big)^3 \Delta t^4 |||\psi_{tt}|||_{4,0}^4 + \tfrac{C_\epsilon^{-1}}{4}\big(\tfrac{\delta_M}{L}\big)^3 |||\nabla e_h^{n+\frac{1}{2}}|||^2. \qquad (3.48)
\end{aligned}$$

Using norm equivalence, (3.41), (3.42), (3.43), (3.46), (3.47) and (3.48) in (3.37) we obtain

$$\begin{aligned}
&C_E^{-1} Ro \|e_h^M\|^2 + C_\epsilon^{-1} \Delta t \big(\tfrac{\delta_M}{L}\big)^3 \sum_{n=0}^{M-1} \|\nabla e_h^{n+\frac{1}{2}}\|^2 \\
&\leq \Delta t \sum_{n=0}^{M-1} \big(\tfrac{L}{\delta_M}\big)^3 \big(C + CRo^2 h^{2k} |||\omega^{n+\frac{1}{2}}|||_{k+1}^2 + CRo^2 |||\overline{\omega}^{n+\frac{1}{2}}|||_{k+1}^2 + CRo^2 |||\nabla \omega^{n+\frac{1}{2}}|||_1^2\big) |||e_h^{n+\frac{1}{2}}|||^2 \\
&+ \big(\tfrac{L}{\delta_M}\big)^3 \big[Ch^{2k} |||\psi^{1/2}|||_{2,k+1}^2 + Ch^{2k+2} |||\omega^{1/2}|||_{2,k+1}^2 + \big(C\alpha^4 + C\alpha^2 h^{2k} + Ch^{2k+2}\big) |||\overline{\omega}^{1/2}|||_{2,k+1}^2\big] \\
&+ C\big(\tfrac{\delta_M}{L}\big)^3 h^{2k} |||\omega^{1/2}|||_{2,k+1}^2 + CRo^2\big(\tfrac{L}{\delta_M}\big)^3 h^{2k} \big(|||\nabla \omega^{1/2}|||_{4,1}^4 + |||\psi^{1/2}|||_{k+1}^4\big) \\
&+ CRo^2\big(\tfrac{L}{\delta_M}\big)^3 Ch^{2k+2} |||\omega^{1/2}|||_{4,k+1}^4 + Ro^2\big(\tfrac{L}{\delta_M}\big)^3 \big(C\alpha^4 + C\alpha^2 h^{2k} + h^{2k+2}\big)\big(|||\nabla \omega^{1/2}|||_{4,1}^4 + |||\overline{\omega}^{1/2}|||_{4,k+1}^4\big) \\
&+ CRo^2\big(\tfrac{L}{\delta_M}\big)^3 h^{2k+2} |||\omega^{1/2}|||_{4,k+1}^4 + Ro^2\big(\tfrac{L}{\delta_M}\big)^3 h^{2k+2} |||\overline{\omega}^{1/2}|||_{4,k+1}^4 \\
&+ C\big(\tfrac{L}{\delta_M}\big)^3 Ro^2 \big(\alpha^4 + \alpha^2 h^{2k} + h^{2k+2}\big)\big(C|||\overline{\omega}^{1/2}|||_{4,k+1}^4 + C|||\omega^{1/2}|||_{4,1}^4 + C|||\psi^{1/2}|||_{4,k+1}^4\big) \\
&+ CRo^2\big(\tfrac{L}{\delta_M}\big)^3 h^{2k+2} \big(|||\omega^{1/2}|||_{4,1}^4 + |||\psi^{1/2}|||_{4,k+1}^4\big) + Ro^2\big(\tfrac{L}{\delta_M}\big)^3 \big(Ch^{2k+2} + Ch^{4k}\big) |||\omega^{1/2}|||_{4,k+1}^4 \\
&+ Ro^2\big(\tfrac{L}{\delta_M}\big)^3 \big(Ch^{2k}\alpha^4 + C\alpha^2 h^{2k+2} + Ch^{2k+4}\big)^2 |||\overline{\omega^{1/2}}|||_{4,k+1}^4 + CRo^2\big(\tfrac{L}{\delta_M}\big)^3 \Delta t^4 |||\omega_{ttt}|||_{2,0}^2 \\
&+ C\big(\tfrac{\delta_M}{L}\big)^3 \Delta t^4 |||\nabla \omega_{tt}|||_{2,0}^2 + CRo^2 \Delta t^4 \big(\tfrac{L}{\delta_M}\big)^3 |||\nabla \psi^{1/2}|||_{4,1}^4 + CRo^2\big(\tfrac{L}{\delta_M}\big)^3 \Delta t^4 |||\omega_{tt}|||_{4,0}^4 \\
&+ C\big(\tfrac{L}{\delta_M}\big)^3 \Delta t^4 |||\psi_{tt}|||_{2,0}^2 + CRo^2\big(\tfrac{L}{\delta_M}\big)^3 \Delta t^4 |||\nabla \omega(t^{1/2})|||_{4,1}^4 + CRo^2\big(\tfrac{L}{\delta_M}\big)^3 \Delta t^4 |||\psi_{tt}|||_{4,0}^4.
\end{aligned}$$

Next, assuming $\Delta t \leq \frac{\left(\delta_M/L\right)^3}{C+CRo^2h^{2k}\|\omega^{n+\frac{1}{2}}\|_{k+1}^2+CRo^2\|\overline{\omega}^{n+\frac{1}{2}}\|_{k+1}^2+CRo^2\|\nabla\omega^{n+\frac{1}{2}}\|_1^2}$, we can apply the discrete Gronwall inequality from [44] to get

$$
\begin{aligned}
&C_E^{-1}Ro\|e_h^M\|^2 + C_\epsilon^{-1}\Delta t\big(\frac{\delta_M}{L}\big)^3\sum_{n=0}^{M-1}\|\nabla e_h^{n+\frac{1}{2}}\|^2 \leq \\
&C^*\big\{\big(\tfrac{L}{\delta_M}\big)^3\big[Ch^{2k}|||\psi^{1/2}|||_{2,k+1}^2 + Ch^{2k+2}|||\omega^{1/2}|||_{2,k+1}^2 + \big(C\alpha^4 + C\alpha^2h^{2k} + Ch^{2k+2}\big)|||\overline{\omega}^{1/2}|||_{2,k+1}^2\big] \\
&+ C\big(\tfrac{\delta_M}{L}\big)^3h^{2k}|||\omega^{1/2}|||_{2,k+1}^2 + CRo^2\big(\tfrac{L}{\delta_M}\big)^3h^{2k}\big(|||\nabla\omega^{1/2}|||_{4,1}^4 + |||\psi^{1/2}|||_{k+1}^4\big) \\
&+ CRo^2\big(\tfrac{L}{\delta_M}\big)^3Ch^{2k+2}|||\omega^{1/2}|||_{4,k+1}^4 + Ro^2\big(\tfrac{L}{\delta_M}\big)^3\big(C\alpha^4 + C\alpha^2h^{2k} + h^{2k+2}\big)\big(|||\nabla\omega^{1/2}|||_{4,1}^4 + |||\overline{\omega}^{1/2}|||_{4,k+1}^4\big) \\
&+ CRo^2\big(\tfrac{L}{\delta_M}\big)^3h^{2k+2}|||\omega^{1/2}|||_{4,k+1}^4 + Ro^2\big(\tfrac{L}{\delta_M}\big)^3h^{2k+2}|||\overline{\omega}^{1/2}|||_{4,k+1}^4 \\
&+ CRo^2\big(\tfrac{L}{\delta_M}\big)^3\big(\alpha^4 + \alpha^2h^{2k} + h^{2k+2}\big)\big(C|||\overline{\omega}^{1/2}|||_{4,k+1}^4 + C|||\omega^{1/2}|||_{4,1}^4 + C|||\psi^{1/2}|||_{4,k+1}^4\big) \\
&+ CRo^2\big(\tfrac{L}{\delta_M}\big)^3h^{2k+2}\big(|||\omega^{1/2}|||_{4,1}^4 + |||\psi^{1/2}|||_{4,k+1}^4\big) + Ro^2\big(\tfrac{L}{\delta_M}\big)^3\big(Ch^{2k+2} + Ch^{4k}\big)|||\omega^{1/2}|||_{4,k+1}^4 \\
&+ Ro^2\big(\tfrac{L}{\delta_M}\big)^3\big(Ch^{2k}\alpha^4 + C\alpha^2h^{2k+2} + Ch^{2k+4}\big)^2|||\overline{\omega^{1/2}}|||_{4,k+1}^4 + C\big(\frac{\delta_M}{L}\big)^3\Delta t^4|||\nabla\omega_{tt}|||_{2,0}^2 \\
&+ C\big(\tfrac{L}{\delta_M}\big)^3\Delta t^4|||\psi_{tt}|||_{2,0}^2 + C\Delta t^4\big(\tfrac{L}{\delta_M}\big)^3|||\nabla\psi^{1/2}|||_{4,1}^4 + C\big(\tfrac{L}{\delta_M}\big)^3\Delta t^4|||\omega_{tt}|||_{4,0}^4 \\
&+ C\big(\tfrac{L}{\delta_M}\big)^3\Delta t^4|||\nabla\omega(t^{1/2})|||_{4,1}^4 + C\big(\tfrac{L}{\delta_M}\big)^3\Delta t^4|||\psi_{tt}|||_{4,0}^4\big\},
\end{aligned}
\tag{3.49}
$$

where

$$
C^* = \exp\Big(\Delta t\sum_{n=0}^{M-1}\frac{\left(\frac{L}{\delta_M}\right)^3\left(C+CRo^2h^{2k}\|\omega^{n+\frac{1}{2}}\|_{k+1}^2+CRo^2\|\overline{\omega}^{n+\frac{1}{2}}\|_{k+1}^2+CRo^2\|\nabla\omega^{n+\frac{1}{2}}\|_1^2\right)}{1-\Delta t\left(\frac{L}{\delta_M}\right)^3\left(C+CRo^2h^{2k}\|\omega^{n+\frac{1}{2}}\|_{k+1}^2+CRo^2\|\overline{\omega}^{n+\frac{1}{2}}\|_{k+1}^2+CRo^2\|\nabla\omega^{n+\frac{1}{2}}\|_1^2\right)}\Big).
\tag{3.50}
$$

The estimate (3.31) now follows from the triangle inequality and (3.49). For estimate (3.32), we use (3.49) and

$$
\begin{aligned}
\|\nabla\big(\omega\big(t^{n+\frac{1}{2}}\big) - \omega_h^{n+\frac{1}{2}}\big)\|^2 &\leq \|\nabla\big(\omega\big(t^{n+\frac{1}{2}}\big) - \omega^{n+\frac{1}{2}}\big)\|^2 + \|\nabla e_\perp^{n+\frac{1}{2}}\|^2 + \|\nabla e_h^{n+\frac{1}{2}}\|^2 \\
&\leq \tfrac{\Delta t^3}{48}\int_{t^n}^{t^{n+1}}\|\omega_{tt}\|^2dt + Ch^{2k}\|\omega^{n+\frac{1}{2}}\|_{k+1}^2 + \|\nabla e_h^{n+\frac{1}{2}}\|^2,
\end{aligned}
$$

which completes the proof. □

3.5 Numerical experiments

In this section, we provide two numerical examples to verify the theoretical results and show that good results can be obtained with the proposed model/scheme. The first numerical test is to confirm the predicted convergence rates, and the second tests the model's ability to find accurate coarse mesh solution to a double gyre wind forcing benchmark test. We use the software FreeFem++[40] to perform the computational tests; Newton's method is used to resolve the nonlinear problems at each timestep, and we use UMFPACK to solve the linear systems. We note that we also tested linearized analogues of the proposed scheme, and found overall worse results, particularly on the double gyre benchmark test.

3.5.1 Convergence rate confirmation

Now we estimate the convergence rates for the BV-Bardina scheme using a known analytical solution. Using $\Omega = (0,1) \times (-1,1)$, $T = 1$, and setting $F = -\pi \exp\big[-\frac{2\pi^2}{Ro}\big(\frac{\delta_M}{L}\big)^3 t\big] \cos \pi x \sin \pi y$, we obtain the following time dependent analytical solution for BV (with homogeneous Dirichlet boundary conditions):

$$\begin{aligned}\psi &= \exp\big[-\tfrac{2\pi^2}{Ro}\big(\tfrac{\delta_M}{L}\big)^3 t\big] \sin \pi x \sin \pi y,\\ \omega &= 2\pi^2 \exp\big[-\tfrac{2\pi^2}{Ro}\big(\tfrac{\delta_M}{L}\big)^3 t\big] \sin \pi x \sin \pi y.\end{aligned}$$

To estimate convergence rates, we considered $h = 1/4$ (which corresponds to a grid with 4×8 squares), $1/8$ (8×16), $1/16$ (16×32), $1/32$ (32×64) and $1/64$ (64×128) where h is the mesh-width. Figure 3.1 presents the coarsest mesh used in this experiment. In the remainder of the text we will refer to our meshes as $n \times 2n$ for $n = 4, 8, 16, 32, 64$. In all cases we chose $\alpha = h$, and the timestep was chosen in terms of h in order to balance the errors sources from the convergence theorem. That is, for P_1 elements and $\alpha = h$, the $L^2(0,T;H^1(\Omega))$ vorticity error and $L^\infty(0,T;H^1(\Omega))$ streamfunction error from the theorem is $O(\Delta t^2 + h)$, and thus we chose $\Delta t = \sqrt{h}$ (but slightly rounded so that Δt evenly divided T), and thus here we expect first order convergence in these norms as $\Delta t,\ h \to 0$. For P_2 elements, we chose $\Delta t = h$, and expect second order convergence of these norms.

Table 3.1 presents the errors and convergence rates obtained for decreasing h and Δt, using $\frac{\delta_M}{L} = 0.02$ and $Ro = 1.0$. From the table we observe the convergence of the numerical solution to the exact solution is optimal and agrees with the convergence theory presented in this chapter, for both choices of elements.

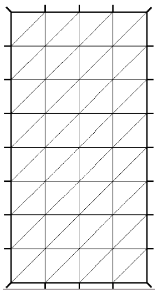

Figure 3.1: Mesh with $h = 1/4$ which corresponds to a grid with 4x8 squares.

Element	h^{-1}	$\|\|w - w_h\|\|_{2,1}$	Rate	$\|\|w - w_h\|\|_{\infty,0}$	Rate	$\|\|\psi - \psi_h\|\|_{\infty,1}$	Rate
P_1	4	186.05		14.604		2.876	
$(\Delta t = \sqrt{h})$	8	53.756	1.79	3.8843	1.91	1.388	1.05
	16	18.219	1.56	0.9873	1.98	0.6898	1.01
	32	7.592	1.26	0.2479	1.99	0.3447	1.00
	64	3.528	1.11	0.06205	2.00	0.17235	1.00
	128	1.717	1.04	0.01552	2.00	0.08617	1.00
P_2	4	76.697		17.162		0.18342	
$(\Delta t = h)$	8	19.176	2.00	4.3026	2.00	0.047225	1.96
	16	4.8116	1.99	1.0761	2.00	0.011906	1.99
	32	1.2159	1.98	0.26905	2.00	0.0029831	2.00
	64	0.3067	1.99	0.067264	2.00	0.0007462	2.00

Table 3.1: Convergence rates for BV-Bardina model with $\frac{\delta_M}{L} = 0.02$ and $Ro = 1.0$.

3.5.2 Double gyre wind forcing experiment

We now test the model on the double gyre wind forcing benchmark test. This problem has been used as a model of more realistic ocean dynamics in several studies, and has also been used as a benchmark test to analyze new techniques to deal with turbulence in geophysical flows [81, 47, 100]. When the BV equations are forced by a double gyre wind forcing in a rectangular basin and dissipation is weak, the instantaneous field of vorticity and streamfunction are highly variable. However, the mean fields show a well defined four gyre pattern in which the two central gyres are driven by the wind with its same orientation, and the northern and southern ends of the basin circulate in opposite direction, being driven by the eddy flux of potential vorticity [37, 47]. The dominant balance is between the wind forcing and the divergence of the eddy flux of potential vorticity with dissipation playing only a minor role. The outer gyres are not a linear effect but, rather, are a result of a mean balance between eddy flux of potential vorticity and wind forcing. However this distinctive four gyre pattern is susceptible to destruction by excessive dissipation [47].

The setup of this problem is as follows [100]. The domain is $\Omega = (0, 1) \times (-1, 1)$, the forcing is $F = \sin(\pi y)$, ${}^{\delta_M}/_{L} = 0.02$ and $Ro = 0.0016$ (which corresponds to $Re = 200$). The computations were run until $T = 100$, and time averages were taken from $T = 20$ to $T = 100$. We follow [100] and adopt standard LES methodology: first we run a high resolution simulation with the BV-model (no treatment of turbulence), and then we run several experiments using coarse resolution with the BV and BV-Bardina models and compare them with the high resolution BV model solution as reference. For comparison, we will also run the related BV-α model, and compute solutions to it using a scheme analogous to the BV-Bardina scheme. All computations in this section use P_2 elements.

The high spatial resolution computation with the BV-model was made using a uniform triangular mesh with 16,384 triangles (33,153 degrees of freedom, corresponding to a grid with 64 × 128 squares), and thus the mean length of a triangle edge is about 0.015, which is smaller than the Munk scale (δ_M), and timestep $\Delta t = 0.001$. Solutions for the high resolution experiment are presented respectively in Figures 3.2(a) and 3.3(a), as time averaged streamfunction and potential vorticity, respectively. We observe that the high resolution solution produced by our FE scheme matches that of [100] very well, and we note it does reproduce the four gyre pattern observed by [100] in their DNS experiment.

We next ran the BV (no regularization) on a coarse analogous mesh with 1,024 triangles and 2,145 degrees of freedom, corresponding to a grid with 16×32 squares (we use this same coarse mesh for all coarse mesh experiments), and $\Delta t = 0.001$. In figures 3.2(b) and 3.3(b) we present respectively the streamfunction and vorticity average solutions obtained in the coarse mesh. This figures clearly show that solutions are negatively affected by decreasing the mesh resolution. More specifically, in figure 3.2(b) the four gyre pattern is dramatically intensified when compared with the high resolution solution, and in the vorticity field, figure 3.3(b), we observe that solution has significant oscillations.

Next we present the results of running the BV model on the coarse mesh using artificial viscosity, that is, we increase $\left(\frac{\delta_M}{L}\right)^3$ from 0.02 to 0.04, still using $\Delta t = 0.001$. Results are shown in figure 3.2(c) and 3.3(c), and it is clear that the solution is dramatically different from the high resolution $\left(\frac{\delta_M}{L}\right)^3$=0.02 solution. This is similar to what was reported in [37, 47], since the four gyre pattern (figure 3.2(c)) degenerates in two gyres due to the excess of dissipation. We also observe that the vorticity field (figures 3.3(c)) also degenerates with respect to the high resolution solution.

Finally, we present our coarse mesh results obtained with the BV-Bardina model ($\alpha = \frac{1}{64}$) in figures 3.2(d) and 3.3(d), and for BV-α in 3.2(e) and 3.3(e). Both of these models successfully predict the four-gyre pattern, however by comparing the intensities of the streamfunction, we observe the BV-Bardina model to be more accurate. The BV-Bardina and BV-α plots of filtered vorticity have similar accuracy.

Run times for the BV model in the fine and coarse mesh (16×32) and for BV-α and BV-Bardina in the coarse mesh (16×32) are presented in Table 3.2.

In this experiment we see again that the BV-Tikhonov solution, as well as recovering the expected four gyre pattern, it is significant faster than solving the BV model in the fine mesh.

Fine	Coarse	Art. Visc.	alpha	Bardina
9.82e5	3.69e4	2.71e4	8.62e4	8.50e4

Table 3.2: Run times (in seconds) obtained for $Ro = 0.0016$ in the fine (64×128) and coarse (16×32) mesh with the BV model and in the coarse mesh (16×32) with BV-α and BV-Bardina models. The experiments were made in a Intel® Core™ i7 3.70 GHz.

Remark 3.3. *We have also tested the leapfrog with the Robert/Asselin filter algorithm which is commonly used in meteorological and oceanic models. The leapfrog-RA scheme [111] is given by:*

Algorithm 3.2 (Leapfrog-RA BV-Bardina). *Given ω_h^0 and ψ_h^0 as the $L^2(\Omega)$ projections into X_h of $\omega_0 \in X$ and $\psi_0 \in X$, endtime T, $F \in L^\infty(0,T;L^2(\Omega))$, and timestep $\Delta t > 0$, set $M = \frac{T}{\Delta t}$ and for n=0,...,M-1, find $(\omega_h^{n+1}, \psi_h^{n+1}, \overline{\omega_h^{n+1}}^h) \in X_h \times X_h \times X_h$ satisfying*

$$
\begin{aligned}
Ro\big\langle \tfrac{\omega_h^{n+1} - F_{RA}\omega_h^{n-1}}{2\Delta t}, v_h\big\rangle + Ro\ b\big(\psi_h^n, \overline{\omega_h^n}^h, v_h\big) - \big\langle \tfrac{\partial \psi_h^n}{\partial x}, v_h\big\rangle &\\
+\big(\tfrac{\delta_M}{L}\big)^3\big\langle \nabla\omega_h^n, \nabla v_h\big\rangle &= \big\langle F^n, v_h\big\rangle\ \forall v_h \in X_h,\\
\big\langle \nabla\psi_h^{n+1}, \nabla\chi\big\rangle - \big\langle \overline{\omega_h^{n+1}}^h, \chi\big\rangle &= 0\ \forall \chi \in X_h,\\
\alpha^2\big\langle \nabla\overline{\omega_h^{n+1}}^h, \nabla\xi\big\rangle + \big\langle \overline{\omega_h^{n+1}}^h, \xi\big\rangle - \big\langle \omega_h^{n+1}, \xi\big\rangle &= 0\ \forall \xi \in X_h.
\end{aligned}
$$

where $F_{RA}\omega^n = \omega^n + \frac{\nu}{2}\big(\omega^{n-1} - 2\omega^n + \omega^{n+1}\big)$ is the Robert/Asselin filter and ν is a dimensionless positive filter parameter. We have used $\nu = 0.1$.

The leapfrog-RA scheme has the advantage of decouple the vorticity equation from the streamfunction and filter equations, but on the other hand it has a timestep restriction due to its conditionally stability. We tested the leapfrog-RA version of the BV-Bardina model and it has only run without blow up for $\Delta t = 0.0001$, *which is* $^{1}/_{10}$ *of the timestep used in the Crank-Nicolson version. However, both schemes took the same computational time to attain similar solutions. Thus we believe that Crank-Nicolson version of BV-Bardina can be more useful than the leapfrog-RA version because it is unconditionally stable. In real geophysical applications, the use of unconditionally stable schemes can avoid the use of artificial viscosity to stabilize the model which would reduce the convergence order of the numerical scheme. This is specially recommended in the case of a non-dissipative regularization, as the Bardina regularization.*

Thus, for this experiment, we conclude that both BV-Bardina and BV-α, correctly predict the four gyre pattern on the coarse mesh where BV is inaccurate, with BV-Bardina being somewhat more accurate that BV-α. The artificial viscosity model was unable to predict the four gyre pattern.

3.6 Conclusions

In this work we proposed a Crank-Nicolson/FEM discretization for a Bardina regularization of the BV model for geophysical flows. We proved that the scheme is unconditionally stable and optimally convergent. Numerical simulations were provided that verified the predicted convergence rates, and showed the effectiveness of the model/scheme at finding good coarse mesh solutions for the double gyre wind forcing benchmark test. Moreover, on the double gyre test, results were found to be better than the related BV-α model. In the same way as was made for the approximate deconvolution-BV model ([100] and [99]), we intend in a future work to extent the BV-Bardina model for two layers in order to consider the first baroclinic mode, which will allow us to evaluate this regularization in a situation more similar with the true threedimensional ocean dynamic.

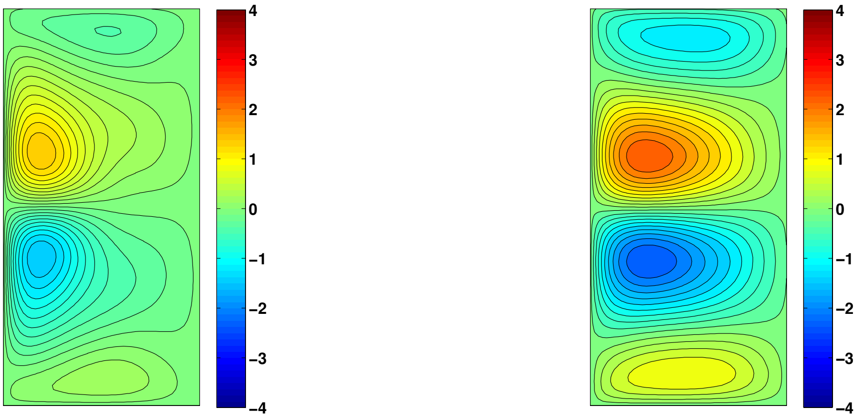

(a) BV (high res.), ψ_{min}= -1.39, ψ_{max}=1.39

(b) BV (Coarse), ψ_{min}=-2.281, ψ_{max}=2.361

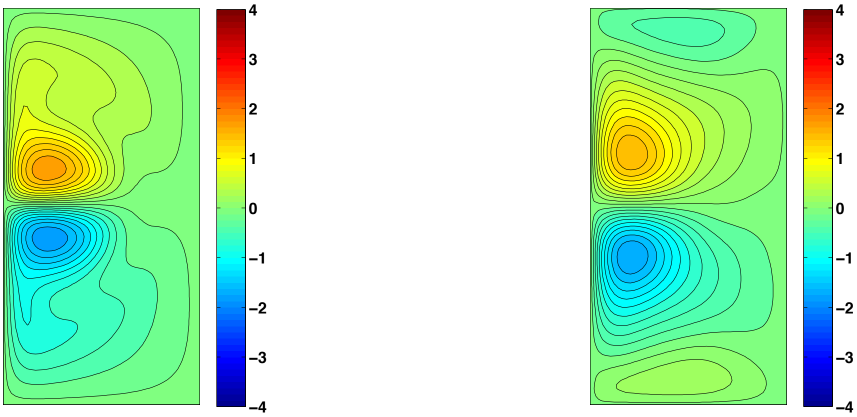

(c) BV + Art. Visc. (Coarse), ψ_{min}=-1.794, ψ_{max}=1.828

(d) BV-Bardina (Coarse), ψ_{min}=-1.616, ψ_{max}=1.670

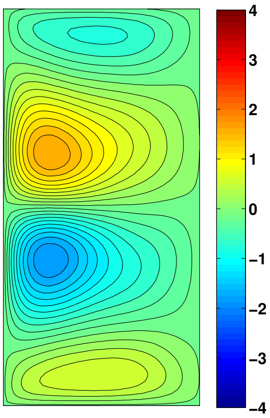

(e) BV-α (Coarse), ψ_{min}=-1.829, ψ_{max}=1.745

Figure 3.2: Mean fields of streamfunction with Ro = 0.0016 for the high resolution solution of the BV model (a), for the coarse (16x32) BV model solution (b), for the coarse BV model + artificial viscosity (c), from the 8x16 BV-Bardina model (d) and BV-α model (e).

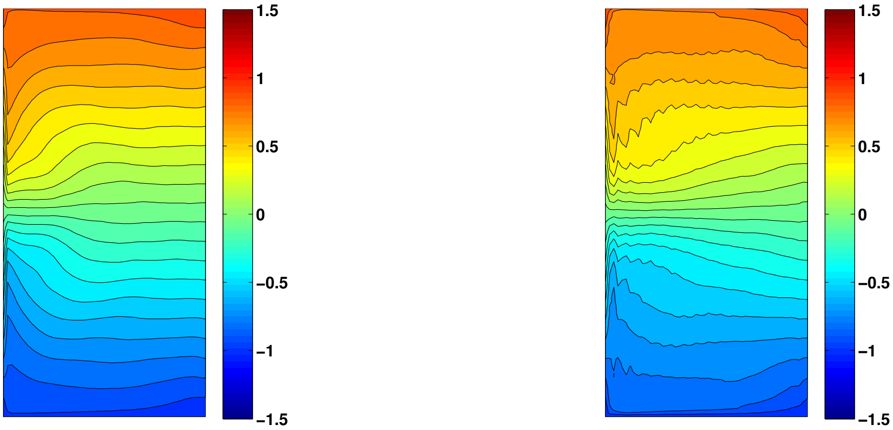

(a) Vort. - BV mod. - high res. (b) Vort. - BV mod. - Coarse

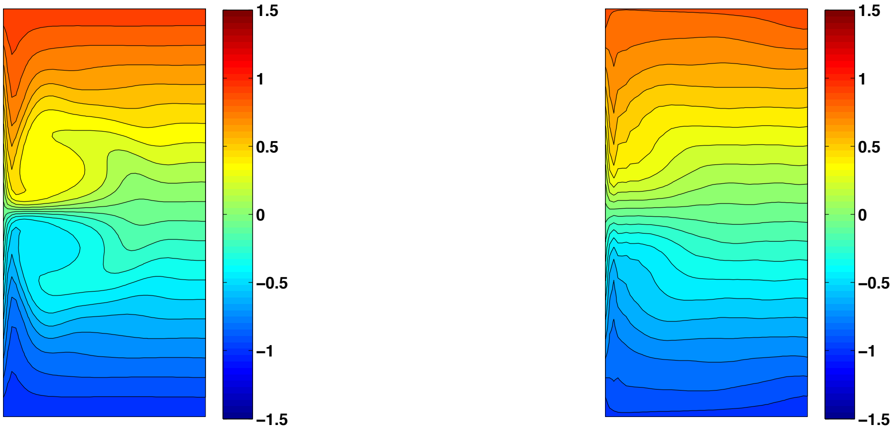

(c) Vort. - BV mod. - Coarse + Art. Visc. (d) Vort. - BV-Bardina mod. - Coarse

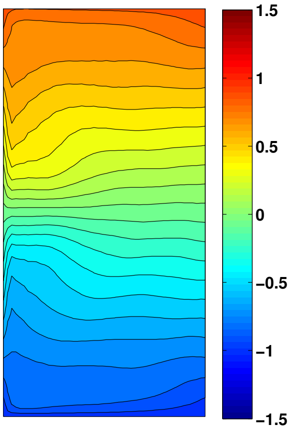

(e) Vort. - BV-α mod. - Coarse

Figure 3.3: Mean fields of vorticity with $Ro = 0.0016$ for the high resolution BV model, and coarse mesh solutions for BV model and various models.

4 BAROTROPIC VORTICITY-α MODEL WITH VAN CITTERT APPROXIMATE DECONVOLUTION[1]

4.1 Introduction

Accurate simulations of geophysical flows are critically important in understanding climate change and ocean and weather forecast. Furthermore, they can assist in prediction of biological and pollutant transport, oil exploration, and many other applications. One of the simplest nonlinear models to simulate a geophysical flow is the Barotropic Vorticity (BV) model, which, in dimensionless, form is given by [47, 100]

$$\begin{aligned} Ro\tfrac{\partial\omega}{\partial t} + RoJ(\psi,\omega) - \tfrac{\partial\psi}{\partial x} - \left(\tfrac{\delta_M}{L}\right)^3\Delta\omega &= \mathcal{F}, && (4.1a)\\ \Delta\psi &= -\omega, && (4.1b)\end{aligned}$$

where ω is the vorticity, ψ is the streamfunction, $J(\psi,\omega) = \frac{\partial\psi}{\partial x}\frac{\partial\omega}{\partial y} - \frac{\partial\psi}{\partial y}\frac{\partial\omega}{\partial x}$ is the Jacobian, Ro is the Rossby number, δ_M is the Munk scale, L is the length scale and $\mathcal{F}$ is the forcing term. The BV model is widely used to study the midlatitude, wind-driven ocean circulation, and it recently has been used in studies involving data assimilation [113, 21, 58], climate [95, 73, 36] and oceanic and atmosphere processes [12, 108, 96].

Despite its simplicity, the BV model is very sensitive to the mesh resolution [37, 81, 47, 100], making full representation of the solution computationally expensive. This becomes critical when long time integration is necessary, as in climate modeling. Traditionally, simulations are done on coarse meshes and (essen-

---

[1] The content of this chapter is coauthored by Professor Carolina C. Manica and was published in Volume 5, Number 4, Pages 317-338 (2014) of the International Journal of Numerical Analysis and Modelling, Series B, with the title *Improving numerical accuracy in a regularized Barotropic Vorticity model of geophysical flow.*

tially) dissipative techniques such as eddy viscosity parametrizations have been used to model the under-resolved scales of the flow. However, according to [47], increasing artificial viscosity tends to reduce variability, and nonlinear structures can be destroyed by excess of dissipation [37, 47]. Thus some methods such as Approximate Deconvolution Modeling [100, 99], Barotropic Vorticity-α (BV-α) [82, 81, 47] and Barotropic Vorticity-Bardina [59] have been developed with success to improve accuracy and reduce the degrees of freedom in computational simulations. The BV-α model is a regularization of the BV model proposed in [47] that allows a significant reduction of degrees of freedom in simulations. In BV-α, the nonlinearity is altered so that the flow at length scales that are smaller than the alpha length scale are nonlinearly removed by motions at the larger scales. Thus there is seemingly no need to introduce additional dissipative terms or increase the viscosity coefficient, which is often done in the BV equations. The BV-α model is given by

$$\begin{aligned} Ro\tfrac{\partial \omega}{\partial t} + RoJ(\psi,\omega) - \tfrac{\partial \psi}{\partial x} - \left(\tfrac{\delta_M}{L}\right)^3 \Delta\omega &= \mathcal{F}, && (4.2a) \\ \Delta\psi &= -\overline{\omega}, && (4.2b) \\ -\alpha^2\Delta\overline{\omega} + \overline{\omega} &= \omega, && (4.2c) \end{aligned}$$

where $\overline{\omega}$ is the filtered vorticity and α is the filter length scale. A more complete description of BV-α is presented in [47].

Despite being physically accurate, the BV-α model naturally has a consistency error from the BV model. It is clear from (4.2) that one cannot expect accuracy better than $O(\alpha^2)$. Since frequently $\alpha = O(h)$, the BV-α model is often only second order accurate. Following [76], we attempt to fix the consistency error in the BV-α model by increasing its accuracy through the van Cittert method of approximate deconvolution [107, 1, 106]. The method constructs a family D_N of approximate inverses to the filter F as the truncation of the nonconvergent formal power series $F^{-1} = \sum_{n=0}^{\infty}(I - F)^n$:

$$D_N = \sum_{n=0}^{N}(I - F)^n.$$

In [93], it is shown how to apply the deconvolution operator in the Navier-Stokes-α to achieve accuracy $O(\alpha^{2N+2})$, where N is the order of deconvolution. Thus we adopt the above mentioned approach and introduce the BV-α model with deconvolution (BV-α-Deconvolution) by

$$\begin{aligned}
Ro\tfrac{\partial\omega}{\partial t} + RoJ(\psi,\omega) - \tfrac{\partial\psi}{\partial x} - \left(\tfrac{\delta_M}{L}\right)^3\Delta\omega &= \mathcal{F},\\
\Delta\psi &= -D_N\overline{\omega},\\
-\alpha^2\Delta\overline{\omega} + \overline{\omega} &= \omega.
\end{aligned}$$

The BV-α-Deconvolution model, as we will show in the next sections, will allow a reduction in the degrees of freedom in simulations but with a consistency error $O(\alpha^{2N+2})$ when compared to the BV model.

The paper is organized as follows: Section 4.2 introduces a finite element scheme for BV-α-Deconvolution and some necessary notation and mathematical preliminaries. Section 4.3 presents the stability analysis of the proposed scheme. Section 4.4 presents the convergence analysis. Convergence rates are estimated and the double gyre experiment is performed in Section 4.5. Finally, some conclusions and remarks are summarized in Section 4.6.

4.2 The finite element scheme and preliminaries

Let $\Omega \subset \mathbb{R}^2$ be a polygonal domain and τ_h be a regular discretization of Ω. Let $H^1 = H^1(\Omega)$ be the Sobolev space $W_2^1(\Omega)$ and $X := H_0^1(\Omega)$ its subspace with zero boundary condition. Let Y_h be the continuous finite element (FE) space with kth degree polynomials on each element of the triangulation τ_h, and X_h be the subspace of Y_h with zero boundary values. Denote by $\langle\cdot,\cdot\rangle$ and $\|\cdot\|$ the inner product and norm in $L^2(\Omega)$, and $\|\cdot\|_k$ the norm in the space H^k.

For continuous in time functions we denote for $1 \leq m < \infty$,

$$\|f\|_{\infty,k} := \operatorname*{ess\,sup}_{t\in(0,T)} \|f(t,\cdot)\|_k \text{ and } \|f\|_{m,k} := \Big\{ \int_0^T \|f(t,\cdot)\|_k^m dt\Big\}^{\frac{1}{m}}.$$

For the discrete case we denote

$$|||f|||_{\infty,k} := \operatorname*{ess\,sup}_{0\leq n\leq M} \|f^n\|_k,\ \ |||f^{1/2}|||_{\infty,k} := \operatorname*{ess\,sup}_{0\leq n\leq M} \|f(t^{n+\frac{1}{2}})\|_k,$$

$$|||f|||_{m,k} := \Big\{ \sum_{n=0}^{M} \|f^n\|_k^m dt\Big\}^{\frac{1}{m}},\ \ |||f^{1/2}|||_{m,k} := \Big\{ \sum_{n=0}^{M} \|f(t^{n+\frac{1}{2}})\|_k^m dt\Big\}^{\frac{1}{m}}.$$

As in [100], in this work we will consider slip boundary conditions for the velocity, which translate into the homogeneous Dirichlet condition $\omega|_{\partial\Omega} = 0$ and the impermeability condition $\psi|_{\partial\Omega} = 0$. Multiplying (4.1) by test functions and integrating by parts we have the following variational formulation to the BV model: find $(\omega,\psi) \in X \times X$ such that

$$\big\langle \tfrac{\partial\omega}{\partial t}, \lambda\big\rangle + b\big(\psi,\omega,\lambda\big) - \big\langle \tfrac{\partial\psi}{\partial x}, \lambda\big\rangle + \big(\tfrac{\delta_M}{L}\big)^3 \big\langle \nabla\omega, \nabla\lambda\big\rangle = \big\langle \mathcal{F}, \lambda\big\rangle \ \forall\lambda \in H_0^1, \tag{4.4a}$$

$$\big\langle \nabla\psi, \nabla\chi\big\rangle = \big\langle \omega, \chi\big\rangle \ \forall\chi \in H_0^1, \tag{4.4b}$$

where $b\big(\cdot,\cdot,\cdot\big) := \big\langle J\big(\cdot,\cdot\big),\cdot\big\rangle$ represents the trilinear form.

Analogously, the variational formulation for BV-α-Deconvolution is given by: find $(\omega,\psi,\overline{\omega}) \in X \times X \times X$ such that

$$\begin{aligned}\big\langle \tfrac{\partial\omega}{\partial t}, \lambda\big\rangle + b\big(\psi,\omega,\lambda\big) - \big\langle \tfrac{\partial\psi}{\partial x}, \lambda\big\rangle + \big(\tfrac{\delta_M}{L}\big)^3 \big\langle \nabla\omega, \nabla\lambda\big\rangle &= \big\langle \mathcal{F}, \lambda\big\rangle \ \forall\lambda \in H_0^1 \\ \big\langle \nabla\psi, \nabla\chi\big\rangle &= \big\langle D_N\overline{\omega}, \chi\big\rangle \ \forall\chi \in H_0^1 \\ \alpha^2\big\langle \nabla\overline{\omega}, \nabla\xi\big\rangle + \big\langle \overline{\omega}, \xi\big\rangle &= \big\langle \omega, \xi\big\rangle \ \forall\xi \in H_0^1\end{aligned}$$

where, as in [47], we considered the additional homogeneous Dirichlet condition $\overline{\omega}|_{\partial\Omega} = 0$ in the filter equation.

Now we define two projection operators which are useful in the subsequent analysis. Given $\xi \in X$, let $P\xi \in X^h$ be the standard L^2 orthogonal projection of ξ onto X^h such that

$$\big\langle \xi - P\xi, \phi \big\rangle = 0 \ \forall \phi \in X^h,$$

and let $\Pi\xi \in X^h$ be the elliptic orthogonal projection of ξ onto X^h such that

$$\big\langle \nabla(\xi - \Pi\xi), \nabla\phi \big\rangle = 0 \ \forall \phi \in X^h.$$

Lemma 4.1. *Given $\xi \in H^k$ we have the following estimates [109]*

$$\begin{aligned} &i)\ \|\xi - P\xi\| \le Ch^{k+1}\|\xi\|_{k+1},\\ &ii)\ \|\nabla(\xi - P\xi)\| \le Ch^{k}\|\xi\|_{k+1},\\ &iii)\ \|\nabla(\xi - \Pi\xi)\| \le Ch^{k}\|\xi\|_{k+1}. \end{aligned}$$

Lemma 4.2 (Skew-symmetry of the trilinear form)**.** *For ψ, $\xi \in X_h$ and $\chi \in Y_h$,*

$$b\big(\psi, \chi, \xi\big) = -b\big(\psi, \xi, \chi\big), \quad \forall \xi \in X_h. \tag{4.7}$$

Proof. We start from the vector identity

$$\big[(\nabla\psi \times \mathbf{k}) \cdot \nabla\chi\big]\xi = \nabla \cdot \big(\nabla\psi \times \mathbf{k}\big)\chi\xi - \big[(\nabla\psi \times \mathbf{k}) \cdot \nabla\xi\big]\chi - \nabla \cdot \big[\big(\nabla\psi \times \mathbf{k}\big)\chi\xi\big].$$

Integrating and using the divergence theorem, the result follows because of the cyclic continuity inside an element and since $\xi \in X_h$. □

We have the following estimate for the nonlinear term.

Lemma 4.3. *Let $\zeta, \phi \in X$ and $\xi \in H^2 \cap X$. Then*

$$|b\big(\xi, \phi, \zeta\big)| \le C(\Omega)\|\nabla\xi\|_1\|\nabla\phi\|\|\zeta\|_1.$$

Proof. We use Holder's inequality with $p, q = 4$ and $r = 2$. The result follows from the embedding $H^1 \hookrightarrow L^4$. □

4.2.1 Discrete filtering

Definition 4.1. *We define the discrete Laplacian operator* $\Delta_h : H_0^1 \to X^h$ *in the usual way by*

$$\langle \Delta_h \psi, \chi \rangle = -\langle \nabla \psi, \nabla \chi \rangle, \ \forall \chi \in X^h.$$

Now we introduce the discrete filtering and the discrete deconvolution operators.

Definition 4.2 (Discrete filtering operator)**.** *Given* $\phi \in L^2(\Omega)$*, and* $\alpha > 0$*, the filtered* $\overline{\phi}^h =: F_h \phi$ *is the unique solution in* X^h *of*

$$\alpha^2 \langle \nabla \overline{\phi}^h, \nabla \xi \rangle + \langle \overline{\phi}^h, \xi \rangle = \langle \phi, \xi \rangle \ \forall \xi \in X^h.$$

Given $\phi \in L^2(\Omega)$*, the discrete van Cittert deconvolution operator* D_N^h *is defined by*

$$D_N^h \phi = \sum_{i=0}^{N} (I - F_h)^i \phi.$$

Definition 4.3. *As in [76], we define the energy norm for the BV-*α*-Deconvolution model to be*

$$\|\phi\|_{E,N}^2 := \langle \phi, D_N^h \overline{\phi}^h \rangle. \tag{4.8}$$

With this definition we have the following equivalence between norms (see [76]).

Lemma 4.4. *For* $\phi \in X^h$ *and for each natural number* N*, the energy norm defined by (4.8) is equivalent to the zeroth order energy norm also defined by (4.8). That is,*

$$\|\phi\|_{E,0} \leq \|\phi\|_{E,N} \leq \sqrt{N} \|\phi\|_{E,0}.$$

The following inequalities are useful in the subsequent analysis.

Lemma 4.5. *For $\phi \in X^h$. We have the following inequalities*

$$\begin{aligned} \|D_N^h \overline{\phi}^h\| &\leq N\|\phi\|_{E,0}, \\ \|I - F_h\| &\leq 1, \\ \|D_N^h \phi\| &\leq (N+1)\|\phi\|, \\ \|\overline{\phi}^h\| &\leq \|\phi\|. \end{aligned}$$

Proof. For first and second inequalities see [76]. For the third, we have

$$\|D_N^h \phi\| \leq \sum_{n=0}^{N} \|I - F_h\|^n \|\phi\| \leq (N+1)\|\phi\|,$$

where we used the second inequality. For the last inequality, we choose the test function equal to $\overline{\phi}^h$ in the filter equation to obtain

$$\alpha^2 \|\nabla \overline{\phi}^h\|^2 + \|\overline{\phi}^h\|^2 = \langle \phi, \overline{\phi}^h \rangle.$$

The result follows after applying the Cauchy-Schwarz inequality. □

Lemma 4.6. *The operator $D_N^h : X^h \to X^h$ is a bounded, self-adjoint positive operator. For $\phi \in X^h$,*

$$\phi = D_N^h \overline{\phi}^h + \big(-1\big)^{(N+1)} \alpha^{2N+2} \Delta_h^{N+1} F_h^{N+1} \phi.$$

Proof. See [76]. □

4.3 Numerical scheme for BV-α-Deconvolution

Let $\phi(t^{n+\frac{1}{2}}) = \phi(({t^{n+1} + t^n})/2)$ for continuous variables and $\phi^{n+\frac{1}{2}} = ({\phi^{n+1} + \phi^n})/2$ for both the continuous and discrete variables. Based in the above variational formulation for the BV model, we define the following Crank-Nicolson type algorithm for BV-α-Deconvolution model.

Algorithm 4.1 (Crank-Nicolson - BV-α-Deconvolution model). *Set* $M = \frac{T}{\Delta t}$ *and for n=0,...,M-1, find* $(\omega^n, \psi^n, \omega^n) \in X_h \times X_h \times X_h$ *satisfying:*

$$Ro\big\langle \tfrac{\omega_h^{n+1} - \omega_h^n}{\Delta t}, \lambda\big\rangle + Rob\big(\psi_h^{n+\frac{1}{2}}, \omega_h^{n+\frac{1}{2}}, \lambda\big) - \big\langle \tfrac{\partial \psi_h^{n+\frac{1}{2}}}{\partial x}, \lambda\big\rangle$$

$$+ \big(\tfrac{\delta_M}{L}\big)^3 \big\langle \nabla \omega_h^{n+\frac{1}{2}}, \nabla \lambda\big\rangle = \big\langle \mathcal{F}^{n+\frac{1}{2}}, \lambda\big\rangle \ \forall \lambda \in X^h, \tag{4.9a}$$

$$\big\langle \nabla \psi_h^{n+1}, \nabla \chi\big\rangle = \big\langle D_N^h \overline{\omega_h^{n+1}}^h, \chi\big\rangle \ \forall \chi \in X^h, \tag{4.9b}$$

$$\alpha^2 \big\langle \nabla F_h \omega_h^{n+1}, \nabla \xi\big\rangle + \big\langle F_h \omega_h^{n+1}, \xi\big\rangle = \big\langle \omega_h^{n+1}, \xi\big\rangle \ \forall \xi \in X^h. \tag{4.9c}$$

where we assume that timestep $\Delta t > 0$*, endtime* $T > \Delta t$*, Rossby number* $Ro > 0$*, Munk scale* $\frac{\delta_M}{L} > 0$ *and filter radius* $\alpha > 0$ *are given.*

Now we present a lemma that will be useful in the stability analysis:

Lemma 4.7. *Let* $\big(\omega_h, \psi_h\big) \in X^h \times X^h$ *be a solution of Algorithm 4.1. Then we have*

$$\big\langle \omega_h, \psi_h\big\rangle = \|\nabla \psi_h\|^2 + \alpha^2 \sum_{i=0}^{N} \|(I - F_h)^{\frac{N+i}{2}} \omega_h\|^2, \tag{4.10}$$

$$\big\langle \nabla \omega_h, \nabla \psi_h\big\rangle = \big\langle D_N^h \overline{\omega_h}^h, \omega_h\big\rangle = \|(D_N^h F_h)^{\frac{1}{2}} \omega_h\|^2, \tag{4.11}$$

$$= \|D_N^h \overline{\omega_h}^h\|^2 + \alpha^2 \sum_{i=0}^{N} \|\nabla (I - F_h)^{\frac{N+i}{2}} \overline{\omega_h}^h\|^2. \tag{4.12}$$

Proof. Using Lemma 4.6 gives

$$\big\langle \omega_h, \psi_h\big\rangle = \big\langle D_N^h \overline{\omega}_h^h, \psi_h\big\rangle + \big(-1\big)^{N+1} \alpha^{2N+2} \big\langle \Delta_h^{N+1} F_h^{N+1} \omega_h, \psi_h\big\rangle. \tag{4.13}$$

Now, evaluating the two terms in the RHS - for the first term, we choose $\chi = \psi_h$ in (4.9b) to obtain

$$\|\nabla \psi_h\|^2 = \big\langle D_N^h \overline{\omega_h}, \psi_h\big\rangle.$$

For the second term on the RHS of (4.13), we rewrite (4.9b) using the discrete Laplacian and choose $\chi = \Delta_h^N F_h^N \overline{\omega}_h^h$ to obtain

$$-\big\langle \psi_h, \Delta_h \Delta_h^N F_h^N \overline{\omega}_h^h\big\rangle = \big\langle D_N^h \overline{\omega}_h^h, \Delta_h^N F_h^N \overline{\omega}_h^h\big\rangle.$$

Thus

$$-\big\langle \Delta_h^{N+1} F_h^{N+1} \omega_h, \psi_h \big\rangle = \big\langle D_N^h \overline{\omega}_h^h, \Delta_h^N F_h^N \overline{\omega}_h^h \big\rangle = \sum_{n=0}^{N} \big\langle (I - F_h)^n \overline{\omega}_h^h, \Delta_h^N F_h^N \overline{\omega}_h^h \big\rangle, \tag{4.14}$$

and moreover, we have

$$\Delta_h F_h = \tfrac{-\alpha^2}{-\alpha^2} \Delta_h F_h = -\tfrac{1}{\alpha^2}\big[\big(F_h - \alpha^2 \Delta_h\big) - F_h\big] = -\tfrac{1}{\alpha^2}\big[I - F_h\big],$$

which implies

$$\Delta_h^N F_h^N = \big(-\tfrac{1}{\alpha^2}\big)^N \big(I - F_h\big)^N. \tag{4.15}$$

Multiplying (4.14) by $\big(-1\big)^N \alpha^{2N}$ and applying (4.15) produces

$$\begin{aligned} \big(-1\big)^{N+1} \alpha^{2N} \big\langle \Delta_h^{N+1} F_h^{N+1} \omega_h, \psi_h \big\rangle &= \sum_{i=0}^{N} \big\langle (I - F_h)^i \overline{\omega}_h^h, (I - F_h)^N \overline{\omega}_h^h \big\rangle \\ &= \sum_{i=0}^{N} \|(I - F_h)^{\frac{N+i}{2}} \overline{\omega}_h^h\|^2. \end{aligned}$$

(4.10) follows after we use the above equation multiplied by α^2.

Now, we prove (4.11) and (4.12). (4.11) follows from (4.9b) with $\chi = \omega_h$ because F_h and D_N^h are self-adjoint and positive [76]. For (4.12), we use (4.15) and Lemma (4.6) to obtain

$$\omega_h = D_N^h \overline{\omega_h}^h + \big(I - F_h\big)^{N+1} \omega_h.$$

Thus, using (4.9b) with $\chi = \omega_h$,the definition of D_N^h and as F_h is self-adjoint and positive results

$$\begin{aligned} \big\langle \nabla \psi_h, \nabla \omega_h \big\rangle &= \big\langle D_N^h \overline{\omega_h}^h, \omega_h \big\rangle = \big\langle D_N^h \overline{\omega_h}^h, D_N^h \overline{\omega_h}^h \big\rangle + \big\langle D_N^h \overline{\omega_h}^h, \big(I - F_h\big)^{N+1} \omega_h \big\rangle \\ &= \|D_N^h \overline{\omega_h}^h\|^2 + \sum_{i=0}^{N} \big\langle \big(I - F_h\big)^i \overline{\omega_h}^h, \big(I - F_h\big)^N \big(I - F_h\big) \omega_h \big\rangle \\ &= \|D_N^h \overline{\omega_h}^h\|^2 + \sum_{i=0}^{N} \big\langle \big(I - F_h\big)^{\frac{N+i}{2}} \overline{\omega_h}^h, \big(I - F_h\big)\big(I - F_h\big)^{\frac{N+i}{2}} \omega_h \big\rangle. \end{aligned}$$

Finally, applying the filter equation to $(I-F_h)^{\frac{N+i}{2}}\omega_h$, choosing the test function to be $(I-F_h)^{\frac{N+i}{2}}\overline{\omega_h}^h$, and using the fact that $(I-F_h)^{\frac{N+i}{2}}$ commutes with F_h, we obtain

$$\alpha^2\|\nabla(I-F_h)^{\frac{N+i}{2}}\overline{\omega_h}^h\| = \big\langle (I-F_h)(I-F_h)^{\frac{N+i}{2}}\omega_h, (I-F_h)^{\frac{N+i}{2}}\overline{\omega_h}^h\big\rangle$$

from which we have

$$\begin{aligned}\big\langle \nabla\psi_h, \nabla\omega_h\big\rangle &= \|D_N^h\overline{\omega_h}^h\|^2 + \alpha^2\sum_{i=0}^{N}\big\langle \nabla\big(I-F_h\big)^{\frac{N+i}{2}}\overline{\omega_h}^h, \nabla F_h\big(I-F_h\big)^{\frac{N+i}{2}}\omega_h\big\rangle \\ &= \|D_N^h\overline{\omega_h}^h\|^2 + \alpha^2\sum_{i=0}^{N}\|\nabla(I-F_h)^{\frac{N+i}{2}}\overline{\omega_h}^h\|^2.\end{aligned}$$

□

Thus, we define the modified BV-α-Deconvolution kinetic energy, energy dissipation and enstrophy respectively as:

$$\begin{aligned}E_\alpha^N(\psi,\omega) &:= \tfrac{1}{2}\big\langle\psi,\omega\big\rangle = \tfrac{1}{2}\|\nabla\psi\|^2 + \tfrac{1}{2}\alpha^2\sum_{i=0}^{N}\|(I-F_h)^{\frac{N+i}{2}}\overline{\omega}^h\|^2, \\ \epsilon_\alpha^N(\omega) &:= \big(\tfrac{\delta_M}{L}\big)^3\big\langle\nabla\psi,\nabla\omega\big\rangle = \big(\tfrac{\delta_M}{L}\big)^3\|D_N^h\overline{\omega}^h\|^2 + \big(\tfrac{\delta_M}{L}\big)^3\alpha^2\sum_{i=0}^{N}\|\nabla(I-F_h)^{\frac{N+i}{2}}\overline{\omega}^h\|^2, \\ \mathcal{E}(\omega) &:= \tfrac{1}{2}\|\omega\|^2.\end{aligned}$$

Remark 4.1. *Due to linearity of equation (4.9b), in both F_h and D_N^h we have*

$$\big\langle\omega^{n+1}-\omega^n, \psi^{n+\frac{1}{2}}\big\rangle = E_\alpha^N(\psi_h^{n+1},\omega_h^{n+1}) - E_\alpha^N(\psi_h^n,\omega_h^n).$$

Lemma 4.8 (Conservation of Kinetic Energy)**.** *The BV-α-Deconvolution model solution satisfies*

$$E_\alpha^N(\psi_h^M,\omega_h^M) + \tfrac{\Delta t}{Ro}\sum_{n=0}^{M-1}\epsilon_\alpha^N(\omega_h^{n+\frac{1}{2}}) = E_\alpha^N(\psi_h^0,\omega_h^0) + \tfrac{\Delta t}{Ro}\sum_{n=0}^{M-1}\big\langle\mathcal{F}^{n+\frac{1}{2}},\psi_h^{n+\frac{1}{2}}\big\rangle.$$

In particular, if $\delta_M = 0$ and $\mathcal{F} = 0$ we have $E_\alpha^N(\psi_h^M,\omega_h^M) = E_\alpha^N(\psi_h^0,\omega_h^0)$.

Proof. We rewrite the nonlinear term in (4.9a) as $b(\psi_h^{n+\frac{1}{2}}, Ro\omega_h^{n+\frac{1}{2}} + y, \lambda)$ and choose $\lambda = \psi_h^{n+\frac{1}{2}}$. We obtain, after we use the definition of modified energy and dissipation and the skew-symmetry of the trilinear form,

$$E_\alpha^N(\psi_h^{n+1}, \omega_h^{n+1}) - E_\alpha^N(\psi_h^n, \omega_h^n) + \tfrac{\Delta t}{Ro}\epsilon_N^\alpha(\omega_h^{n+\frac{1}{2}}) = \big\langle \mathcal{F}^{n+\frac{1}{2}}, \psi_h^{n+\frac{1}{2}} \big\rangle. \tag{4.16}$$

The result follows after we sum from $n = 0, ..., M-1$. □

Algorithm 4.1 also conserves enstrophy.

Lemma 4.9 (Conservation of enstrophy). *The BV-α-Deconvolution model solution satisfies*

$$\mathcal{E}(\omega_h^M) + \tfrac{\Delta t}{Ro}\big(\tfrac{\delta_M}{L}\big)^3 \sum_{n=0}^{M} \big\|\nabla\omega_h^{n+\frac{1}{2}}\big\|^2 =$$
$$\mathcal{E}(\omega_h^0) + \tfrac{\Delta t}{Ro} \sum_{n=0}^{M} \big\langle \tfrac{\partial\psi_h^{n+\frac{1}{2}}}{\partial x}, \omega_h^{n+\frac{1}{2}} \big\rangle + \tfrac{\Delta t}{Ro} \sum_{n=0}^{M} \big\langle \mathcal{F}^{n+\frac{1}{2}}, \omega_h^{n+\frac{1}{2}} \big\rangle.$$

In particular, if $\delta_M = \mathcal{F} = 0$ and $Ro \to \infty$, $\mathcal{E}(\omega_h^M) = \mathcal{E}(\omega_h^0)$.

Proof. Choosing $\lambda = \omega_h^{n+\frac{1}{2}} = \frac{1}{2}(\omega_h^{n+1} + \omega_h^n)$ in (4.9a), using the skew-symmetry of the trilinear term, the enstrophy definition, and multiplying by $\frac{\Delta t}{Ro}$ gives

$$\mathcal{E}(\omega_h^{n+1}) + \tfrac{\Delta t}{Ro}\Big(\tfrac{\delta_M}{L}\Big)^3 \|\nabla\omega_h^{n+\frac{1}{2}}\|^2 = \mathcal{E}(\omega_h^n) + \tfrac{\Delta t}{Ro}\big\langle \tfrac{\partial\psi_h^{n+\frac{1}{2}}}{\partial x}, \omega_h^{n+\frac{1}{2}} \big\rangle + \tfrac{\Delta t}{Ro}\big\langle \mathcal{F}^{n+\frac{1}{2}}, \omega_h^{n+\frac{1}{2}} \big\rangle. \tag{4.17}$$

The result now follows after we sum from $n = 0, ..., M-1$. □

Lemma 4.10 (Stability). *Algorithm 4.1 is unconditionally stable. Its solutions satisfy*

$$Ro\|\nabla\psi_h^M\|^2 + Ro\tfrac{\alpha^2}{2} \sum_{i=0}^{N} \|(I - F_h)^{\frac{N+i}{2}} \overline{\omega_h}^h\|^2 + \tfrac{\Delta t}{2N}\big(\tfrac{\delta_M}{L}\big)^3 \sum_{n=0}^{M} \|\Delta_h\psi_h^{n+\frac{1}{2}}\|^2 \leq C(data), \tag{4.18}$$

$$\|\omega_h^M\|^2 + \tfrac{\Delta t}{2Ro}\big(\tfrac{\delta_M}{L}\big)^3 \textstyle\sum_{n=0}^{M} \big\|\nabla\omega_h^{n+\frac{1}{2}}\big\|^2 \leq C(data). \tag{4.19}$$

Remark 4.2. *The bounds* (4.18)-(4.19) *are sufficient for the Leray-Schauder fixed point theorem to be applied, in order to prove existence of a solution at each timestep (as in [60]). Uniqueness can be proven in the standard way, and will hold provided a timestep restriction.*

Proof. For any $\Delta t > 0$ we start with the estimate (4.18). First, note that using the definition of the discrete Laplacian, equation (4.9b), choosing $\chi = \Delta_h \psi_h^{n+\frac{1}{2}}$ and using Cauchy-Schwarz yields:

$$\|\Delta_h \psi_h^{n+\frac{1}{2}}\| \leq \|D_N^h \overline{\omega_h^{n+\frac{1}{2}}}^h\|.$$

Now using Lemma 4.5 and norm equivalence in Lemma 4.4

$$\|\Delta_h \psi_h^{n+\frac{1}{2}}\|^2 \leq N\|\omega_h^{n+\frac{1}{2}}\|_{E,N} = N\big\langle D_N^h \overline{\omega_h^{n+\frac{1}{2}}}^h, \omega_h^{n+\frac{1}{2}}\big\rangle = N\big\langle \nabla \psi_h^{n+\frac{1}{2}}, \nabla \omega_h^{n+\frac{1}{2}}\big\rangle. \quad (4.20)$$

Using inequality (4.20), equation (4.16) and Cauchy-Schwarz inequality we obtain

$$E_\alpha^N(\psi_h^{n+1}, \omega_h^{n+1}) - E_\alpha^N(\psi_h^n, \omega_h^n) + \tfrac{\Delta t}{NRo}\big(\tfrac{\delta_M}{L}\big)^3 \|\Delta_h \psi_h^{n+\frac{1}{2}}\|^2 \leq \tfrac{\Delta t}{Ro}\|\mathcal{F}^{n+\frac{1}{2}}\|_{-1}\|\nabla \psi_h^{n+\frac{1}{2}}\|. \quad (4.21)$$

Averaging the definition of modified Laplacian and choosing $\chi = \psi_h^{n+\frac{1}{2}}$ we find

$$\|\nabla \psi_h^{n+\frac{1}{2}}\| \leq C_{PF}\|\Delta_h \psi_h^{n+\frac{1}{2}}\|. \quad (4.22)$$

Then we obtain estimate (4.18) using (4.22) in (4.21), Young's inequality with $\epsilon = \left(\frac{L}{\delta_M}\right)^3$ and summing from $n = 0, ..., M-1$.

For estimate (4.19), we use (4.17), Cauchy-Schwarz and Young's inequalities and the definition of enstrophy. Summing from $n = 0, ..., M-1$ finishes the proof. □

4.4 Convergence

The following lemma is the key to handling the consistency error in the BV-α-Deconvolution model.

Lemma 4.11. *For smooth, periodic ϕ, or ϕ satisfying $\Delta^j \phi = 0$ on $\partial\Omega$ for $0 \leq j \leq \frac{k+1}{2} - 1$, the discrete approximate deconvolution operator satisfies*

$$\|\phi - D_N^h \overline{\phi}^h\| \leq C\alpha^{2N+2} \|\Delta^{N+1} F^{N+1} \phi\| + C(\alpha h^k + h^{k+1}) \big(\sum_{i=1}^{N} |F^{i+1}\phi|_{k+1} \big),$$

and thus for $k \geq 1$ we have

$$\|\phi - D_N^h \overline{\phi}^h\| \leq C(\alpha^{2N+2} + \alpha h^k + h^{k+1}) \big(\sum_{i=1}^{N} |F^{i+1}\phi|_{k+1} \big).$$

Proof. See [64]. □

Theorem 4.1 (Convergence)**.** *Consider the discrete BV-α-Deconvolution model. Let $(\omega(t), \psi(t)) \in X \times X$ be a smooth strong solution of the BV model satisfying free slip boundary conditions such that the norms of $(\omega(t), \psi(t))$ on the right hand side of (4.23) and (4.24) are finite. Suppose ω_h, ψ_h solves the Crank-Nicolson approximation (4.9a)-(4.9c) of the BV-α-Deconvolution model. Then for Δt small enough (in order to apply the discrete Gronwall inequality), we have*

$$\big\|\!|\omega - \omega_h|\!\big\|_{\infty,0} \leq f\big(\Delta t, h, \alpha\big) + Ch^{k+1} \big\|\!|\omega|\!\big\|_{\infty,k+1}, \tag{4.23}$$

$$\begin{aligned}\Big(\big(\tfrac{\delta_M}{L}\big)^3 \sum_{n=0}^{M-1} \Delta t \big\|\nabla\big(\omega(t^{n+\frac{1}{2}}) - \omega_h^{n+\frac{1}{2}}\big)\big\|^2 \Big)^{1/2} &\leq f\big(\Delta t, h, \alpha\big) + C\Delta t^2 \big(\tfrac{\delta_M}{L}\big)^{3/2} \big\|\omega_{tt}\big\|_{2,0} \\ &\quad + C\big(\tfrac{\delta_M}{L}\big)^{3/2} h^k \big\|\!|\omega|\!\|_{2,k+1},\end{aligned} \tag{4.24}$$

where

$$\begin{aligned}
&f\big(\Delta t, h, \alpha\big) := \\
&C^* \big\{ h^k \big[\tfrac{C}{Ro^{\frac{1}{2}}} \big(\tfrac{\delta_M}{L}\big)^{\frac{3}{2}} |||\omega^{1/2}|||_{2,k+1} + \tfrac{C}{Ro^{\frac{1}{2}}} \big(\tfrac{L}{\delta_M}\big)^{\frac{3}{2}} |||\psi^{1/2}|||_{2,k+1} + h \tfrac{C}{Ro^{\frac{1}{2}}} \big(\tfrac{L}{\delta_M}\big)^{\frac{3}{2}} |||\omega^{1/2}|||_{2,k+1} \\
&+ C\big(\tfrac{L}{\delta_M}\big)^{\frac{3}{2}} |||\nabla\omega^{1/2}|||_{4,1}^2 + C\big(\tfrac{L}{\delta_M}\big)^{\frac{3}{2}} |||\psi^{1/2}|||_{4,k+1}^2 + hC\big(\tfrac{L}{\delta_M}\big)^{\frac{3}{2}} |||\omega^{1/2}|||_{4,k+1}^2 + hC\big(\tfrac{L}{\delta_M}\big)^{\frac{3}{2}} |||\psi^{1/2}|||_{4,k+1}^2 \big] \\
&+ (\alpha^{2N+2} + \alpha h^k + h^{k+1}) \big[C \sum_{i=1}^{N} |||F^{i+1}\omega^{1/2}|||_{2,k+1} + C\big(\tfrac{L}{\delta_M}\big)^{\frac{3}{2}} |||\nabla\omega^{1/2}|||_{4,1}^2 + C\big(\tfrac{L}{\delta_M}\big)^{\frac{3}{2}} \sum_{i=1}^{N} |||F^{i+1}\omega^{1/2}|||_{4,k+1}^2 \\
&+ C\big(\tfrac{L}{\delta_M}\big)^{\frac{3}{2}} |||\omega^{1/2}|||_{4,k+1}^2 \big] + \Delta t^2 \big[\big(\tfrac{L}{\delta_M}\big)^{\frac{3}{2}} C\|\omega_{ttt}\|_{2,0} + C\big(\tfrac{\delta_M}{L}\big)^{\frac{3}{2}} \|\nabla\omega_{tt}\|_{2,0} + C\big(\tfrac{L}{\delta_M}\big)^{\frac{3}{2}} \|\psi_{tt}\|_{2,0} \\
&+ C\big(\tfrac{L}{\delta_M}\big)^{\frac{3}{2}} |||\nabla\psi^{\frac{1}{2}}|||_{4,1}^2 + C\big(\tfrac{L}{\delta_M}\big)^{\frac{3}{2}} \|\omega_{tt}\|_{4,1}^2 + C\big(\tfrac{L}{\delta_M}\big)^{\frac{3}{2}} \big|\big|\big|\nabla\omega^{1/2}\big|\big|\big|_{4,1}^2 + C\big(\tfrac{L}{\delta_M}\big)^{\frac{3}{2}} \|\psi_{tt}\|_{4,1}^2 \big] \big\}.
\end{aligned}$$

Corollary 4.1. *Suppose that the indicated norms on the right hand side of (4.23)-(4.24) are finite. Then the error in the Crank-Nicolson finite element scheme for* *the BV-α-deconvolution is of the order*

$$\big|\big|\big|\omega - \omega_h\big|\big|\big|_{\infty,0} + \Big(\big(\tfrac{\delta_M}{L}\big)^3 \sum_{n=0}^{M-1} \Delta t \|\nabla(\omega(t^{n+\frac{1}{2}}) - \omega_h^{n+\frac{1}{2}})\|^2\Big)^{1/2}$$
$$\leq O\big(h^k + \Delta t^2 + \alpha^{2N+2} \sum_{i=1}^{N} |||F^{i+1}\omega|||_{2,k+1}\big).$$

Moreover,

$$|||\psi - \psi_h|||_{2,1} \leq O\big(h^k + \Delta t^2 + \alpha^{2N+2} \sum_{i=0}^{N} |||F^{i+1}\omega|||_{2,k+1}\big). \tag{4.25}$$

Proof of Theorem 4.1. The BV model solution satisfies

$$Ro\big\langle \tfrac{\omega^{n+1}-\omega^n}{\Delta t}, v_h\big\rangle + Rob\big(\psi^{n+\frac{1}{2}}, \omega^{n+\frac{1}{2}}, v_h\big) - \big\langle \tfrac{\partial \psi^{n+\frac{1}{2}}}{\partial x}, v_h\big\rangle + \Big(\tfrac{\delta_M}{L}\Big)^3 \big\langle \nabla\omega^{n+\frac{1}{2}}, \nabla v_h\big\rangle$$
$$= \big\langle \mathcal{F}^{n+\frac{1}{2}}, v_h\big\rangle + Intp(\omega^n, \psi^n; v_h)\ \forall v_h \in X^h, \tag{4.26}$$

where

$$Intp(\omega^n, \psi^n; v_h) := Ro\big\langle \tfrac{\omega^{n+1}-\omega^n}{\Delta t} - \omega_t(t^{n+\frac{1}{2}}), v_h\big\rangle + \Big(\tfrac{\delta_M}{L}\Big)^3 \big\langle \nabla\omega^{n+\frac{1}{2}} - \nabla\omega(t^{n+\frac{1}{2}}), \nabla v_h\big\rangle$$
$$-\big\langle \tfrac{\partial\psi^{n+\frac{1}{2}}}{\partial x} - \tfrac{\partial\psi(t^{n+\frac{1}{2}})}{\partial x}, v_h\big\rangle + Ro\big[b\big(\psi^{n+\frac{1}{2}}, \omega^{n+\frac{1}{2}}, v_h\big) - b\big(\psi(t^{n+\frac{1}{2}}), \omega(t^{n+\frac{1}{2}}), v_h\big)\big]. \tag{4.27}$$

We define the vorticity and streamfunction error as

$$e := \omega - \omega_h = \big(\omega - P\omega\big) - \big(\omega_h - P\omega\big) = e_\perp - e_h,$$
$$E := \psi - \psi_h = \big(\psi - \Pi\psi\big) - \big(\psi_h - \Pi\psi\big) = E_\perp - E_h.$$

Now we subtract (4.9a) from (4.26), add $\pm b\big(\psi_h^{n+\frac{1}{2}}, \omega^{n+\frac{1}{2}}, v_h\big)$ and fix $v_h = e_h^{n+\frac{1}{2}}$

$$\|e_h^{n+1}\|^2 - \|e_h^n\|^2 + \tfrac{2\Delta t}{Ro}\Big(\tfrac{\delta_M}{L}\Big)^3 \|\nabla e_h^{n+\frac{1}{2}}\|^2 = \tfrac{2\Delta t}{Ro}\Big(\tfrac{\delta_M}{L}\Big)^3 \big\langle \nabla e_\perp^{n+\frac{1}{2}}, \nabla e_h^{n+\frac{1}{2}}\big\rangle$$
$$-\tfrac{2\Delta t}{Ro}\big\langle \tfrac{\partial E^{n+\frac{1}{2}}}{\partial x}, e_h^{n+\frac{1}{2}}\big\rangle + 2\Delta t\big[b\big(\psi_h^{n+\frac{1}{2}}, e_\perp^{n+\frac{1}{2}}, e_h^{n+\frac{1}{2}}\big) + b\big(E^{n+\frac{1}{2}}, \omega^{n+\frac{1}{2}}, e_h^{n+\frac{1}{2}}\big)\big]$$
$$- \tfrac{2\Delta t}{Ro} Intp(\omega^n, \psi^n; e_h^{n+\frac{1}{2}}), \tag{4.29}$$

because $\big\langle e_\perp^{n+1} - e_\perp^n, e_h^{n+\frac{1}{2}}\big\rangle = 0$ and $b\big(\psi_h^{n+\frac{1}{2}}, e_h^{n+\frac{1}{2}}, e_h^{n+\frac{1}{2}}\big) = 0$.

The next step is to bound the RHS terms in (4.29). The term below is bounded in a standard way using Cauchy-Schwarz and Young inequalities and Lemma 4.1.

$$\Big|\big(\tfrac{\delta_M}{L}\big)^3\big\langle\nabla e_\perp^{n+\frac{1}{2}}, \nabla e_h^{n+\frac{1}{2}}\big\rangle\Big| \leq \tfrac{1}{16}\big(\tfrac{\delta_M}{L}\big)^3\|\nabla e_h^{n+\frac{1}{2}}\|^2 + Ch^{2k}\big(\tfrac{\delta_M}{L}\big)^3\|\omega^{n+\frac{1}{2}}\|_{k+1}^2. \tag{4.30}$$

Using Poincaré and Young inequalities with $\epsilon = \frac{1}{8}\big(\frac{\delta_M}{L}\big)^3$ we obtain

$$\Big|\big\langle\tfrac{\partial E^{n+\frac{1}{2}}}{\partial x}, e_h^{n+\frac{1}{2}}\big\rangle\Big| \leq \tfrac{1}{16}\big(\tfrac{\delta_M}{L}\big)^3\|\nabla e_h^{n+\frac{1}{2}}\|^2 + C\Big(\frac{L}{\delta_M}\Big)^3\|\nabla E^{n+\frac{1}{2}}\|^2.$$

Now we have to estimate the term $\|\nabla E^{n+\frac{1}{2}}\|$. Averaging and subtracting (4.4b) from (4.9b), choosing $v_h = E_h^{n+\frac{1}{2}}$ and using Cauchy-Schwarz and Poincaré inequalities, we obtain

$$\|\nabla E_h^{n+\frac{1}{2}}\|^2 \leq C\|D_N^h\overline{(\omega_h^{n+\frac{1}{2}} - \omega^{n+\frac{1}{2}})}^h\|\|\nabla E_h^{n+\frac{1}{2}}\| + C\|D_N^h\overline{\omega^{n+\frac{1}{2}}}^h - \omega^{n+\frac{1}{2}}\|\|\nabla E_h^{n+\frac{1}{2}}\|. \tag{4.31}$$

Using (4.31) and Lemma 4.5 we obtain

$$\|\nabla E^{n+\frac{1}{2}}\|^2 \leq \|\nabla E_\perp^{n+\frac{1}{2}}\|^2 + C\|e_h^{n+\frac{1}{2}}\|^2 + C\|e_\perp^{n+\frac{1}{2}}\|^2 + C\|D_N^h\overline{\omega^{n+\frac{1}{2}}}^h - \omega^{n+\frac{1}{2}}\|^2. \tag{4.32}$$

Using (4.32) and Lemmas 4.1 and 4.11

$$\begin{aligned}
&\Big|\big\langle\tfrac{\partial E^{n+\frac{1}{2}}}{\partial x}, e_h^{n+\frac{1}{2}}\big\rangle\Big| \leq \tfrac{1}{16}\big(\tfrac{\delta_M}{L}\big)^3\|\nabla e_h^{n+\frac{1}{2}}\|^2 \\
&+ C\Big(\frac{L}{\delta_M}\Big)^3\Big(C\|\nabla E_\perp^{n+\frac{1}{2}}\|^2 + C\|e_\perp^{n+\frac{1}{2}}\|^2 + C\|e_h^{n+\frac{1}{2}}\|^2 + C\|D_N^h\overline{\omega^{n+\frac{1}{2}}}^h - \omega^{n+\frac{1}{2}}\|^2\Big) \\
&\leq \tfrac{1}{16}\big(\tfrac{\delta_M}{L}\big)^3\|\nabla e_h^{n+\frac{1}{2}}\|^2 + C\Big(\frac{L}{\delta_M}\Big)^3\|e_h^{n+\frac{1}{2}}\|^2 + \Big(\frac{L}{\delta_M}\Big)^3\Big[Ch^{2k}\|\psi^{n+\frac{1}{2}}\|_{k+1}^2 \\
&+ Ch^{2k+2}\|\omega^{n+\frac{1}{2}}\|_{k+1}^2 + C(\alpha^{4N+4} + \alpha^2h^{2k} + h^{2k+2})\Big(\sum_{i=1}^{N}|F^{i+1}\omega^{n+\frac{1}{2}}|_{k+1}^2\Big)\Big].
\end{aligned} \tag{4.33}$$

For the first trilinear term we use Lemma 4.3, Young inequality with $\epsilon = \frac{1}{8Ro}\left(\frac{\delta_M}{L}\right)^3$, Poincaré inequality, (4.32), Lemmas 4.1 and 4.11 and as $k \geq 1$ we have

$$
\begin{aligned}
&\left|b\left(E^{n+\frac{1}{2}}, \omega^{n+\frac{1}{2}}, e_h^{n+\frac{1}{2}}\right)\right| \leq \tfrac{1}{16}\left(\tfrac{\delta_M}{L}\right)^3 \|\nabla e_h^{n+\frac{1}{2}}\|^2 + C\left(\tfrac{L}{\delta_M}\right)^3 \|\nabla \omega^{n+\frac{1}{2}}\|_1^2 \|\nabla E^{n+\frac{1}{2}}\|^2 \\
&\leq \tfrac{1}{16}\left(\tfrac{\delta_M}{L}\right)^3 \|\nabla e_h^{n+\frac{1}{2}}\|^2 + C\left(\tfrac{L}{\delta_M}\right)^3 \|\nabla \omega^{n+\frac{1}{2}}\|_1^2 \|e_h^{n+\frac{1}{2}}\|^2 \\
&+ \left(\tfrac{L}{\delta_M}\right)^3 \|\nabla \omega^{n+\frac{1}{2}}\|_1^2 \left(Ch^{2k}\|\psi^{n+\frac{1}{2}}\|_{k+1}^2 + Ch^{2k+2}\|\omega^{n+\frac{1}{2}}\|_{k+1}^2 + C\|D_N^h \overline{\omega^{n+\frac{1}{2}}}^h - \omega^{n+\frac{1}{2}}\|^2\right) \\
&\leq \tfrac{1}{16}\left(\tfrac{\delta_M}{L}\right)^3 \|\nabla e_h^{n+\frac{1}{2}}\|^2 + C\left(\tfrac{L}{\delta_M}\right)^3 \|\nabla \omega^{n+\frac{1}{2}}\|_1^2 \|e_h^{n+\frac{1}{2}}\|^2 \\
&+ C\left(\tfrac{L}{\delta_M}\right)^3 h^{2k}(\|\nabla \omega^{n+\frac{1}{2}}\|_1^4 + \|\psi^{n+\frac{1}{2}}\|_{k+1}^4) + C\left(\tfrac{L}{\delta_M}\right)^3 Ch^{2k+2}\|\omega^{n+\frac{1}{2}}\|_{k+1}^4 \\
&+ C\left(\tfrac{L}{\delta_M}\right)^3(\alpha^{4N+4} + \alpha^2 h^{2k} + h^{2k+2})\left(\|\nabla \omega^{n+\frac{1}{2}}\|_1^4 + \sum_{i=1}^{N} |F^{i+1}\omega^{n+\frac{1}{2}}|_{k+1}^4\right). \qquad (4.34)
\end{aligned}
$$

Using Holder's inequality with $p = \infty$ and $q = r = 2$,

$$
\left|b\left(\psi_h^{n+\frac{1}{2}}, e_\perp^{n+\frac{1}{2}}, e_h^{n+\frac{1}{2}}\right)\right| \leq \|\nabla \psi_h^{n+\frac{1}{2}}\|_\infty \|e_\perp^{n+\frac{1}{2}}\|^2 \|\nabla e_h^{n+\frac{1}{2}}\|^2.
$$

From $\|\nabla \psi_h^{n+\frac{1}{2}} - \nabla \psi^{n+\frac{1}{2}}\|_\infty = \|\nabla E^{n+\frac{1}{2}}\|_\infty$ and using the embedding $H^2 \hookrightarrow L^\infty$ and the regularity estimate for elliptic equations

$$
\begin{aligned}
\|\nabla \psi_h^{n+\frac{1}{2}}\|_\infty &\leq \|\nabla E^{n+\frac{1}{2}}\|_\infty + \|\nabla \psi^{n+\frac{1}{2}}\|_\infty \leq \|\nabla E^{n+\frac{1}{2}}\|_\infty + C\|\psi^{n+\frac{1}{2}}\|_3 \\
&\leq \|\nabla E^{n+\frac{1}{2}}\|_\infty + C\|\omega^{n+\frac{1}{2}}\|_1.
\end{aligned}
$$

Now we have to estimate the term $\|\nabla E^{n+\frac{1}{2}}\|_\infty$ in the above inequality. Let I^h be a global Lagrangian interpolator, we have $\|\nabla E^{n+\frac{1}{2}}\|_\infty \leq \|\nabla(I^h\psi^{n+\frac{1}{2}} - \psi_h^{n+\frac{1}{2}})\|_\infty + \|\nabla(\psi^{n+\frac{1}{2}} - I^h\psi^{n+\frac{1}{2}})\|_\infty$. Using an inverse inequality for $\|\nabla(I^h\psi^{n+\frac{1}{2}} - \psi_h^{n+\frac{1}{2}})\|_\infty$ (Theorem 4.5.11 in [11]) and a standard estimate for $\|\nabla(\psi^{n+\frac{1}{2}} - I^h\psi^{n+\frac{1}{2}})\|_\infty$ (estimate (4.4.22) of Theorem 4.4.20 in [11] with $p = 2$, $n = 2$, $s = 1$ and $m = k+1$) we have

$$
\begin{aligned}
&\|\nabla E^{n+\frac{1}{2}}\|_\infty \leq Ch^{-1}\|\nabla(I^h\psi^{n+\frac{1}{2}} - \psi_h^{n+\frac{1}{2}})\| + Ch^{k-1}\|\psi^{n+\frac{1}{2}}\|_{k+1} \\
&\leq Ch^{-1}\|\nabla(I^h\psi^{n+\frac{1}{2}} - \psi^{n+\frac{1}{2}} - E^{n+\frac{1}{2}})\| + Ch^{k-1}\|\psi^{n+\frac{1}{2}}\|_{k+1} \\
&\leq Ch^{-1}\|\nabla E_h^{n+\frac{1}{2}}\| + Ch^{k-1}\|\psi^{n+\frac{1}{2}}\|_{k+1}.
\end{aligned}
$$

Thus, for $0 < h \leq 1$ and for $k \geq 1$ we have

$$\|\nabla \psi_h^{n+\frac{1}{2}}\|_\infty \leq C h^{-1} \|\nabla E_h^{n+\frac{1}{2}}\| + C\|\omega^{n+\frac{1}{2}}\|_1 + C\|\psi^{n+\frac{1}{2}}\|_{k+1}.$$

Therefore, for $0 < h \leq 1$ and $k \geq 1$ and using Lemma 4.1

$$\begin{aligned}
&\big|b\big(\psi_h^{n+\frac{1}{2}}, e_\perp^{n+\frac{1}{2}}, e_h^{n+\frac{1}{2}}\big)\big| \leq \big(Ch^{-1}\|\nabla E_h^{n+\frac{1}{2}}\| + \|\omega^{n+\frac{1}{2}}\|_1 + \|\psi^{n+\frac{1}{2}}\|_{k+1}\big)\|e_\perp^{n+\frac{1}{2}}\|\|\nabla e_h^{n+\frac{1}{2}}\| \\
&\leq C\|\omega^{n+\frac{1}{2}}\|_{k+1}\|\nabla E_h^{n+\frac{1}{2}}\|\|\nabla e_h^{n+\frac{1}{2}}\| + C\big(\|\omega^{n+\frac{1}{2}}\|_1 + \|\psi^{n+\frac{1}{2}}\|_{k+1}\big)\|e_\perp^{n+\frac{1}{2}}\|\|\nabla e_h^{n+\frac{1}{2}}\|.
\end{aligned}$$

From Young inequality ($\epsilon = \frac{1}{16CRo}\big(\frac{\delta_M}{L}\big)^3$), (4.31), $k \geq 1$ and Lemma 4.1

$$\begin{aligned}
&\big|b\big(\psi_h^{n+\frac{1}{2}}, e_\perp^{n+\frac{1}{2}}, e_h^{n+\frac{1}{2}}\big)\big| \leq \tfrac{1}{16}\Big(\tfrac{\delta_M}{L}\Big)^3\|\nabla e_h^{n+\frac{1}{2}}\|^2 + 8\Big(\tfrac{L}{\delta_M}\Big)^3\|\psi^{n+\frac{1}{2}}\|_{k+1}^2\|e_\perp^{n+\frac{1}{2}}\|^2 \\
&+ 8\Big(\tfrac{L}{\delta_M}\Big)^3\|\omega^{n+\frac{1}{2}}\|_{k+1}^2\big(C\|e_\perp^{n+\frac{1}{2}}\|^2 + C\|e_h^{n+\frac{1}{2}}\|^2 + C\|D_N^h\overline{\omega^{n+\frac{1}{2}}}^h - \omega^{n+\frac{1}{2}}\|^2 + C\|e_\perp^{n+\frac{1}{2}}\|^2\big) \\
&\leq \tfrac{1}{16}\Big(\tfrac{\delta_M}{L}\Big)^3\|\nabla e_h^{n+\frac{1}{2}}\|^2 + C\Big(\tfrac{L}{\delta_M}\Big)^3\|\omega^{n+\frac{1}{2}}\|_{k+1}^2\|e_h^{n+\frac{1}{2}}\|^2 + \Big(\tfrac{L}{\delta_M}\Big)^3\big[\big(\alpha^{4N+4} + \alpha^2h^{2k} + Ch^{2k+2}\big)\|\omega^{n+\frac{1}{2}}\|_{k+1}^4 \\
&+ Ch^{2k+2}\|\psi^{n+\frac{1}{2}}\|_{k+1}^4 + C(\alpha^{4N+4} + \alpha^2h^{2k} + h^{2k+2})\big(\sum_{i=1}^{N}|F^{i+1}\omega^{n+\frac{1}{2}}|_{k+1}^4\big)\big].
\end{aligned} \tag{4.35}$$

It remains to bound the term $Intp$ in (4.27). Standard analysis for the interpolation error (see, e.g., [65] and [76]) gives

$$\begin{aligned}
&\sum_{n=0}^{M-1}\Delta t\big|Intp(\omega^n, \overline{\psi^n}^h; e_h^{n+\frac{1}{2}})\big| \leq \sum_{n=0}^{M-1}\tfrac{\Delta t}{4}\Big(\tfrac{\delta_M}{L}\Big)^3\Big\|\nabla e_h^{n+\frac{1}{2}}\Big\|^2 + CRo^2\Big(\tfrac{L}{\delta_M}\Big)^3\Delta t^4\|\omega_{ttt}\|_{2,0}^2 \\
&+ C\Big(\tfrac{\delta_M}{L}\Big)^3\Delta t^4\|\nabla\omega_{tt}\|_{2,0}^2 + C\Big(\tfrac{L}{\delta_M}\Big)^3\Delta t^4\|\psi_{tt}\|_{2,0}^2 + C\Delta t^4\Big(\tfrac{L}{\delta_M}\Big)^3\Big\|\nabla\psi^{1/2}\Big\|_{4,1}^4 \\
&+ C\Delta t^4\Big(\tfrac{L}{\delta_M}\Big)^3\|\omega_{tt}\|_{4,1}^4 + C\Delta t^4\Big(\tfrac{\delta_M}{L}\Big)^3\Big\|\nabla\omega^{1/2}\Big\|_{4,1}^4 + C\Delta t^4\Big(\tfrac{L}{\delta_M}\Big)^3\|\psi_{tt}\|_{4,1}^4.
\end{aligned} \tag{4.36}$$

Now, using (4.30), (4.33), (4.34), (4.35) in (4.29), summing from $n = 0$ to $n = M - 1$ and using (4.36) we obtain

$$
\begin{aligned}
&\|e_h^M\|^2 - \|e_h^0\|^2 + \tfrac{\Delta t}{Ro}\big(\tfrac{\delta_M}{L}\big)^3 \sum_{n=0}^{M-1} \|\nabla e_h^{n+\frac{1}{2}}\|^2 \le h^{2k}\tfrac{C}{Ro}\big(\tfrac{\delta_M}{L}\big)^3 |||\omega^{1/2}|||_{2,k+1}^2 + h^{2k}\tfrac{C}{Ro}\big(\tfrac{L}{\delta_M}\big)^3 |||\psi^{1/2}|||_{2,k+1}^2 \\
&+ h^{2k+2}\tfrac{C}{Ro}\big(\tfrac{L}{\delta_M}\big)^3 |||\omega^{1/2}|||_{2,k+1}^2 + (\alpha^{4N+4} + \alpha^2 h^{2k} + h^{2k+2})\tfrac{C}{Ro}\big(\tfrac{L}{\delta_M}\big)^3 \big(\sum_{i=1}^{N} |||F^{i+1}\omega^{1/2}|||_{2,k+1}^2\big) \\
&+ h^{2k}C\Big(\tfrac{L}{\delta_M}\Big)^3 |||\nabla\omega^{1/2}|||_{4,1}^4 + h^{2k}C\Big(\tfrac{L}{\delta_M}\Big)^3 |||\psi^{1/2}|||_{4,k+1}^4 + h^{2k+2}C\big(\tfrac{L}{\delta_M}\big)^3 |||\omega^{1/2}|||_{4,k+1}^4 \\
&+ (\alpha^{4N+4} + \alpha^2 h^{2k} + h^{2k+2})C\big(\tfrac{L}{\delta_M}\big)^3 \big(|||\nabla\omega^{1/2}|||_{4,1}^4 + \sum_{i=1}^{N} |||F^{i+1}\omega^{1/2}|||_{4,k+1}^4\big) \\
&+ h^{2k+2}\big(\tfrac{L}{\delta_M}\big)^3 C|||\psi^{1/2}|||_{4,k+1}^4 + (\alpha^{4N+4} + \alpha^2 h^{2k} + Ch^{2k+2})\big(\tfrac{L}{\delta_M}\big)^3 C|||\omega^{1/2}|||_{4,k+1}^4 \\
&+ (\alpha^{4N+4} + \alpha^2 h^{2k} + h^{2k+2})C\big(\tfrac{L}{\delta_M}\big)^3 \sum_{i=1}^{N} |||F^{i+1}\omega^{1/2}|||_{4,k+1}^4 + \Delta t^4\big(\tfrac{L}{\delta_M}\big)^3 \|\omega_{ttt}\|_{2,0}^2 \\
&+ \Delta t^4\tfrac{C}{Ro}\big(\tfrac{\delta_M}{L}\big)^3 \|\nabla\omega_{tt}\|_{2,0}^2 + \Delta t^4 C\Big(\tfrac{L}{\delta_M}\Big)^3 \|\psi_{tt}\|_{2,0}^2 + \Delta t^4 C\Big(\tfrac{L}{\delta_M}\Big)^3 \Big|\Big|\Big|\nabla\psi^{1/2}\Big|\Big|\Big|_{4,1}^4 \\
&+ \Delta t^4 C\Big(\tfrac{L}{\delta_M}\Big)^3 \|\omega_{tt}\|_{4,1}^4 + \Delta t^4\tfrac{C}{Ro}\Big(\tfrac{L}{\delta_M}\Big)^3 \Big|\Big|\Big|\nabla\omega^{1/2}\Big|\Big|\Big|_{4,1}^4 + \Delta t^4 C\big(\tfrac{L}{\delta_M}\big)^3 \|\psi_{tt}\|_{4,1}^4 \\
&+ \sum_{n=0}^{M-1} \Delta t\big(\tfrac{L}{\delta_M}\big)^3 \big(C + C\|\nabla\omega^{n+\frac{1}{2}}\|_1^2 + C\|\omega^{n+\frac{1}{2}}\|_{k+1}^2\big)\|e_h^{n+\frac{1}{2}}\|^2.
\end{aligned}
$$

Considering $\Delta t < \frac{\left(\delta_M/L\right)^3}{C + C\|\nabla\omega^{n+\frac{1}{2}}\|_1^2 + C\|\omega^{n+\frac{1}{2}}\|_{k+1}^2}$ (such that we can apply Gronwall inequality) we have

$$
\begin{aligned}
&\|e_h^M\|^2 - \|e_h^0\|^2 + \tfrac{\Delta t}{Ro}\big(\tfrac{\delta_M}{L}\big)^3 \sum_{n=0}^{M-1} \|\nabla e_h^{n+\frac{1}{2}}\|^2 \le C^*\big\{h^{2k}\tfrac{C}{Ro}\big(\tfrac{\delta_M}{L}\big)^3 |||\omega^{1/2}|||_{2,k+1}^2 \\
&+ h^{2k}\tfrac{C}{Ro}\big(\tfrac{L}{\delta_M}\big)^3 |||\psi^{1/2}|||_{2,k+1}^2 + h^{2k+2}\tfrac{C}{Ro}\big(\tfrac{L}{\delta_M}\big)^3 |||\omega^{1/2}|||_{2,k+1}^2 \\
&+ (\alpha^{4N+4} + \alpha^2 h^{2k} + h^{2k+2})\tfrac{C}{Ro}\big(\tfrac{L}{\delta_M}\big)^3 \big(\sum_{i=1}^{N} |||F^{i+1}\omega^{1/2}|||_{2,k+1}^2\big) + h^{2k}C\Big(\tfrac{L}{\delta_M}\Big)^3 |||\nabla\omega^{1/2}|||_{4,1}^4 \\
&+ h^{2k}C\Big(\tfrac{L}{\delta_M}\Big)^3 |||\psi|||_{4,k+1}^4 + h^{2k+2}C\big(\tfrac{L}{\delta_M}\big)^3 |||\omega^{1/2}|||_{4,k+1}^4 \\
&+ (\alpha^{4N+4} + \alpha^2 h^{2k} + h^{2k+2})C\big(\tfrac{L}{\delta_M}\big)^3 \big(|||\nabla\omega^{1/2}|||_{4,1}^4 + \sum_{n=1}^{N} |||F^{i+1}\omega^{1/2}|||_{4,k+1}^4\big) \\
&+ h^{2k+2}\big(\tfrac{L}{\delta_M}\big)^3 C|||\psi^{1/2}|||_{4,k+1}^4 + (\alpha^{4N+4} + \alpha^2 h^{2k} + Ch^{2k+2})\big(\tfrac{L}{\delta_M}\big)^3 C|||\omega^{1/2}|||_{4,k+1}^4 \\
&+ (\alpha^{4N+4} + \alpha^2 h^{2k} + h^{2k+2})C\big(\tfrac{L}{\delta_M}\big)^3 \sum_{i=1}^{N} |||F^{i+1}\omega^{1/2}|||_{4,k+1}^4 + \Delta t^4\big(\tfrac{L}{\delta_M}\big)^3 \|\omega_{ttt}\|_{2,0}^2 \\
&+ \Delta t^4\tfrac{C}{Ro}\big(\tfrac{\delta_M}{L}\big)^3 \|\nabla\omega_{tt}\|_{2,0}^2 + \Delta t^4 C\Big(\tfrac{L}{\delta_M}\Big)^3 \|\psi_{tt}\|_{2,0}^2 + \Delta t^4 C\Big(\tfrac{L}{\delta_M}\Big)^3 \Big|\Big|\Big|\nabla\psi^{1/2}\Big|\Big|\Big|_{4,1}^4 \\
&+ \Delta t^4 C\Big(\tfrac{L}{\delta_M}\Big)^3 \|\omega_{tt}\|_{4,1}^4 + \Delta t^4\tfrac{C}{Ro}\Big(\tfrac{L}{\delta_M}\Big)^3 \Big|\Big|\Big|\nabla\omega^{1/2}\Big|\Big|\Big|_{4,1}^4 + \Delta t^4 C\big(\tfrac{L}{\delta_M}\big)^3 \|\psi_{tt}\|_{4,1}^4\big\}. \qquad (4.37)
\end{aligned}
$$

where

$$C^* := \exp\Big\{\Delta t \sum_{n=0}^{M-1} \frac{\Big(\frac{L}{\delta_M}\Big)^3\big(C + C\|\nabla\omega^{n+\frac{1}{2}}\|_1^2 + C\|\omega^{n+\frac{1}{2}}\|_{k+1}^2\big)}{1-\Delta t\Big(\frac{L}{\delta_M}\Big)^3\big(C + C\|\nabla\omega^{n+\frac{1}{2}}\|_1^2 + C\|\omega^{n+\frac{1}{2}}\|_{k+1}^2\big)}\Big\}.$$

Thus we obtain (4.23) from the triangle inequality and (4.37).

For estimate (4.24), we apply (4.37) in

$$\begin{aligned}\|\nabla\big(\omega(t^{n+\frac{1}{2}}) - \omega_h^{n+\frac{1}{2}}\big)\|^2 &\le \|\nabla\big(\omega(t^{n+\frac{1}{2}}) - \omega^{n+\frac{1}{2}}\big)\|^2 + \|\nabla e_\perp^{n+\frac{1}{2}}\|^2 + \|\nabla e_h^{n+\frac{1}{2}}\|^2 \\ &\le \tfrac{\Delta t^3}{48}\int_{t^n}^{t^{n+1}} \|\omega_{tt}\|^2 dt + Ch^{2k}\|\omega^{n+\frac{1}{2}}\|_{k+1}^2 + \|\nabla e_h^{n+\frac{1}{2}}\|^2.\end{aligned}$$

□

Proof of Corollary 4.1. This follows directly from

$$\|\nabla(\psi(t^{n+\frac{1}{2}}) - \psi_h^{n+\frac{1}{2}})\|^2 \le \|\nabla\big(\psi(t^{n+\frac{1}{2}}) - \psi^{n+\frac{1}{2}}\big)\|^2 + \|\nabla E^{n+\frac{1}{2}}\|^2, \tag{4.38}$$

after we apply inequality (4.32), Lemma 4.11, Lemma 4.1, sum from $n = 0, ..., M-1$ and apply Theorem 4.1. □

4.5 Numerical experiments

In this section, we provide two different experiments to present the results obtained with the proposed scheme. In the first we validate our computational implementation and estimate convergence rates using an analytical solution. In the second, we simulate the more realistic and traditional double-gyre wind forcing benchmark. The software FreeFem++[40] was used to implement the proposed scheme. To solve the resulting nonlinear system, we used a Newtonian iteration at each timestep. In addition, a multi-frontal Gauss LU factorization implemented in the package UMFPACK (provided with FreeFem++ software) was used as our linear solver.

4.5.1 Convergence rates verification

Now we validate our computational implementation and confirm the convergence analysis presented above using a known analytical solution to estimate convergence rates. Considering the domain $\Omega = (0,1) \times (-1,1)$, $t \in (0,1]$, and for

$$\mathcal{F} = -\pi \exp\big[-\tfrac{2\pi^2}{Ro}\big(\tfrac{\delta_M}{L}\big)^3 t\big] \cos \pi x \sin \pi y,$$

the BV model has the following time dependent analytical solution (with homogeneous Dirichlet boundary conditions):

$$\begin{aligned} \psi &= \exp\big[-\tfrac{2\pi^2}{Ro}\big(\tfrac{\delta_M}{L}\big)^3 t\big] \sin \pi x \sin \pi y, \\ \omega &= 2\pi^2 \exp\big[-\tfrac{2\pi^2}{Ro}\big(\tfrac{\delta_M}{L}\big)^3 t\big] \sin \pi x \sin \pi y. \end{aligned}$$

Using this known solution, convergence rates were estimated through simulations using regular triangular meshes with $h = \frac{1}{4}$, $h = \frac{1}{8}$, $h = \frac{1}{16}$, $h = \frac{1}{32}$, $h = \frac{1}{64}$ and $h = \frac{1}{128}$, where h is the mesh-width. Figure 4.1 presents the coarsest mesh used in this experiment. In all cases we chose $\alpha = h$, and the timestep was chosen in terms of h in order to balance the error sources from the convergence theorem. That is, for P_1 elements and $\alpha = h$, the $L^2(0,T;H^1(\Omega))$ vorticity error and $L^\infty(0,T;H^1(\Omega))$ streamfunction error from the theorem are $O(\Delta t^2 + h)$, and thus we chose $\Delta t = \sqrt{h}$ (but slightly rounded so that Δt evenly divided T), and thus here we expect first order convergence in these norms as $\Delta t,\ h \to 0$. For P_2 and P_3 elements, we chose $\Delta t = h$ and $\Delta t = \sqrt{h^3}$, and expect second and third order convergence in these norms, respectively.

Tables 4.1, 4.2 and 4.3 present the errors and convergence rates obtained for decreasing h and Δt, using $\frac{\delta_M}{L} = 0.02$ and $Ro = 1.0$. From these tables we observe that the convergence of the numerical solution to the exact solution is optimal and agrees with the convergence theory presented above, for any choices of elements. We remind that, according to the convergence analysis presented in the latter section, for $N = 0$, the $L^2(0,T;H^1(\Omega))$ error is $O(h^k + h^2)$, for $N = 1$ the $L^2(0,T;H^1(\Omega))$

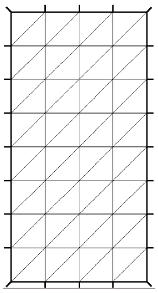

Figure 4.1: Mesh with $h = 1/4$ which corresponds to a grid with 4x8 squares.

error is $O(h^k + h^4)$ and for $N = 2$, the $L^2(0, T; H^1(\Omega))$ error is $O(h^k + h^6)$, which are confirmed by the convergence rates presented in the tables 4.1, 4.2 and 4.3. That is, provided a smooth solution, BV-α-$D1$ and BV-α-$D2$ will converge faster than the BV-α (D_0).

Element	h^{-1}	$\|w - w_h\|_{2,1}$	Rate	$\|w - w_h\|_{\infty,0}$	Rate	$\|\psi - \psi_h\|_{\infty,1}$	Rate
P_1	4	24.189		1.9868		2.1732	
($\Delta t = \sqrt{h}$)	8	12.376	0.97	0.61369	1.69	1.0117	1.10
	16	6.1545	1.01	0.16167	1.92	0.39299	1.36
	32	3.0614	1.01	0.041218	1.97	0.16706	1.23
	64	1.5259	1.00	0.010349	1.99	0.078803	1.08
	128	0.76181	1.00	0.002606	1.99	0.038768	1.02
P_2	4	6.3875		0.79216		1.7469	
($\Delta t = h$)	8	2.7885	1.20	0.28037	1.50	0.74236	1.23
	16	1.0076	1.47	0.078785	1.83	0.22523	1.72
	32	0.33616	1.58	0.020767	1.92	0.05949	1.92
	64	0.10476	1.68	0.0052803	1.98	0.015086	1.98
	128	0.02967	1.82	0.0013261	1.99	0.003785	1.99
P_3	4	7.5925		0.88577		1.7349	
($\Delta t = \sqrt{h^3}$)	8	3.6645	1.05	0.28925	1.61	0.7405	1.23
	16	1.1144	1.72	0.079633	1.86	0.22489	1.72
	32	0.36152	1.62	0.020844	1.93	0.059414	1.92
	64	0.10877	1.73	0.005286	1.98	0.015067	1.98

Table 4.1: Convergence rates for BV-α-D_0 ($N = 0$) model with $\frac{\delta_M}{L} = 0.02$ and $Ro = 1.0$.

Element	h^{-1}	$\|w - w_h\|_{2,1}$	Rate	$\|w - w_h\|_{\infty,0}$	Rate	$\|\psi - \psi_h\|_{\infty,1}$	Rate
P_1	4	23.976		1.9716		1.6753	
$(\Delta t = \sqrt{h})$	8	12.202	0.97	0.54573	1.85	0.66267	1.34
	16	6.1025	1.00	0.14161	1.95	0.30999	1.10
	32	3.049	1.00	0.036064	1.97	0.15426	1.01
	64	1.5232	1.00	0.0090863	1.99	0.077105	1.00
	128	0.76126	1.00	0.0022755	2.00	0.038553	1.00
P_2	4	4.5291		0.36528		0.9807	
$(\Delta t = h)$	8	1.1333	2.00	0.059717	2.61	0.18122	2.44
	16	0.27668	2.03	0.0061093	3.29	0.020044	3.18
	32	0.081142	1.77	0.00058915	3.37	0.0031885	2.65
	64	0.025527	1.67	8.0004e-5	2.88	7.497e-4	2.09
	128	0.0071309	1.84	9.5087e-6	3.07	1.8665e-4	2.01
P_3	4	4.4873		0.38391		0.95793	
$(\Delta t = \sqrt{h^3})$	8	0.86042	2.38	0.058728	2.71	0.17452	2.46
	16	0.077881	3.47	0.0055599	3.40	0.016097	3.44
	32	0.0068168	3.51	0.00039313	3.82	0.0011237	3.84
	64	0.00052529	3.70	2.5343e-5	3.96	7.2312e-5	3.96

Table 4.2: Convergence rates for BV-α-D_1 ($N = 1$) model with $\frac{\delta_M}{L} = 0.02$ and $Ro = 1.0$.

4.5.2 Double gyre wind experiment

As presented in [37, 47], when the BV equations are forced in a rectangular basin by a double gyre wind forcing on the ocean surface and dissipation is weak, despite the instantaneous streamfunction field being highly variable, time averaged streamfunction field presents a well defined four gyre pattern. This pattern is composed by two inner gyres, which are driven by the wind, and two extremal gyres, at the northern and southern ends of the basin, which are driven by the eddy flux of potential vorticity. Moreover, according to [47], the extremal gyres are not a linear effect, but a result of a mean balance between the eddy flux of potential vorticity and wind forcing being susceptible to destruction by excessive dissipation.

The double gyre forcing experiment has been used as a model of more realistic ocean dynamics in several studies, and recently it has been used as a bench-

Element	h^{-1}	$\|w-w_h\|_{2,1}$	Rate	$\|w-w_h\|_{\infty,0}$	Rate	$\|\psi-\psi_h\|_{\infty,1}$	Rate
P_1	4	23.906		1.9666		1.4363	
$(\Delta t=\sqrt{h})$	8	12.184	0.97	0.5435	1.86	0.6239	1.20
	16	6.1012	1.00	0.14125	1.94	0.3086	1.02
	32	3.0489	1.00	0.03604	1.97	0.15422	1.00
	64	1.5232	1.00	0.0090846	1.99	0.077104	1.00
	128	0.76126	1.00	0.0022754	2.00	0.038553	1.00
P_2	4	4.5291		0.36528		0.9807	
$(\Delta t=h)$	8	1.1333	2.00	0.059717	2.61	0.18122	2.44
	16	0.27668	2.03	0.0061093	3.29	0.020044	3.18
	32	0.081142	1.77	0.00058915	3.37	0.0031885	2.65
	64	0.025527	1.67	8.0004e-5	2.88	7.497e-4	2.09
	128	0.0071309	1.84	9.5087e-6	3.07	1.8665e-4	2.01
P_3	4	4.4873		0.38391		0.95793	
$(\Delta t=\sqrt{h^3})$	8	0.86042	2.38	0.058728	2.71	0.17452	2.46
	16	0.077881	3.47	0.0055599	3.40	0.016097	3.44
	32	0.0068168	3.51	0.00039313	3.82	0.0011237	3.84
	64	0.00052529	3.70	2.5343e-5	3.96	7.2312e-5	3.96

Table 4.3: Convergence rates for BV-α-D_2 ($N=2$) model with $\frac{\delta_M}{L}=0.02$ and $Ro=1.0$.

mark test to analyze new techniques to deal with turbulence in geophysical flows [81, 47, 100]. In the double gyre wind forcing experiment, the wind effect on the ocean's surface is prescribed setting $\mathcal{F}=\mathcal{F}_0\sin(\pi y)$ with $\mathcal{F}_0=1$.

In this section we follow [100] and adopt the standard LES methodology: first we run a high resolution simulation with BV-model (no treatment of turbulence). Next, we run several experiments in a coarse resolution mesh with BV model and BV-α-Deconvolution model and compare them with the high resolution BV model solution as reference.

Following the experiments presented in [37, 81, 47, 100], we run simulations in different regular triangular meshes in the dimensionless rectangular domain $(0,1)\times(-1,1)$ using P_2 finite elements and consider meshes with different resolutions setting $h={}^1\!/\!_4$ (which corresponds to a grid with 4x8 squares), ${}^1\!/\!_8$ (8x16), ${}^1\!/\!_{16}$

(16x32), $^1/_{32}$ (32x64) and $^1/_{64}$ (64x128) where h is the mesh-width. In the remainder of this section we will refer to theses meshes as $n \times 2n$ for $n = 4, 8, 16, 32, 64$.

Experiments were made starting from $t = 0$ up until $t = 100$ as in [100] and we adopt $\Delta t = 0.001$ in all simulations. In this and in the next section we present figures of the average fields of streamfunction (ψ) and potential vorticity (given by $q = Ro\omega + y$), calculated using results from $t = 20$ until 100 as in [100]. For the double gyre wind forcing experiment we considered two interesting cases: i) $^{\delta_M}/_L = 0.02$ and $Ro = 0.0016$ (which is presented in [100]) and ii) $^{\delta_M}/_L = 0.01$ and $Ro = 0.0002$.

4.5.2.1 Experiment for $Ro = 0.0016$

First, we present the results found for the double gyre experiment considering the same case as in [100], that is, $Ro = 0.0016$ and $\left(\frac{\delta_M}{L}\right)^3 = 0.02$. In Figures 4.2(a) and 4.3(a) we present respectively the streamfunction and vorticity solutions obtained in the high resolution (64×128 mesh) experiment using the BV model. In these figures we can see that the streamfunction and vorticity solutions obtained in this experiment are very similar with the results presented in [100] in their DNS experiment.

As reported in [100, 47], decreasing the mesh resolution, the streamfunction solution obtained with the BV model degenerates in two gyres as it can be seen in Figure 4.2(b). In this case, using the BV-α model ($\alpha = \frac{1}{12}$) we can recover the four gyre pattern (Figure 4.2(c)), but the streamfunction is intensified in comparison with the streamfunction solution obtained in the high resolution experiment (Figure 4.2(a)) and the vorticity field is very noisy (Figure 4.3(c)). However, when we increase the order in the deconvolution operator (Figures 4.2(d), 4.2(e) and 4.2(f)), we can obtain more accurate solutions in comparison with the BV and BV-α model. In this figures, clearly we can see that the larger is the deconvolution order, the more accurate is the BV-α-deconvolution solution. In the BV-α-deconvolution vorticity solution we observe the same pattern (Figure 4.2(d), 4.2(e) and 4.2(f)). This improvement is related to the consistency error present in the BV-α-deconvolution model that, according to our convergence analysis, has order $2N+2$, which for larger values of N permits more accuracy in the solution.

In Table 4.4 we also present run times for the BV model in the fine (64×128) and coarse mesh (4×8) and for BV-α-Deconvolution in the coarse mesh (4×8) are presented. We see that, although the computational time is increased by increasing the deconvolution order in the BV-α-Deconvolution model, it is significant faster than solving the BV model in the fine mesh.

Fine	Coarse	alpha (D_0)	BV-α-D_1	BV-α-D_2	BV-α-D_3
9.82e5	2.50e3	4.5e3	9.4e3	1.73e4	2.98e4

Table 4.4: Run times (in seconds) obtained for $Ro = 0.0016$ in the fine (64×128) and coarse (4×8) mesh with the BV model and in the coarse mesh (4×8) with BV-α-Deconvolution model. The experiments were made in a Intel® Core™ i7 3.70 GHz.

4.5.2.2 Experiment for $Ro = 0.0002$

Now we present the results obtained for the double gyre experiment considering $Ro = 0.0002$ and $\left(\frac{\delta_M}{L}\right)^3 = 0.01$. Figures 4.4(a) and 4.5(a) present the streamfunction and vorticity solutions obtained in the high resolution mesh (50×100 mesh). We observe that in this experiment, the solution presents a distinct six gyre pattern. Futhermore, as we can see in Figure 4.4(b), this pattern is also susceptible to the mesh resolution. That is, when we simulate this experiment using the BV model in a coarse 8×16 mesh the six gyre pattern degenerates into two gyres. Moreover, the vorticity field produced in the coarse mesh becomes noisy.

Using the BV-α ($\alpha = \frac{1}{8}$) model we recover the four gyre pattern (Figure 4.4(c)), but not the six gyre pattern observed in the high resolution solution and, as for $Ro = 0.0016$, it is intensified compared to the high resolution solution. On the other hand, the streamfunction solutions produced with the BV-α-Deconvolution model for $N \geq 1$ are less intensified (Figures 4.4(d), 4.4(e) and 4.4(f)). Moreover, for $N = 3$ the BV-α-deconvolution model recovers the six gyre pattern (Figure 4.4(f)). In the vorticity field (Figures 4.5(d), 4.5(e) and 4.5(f)) we observe that, increasing the deconvolution order, the solution becomes less noisy and more similar to the high resolution solution. Computational times for the BV model in the fine (50×100) and coarse mesh (8×16) and for BV-α-Deconvolution in the coarse mesh (8×16) are presented in Table 4.5. We see that, although the computational time is increased by increasing the deconvolution order in the BV-α-Deconvolution model, it is significant faster than solving the BV model in the fine mesh.

Again, the results presented in this experiment corroborate the convergence analysis presented herein: increasing the deconvolution order makes solutions more accurate.

Fine	Coarse	alpha (D_0)	BV-α-D_1	BV-α-D_2	BV-α-D_3
9.82e5	8.22e3	3.31e4	4.92e3	9.06e4	1.57e5

Table 4.5: Run times (in seconds) obtained for $Ro = 0.0016$ in the fine (50×100) and coarse (4×8) mesh with the BV model and in the coarse mesh (4×8) with BV-α-Deconvolution model. The experiments were made in a Intel® Core™ i7 3.70 GHz.

4.6 Conclusion and final remarks

We have proposed and analysed an FEM scheme for the BV-α-Deconvolution model of geophysical flows that regularizes the flow and improves accuracy compared to the BV-α model. We proved that the scheme is both unconditionally stable and optimally convergent. Furthermore, we confirmed the predicted convergence rates through numerical simulations. Finally, we tested the BV-α-Deconvolution model in the traditional double gyre wind experiment, which is a more realistic model of the ocean dynamics, and found very good results. In this test we corroborate that increasing the deconvolution order in the model produces a more accurate solution.

In the present article we tested the BV-α-Deconvolution in a situation in which only the barotropic mode of ocean dynamics is present. As in [99], in a future work we intend to extend the BV-α-Deconvolution model for two layers in order apply this regularization to a more baroclinic situation. That will be an important step in the direction of true ocean dynamics.

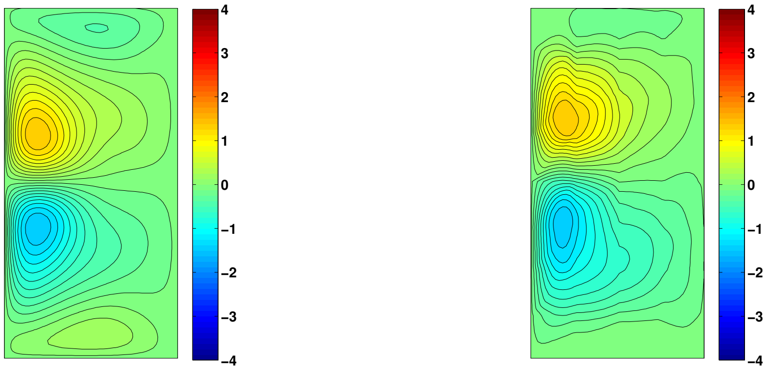

(a) Str. func. - 64x128

$\psi_{min} = -1.39, \psi_{max} = 1.39$

(b) Str. func. - 4x8

$\psi_{min} = -1.40, \psi_{max} = 1.46$

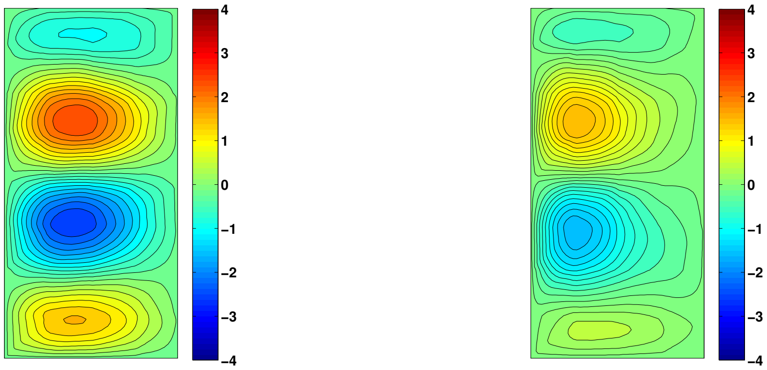

(c) Str. func. - 4x8 - α

$\psi_{min} = -2.58, \psi_{max} = 2.56$

(d) Str. func. - 4x8 - D_1

$\psi_{min} = -1.59, \psi_{max} = 1.63$

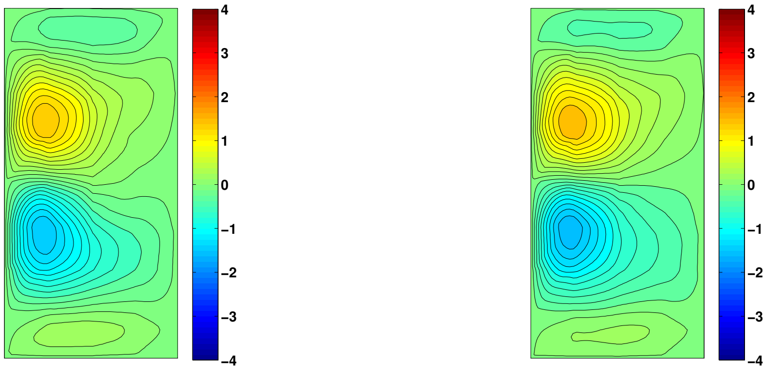

(e) Str. func. - 4x8 - D_2

$\psi_{min} = -1.48, \psi_{max} = 1.43$

(f) Str. func. - 4x8 - D_3

$\psi_{min} = -1.60, \psi_{max} = 1.52$

Figure 4.2: Streamfunction fields in the experiment with $^{\delta_M}/_{L} = 0.02$ and $Ro = 0.0016$ for (a) the high resolution BV model solution, (b) coarse (4×8) BV model solution and coarse (4×8) (c) BV-α, (d) BV-α-D_1, (e) BV-α-D_2 and (f) BV-α-D_3.

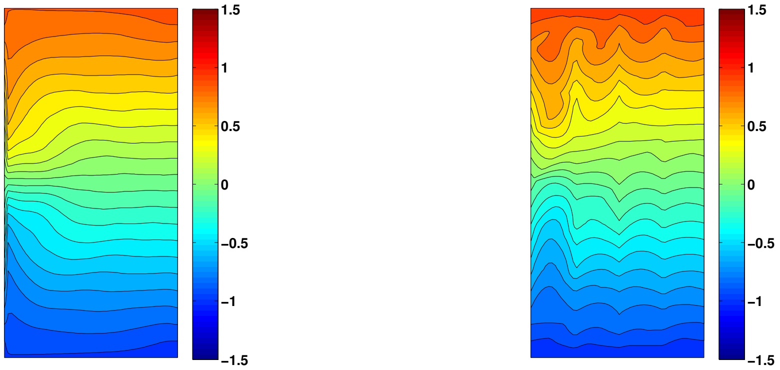

(a) Vort. - 64x128 (b) Vort. - 4x8

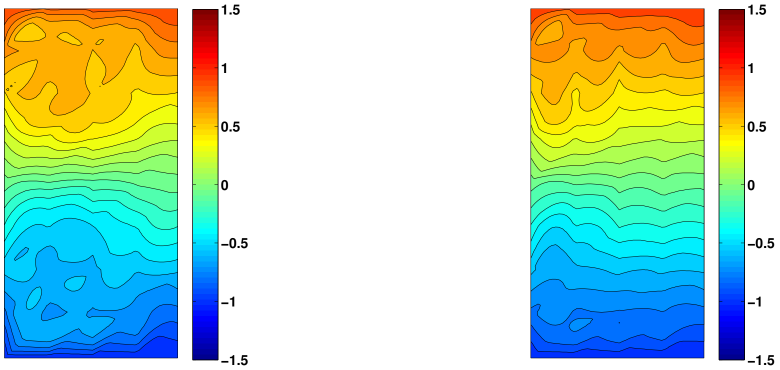

(c) Vort. - 4x8 - α (d) Vort. - 4x8 - D_1

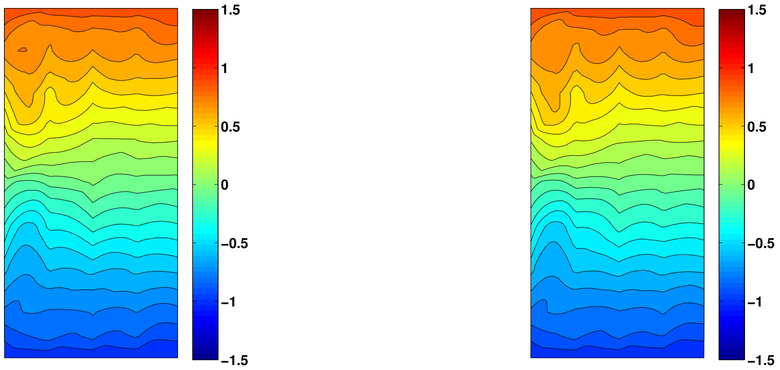

(e) Vort. - 4x8 - D_2 (f) Vort. - 4x8 - D_3

Figure 4.3: Vorticity fields in the experiment with ${}^{\delta_M}\!/_{L} = 0.02$ and $Ro = 0.0016$ for (a) the high resolution BV model solution, (b) coarse (4×8) BV model solution and coarse (4×8) (c) BV-α, (d) BV-α-D_1, (e) BV-α-D_2 and (f) BV-α-D_3.

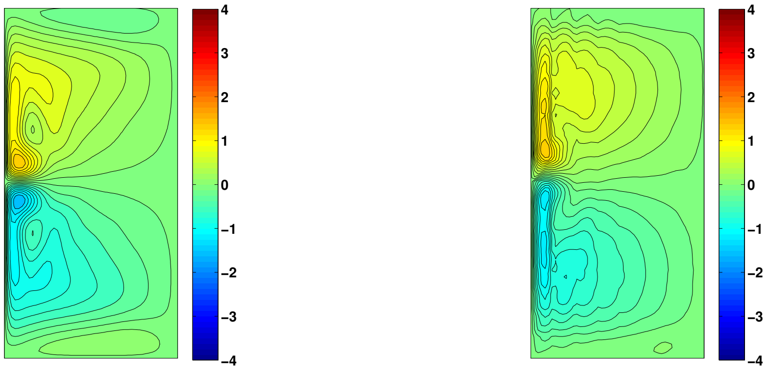

(a) Str. func. - 50x100

$\psi_{min} = -1.51, \psi_{max} = 1.50$

(b) Str. func. - 8x16

$\psi_{min} = -1.22, \psi_{max} = 1.41$

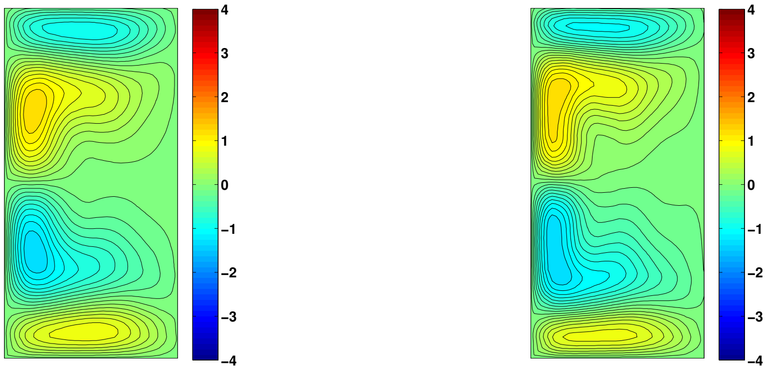

(c) Str. func.- 8x16 - α

$\psi_{min} = -1.34, \psi_{max} = 1.34$

(d) Str. func.- 8x16 - D_1

$\psi_{min} = -1.25, \psi_{max} = 1.30$

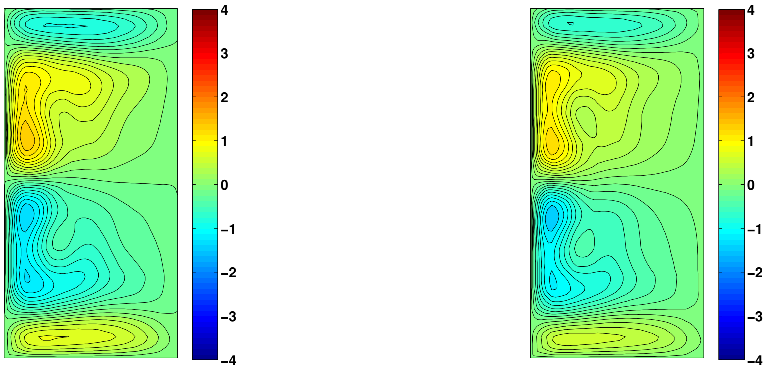

(e) Str. func.- 8x16 - D_2

$\psi_{min} = -1.31, \psi_{max} = 1.42$

(f) Str. func.- 8x16 - D_3

$\psi_{min} = -1.37, \psi_{max} = 1.37$

Figure 4.4: Streamfunction fields in the experiment with ${}^{\delta_M}/_{L} = 0.01$ and $Ro = 0.0002$ for (a) the high resolution BV model solution, (b) coarse (4×8) BV model solution and coarse (4×8) (c) BV-α, (d) BV-α-D_1, (e) BV-α-D_2 and (f) BV-α-D_3.

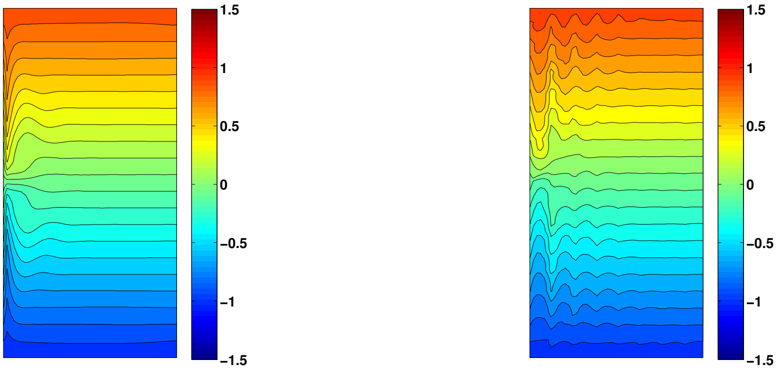

(a) Vort. - 50x100 (b) Vort. - 8x16

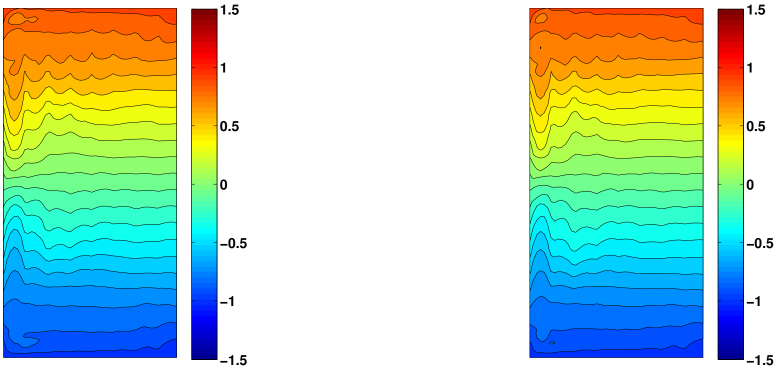

(c) Vort. - 8x16 - α (d) Vort. - 8x16 - D_1

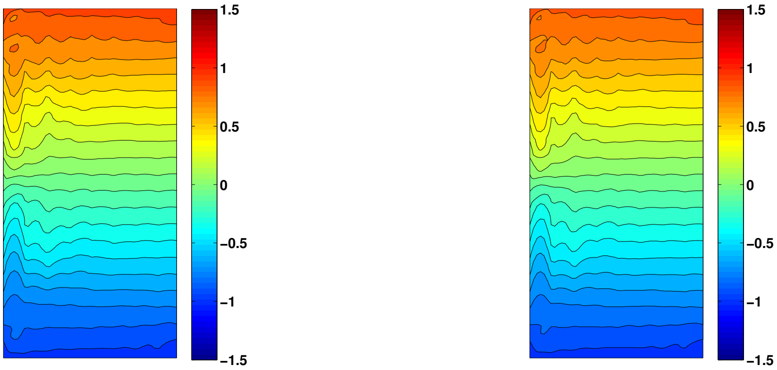

(e) Vort. - 8x16 - D_2 (f) Vort. - 8x16 - D_3

Figure 4.5: Vorticity fields in the experiment with ${}^{\delta_M}\!/\!_L = 0.01$ and $Ro = 0.0002$ for (a) the high resolution BV model solution, (b) coarse (8x16) BV model solution and coarse (8x16) (c) BV-α, (d) BV-α-D_1, (e) BV-α-D_2 and (f) BV-α-D_3.

5 REGULARIZED BOUSSINESQ MODEL[1]

5.1 Introduction

Density currents are one of the most important kind of geophysical flow. They can be defined as flows forced by the buoyant force due to density gradients in the fluid. In atmosphere, important examples are the large scale Hadley and Walker cells in the general atmospheric circulation and the small scale thunderstorms and seabreeze. In the ocean, examples are the large scale Global Conveyor Belt resulting from the thermohaline circulation and the small/meso scale upwelling/downwelling mechanism as well as seafloor turbidity currents. Moreover, density currents are also quite important in engineering applications.

Despite of the relevance of density currents, they very often cannot be fully represented in simulations because several geophysical models adopt the hydrostatic approximation. Only recently, studies using non-hydrostatic models have been performed. In [84] a density current was simulated in a model in the vorticity-streamfunction variables. In [90], results produced by a non-hydrostatic model were compared with density current data from the Red Sea. Also, threedimensional simulations were performed in [86]. More recently, other aspects involving density current modeling has been investigated in non-hydrostatic models, e. g., the effect of generalized coordinates [43], topography [85, 48], vertical mixing [16, 50], boundary conditions [7] and domain geometry [13, 49].

---

[1] We are very grateful to Professor Leo G. Rebholz for his thoughts and advices on the results presented in this chapter.

One of the most commonly used models to represent density currents is the Boussinesq model given by

$$\frac{\partial u}{\partial t} - u \times \nabla \times u - Re^{-1}\Delta u + \nabla p - RiT\hat{k} = f, \tag{5.1a}$$

$$\nabla \cdot u = 0, \tag{5.1b}$$

$$\frac{\partial T}{\partial t} + u \cdot \nabla T - (RePr)^{-1}\Delta T = 0. \tag{5.1c}$$

where u is velocity, p is pressure, T is temperature, f is a given force and Re, Ri and Pr are the Reynolds, Richardson and Prantdl number, respectively.

Simulations using non-hydrostatic models, such as those for density current, demand a large computational cost and are restrict only to modest complexity flows, i.e., low Reynolds numbers. Thus, several studies have been done aimed at providing methods in order to reduce the computational cost when simulating this kind of flow. Some methods already studied were mixing parametrization [16], large-eddy simulation (LES) [89, 87, 88, 49, 6], adaptive meshing [46] and Proper Orthogonal Decomposition reduced order modeling [70, 98].

In this chapter, an alternative approach, called regularized modeling, is studied aimed at reducing the computational cost in simulations with the Boussinesq model. The Navier-Stokes-α (NS-α) model is an example of regularization model which has interesting mathematical, physical and computational properties (see [76] and references therein). The most important property of NS-α probably is that it allows a significant reduction in the degrees of freedom in simulations. In the NS-α model, the nonlinearity is altered so that the flow at length scales that are smaller than the alpha length scale are nonlinearly removed by motions at the larger scales. Thus, the flow can be computationally solved with a significant decrease in the model degrees of freedom in comparison to the original NS equations, and there is no need to introduce additional dissipative terms or increase the viscosity coefficient. The NS-ω [65, 75], Leray-α [64, 9] and Modified-Leray-α [51] are also regularizations of the Navier-Stokes equations which differ from the NS-α by a modification in the nonlinearity. They have been recently tested and enjoyed success in simulations.

NS-α, NS-ω, Leray-α and Modified-Leray-α are respectively defined to be

$$\begin{aligned} u_t - \overline{u} \times (\nabla \times u) + \nabla p - \nu \Delta u &= f, \\ u_t - u \times (\nabla \times \overline{u}) + \nabla p - \nu \Delta u &= f, \\ u_t - \overline{u} \cdot \nabla u + \nabla p - \nu \Delta u &= f, \\ u_t - u \cdot \nabla \overline{u} + \nabla p - \nu \Delta u &= f, \end{aligned}$$

where ν is the viscosity, f is a forcing and $\overline{u}$ is the filtered velocity given by

$$\overline{u} := Fu := (-\alpha^2 \Delta + I)^{-1} u.$$

In light of the above, the objective of this chapter is to study regularized versions of the Boussinesq model, namely, Boussinesq-α, Boussinesq-ω, Boussinesq-Leray and Modified-Boussinesq-Leray, through numerical analysis and simulations. We believe the advantage of regularization models over other approaches is because it combine simpler implementation and smaller computational cost with sound mathematical and physical fundamentals.

In addition, we take the cumulative existing experience with α models and use it in their Boussinesq variations. For instance, in wall bounded flows we cannot guarantee a non-divergent filtered velocity, hence a natural technique is to introduce a Langrange multiplier in the filter equation in order to allow the physically important incompressibility contraint [76]. Moreover, in [63] it is shown that the velocity error in the Navier-Stokes equations scales as *velocity error* $\approx$ *Re*$\times$*pressure error* and, if the mesh is not sufficiently fine, large pressure errors can produce large velocity errors. This problem can be fixed using the modified grad-div stabilization proposed in [76], which is a modification of the grad-div technique used in [19] for the Navier-Stokes equations, but that avoids stability problems in regularized models. Another important technique applied in alpha models to reduce computional cost is the Baker extrapolation in the nonlinear term. This technique consists in linearly or quadratically extrapolating one of the velocities in the nonlinear term in order to linearize the equations, avoiding the fixed point iteration necessary when solving the nonlinear system. In a recent study, [52] shows that, with a small modification in the Baker extrapolation, interesting advantages can be gained both from the analytical and computational viewpoint. Lastly, from the filter equation it is clearly possible to see that for any alpha model we cannot expect accuracy better than $O(\alpha^2)$ from the model itself, even before any computational error is introduced. In [93, 94] a fix is proposed based in the van Cittert method of approximate deconvolution, which increase the consistency error in the Navier-Stokes-α model from $O(\alpha^2)$ to $O(\alpha^{2N+2})$ where N is the order of deconvolution operator. Besides, in [63, 94, 76, 9] it is shown that approximate deconvolution also improves solution even in situations in which the model error is not dominated by the consistency error. In this chapter, the regularized versions of the Boussinesq model, along with the above mentioned techniques, are mathematically analysed and computationally tested with respect to their ability to provide accurate solutions to density currents.

The chapter is outlined as follows: Section 5.2 presents notation and some preliminary results. In Section 5.3 an algorithm for a general regularized Boussinesq model is proposed and studied with respect to its stability and convergence. Numerical experiments are presented in Section 5.4. Lastly, conclusions and final remarks are summarized in Section 5.5.

5.2 The finite element scheme and preliminaries

Let $\Omega \subset \mathbb{R}^d$ ($d = 2$ or 3) be a polyhedral domain and τ_h be a regular discretization of Ω. Let H^1 be the Sobolev space $W_2^1(\Omega)$ and $X = H_0^1$ its subspace with zero boundary condition. Let Y_h be a continuous finite element (FE) space with kth degree polynomials on each element of the triangulation τ_h, and $(X_h, Q_h) \subset (H_0^1(\Omega)^d, L_0^2(\Omega))$ be a velocity-pressure space given by $X_h := \{v \in C^0 \cap P_k(e) \forall e \in \tau_h\}$ and $Q_h := \{v \in C^0 \cap P_{k-1}(e) \forall e \in \tau_h\}$ satisfying the discrete inf-sup condition [39]. Denote by $\langle \cdot, \cdot \rangle$ and $\| \cdot \|$ respectively the inner product and norm in $L^2(\Omega)$, and $\|\cdot\|_k$ for the norm in the H^k space. The subspace $V_h = \{v_h \in X_h : \langle \nabla \cdot v_h, q_h \rangle = 0 \ \forall q_h \in Q_h\}$ of X_h will also be helpful in the subsequent analysis.

For continuous in time functions, we denote for $1 \le m < \infty$, $\|f\|_{m,k} := \left\{ \int_0^T \|f(t,\cdot)\|_k^m dt \right\}^{1/m}$ and, for the discrete case, we denote $|||f|||_{\infty,k} := \operatorname{ess\,sup}_{0 \le n \le M} \|f^n\|_k$,, $\|f^{1/2}\|_{m,k} := \left\{ \sum_{n=0}^M \|f(t^{n+\frac{1}{2}})\|_k^m dt \right\}^{1/m}$ and $|||f^{1/2}|||_{m,k} := \left\{ \sum_{n=0}^M \|f^{n+\frac{1}{2}}\|_k^m dt \right\}^{1/m}$.

The following approximation estimates are also useful ([35, 11, 39])

$$\inf_{v \in X_h} \|u - v\| \le Ch^{k+1}|u|_{k+1}, \ u \in (H^{k+1}(\Omega))^d,$$

$$\inf_{v \in X_h} \|u - v\|_1 \le Ch^{k}|u|_{k+1}, \ u \in (H^{k+1}(\Omega))^d,$$

$$\inf_{r \in Q_h} \|p - r\| \le Ch^{s+1}|u|_{s+1}, \ u \in (H^{s+1}(\Omega))^d.$$

We also make use of the four trilinear forms:

Definition 5.1. *Let* $\beta \in [0,1]$ *and define* $a_1, a_1^*, a_2, a_\beta : X \times X \times X \longrightarrow \mathbb{R}$*, by*

$$\begin{aligned}
a_1(u,v,w) &:= \langle u \cdot \nabla v, w \rangle, \\
a_1^*(u,v,w) &:= \tfrac{1}{2}\left[a_1(u,v,w) - a_1(u,w,v)\right], \\
a_2(u,v,w) &:= \langle (\nabla \times u) \times v, w \rangle, \\
a_\beta(u,v,w) &:= \beta a_2(u,v,w) + (1-\beta) a_1^*(u,v,w).
\end{aligned}$$

The following estimates hold for the above trilinear forms:

Lemma 5.1. *Let* $u, v, w \in H^1$ *and* $\beta \in [0,1]$*. Then*

$$\begin{aligned}
|a_1^*(u,v,w)| &\le A_1(\Omega)\|\nabla u\|\|\nabla v\|\|\nabla w\|, \\
|a_1^*(u,v,w)| &\le A_2(\Omega)\|u\|^{1/2}\|\nabla u\|^{1/2}\|\nabla v\|\|\nabla w\|, \\
|a_2(u,v,w)| &\le B_1(\Omega)\|\nabla u\|\|\nabla v\|\|\nabla w\|, \\
|a_2(u,v,w)| &\le B_2(\Omega)\|u\|^{1/2}\|\nabla u\|^{1/2}\|\nabla v\|\|\nabla w\|, \\
|a_\beta(u,v,w)| &\le \sigma_1(\Omega)\|\nabla u\|\|\nabla v\|\|\nabla w\|, \\
|a_\beta(u,v,w)| &\le \sigma_2(\Omega)\|u\|^{1/2}\|\nabla u\|^{1/2}\|\nabla v\|\|\nabla w\|.
\end{aligned}$$

Proof. The first and second estimates are well-known and follow from Hölder and Ladyzhenskaya inequalities (see [60]). The third also follows from Hölder and Ladyzhenskaya inequality and the Sobolev embedding Theorem, where we also made use of $\|\nabla \times u\| \leq \|\nabla u\|$ for $u \in H_0^1$. The fourth follows from Hölder with $p = 2$, $q = 3$ and $r = 6$, interpolation inequality for L^p spaces and Ladyzhenskaya inequality. For the fifth, we made use of $[a \times b] \cdot c = [c \times b] \cdot a$ and that the curl is self-adjoint in X, i.e,

$$\begin{aligned}|\langle(\nabla \times u) \times v, w\rangle| &= |\langle w \times v, \nabla \times u\rangle| = |\langle\nabla \times (w \times v), u\rangle| \\ &\leq |\langle v \cdot \nabla w, u\rangle| + |\langle w \cdot \nabla v, u\rangle| + |\langle(\nabla \cdot v)w, u\rangle| + |\langle(\nabla \cdot w)v, u\rangle|\end{aligned}$$

where we used the identity $\nabla \times (a \times b) = a \cdot \nabla b - b \cdot \nabla a + (\nabla \cdot a)b + (\nabla \cdot b)a$. The result follows after applying Hölder with $p = 2$, $q = 3$ and $r = 6$, interpolation inequality for L^p spaces and Ladyzhenskaya inequality. The last two identities follow from the previous, defining $\sigma_1(\Omega) := \max\{B_1(\Omega), A_1(\Omega)\}$ and $\sigma_2(\Omega) := \max\{B_2(\Omega), A_3(\Omega)\}$. □

Also, Taylor expansion with integral remainder gives [60]:

Lemma 5.2. *Let $u \in C^0(t^n, t^{n+1}; L^2(\Omega))$ and twice differentiable in time with $u_{tt} \in L^2((t^n, t^{n+1}) \times \Omega)$. Then*

$$\begin{aligned}\|u^{n+\frac{1}{2}} - u(t^{n+\frac{1}{2}})\|^2 &\leq \tfrac{1}{48}(\Delta t)^3 \int_{t^n}^{t^{n+1}} \|u_{tt}\|^2 dt, \\ \|u^{n+\frac{1}{2}} - (2u^{n-\frac{1}{2}} - u^{n-\frac{3}{2}})\|^2 &\leq (\Delta t)^3 \int_{t^{n-1}}^{t^{n+1}} \|u_{tt}\|^2 dt.\end{aligned}$$

If $u_{ttt} \in L^2((t^n, t^{n+1}) \times \Omega)$ then

$$\left\|\tfrac{u^{n+1} - u^n}{\Delta t} - u_t(t^{n+\frac{1}{2}})\right\|^2 \leq \tfrac{1}{1280}(\Delta t)^3 \int_{t^n}^{t^{n+1}} \|u_{ttt}\|^2 dt.$$

If $\nabla u \in C^0(t^n, t^{n+1}; L^2(\Omega))$ and $\nabla u_{tt} \in L^2((t^n, t^{n+1}) \times \Omega)$ then

$$\|\nabla u^{n+\frac{1}{2}} - \nabla u(t^{n+\frac{1}{2}})\|^2 \leq \tfrac{1}{48}(\Delta t)^3 \int_{t^n}^{t^{n+1}} \|\nabla u_{tt}\|^2 dt.$$

where $u^{n+\frac{1}{2}} = \frac{u^{n+1} + u^n}{2}$ and $u(t^{n+\frac{1}{2}}) = u({(t^{n+1} + t^n)}/{2})$.

5.2.1 Discrete filtering

Following [76], given $w \in L^2(\Omega)$ and parameters $\alpha, \kappa, Re > 0$, discrete filtering $F_h : L^2(\Omega) \to X_h$ is defined as the unique solution $F_h w = \overline{w}^h \in X_h$ and $\lambda_h \in Q_h$, such that $\forall \{v_h, q_h\} \in X_h \times Q_h$,

$$\alpha^2 \left(\langle \nabla \overline{w}^h, \nabla v_h \rangle + \kappa Re \langle \nabla \cdot \overline{w}^h, \nabla \cdot v_h \rangle \right) - \langle \lambda_h, \nabla \cdot v_h \rangle + \langle q_h, \nabla \cdot \overline{w}^h \rangle + \langle \overline{w}^h, v_h \rangle = \langle w, v_h \rangle.$$

Given $w \in X$ and parameters $\kappa, Re > 0$, the modified discrete Laplacian operator $\tilde{\Delta}_h : X \to V_h$ (see [76]) is the unique solution $\tilde{\Delta}_h w$ such that:

$$\langle \tilde{\Delta}_h w, v_h \rangle = -\langle \nabla w, \nabla v_h \rangle - \kappa Re \langle \nabla \cdot w, \nabla \cdot v_h \rangle, \, \forall v_h \in V_h.$$

Thus, $F_h : L^2(\Omega) \to V_h$ can be defined equivalently as $\overline{w}^h \in V_h$ such that

$$-\alpha^2 \langle \tilde{\Delta}_h \overline{w}^h, v_h \rangle + \langle \overline{w}^h, v_h \rangle = \langle w, v_h \rangle \; \forall v_h \in V_h. \tag{5.3}$$

The following equalities involving F_h and $\tilde{\Delta}_h$ hold:

Lemma 5.3.

$$\begin{aligned} \langle \tilde{\Delta}_h u_h, v_h \rangle &= \langle u_h, \tilde{\Delta}_h v_h \rangle \; \forall u_h, v_h \in X_h, \\ \langle F_h u, v \rangle &= \langle u, F_h v \rangle \; \forall u, v \in X, \\ \tilde{\Delta}_h F_h u_h &= F_h \tilde{\Delta}_h u_h \; \forall u_h \in V_h, \\ F_h P_h u &= F_h u \; \forall u \in X. \end{aligned}$$

That is, $\tilde{\Delta}_h$ is self-adjoint and commutes with F_h in X_h and F_h is self-adjoint in X.

Proof. For the first, given $u_h, v_h \in X_h$ and using the definition of $\tilde{\Delta}_h$ we have

$$\langle \tilde{\Delta}_h u_h, v_h \rangle = -\langle \nabla u_h, \nabla v_h \rangle - \kappa Re \langle \nabla \cdot u_h, \nabla \cdot v_h \rangle = \langle u_h, \tilde{\Delta}_h v_h \rangle.$$

For the second, given $u, v \in X$, using the filter equation, $F_h u \in V_h$ satisfies

$$\alpha^2 \langle \nabla F_h u, \nabla F_h v \rangle + \alpha^2 \kappa Re \langle \nabla \cdot F_h u, \nabla \cdot F_h v \rangle + \langle F_h u, F_h v \rangle = \langle u, F_h v \rangle, \qquad (5.4)$$

where we chose $v_h = F_h v \in V_h$.

On the other hand, using again the filter equation, $F_h v \in V_h$ satisfies

$$\alpha^2 \langle \nabla F_h v, \nabla F_h u \rangle + \alpha^2 \kappa Re \langle \nabla \cdot F_h v, \nabla \cdot F_h u \rangle + \langle F_h v, F_h u \rangle = \langle v, F_h u \rangle, \qquad (5.5)$$

where, in the above equation, we chose $v_h = F_h u \in V_h$. Now, subtracting (5.4) from (5.5) gives the result.

For the third, the filter equation gives

$$-\alpha^2 \langle \tilde{\Delta}_h F_h u_h, v_h \rangle + \langle F_h u_h, v_h \rangle = \langle u_h, v_h \rangle \ \forall u_h, v_h \in V_h.$$

Because F_h and $\tilde{\Delta}_h$ are self-adjoint in V_h, the filter equation gives

$$-\alpha^2 \langle F_h \tilde{\Delta}_h u_h, v_h \rangle + \langle F_h u_h, v_h \rangle = \langle u_h, v_h \rangle \ u_h, v_h \in V_h.$$

where we also use that $u_h, v_h \in V_h$ are arbitrary. Subtracting both equations gives

$$-\alpha^2 \langle (\tilde{\Delta}_h F_h - F_h \tilde{\Delta}_h) u_h, v_h \rangle = 0,$$

which gives the result, after we choose $v_h = (\tilde{\Delta}_h F_h - F_h \tilde{\Delta}_h) u_h$.

Finally, for the last one, given $u \in X$, we consider respectively filtering u and $P_h u$, $\forall v_h \in V_h$,

$$\alpha^2 \left(\langle \nabla F_h u, \nabla v_h \rangle + \kappa Re \langle \nabla \cdot F_h u, \nabla \cdot v_h \rangle \right) + \langle F_h u, v_h \rangle = \langle u, v_h \rangle,$$
$$\alpha^2 \left(\langle \nabla F_h P_h u, \nabla v_h \rangle + \kappa Re \langle \nabla \cdot F_h P_h u, \nabla \cdot v_h \rangle \right) + \langle F_h P_h u, v_h \rangle = \langle P_h u, v_h \rangle = \langle u, v_h \rangle.$$

which gives the result, after we subtract them and choose $v_h = (F_h P_h - F_h) u$. □

In addition, the following bounds hold for filtered quantities:

Lemma 5.4. *For $u \in X$, the following inequalities hold:*

$$\|\overline{u}^h\| \leq \|u\|, \tag{5.6a}$$

$$\|\nabla \overline{u}^h\| \leq c(\Omega)\|\nabla u\|, \tag{5.6b}$$

$$\|(I - F_h)u\| \leq \|u\|, \tag{5.6c}$$

$$\langle F_h u, u\rangle \geq 0, \tag{5.6d}$$

$$\langle (I - F_h)u, u\rangle \geq 0. \tag{5.6e}$$

In particular, for $u \in X_h$,

$$\langle -\Delta_h u, u\rangle \geq 0. \tag{5.6f}$$

Proof. The first follows choosing $v_h = \overline{u}^h$ in (5.3) and using Cauchy-Schwarz inequality. For the second, we choose $v_h = \Delta_h \overline{u}^h$ in (5.3) to obtain

$$\begin{aligned} \alpha^2\|\tilde{\Delta}_h \overline{u}^h\|^2 + \|\nabla \overline{u}^h\|^2 + \kappa Re\|\nabla \cdot \overline{u}^h\|^2 &= -\langle u, \Delta_h \overline{u}^h\rangle = -\langle P_h u, \Delta_h \overline{u}^h\rangle \\ &= \langle \nabla P_h u, \nabla \overline{u}^h\rangle + \kappa Re\langle \nabla \cdot P_h u, \nabla \cdot \overline{u}^h\rangle. \end{aligned}$$

The result follows using Cauchy-Schwarz inequality. For the third inequality, using

$$\|(I - F_h)u\|^2 = \langle (I - F_h)u, (I - F_h)u\rangle = \|u\|^2 - 2\langle u, \overline{u}^h\rangle + \|\overline{u}^h\|^2.$$

Now, choosing $v_h = \overline{u}^h$ in (5.3) and substituting in the above formula, we have

$$\|(I - F_h)u\|^2 = \|u\|^2 - \|\overline{u}^h\|^2 - 2\alpha^2\|\nabla \overline{u}^h\|^2 - 2\alpha^2\kappa Re\|\nabla \cdot \overline{u}^h\|^2,$$

from which the result follows. For the fourth inequality, we have only to choose $v_h = F_h u$ in the filter equation (5.3). For the fifth, first note that using Cauchy-Schwarz inequality and the first inequality we have $-\langle F_h u, u\rangle \geq -\|u\|^2$. Then,

$$\langle (I - F_h)u, u\rangle = \|u\|^2 - \langle F_h u, u\rangle,$$

gives the result. The sixth inequality follows directly from the $\tilde{\Delta}_h$ definition. □

Given $u \in X$, the van Cittert deconvolution operator D_N^h is defined by

$$D_N^h u = \sum_{i=0}^{N} (I - F_h)^i\, u \tag{5.7}$$

Lemma 5.5. *The operator* D_N^h *is continuous and the following formulae hold*

$$\sum_{i=0}^{N} (I - F_h)^i F_h = I - (I - F_h)^{N+1},$$

$$(I - F_h)^i = (-1)^i \alpha^{2i} (\tilde{\Delta}_h F_h)^i,$$

$$D_N^h F_h = I - (I - F_h)^{N+1},$$

$$D_N^h F_h = I - (-1)^{N+1} \alpha^{2N+2} (\tilde{\Delta}_h F_h)^{N+1}.$$

Proof. That operator D_N^h is continuous follows from the continuity of F_h. For the first formula we use the algebraic identity $B^{N+1} - I = (B - I)(B^N + B^{N-1} + ... + I)$ with $B = I - F_h$. For the second, using the filter equation (5.3), $-\alpha^2 \tilde{\Delta}_h F_h = I - F_h$ gives the result. Finally, for the third, we use the definition of D_N^h and the first formula. For the last one, we combine the second and third formulae. ☐

Lemma 5.6. *Given* $u \in X$*, we have the following formulae*

$$\langle P_h u, D_N^h \overline{u_h} \rangle = \| D_N^h \overline{u}^h \|^2 + \alpha^2 \| \nabla (I - F_h)^{\frac{N+n}{2}} \overline{u}^h \|^2 + \alpha^2 \kappa Re \| \nabla \cdot (I - F_h)^{\frac{N+n}{2}} \overline{u}^h \|^2,$$

$$-\langle \tilde{\Delta}_h P_h u, D_N^h \overline{u}^h \rangle = \| \nabla D_N^h \overline{u}^h \|^2 + \alpha^2 \kappa Re \| \nabla \cdot D_N^h \overline{u}^h \|^2 + \alpha^2 \| \tilde{\Delta}_h (I - F_h)^{\frac{N+n}{2}} \overline{u}^h \|^2.$$

Proof. Using the third formula in Lemma 5.5, $u = D_N^h \overline{u}^h + (I - F_h)^{N+1} u$. Then

$$\begin{aligned}
\langle P_h u, D_N^h \overline{u}^h \rangle = \langle u, D_N^h \overline{u}^h \rangle &= \| D_N^h \overline{u}^h \|^2 + \langle (I - F_h)^{N+1} u, D_N^h \overline{u}^h \rangle \\
&= \| D_N^h \overline{u}^h \|^2 + \sum_{i=0}^{N} \langle (I - F_h)^{N+1} u, (I - F_h)^i \overline{u}^h \rangle \\
&= \| D_N^h \overline{u}^h \|^2 + \sum_{i=0}^{N} \langle (I - F_h)(I - F_h)^{\frac{N+i}{2}} u, (I - F_h)^{\frac{N+i}{2}} \overline{u}^h \rangle
\end{aligned}$$

where we have used that F_h and $(I - F_h)$ are positive (Lemmas 5.3 and 5.4).

Now rewriting filter equation as $\alpha^2 \langle \nabla F_h w, \nabla v_h \rangle + \alpha^2 \kappa Re \langle \nabla \cdot F_h w, \nabla \cdot v_h \rangle = \langle w - F_h w, v_h \rangle \; \forall v_h \in V_h$ and using $w = (I - F_h)^{\frac{N+i}{2}} u$ and $v_h = (I - F_h)^{\frac{N+i}{2}} \overline{u}^h$

$$\alpha^2 \| \nabla (I - F_h)^{\frac{N+i}{2}} \overline{u}^h \|^2 + \alpha^2 \kappa Re \| \nabla \cdot (I - F_h)^{\frac{N+i}{2}} \overline{u}^h \|^2 = \langle (I - F_h)(I - F_h)^{\frac{N+i}{2}} u, (I - F_h)^{\frac{N+i}{2}} \overline{u}^h \rangle$$

which gives the first formula.

For the second, we use again $u = D_N^h \overline{u}^h + (I - F_h)^{N+1} u$ to obtain

$$-\langle \tilde{\Delta}_h P_h u, D_N^h \overline{u}^h \rangle = \|\nabla D_N^h \overline{u}^h\|^2 + \kappa Re \|\nabla \cdot D_N^h \overline{u}^h\|^2 - \langle \tilde{\Delta}_h P_h (I - F_h)^{N+1} u, D_N^h \overline{u}^h \rangle$$

Now, using the filter equation $-\alpha^2 \langle \tilde{\Delta}_h F_h w, v_h \rangle = \langle w - F_h w, v_h \rangle \ \forall v_h \in V_h$ with $w = (I - F_h)^N u$ and $v_h = \tilde{\Delta}_h D_N^h \overline{u}^h$

$$-\langle \tilde{\Delta}_h P_h u, D_N^h \overline{u}^h \rangle = \|\nabla D_N^h \overline{u}^h\|^2 + \kappa Re \|\nabla \cdot D_N^h \overline{u}^h\|^2 + \alpha^2 \langle \tilde{\Delta}_h (I - F_h)^N \overline{u}^h, \tilde{\Delta}_h D_N^h \overline{u}^h \rangle$$

$$= \|\nabla D_N^h \overline{u}^h\|^2 + \kappa Re \|\nabla \cdot D_N^h \overline{u}^h\|^2 + \alpha^2 \sum_{i=0}^{N} \langle (I - F_h)^N \tilde{\Delta}_h \overline{u}^h, (I - F_h)^i \tilde{\Delta}_h \overline{u}^h \rangle$$

which gives the result. □

Now, following [79, 76] and using Lemma 5.6, we define the energy $\|\cdot\|_{E,N}$ and the energy dissipation $\|\cdot\|_{\epsilon,N}$ norms as

$$\|u\|_{E,N} := \langle P_h u, D_N^h \overline{u}^h \rangle^{1/2} \tag{5.8}$$

$$\|u\|_{\epsilon,N} := -\langle \tilde{\Delta}_h P_h u, D_N^h \overline{u}^h \rangle^{1/2} \tag{5.9}$$

The following equivalence norm Lemmas which are presented in [79] and [76] are very helpful in the subsequent analysis.

Lemma 5.7. *For $u \in V_h$ and for each natural number N, the energy norm defined by (5.8) is equivalent to the zeroth energy norm also defined by (5.8). That is*

$$\|u\|_{E,0} \leq \|u\|_{E,N} \leq D_1 \|u\|_{E,0}$$

Additionally, for $u \in V_h$ and for each natural number N, the energy dissipation norm defined by (5.9) is equivalent to the zeroth energy dissipation norm also defined by (5.9). That is

$$\|u\|_{\epsilon,0} \leq \|u\|_{\epsilon,N} \leq D_1 \|u\|_{\epsilon,0}$$

where $D_1 := \sqrt{N+1}$.

Lemma 5.8. *If the filtering radius* α *is chosen so that* $\alpha \leq O(h)$ *then the zeroth energy norm* $\|\cdot\|_{E,0}$ *is equivalent to the usual* L^2 *norm in* V_h*: for* $u \in V_h$*, there exists* C_E *independent of* h*,* u *satisfying*

$$\|u\|_{E,0} \leq \|u\| \leq C_E \|u\|_{E,0}$$

Additionally, the zeroth energy dissipation norm $\|\cdot\|_{\epsilon,0}$*, is equivalent to the* H^1 *norm in* V_h*: there exists* C_ϵ *independent of* h, u *satisfying*

$$\|u\|_{\epsilon,0} \leq \|\nabla u\| \leq C_\epsilon \|u\|_{\epsilon,0}$$

Remark 5.1. *Combining the estimates presented in Lemmas 5.7 and 5.8, we have the following norm equivalence result: for every* $u \in V_h$

$$\begin{aligned} D_1^{-1}\|u\|_{E,N} &\leq \|u\| \leq C_E \|u\|_{E,N}, \\ D_1^{-1}\|u\|_{\epsilon,N} &\leq \|\nabla u\| \leq C_\epsilon \|u\|_{\epsilon,N}. \end{aligned}$$

The following estimates are useful in the convergence analysis

Lemma 5.9. *Given* $u \in V$*, the inequalities hold*

$$\begin{aligned} \|u\|_{E,N} &\leq D_1 \|u\| \\ \|u\|_{\epsilon,N} &\leq D_2 \|\nabla u\| \end{aligned}$$

where $D_2 := c\sqrt{N+1}\sqrt{1+\kappa Re}$*.*

Proof. Applying the filter equation (5.3) for $D_N^h u$ and choosing $v_h = P_h u$

$$-\alpha^2 \langle \tilde{\Delta}_h F_h D_N^h u, P_h u\rangle + \langle F_h D_N^h u, P_h u\rangle = \langle D_N^h u, P_h u\rangle$$

Now using Lemmas 5.3 and 5.4 we have

$$-\alpha^2 \langle D_N^h F_h u, \tilde{\Delta}_h P_h u\rangle + \langle F_h D_N^h u, P_h u\rangle = \sum_{i=0}^{N} \langle (I - F_h)^i u, P_h u\rangle \leq \sum_{i=0}^{N} \|P_h u\| \|u\|$$

from which the result follows.

For the second, applying the filter equation for $D_N^h P_h u$, choosing $v_h = \tilde{\Delta}_h P_h u$ and using the modified discrete Laplacian definition, we obtain

$$-\alpha^2 \sum_{i=0}^{N} \langle (I - F_h)^i F_h \tilde{\Delta}_h P_h u, \tilde{\Delta}_h P_h u\rangle + \langle D_N^h F_h P_h u, \tilde{\Delta}_h P_h u\rangle = -\langle D_N^h P_h u, -\tilde{\Delta}_h P_h u\rangle.$$

Now, using that F_h, $I - F_h$ and $-\tilde{\Delta}_h$ are positive operators (Lemmas 5.3 and 5.4) and F_h and $\tilde{\Delta}_h$ commutates we have

$$\begin{aligned}
\alpha^2 \sum_{i=0}^{N} \|(I - F_h)^{i/2} F_h^{1/2} \tilde{\Delta}_h P_h u\|^2 + \|u\|_{\epsilon,N}^2 &= -\sum_{i=0}^{N} \langle (I - F_h)^i (-\tilde{\Delta}_h)^{1/2} P_h u, (-\tilde{\Delta}_h)^{1/2} P_h u\rangle \\
&\le (N+1)\langle P_h u, -\tilde{\Delta}_h P_h u\rangle \\
&\le (N+1)(1 + \kappa Re)\|\nabla P_h u\|^2
\end{aligned}$$

from which the result follows. □

Lemma 5.6, norm equivalence and Lemma 5.9 gives

Corollary 5.1. *Let $u \in V$. Then the following inequalities hold:*

$$\begin{aligned}
\|D_N^h \overline{u}^h\| &\le \|u\|_{E,N}, \\
\|\nabla D_N^h \overline{u}^h\| &\le \|u\|_{\epsilon,N}, \\
\|\nabla D_N^h \overline{u}^h\| &\le D_2 \|\nabla u\|.
\end{aligned}$$

Now, given $u \in V$ and $\gamma \in [0, 1]$, we define the H_γ^N operator by

$$H_\gamma^N u = [(1 - \gamma)I + \gamma D_N^h F_h]u \tag{5.10}$$

which is useful in order to define the general regularized Boussinesq model.

We also define the modified energy and modified dissipation norms by

$$\begin{aligned}
\|u\|_{E^\gamma,N} &:= \left\langle P_h u, H_\gamma^N u\right\rangle^{1/2} = [(1 - \gamma)\|u\|^2 + \gamma \|u\|_{E,N}^2]^{1/2}, &(5.11)\\
\|u\|_{\epsilon^\gamma,N} &:= [-\left\langle \tilde{\Delta}_h P_h u, H_\gamma u\right\rangle]^{1/2} \\
&= [(1 - \gamma)\|\nabla P_h u\|^2 + (1 - \gamma)\kappa Re \|\nabla \cdot P_h u\|^2 + \gamma \|u\|_{\epsilon,N}^2]^{1/2}. &(5.12)
\end{aligned}$$

from which the following two lemmas are straightforward from the previous lemmas:

Lemma 5.10. *For $u \in V_h$, $\gamma \in [0,1]$ and for each natural number N, the energy norm defined by (5.11) is equivalent to the L^2 norm in V_h. That is*

$$c_{E^\gamma,N}\|u\|_{E^\gamma,N} \le \|u\| \le C_{E^\gamma,N}\|u\|_{E^\gamma,N}.$$

Additionally, for $u \in V_h$, $\gamma \in [0,1]$ and for each natural number N, the energy dissipation norm defined by (5.12) is equivalent to the H^1 norm in V_h. That is

$$c_{\epsilon^\gamma,N}\|u\|_{\epsilon^\gamma,N} \le \|\nabla u\| \le C_{\epsilon^\gamma,N}\|u\|_{\epsilon^\gamma,N}.$$

Lemma 5.11. *Let $u \in V$ and $w \in V_h$. Then the following inequalities hold:*

$$\begin{aligned}\|H_\gamma^N w\| &\le D_E^\gamma \|w\|_{E^\gamma,N},\\ \|\nabla H_\gamma^N w\| &\le D_\epsilon^\gamma \|w\|_{\epsilon^\gamma,N},\\ \|\nabla H_\gamma^N u\| &\le D_2^\gamma \|\nabla u\|.\end{aligned}$$

The following lemma is the key to handling the consistency error in the regularized Boussinesq model (See [76]).

Lemma 5.12. *For smooth, periodic u, or u satisfying $\Delta^j u = 0$ on $\partial\Omega$ for $0 \le j \le \frac{k+1}{2} - 1$, the discrete approximate deconvolution operator satisfies*

$$\|u - D_N^h \overline{u}^h\| \le C\alpha^{2N+2}\|\Delta^{N+1}F^{N+1}u\| + C(\alpha h^k + h^{k+1})\Big(\sum_{i=1}^{N} |F^{i+1}u|_{k+1}\Big),$$

and thus for $k \ge 1$ we have

$$\|u - D_N^h \overline{u}^h\| \le C(\alpha^{2N+2} + \alpha h^k + h^{k+1})\Big(\sum_{i=1}^{N} \|F^{i+1}u\|_{k+1}\Big).$$

Remark 5.2. *Clearly from (5.10), we have $u - H_\gamma^N u = \gamma\left(u - D_N^h \overline{u}^h\right)$.*

5.3 Algorithm for the general regularized Boussinesq model and its analysis

Now we propose a Crank-Nicolson linearly extrapolated (CNLE) finite element algorithm for a general regularized Boussinesq model. Assume that initial temperature T_h^0 and velocity u_h^0, forcing term f, timestep $\Delta t > 0$ and endtime $T > 0$ are given. Let $v(t^{n+\frac{1}{2}}) = v({(t^{n+1}+t^n)}/2)$ and $v^{n+\frac{1}{2}} = {(v^{n+1}+v^n)}/2$, then:

Algorithm 5.1. *Choose* $\beta, \lambda, \gamma \in [0,1]$ *and set* $M = \frac{T}{\Delta t}$, $u_h^{-2} := u_h^0$, $u_h^{-1} := u_h^0$ *and for* $n = 1, ..., M-1$, *find* $u_h^{n+1} \in V_h$ *and* $T_h^{n+1} \in Y_h$ *satisfying* $\forall v_h, r_h \in V_h$ *and* $\forall s_h \in Y_h$,

$$\Big\langle \tfrac{u_h^{n+1}-u_h^n}{\Delta t}, v_h \Big\rangle + a_\beta\big(H_\lambda^N \xi(u_h^{n+\frac{1}{2}}), H_\gamma^N u_h^{n+\frac{1}{2}}, v_h\big) - Re^{-1}\big\langle \tilde{\Delta}_h u_h^{n+\frac{1}{2}}, v_h\big\rangle$$
$$-Ri\big\langle T_h^{n+\frac{1}{2}}\hat{k}, v_h\big\rangle = \big\langle f^{n+\frac{1}{2}}, v_h\big\rangle \tag{5.13a}$$

$$\Big\langle \tfrac{T_h^{n+1}-T_h^n}{\Delta t}, s_h \Big\rangle + a^*\big(\xi(u_h^{n+\frac{1}{2}}), T_h^{n+\frac{1}{2}}, s_h\big) + (RePr)^{-1}\big\langle \nabla T_h^{n+\frac{1}{2}}, \nabla s_h\big\rangle = 0, \tag{5.13b}$$

$$-\alpha^2\big\langle \tilde{\Delta}_h F_h^{(i)} u_h^{n+1}, r_h\big\rangle + \big\langle F_h^{(i)} u_h^{n+1}, r_h\big\rangle = \big\langle F_h^{(i-1)} u_h^{n+1}, r_h\big\rangle \text{ for } i = 1, .., N. \tag{5.13c}$$

where ξ *is the extrapolation operator defined by* $\xi(u_h^{n+\frac{1}{2}}) = 2u_h^{n-\frac{1}{2}} - u_h^{n-\frac{3}{2}}$.

Remark 5.3. *We also tested an algorithm similar to Algorithm 5.1, but using a deconvolved velocity in the temperature equation. However, solutions obtained with this modification did not show significant differences from solutions obtained with Algorithm 5.1.*

Table 5.3 presents some traditional alpha models arising from Algorithm 5.1.

Table 5.1: Regularization models resulting for particular choices of the β, γ and λ.

Model	β	λ	γ
alpha	1	0	1
omega	1	1	0
Leray	0	0	1
Modified-Leray	0	1	0
Bardina	0	1	1

Remark 5.4. *It is worth mentioning that choosing fractional values of* β, γ *and* λ *gives hybrid regularization models between the above mentioned regularization models.*

Lemma 5.13. *Algorithm 5.1 is well-posed.*

Proof. Restricting to any particular time level n, it is clear that (5.13c) is well-posed. Moreover, equations (5.13a) and (5.13b) are linear and X_h, Y_h are finite dimensional, then uniqueness and existence are equivalent. Given $\xi(u_h^{n+\frac{1}{2}}) \in X_h$, $T^n \in Y_h$ and supposing $T_1^{n+1}, T_2^{n+1} \in Y_h$ satisfies (5.13b), then, subtracting,

$$\left\langle \tfrac{T_2^{n+1}-T_1^{n+1}}{\Delta t}, s_h \right\rangle + a^*\big(\xi(u_h^{n+\frac{1}{2}}), T_2^{n+\frac{1}{2}} - T_1^{n+\frac{1}{2}}, s_h\big) + (RePr)^{-1}\big\langle \nabla(T_2^{n+\frac{1}{2}} - T_1^{n+\frac{1}{2}}), \nabla s_h \big\rangle = 0.$$

Choosing $s_h = T_2^{n+\frac{1}{2}} - T_1^{n+\frac{1}{2}} \in Y_h$, gives $T_2^{n+1} = T_1^{n+1}$.

Now, given $\xi(u_h^{n+\frac{1}{2}}), u_h^n \in X_h$ and $T^{n+\frac{1}{2}} \in Y_h$ if $u_1^{n+1}, u_2^{n+1} \in X_h$ satisfies (5.13a), then, subtracting,

$$\left\langle \tfrac{u_2^{n+1}-u_1^{n}}{\Delta t}, v_h \right\rangle + b_\beta\Big(\xi(H_\lambda^N u_h^{n+\frac{1}{2}}), H_\gamma^N(u_2^{n+\frac{1}{2}} - u_1^{n+\frac{1}{2}}), v_h\Big) - Re^{-1}\Big\langle \tilde{\Delta}_h(u_2^{n+\frac{1}{2}} - u_1^{n+\frac{1}{2}}), v_h \Big\rangle = 0$$

Choosing $v_h = H_\gamma^N(u_2^{n+\frac{1}{2}} - u_1^{n+\frac{1}{2}}) \in X_h$, gives $u_2^{n+1} = u_1^{n+1}$. $\square$

Lemma 5.14 (Energy conservation)**.** *The approximation given by Algorithm 5.1 satisfies*

$$\|u_h^M\|^2_{E^\gamma,N} + Re^{-1}\Delta t \sum_{n=0}^{M-1} \|u_h^{n+\frac{1}{2}}\|^2_{\epsilon^\gamma,N} = \|u_h^0\|^2_{E^\gamma,N} + Ri\sum_{n=0}^{M-1}\langle T^{n+\frac{1}{2}}\hat{k}, H_\gamma^N u_h^{n+\frac{1}{2}}\rangle + \sum_{n=0}^{M-1}\langle f^{n+\frac{1}{2}}, H_\gamma^N u_h^{n+\frac{1}{2}}\rangle,$$

$$\|T_h^M\|^2 + 2(RePr)^{-1}\Delta t \sum_{n=0}^{M-1} \|\nabla T_h^{n+\frac{1}{2}}\|^2 = \|T_h^0\|^2.$$

In particular, if $f = Ri = Re^{-1} = Pr^{-1} = 0$ *then* $\|u_h^M\|^2_{E^\gamma,N} = \|u_h^0\|^2_{E^\gamma,N}$ *and* $\|T_h^M\|^2 = \|T_h^0\|^2$.

Proof. Choosing $s_h = T_h^{n+\frac{1}{2}}$ in (5.13b) and $v_h = H_\gamma^N u_h^{n+\frac{1}{2}}$ in (5.13a) gives

$$\|T_h^{n+1}\|^2 - \|T_h^n\|^2 + 2\Delta t(RePr)^{-1}\|\nabla T_h^{n+\frac{1}{2}}\|^2 = 0 \tag{5.14}$$

$$\|u_h^{n+1}\|^2_{E^\gamma,N} - \|u_h^n\|^2_{E^\gamma,N} + 2Re^{-1}\Delta t\|u_h^{n+\frac{1}{2}}\|^2_{\epsilon^\gamma,N} = Ri\langle T_h^{n+\frac{1}{2}}, H_\gamma^N u_h^{n+\frac{1}{2}}\rangle + \langle f^{n+\frac{1}{2}}, H_\gamma^N u_h^{n+\frac{1}{2}}\rangle. \tag{5.15}$$

in which case the result follows, summing from $n = 0, ..., M-1$. $\square$

Lemma 5.15 (Stability)**.** *Algorithm 5.1 is unconditionally stable.* (u_h^M, T_h^M) *satisfy*

$$C^{-1}_{E^\gamma,N}\|u_h^M\|^2 + (C_{\epsilon^\gamma,N}Re)^{-1}\Delta t\sum_{n=0}^{M-1}\|\nabla u_h^{n+\frac{1}{2}}\|^2 \le C(data),$$

$$\|T_h^M\|^2 + 2(RePr)^{-1}\Delta t\sum_{n=0}^{M-1}\|\nabla T_h^{n+\frac{1}{2}}\|^2 \le C(data).$$

Proof. The second estimate follows directly from (5.14). For the first, we apply Cauchy-Schwarz and Poincaré inequalities and Lemma 5.11 in (5.15) to obtain

$$\|u_h^{n+1}\|^2_{E^\gamma,N} - \|u_h^n\|^2_{E^\gamma,N} + 2Re^{-1}\Delta t\|u_h^{n+\frac{1}{2}}\|^2_{\epsilon^\gamma,N} = RiC_{PF}\Delta t(\|T_h^{n+\frac{1}{2}}\| + \|f^{n+\frac{1}{2}}\|_{-1})\|u_h^{n+\frac{1}{2}}\|_{\epsilon^\gamma,N}.$$

The result follows from Young's inequality, Lemma 5.10 and summing from $n = 0, ..., M-1$. □

5.3.1 Convergence

Theorem 5.1. *Let $(u(t), p(t), T(t))$ be a sufficiently smooth, strong solution of the Boussinesq model (5.1) such that the norms of $(u(t), p(t), T(t))$ on the right hand side of (5.16) - (5.19) are finite. Suppose that (u_0^h, p_0^h, T_0^h) are approximations of $(u(0), p(0), T(0))$ to whithin the accuracy of the interpolant and that $(u_h, p_h, T_h) \in X_h \times Q_h \times Y_h$ is the CNLE-FE approximation to the Boussinesq model given by Algorithm 5.1. Then, for Δt small enough (in order to apply the discrete Gronwall inequality), we have*

$$C^{-1}_{E_\gamma,N}|||u - u^h|||_{\infty,0} \leq G\left(\Delta t, h, \alpha\right) + Ch^{k+1}|||u|||_{\infty,k+1} \text{ and} \tag{5.16}$$

$$\left\{C^{-1}_{\epsilon_\gamma,N}Re^{-1}\Delta t\sum_{n=0}^{M-1}\left\|\nabla\left(u(t^{n+\frac{1}{2}}) - u_h^{n+\frac{1}{2}}\right)\right\|^2\right\}^{\frac{1}{2}} \leq G(\Delta t, h, \alpha) + CRe^{-\frac{1}{2}}\Delta t^2\|\nabla u_{tt}\|_{2,0} + CRe^{-\frac{1}{2}}h^k|||u|||_{2,k+1}, \tag{5.17}$$

and

$$|||T - T^h|||_{\infty,0} \leq G\left(\Delta t, h, \alpha\right) + Ch^{k+1}|||T|||_{\infty,k+1} \text{ and} \tag{5.18}$$

$$\left\{Re^{-1}\Delta t\sum_{n=0}^{M-1}\left\|\nabla\left(T(t^{n+\frac{1}{2}}) - T_h^{n+\frac{1}{2}}\right)\right\|^2\right\}^{\frac{1}{2}} \leq G(\Delta t, h, \alpha) + CRe^{-\frac{1}{2}}\Delta t^2\|\nabla T_{tt}\|_{2,0} + CRe^{-\frac{1}{2}}h^k|||T|||_{2,k+1}, \tag{5.19}$$

where

$$\begin{aligned}
G(\Delta t, h, \alpha) := C^* \Big\{ & h^k \Big[4(RePr)^{-1/2} C |||T^{1/2}|||_{2,k+1} + \sqrt{8} A_1 (RePr)^{1/2} C |||\xi(u^{1/2})|||^2_{4,k+1} \\
& + \sqrt{8} A_1 (RePr)^{1/2} C |||\nabla T^{1/2}|||^2_{4,0} + \sqrt{8} A_2 (RePr)^{1/2} C |||\nabla \xi(u_h^{1/2})|||_{2,0} + \sqrt{8} A_2 (RePr)^{1/2} C |||T^{1/2}|||^2_{4,k+1} \\
& + 2^{11/2} \sqrt{3} A_2^2 Re^{3/2} Pr C_{E^\gamma,N} C_{\epsilon^\gamma,N} C c^{-1}_{E^\gamma,N} (\sqrt{2} \|\nabla T^{\frac{1}{2}}\|^2 + \|\nabla T^{\frac{3}{2}}\|^2) \|u(0)\|_{k+1} \Big] \\
& + \Delta t^2 \Big[\tfrac{(RePr)^{1/2} C_{PF}}{\sqrt{80}} \|T_{ttt}\|_{2,0} + \tfrac{(RePr)^{-1/2}}{3} \|\nabla T_{tt}\|_{2,0} + \tfrac{A_1 (RePr)^{1/2}}{\sqrt{6}} |||\nabla \xi(u^{1/2})|||^2_{4,0} + \tfrac{A_1 (RePr)^{1/2}}{\sqrt{6}} \|\nabla T_{tt}\|^2_{4,0} \\
& + \tfrac{7 A_1 (RePr)^{1/2}}{\sqrt{3}} \|\nabla T^{1/2}\|^2_{4,0} + \tfrac{7 A_1 (RePr)^{1/2}}{\sqrt{3}} \|\nabla u_{tt}\|^2_{4,0} + \sqrt{\tfrac{5}{12}} Re^{1/2} D^\gamma_\epsilon \|p_{tt}\|_{2,0} \Big] + h^{s+1} \sqrt{20} Re^{1/2} C D^\gamma_\epsilon \|p^{1/2}\|_{2,s+1} \\
& + h^k \Big[\sqrt{20} Re^{-1/2} (1 + \kappa Re) C D^\gamma_\epsilon |||u|||_{2,k+1} + \sqrt{10} Re^{1/2} \sigma_1 D^\lambda_2 D^\gamma_\epsilon D^\gamma_2 C |||u^{-1/2}|||^2_{4,k+1} \\
& + \sqrt{10} Re^{1/2} \sigma_1 D^\lambda_2 D^\gamma_\epsilon D^\gamma_2 C |||u^{-3/2}|||^2_{4,k+1} + \sqrt{10} Re^{1/2} \sigma_1 D^\lambda_2 D^\gamma_2 D^\gamma_\epsilon C |||\nabla u|||^2_{4,0} \\
& + \sqrt{10} \sigma_2 Re^{1/2} D^{\lambda 1/2}_E D^{\lambda 1/2}_\epsilon D^\gamma_2 D^\gamma_\epsilon C \|\nabla \xi(u_h)\|_{2,0} + \sqrt{10} Re^{1/2} \sigma_2 D^{\lambda 1/2}_E D^{\lambda 1/2}_\epsilon D^\gamma_2 D^\gamma_\epsilon C |||u|||^2_{4,k+1} \\
& + 20\sqrt{6} Re^{3/2} \sigma_2^2 D^\lambda_E D^\lambda_\epsilon D^{\gamma 2}_\epsilon D^{\gamma 2}_2 C c^{-1}_{E^\gamma,N} (\sqrt{2} \|\nabla u^{\frac{1}{2}}\|^2 + \|\nabla u^{\frac{3}{2}}\|^2) \|u(0)\|_{k+1} + \tfrac{1}{\sqrt{3}} c^{-1}_{\epsilon^\gamma,N} Re^{-1/2} \|u(0)\|_{k+1} \Big] \\
& + \Delta t^2 \Big[\tfrac{1}{\sqrt{1280}} D^\gamma_E \|u_{ttt}\|_{2,0} + \tfrac{1}{\sqrt{3}} D^\gamma_\epsilon C_{PF} \|p_{tt}\|_{2,0} + \tfrac{Re^{-1/2}}{\sqrt{3}} D^\gamma_\epsilon \|\nabla u_{tt}\|_{2,0} + \tfrac{1}{\sqrt{48}} D^\gamma_E \|T_{tt}\|_{2,0} \\
& + \tfrac{1}{\sqrt{6}} \sigma_1 Re^{1/2} D^\gamma_\epsilon \|\nabla u_{tt}\|^2_{4,0} + 2\sigma_1 Re^{1/2} D^\gamma_\epsilon \|\nabla \xi(u^{1/2})\|^2_{4,0} + 2\sigma_1 Re^{1/2} D^\gamma_\epsilon \|\nabla u\|^2_{4,0} \\
& + \tfrac{7}{\sqrt{3}} \sigma_1 Re^{1/2} D^\gamma_\epsilon \|\nabla u_{tt}\|^2_{4,0} \Big] + \gamma(\alpha^{2N+2} + \alpha h^k + h^{k+1}) \sqrt{8} Re^{1/2} C D^\gamma_\epsilon \sum_{i=1}^{N} |||F^{i+1} u^{1/2}|||_{2,k+1} \\
& + \lambda(\alpha^{2N+2} + \alpha h^k + h^{k+1}) \sqrt{8} Re^{1/2} C D^\lambda_\epsilon \sum_{i=1}^{N} \Big(|||F^{i+1} u^{-1/2}|||_{2,k+1} + |||F^{i+1} u^{-3/2}|||_{2,k+1} \Big) \Big\}.
\end{aligned}$$

Remark 5.5. *Supposing that the indicated norms on the right hand side of (5.16) - (5.19) are finite, then the error in the CNLE-FE scheme for the general regularized Boussinesq model is of the order*

$$C^{-1}_{E_\gamma,N} |||u - u^h|||_{\infty,0} + C^{-1}_{\epsilon_\gamma,N} Re^{-1} \Delta t \sum_{n=0}^{M-1} \big\| \nabla \big(u(t^{n+\frac{1}{2}}) - u_h^{n+\frac{1}{2}} \big) \big\|^2 = O(h^k + \Delta t^2 + \alpha^{2N+2})$$

$$|||T - T^h|||_{\infty,0} + (RePr)^{-1} \Delta t \sum_{n=0}^{M-1} \big\| \nabla \big(T(t^{n+\frac{1}{2}}) - T_h^{n+\frac{1}{2}} \big) \big\|^2 = O(h^k + \Delta t^2 + \alpha^{2N+2})$$

Proof. In $t^{n+\frac{1}{2}}$, the temperature solution satisfies

$$\Big\langle \tfrac{T^{n+1} - T^n}{\Delta t}, s_h \Big\rangle + (RePr)^{-1} \big\langle \nabla T^{n+\frac{1}{2}}, \nabla s_h \big\rangle + a_1^* \big(\xi(u^{n+\frac{1}{2}}), T^{n+\frac{1}{2}}, s_h \big) = Intp_1 \quad (5.20)$$

where

$$\begin{aligned}
Intp_1 := & \Big\langle \tfrac{T^{n+1} - T^n}{\Delta t} - T_t(t^{n+\frac{1}{2}}), s_h \Big\rangle + (RePr)^{-1} \Big\langle \nabla T^{n+\frac{1}{2}} - \nabla T(t^{n+\frac{1}{2}}), \nabla s_h \Big\rangle \\
& + \Big[a_1^*(\xi(u^{n+\frac{1}{2}}), T^{n+\frac{1}{2}}, s_h) - a_1^*(u(t^{n+\frac{1}{2}}), T(t^{n+\frac{1}{2}}), s_h) \Big] \qquad (5.21)
\end{aligned}$$

Let $E := T - T_h$, $\mathcal{T}$ be the L^2 projection of T in X^h and defining $E_\perp := T - \mathcal{T}$ and $E_h := T_h - \mathcal{T}$, we have

$$E = E_\perp - E_h$$

Also, let $e := u - u_h$, U be the L^2 projection of u in V^h and defining $e_\perp := u - U$ and $e_h := u_h - U$, we have

$$e = e_\perp - e_h$$

Now, subtracting (5.13b) from (5.20), adding $\pm a_1^*\big(\xi(u_h^{n+\frac{1}{2}}), T^{n+\frac{1}{2}}, s_h\big)$. choosing $s_h = E_h^{n+\frac{1}{2}}$ and using that $a_1^*\big(\xi(u_h^{n+\frac{1}{2}}), E_h^{n+\frac{1}{2}}, E_h^{n+\frac{1}{2}}\big) = 0$

$$\begin{aligned}\tfrac{\|E_h^{n+1}\|^2 - \|E_h^n\|^2}{2\Delta t} + (RePr)^{-1}\|\nabla E_h^{n+\frac{1}{2}}\|^2 &= (RePr)^{-1}\big\langle \nabla E_\perp^{n+\frac{1}{2}}, \nabla E_h^{n+\frac{1}{2}}\big\rangle \\ + \Big[a_1^*\big(\xi(e^{n+\frac{1}{2}}), T^{n+\frac{1}{2}}, E_h^{n+\frac{1}{2}}\big) &- a_1^*\big(\xi(u_h^{n+\frac{1}{2}}), E_\perp^{n+\frac{1}{2}}, E_h^{n+\frac{1}{2}}\big)\Big] + Intp_1 \qquad (5.22)\end{aligned}$$

Now we bound the terms on the RHS of (5.22) individually.

First, using the Cauchy-Schwarz and Young's inequalities

$$\big\langle \nabla E_\perp^{n+\frac{1}{2}}, \nabla E_h^{n+\frac{1}{2}}\big\rangle \le h^{2k} 8C\|T^{n+\frac{1}{2}}\|_{k+1}^2 + \tfrac{1}{32}\|\nabla E_h^{n+\frac{1}{2}}\|^2. \qquad (5.23)$$

Using Lemma 5.1 and Young's inequality

$$\begin{aligned}&a_1^*\big(\xi(e_\perp^{n+\frac{1}{2}}), T^{n+\frac{1}{2}}, E_h^{n+\frac{1}{2}}\big) \le A_1\|\nabla\xi(e_\perp^{n+\frac{1}{2}})\|\|\nabla T^{n+\frac{1}{2}}\|\|\nabla E_h^{n+\frac{1}{2}}\| \\ &\le h^{2k} 4A_1^2 RePrC(\|\xi(u^{n+\frac{1}{2}})\|_{k+1}^4 + \|\nabla T^{n+\frac{1}{2}}\|^4) + \tfrac{(RePr)^{-1}}{32}\|\nabla E_h^{n+\frac{1}{2}}\|^2. \qquad (5.24)\end{aligned}$$

Using Lemmas 5.1 and 5.10 and Young's inequality

$$\begin{aligned}&a_1^*\big(\xi(e_h^{n+\frac{1}{2}}), T^{n+\frac{1}{2}}, E_h^{n+\frac{1}{2}}\big) \le A_2\|\xi(e_h^{n+\frac{1}{2}})\|^{\frac{1}{2}}\|\nabla\xi(e_h^{n+\frac{1}{2}})\|^{\frac{1}{2}}\|\nabla T^{n+\frac{1}{2}}\|\|\nabla E_h^{n+\frac{1}{2}}\| \\ &\le 2^8 3A_2^4 Re^3 Pr^2 C_{E^\gamma,N}^2 C_{\epsilon^\gamma,N}^2\|\nabla T^{n+\frac{1}{2}}\|^4\|\xi(e_h^{n+\frac{1}{2}})\|_{E^\gamma,N}^2 + \tfrac{Re^{-1}}{48}\|\xi(e_h^{n+\frac{1}{2}})\|_{\epsilon^\gamma,N}^2 + \tfrac{(RePr)^{-1}}{32}\|\nabla E_h^{n+\frac{1}{2}}\|^2. \\ &\qquad (5.25)\end{aligned}$$

Using Lemma 5.1 and Young's inequality

$$a_1^*\big(\xi(u_h^{n+\frac{1}{2}}), E_\perp^{n+\frac{1}{2}}, E_h^{n+\frac{1}{2}}\big) \le A_2\|\xi(u_h^{n+\frac{1}{2}})\|^{\frac{1}{2}}\|\nabla\xi(u_h^{n+\frac{1}{2}})\|^{\frac{1}{2}}\|\nabla E_\perp^{n+\frac{1}{2}}\|\|\nabla E_h^{n+\frac{1}{2}}\|$$
$$\le h^{2k}4A_2^2RePrC(\|\nabla\xi(u_h^{n+\frac{1}{2}})\|^2 + \|T^{n+\frac{1}{2}}\|_{k+1}^4) + \tfrac{(RePr)^{-1}}{32}\|\nabla E_h^{n+\frac{1}{2}}\|^2, \tag{5.26}$$

where we also used the stability bound for $u_h^{n+\frac{1}{2}}$ in the above inequality.

Now we bound the interpolation error terms on the RHS of (5.21). Using Cauchy-Schwarz and Young's inequalities and Lemma 5.2

$$\left\langle \tfrac{T^{n+1}-T^n}{\Delta t} - T_t(t^{n+\frac{1}{2}}), E_h^{n+\frac{1}{2}} \right\rangle \le \Delta t^3 \tfrac{RePrC_{PF}^2}{160}\int_{t^n}^{t^{n+1}} \|T_{ttt}\|^2 dt + \tfrac{(RePr)^{-1}}{32}\|\nabla E_h^{n+\frac{1}{2}}\|^2, \tag{5.27}$$

$$\left\langle \nabla T^{n+\frac{1}{2}} - \nabla T(t^{n+\frac{1}{2}}), \nabla E_h^{n+\frac{1}{2}} \right\rangle \le \Delta t^3 \tfrac{1}{6}\int_{t^n}^{t^{n+1}} \|\nabla T_{tt}\|^2 dt + \tfrac{1}{32}\|\nabla E_h^{n+\frac{1}{2}}\|^2. \tag{5.28}$$

Adding and subtracting $a^*(\xi(u^{n+\frac{1}{2}}), T(t^{n+\frac{1}{2}}), E_h^{n+\frac{1}{2}})$, we have

$$a_1^*(\xi(u^{n+\frac{1}{2}}), T^{n+\frac{1}{2}}, E_h^{n+\frac{1}{2}}) - a_1^*(u(t^{n+\frac{1}{2}}), T(t^{n+\frac{1}{2}}), E_h^{n+\frac{1}{2}}) = a_1^*(\xi(u^{n+\frac{1}{2}}), T^{n+\frac{1}{2}} - T(t^{n+\frac{1}{2}}), E_h^{n+\frac{1}{2}})$$
$$+ a_1^*(\xi(u^{n+\frac{1}{2}}) - u^{n+\frac{1}{2}}, T(t^{n+\frac{1}{2}}), E_h^{n+\frac{1}{2}}) + a_1^*(u^{n+\frac{1}{2}} - u(t^{n+\frac{1}{2}}), T(t^{n+\frac{1}{2}}), E_h^{n+\frac{1}{2}}).$$

Using Lemmas 5.1 and 5.2 and Young's inequality

$$a_1^*(\xi(u^{n+\frac{1}{2}}), [T^{n+\frac{1}{2}} - T(t^{n+\frac{1}{2}})], E_h^{n+\frac{1}{2}}) \le A_1\|\nabla\xi(u^{n+\frac{1}{2}})\|\|\nabla[T^{n+\frac{1}{2}} - T(t^{n+\frac{1}{2}})]\|\|\nabla E_h^{n+\frac{1}{2}}\|$$
$$\le \Delta t^3\tfrac{A_1^2RePr}{12}\|\nabla\xi(u^{n+\frac{1}{2}})\|^4 + \Delta t^3\tfrac{A_1^2RePr}{12}\int_{t^n}^{t^{n+1}}\|\nabla T_{tt}\|^4 dt + \tfrac{(RePr)^{-1}}{32}\|\nabla E_h^{n+\frac{1}{2}}\|^2. \tag{5.29}$$

$$a_1^*(\xi(u^{n+\frac{1}{2}}) - u^{n+\frac{1}{2}}, T(t^{n+\frac{1}{2}}), E_h^{n+\frac{1}{2}}) \le A_1\|\nabla[\xi(u^{n+\frac{1}{2}}) - u^{n+\frac{1}{2}}]\|\|\nabla T(t^{n+\frac{1}{2}})\|\|\nabla E_h^{n+\frac{1}{2}}\|$$
$$\le \Delta t^3 8A_1^2RePr(\|\nabla T(t^{n+\frac{1}{2}})\|^4 + \int_{t^{n-1}}^{t^{n+1}}\|\nabla u_{tt}\|^4 dt) + \tfrac{(RePr)^{-1}}{64}\|\nabla E_h^{n+\frac{1}{2}}\|^2. \tag{5.30}$$

$$a_1^*([u^{n+\frac{1}{2}} - u(t^{n+\frac{1}{2}})], T(t^{n+\frac{1}{2}}), E_h^{n+\frac{1}{2}}) \le A_1\|\nabla[u^{n+\frac{1}{2}} - u(t^{n+\frac{1}{2}})]\|\|\nabla T(t^{n+\frac{1}{2}})\|\|\nabla E_h^{n+\frac{1}{2}}\|$$
$$\le \Delta t^3\tfrac{A_1^2RePr}{6}\|\nabla T(t^{n+\frac{1}{2}})\|^4 + \Delta t^3\tfrac{A_1^2RePr}{6}\int_{t^n}^{t^{n+1}}\|\nabla u_{tt}\|^4 dt + \tfrac{(RePr)^{-1}}{64}\|\nabla E_h^{n+\frac{1}{2}}\|^2. \tag{5.31}$$

Using (5.27), (5.28), (5.29), (5.30), (5.31) in (5.21) we have

$$\Delta t \sum_{n=0}^{M-1} |Intp_1| \leq \Delta t \tfrac{(RePr)^{-1}}{8} \sum_{n=0}^{M-1} \|\nabla E_h^{n+\frac{1}{2}}\|^2 + \Delta t^4 \tfrac{RePrC_{PF}^2}{160} \|T_{ttt}\|_{2,0}^2 + \Delta t^4 \tfrac{(RePr)^{-1}}{6} \|\nabla T_{tt}\|_{2,0}^2$$
$$+ \Delta t^4 \tfrac{A_1^2 RePr}{12} (\||\nabla \xi(u^{1/2})|\|_{4,0}^4 + \|\nabla T_{tt}\|_{4,0}^4) + \Delta t^4 \tfrac{49 A_1^2 RePr}{6} (\|\nabla T^{1/2}\|_{4,0}^4 + \|\nabla u_{tt}\|_{4,0}^4). \tag{5.32}$$

Using (5.23), (5.24), (5.25), (5.26) and (5.32) in (5.22) and summing from $n = 0$ to $n = M - 1$ gives

$$\|E_h^M\|^2 - \|E_h^0\|^2 + \tfrac{3}{2} \Delta t (RePr)^{-1} \sum_{n=0}^{M-1} \|\nabla E_h^{n+\frac{1}{2}}\|^2 \leq h^{2k} 16 (RePr)^{-1} C \||T^{1/2}|\|_{2,k+1}^2$$
$$+ h^{2k} 8 A_1^2 RePrC \||\xi(u^{1/2})|\|_{4,k+1}^4 + h^{2k} 8 A_1^2 RePrC \||\nabla T^{1/2}|\|_{4,0}^4 + \tfrac{Re^{-1}}{24} \sum_{n=0}^{M-1} \Delta t \|\xi(e_h^{n+\frac{1}{2}})\|_{\epsilon^\gamma,N}^2$$
$$+ h^{2k} 8 A_2^2 RePrC \||\nabla \xi(u_h^{1/2})|\|_{2,0}^2 + h^{2k} 8 A_2^2 RePrC \||T^{1/2}|\|_{4,k+1}^4 + \Delta t^4 \tfrac{RePrC_{PF}^2}{80} \|T_{ttt}\|_{2,0}^2$$
$$+ \Delta t^4 \tfrac{(RePr)^{-1}}{3} \|\nabla T_{tt}\|_{2,0}^2 + \Delta t^4 \tfrac{A_1^2 RePr}{6} \|\nabla \xi(u^{1/2})\|_{4,0}^4 + \Delta t^4 \tfrac{A_1^2 RePr}{6} \|\nabla T_{tt}\|_{4,0}^4 + \Delta t^4 \tfrac{49 A_1^2 RePr}{3} \|\nabla T\|_{4,0}^4$$
$$+ \Delta t^4 \tfrac{49 A_1^2 RePr}{3} \|\nabla u_{tt}\|_{4,0}^4 + 2^9 3 A_2^4 Re^3 Pr^2 C_{E^\gamma,N}^2 C_{\epsilon^\gamma,N}^2 \Delta t \sum_{n=0}^{M-1} (2\|\nabla T^{n+\frac{1}{2}}\|^4 + \|\nabla T^{n+\frac{3}{2}}\|^4) \|e_h^{n+\frac{1}{2}}\|_{E^\gamma,N}^2$$
$$+ h^{2k+2} 2^{11} 3 A_2^4 Re^3 Pr^2 C_{E^\gamma,N}^2 C_{\epsilon^\gamma,N}^2 C c_{E^\gamma}^{-2} (2\|\nabla T^{\frac{1}{2}}\|^4 + \|\nabla T^{\frac{3}{2}}\|^4) \|u(0)\|_{k+1}^2, \tag{5.33}$$

where we have used that

$$\sum_{n=0}^{M-1} \|\nabla T^{n+\frac{1}{2}}\|^4 \|\xi(e_h^{n+\frac{1}{2}})\|_{E^\gamma,N}^2 \leq \sum_{n=0}^{M-1} (2\|\nabla T^{n+\frac{1}{2}}\|^4 + \|\nabla T^{n+\frac{3}{2}}\|^4) \|e_h^{n+\frac{1}{2}}\|_{E^\gamma,N}^2$$
$$+ h^{2k+2} 4 C c_{E^\gamma}^{-2} (2\|\nabla T^{\frac{1}{2}}\|^4 + \|\nabla T^{\frac{3}{2}}\|^4) \|u(0)\|_{k+1}^2.$$

On the other hand, at $t^{n+\frac{1}{2}}$ the velocity solution satisfies

$$\left\langle \tfrac{u^{n+1} - u^n}{\Delta t}, v_h \right\rangle + a_\beta(H_\lambda^N \xi(u^{n+\frac{1}{2}}), H_\gamma^N u^{n+\frac{1}{2}}, v_h) - Re^{-1} \langle \tilde{\Delta}_h u^{n+\frac{1}{2}}, v_h \rangle$$
$$- \langle p^{n+\frac{1}{2}}, \nabla \cdot v_h \rangle - Ri \langle T^{n+\frac{1}{2}} \hat{k}, v_h \rangle = \langle f^{n+\frac{1}{2}}, v_h \rangle + Intp_2 \ \forall v_h \in V^h, \tag{5.34}$$

$$Intp_2 := \langle \tfrac{u^{n+1} - u^n}{\Delta t} - u_t(t^{n+\frac{1}{2}}), v_h \rangle + \left[a_\beta(H_\lambda^N \xi(u^{n+\frac{1}{2}}), H_\gamma^N u^{n+\frac{1}{2}}, v_h) - a_\beta(u(t^{n+\frac{1}{2}}), u(t^{n+\frac{1}{2}}), v_h) \right]$$
$$- \langle p^{n+\frac{1}{2}} - p(t^{n+\frac{1}{2}}), \nabla \cdot v_h \rangle - Ri \langle (T^{n+\frac{1}{2}} - T(t^{n+\frac{1}{2}})) \hat{k}, v_h \rangle - Re^{-1} \langle \tilde{\Delta}_h [u^{n+\frac{1}{2}} - u(t^{n+\frac{1}{2}})], v_h \rangle. \tag{5.35}$$

Subtracting (5.13a) from (5.34), adding $\pm a_\beta(H_\lambda^N \xi(u_h^{n+\frac{1}{2}}), H_\gamma^N u^{n+\frac{1}{2}}, H_\gamma^N e_h^{n+\frac{1}{2}})$ and choosing $v_h = H_\gamma^N e_h^{n+\frac{1}{2}}$, we obtain

$$\begin{aligned}
&\tfrac{\|e_h^{n+1}\|^2_{E\gamma,N} - \|e_h^n\|^2_{E\gamma,N}}{2\Delta t} + Re^{-1}\|e_h^{n+\frac{1}{2}}\|^2_{\epsilon^\gamma,N} = -\big\langle p^{n+\frac{1}{2}}, \nabla \cdot H_\gamma^N e_h^{n+\frac{1}{2}}\big\rangle - Re^{-1}\big\langle \Delta_h e_\perp^{n+\frac{1}{2}}, H_\gamma^N e_h^{n+\frac{1}{2}}\big\rangle \\
&- Ri\big\langle E_h^{n+\frac{1}{2}}\hat{k}, H_\gamma^N e_h^{n+\frac{1}{2}}\big\rangle + \big[a_\beta(H_\lambda^N \xi(e^{n+\frac{1}{2}}), H_\gamma^N u^{n+\frac{1}{2}}, H_\gamma^N e_h^{n+\frac{1}{2}}) \\
&+ a_\beta(H_\lambda^N \xi(u_h^{n+\frac{1}{2}}), H_\gamma^N e_\perp^{n+\frac{1}{2}}, H_\gamma^N e_h^{n+\frac{1}{2}})\big] + Intp_2, \qquad (5.36)
\end{aligned}$$

because $\langle e_\perp^{n+1} - e_\perp^n, H_\gamma^N e_h^{n+\frac{1}{2}}\rangle = 0$, $\langle E_\perp^{n+\frac{1}{2}}, H_\gamma^N e_h^{n+\frac{1}{2}}\rangle = 0$, $\langle q_h, \nabla \cdot H_\gamma^N e_h^{n+\frac{1}{2}}\rangle = 0$ and $a_\beta(H_\lambda^N \xi(u_h^{n+\frac{1}{2}}), H_\gamma^N e_h^{n+\frac{1}{2}}, H_\gamma^N e_h^{n+\frac{1}{2}}) = 0$.

Now we have to evaluate the terms on RHS of (5.36). Using Cauchy-Schwarz and Young's inequalities and Lemma 5.11 we obtain

$$\big\langle q_h - p^{n+\frac{1}{2}}, \nabla \cdot H_\gamma^N e_h^{n+\frac{1}{2}}\big\rangle \leq 10ReD_\epsilon^{\gamma 2}\|q_h - p^{n+\frac{1}{2}}\|^2 + \tfrac{Re^{-1}}{40}\|e_h^{n+\frac{1}{2}}\|^2_{\epsilon^\gamma,N}. \qquad (5.37)$$

Using Cauchy-Schwarz and Poincaré inequalities, Lemma 5.11 and Young's inequality

$$Ri\big\langle E_h^{n+\frac{1}{2}}\hat{k}, H_\gamma^N e_h^{n+\frac{1}{2}}\big\rangle \leq \tfrac{(RePr)^{-1}}{4}\|\nabla E_h^{n+\frac{1}{2}}\|^2 + C_{PF}^2 Ri^2 RePr D_E^{\gamma 2}\|e_h^{n+\frac{1}{2}}\|^2_{E^\gamma,N}. \quad (5.38)$$

Using Cauchy-Schwarz inequality, Lemma 5.11 and Young's inequality

$$\begin{aligned}
Re^{-1}\big\langle \Delta_h e_\perp^{n+\frac{1}{2}}, H_\gamma^N e_h^{n+\frac{1}{2}}\big\rangle &\leq Re^{-1}(1+\kappa Re)D_\epsilon^\gamma\|\nabla e_\perp^{n+\frac{1}{2}}\|\|e_h^{n+\frac{1}{2}}\|_{\epsilon^\gamma,N} \\
&\leq h^{2k}10Re^{-1}(1+\kappa Re)^2 D_\epsilon^{\gamma 2} C\|u^{n+\frac{1}{2}}\|^2_{k+1} + \tfrac{Re^{-1}}{40}\|e_h^{n+\frac{1}{2}}\|^2_{\epsilon^\gamma,N}. \qquad (5.39)
\end{aligned}$$

Using Lemma 5.1, Lemma 5.11 and Young's inequality

$$\begin{aligned}
&a_\beta(H_\lambda^N \xi(e_\perp^{n+\frac{1}{2}}), H_\gamma^N u^{n+\frac{1}{2}}, H_\gamma^N e_h^{n+\frac{1}{2}}) \leq \sigma_1 D_2^\lambda D_2^\gamma D_\epsilon^\gamma\|\nabla\xi(e_\perp^{n+\frac{1}{2}})\|\|\nabla u^{n+\frac{1}{2}}\|\|e_h^{n+\frac{1}{2}}\|_{\epsilon^\gamma,N}, \\
&\leq \tfrac{Re^{-1}}{40}\|e_h^{n+\frac{1}{2}}\|^2_{\epsilon^\gamma,N} + h^{2k}5Re\sigma_1^2 D_2^{\lambda 2} D_2^{\gamma 2} D_\epsilon^{\gamma 2} C(\|u^{n-\frac{1}{2}}\|^4_{k+1} + \|u^{n-\frac{3}{2}}\|^4_{k+1} + \|\nabla u^{n+\frac{1}{2}}\|^4), \\
&\qquad (5.40)
\end{aligned}$$

where we have used $\|\nabla\xi(e_\perp^{n+\frac{1}{2}})\| \leq 2h^{2k}C(\|u^{n-\frac{1}{2}}\|^2_{k+1} + \|u^{n-\frac{3}{2}}\|^2_{k+1})$.

Using Lemma 5.1, Lemma 5.11 and Young's inequality

$$
\begin{aligned}
&{}'a_\beta(H_\lambda^N \xi(e_h^{n+\frac{1}{2}}), H_\gamma^N u^{n+\frac{1}{2}}, H_\gamma^N e_h^{n+\frac{1}{2}}) \\
\leq&\sigma_2 \| H_\lambda^N \xi(e_h^{n+\frac{1}{2}})\|^{\frac{1}{2}} \|\nabla H_\lambda^N \xi(e_h^{n+\frac{1}{2}})\|^{\frac{1}{2}} \|\nabla H_\gamma^N u^{n+\frac{1}{2}}\| \|\nabla H_\gamma^N e_h^{n+\frac{1}{2}}\|, \\
\leq&\tfrac{Re^{-1}}{40}\|e_h^{n+\frac{1}{2}}\|_{\epsilon^\gamma,N}^2 + \tfrac{Re^{-1}}{48}\|\xi(e_h^{n+\frac{1}{2}})\|_{\epsilon^\gamma,N}^2 + 20^2 3Re^3\sigma_2^4 D_E^{\lambda 2} D_\epsilon^{\lambda 2} D_2^{\gamma 4} D_\epsilon^{\gamma 4} \|\nabla u^{n+\frac{1}{2}}\|^4 \|\xi(e_h^{n+\frac{1}{2}})\|_{E^\gamma,N}^2.
\end{aligned}
\tag{5.41}
$$

Using Lemma 5.1, Lemma 5.11, stability of u_h and Young's inequality

$$
\begin{aligned}
&a_\beta(H_\lambda^N \xi(u_h^{n+\frac{1}{2}}), H_\gamma^N e_\perp^{n+\frac{1}{2}}, H_\gamma^N e_h^{n+\frac{1}{2}}) \\
&\leq \sigma_2 \| H_\lambda^N \xi(u_h^{n+\frac{1}{2}})\|^{1/2} \|\nabla H_\lambda^N \xi(u_h^{n+\frac{1}{2}})\|^{1/2} \|\nabla H_\gamma^N e_\perp^{n+\frac{1}{2}}\| \|\nabla H_\gamma^N e_h^{n+\frac{1}{2}}\|, \\
&\leq \tfrac{Re^{-1}}{40}\|e_h^{n+\frac{1}{2}}\|_{\epsilon^\gamma,N}^2 + h^{2k} 5\sigma_2^2 D_E^\lambda D_\epsilon^\lambda D_2^{\gamma 2} D_\epsilon^{\gamma 2} ReC \Big(\|\nabla \xi(u_h^{n+\frac{1}{2}})\|_{\epsilon^\gamma,N}^2 + \|u^{n+\frac{1}{2}}\|_{k+1}^4 \Big).
\end{aligned}
\tag{5.42}
$$

Now, using (5.37)-(5.40) in (5.36) we obtain and summing from $n = 0, ..., M-1$, we have

$$
\begin{aligned}
&\tfrac{\|e_h^M\|_{E^\gamma,N}^2 - \|e_h^0\|_{E^\gamma,N}^2}{2\Delta t} + \tfrac{7}{8}Re^{-1}\sum_{n=0}^{M-1}\|e_h^{n+\frac{1}{2}}\|_{\epsilon^\gamma,N}^2 \leq \sum_{n=0}^{M-1}|Intp_2| + 10ReD_\epsilon^{\gamma 2}\sum_{n=0}^{M-1}\|q_h - p^{n+\frac{1}{2}}\|^2 \\
&+ \tfrac{(RePr)^{-1}}{4}\sum_{n=0}^{M-1}\|\nabla E_h^{n+\frac{1}{2}}\|^2 + h^{2k}10Re^{-1}(1+\kappa Re)^2 D_\epsilon^{\gamma 2} C \||u|\|_{2,k+1}^2 \\
&+ \tfrac{Re^{-1}}{48}\sum_{n=0}^{M-1}\|\xi(e_h^{n+\frac{1}{2}})\|_{\epsilon^\gamma,N}^2 + h^{2k}5Re\sigma_1^2 D_2^{\lambda 2} D_2^{\gamma 2} D_\epsilon^{\gamma 2} C\|u^{-1/2}\|_{4,k+1}^4 \\
&+ h^{2k}5Re\sigma_1^2 D_2^{\lambda 2} D_2^{\gamma 2} D_\epsilon^{\gamma 2} C\|u^{-3/2}\|_{4,k+1}^4 + h^{2k}5Re\sigma_1^2 D_2^{\lambda 2} D_2^{\gamma 2} D_\epsilon^{\gamma 2} C\||\nabla u|\|_{4,0}^4 \\
&+ h^{2k}5\sigma_2^2 D_E^\lambda D_\epsilon^\lambda D_2^{\gamma 2} D_\epsilon^{\gamma 2} ReC\||\nabla \xi(u_h)|\|_{2,0}^2 + h^{2k}5\sigma_2^2 D_E^\lambda D_\epsilon^\lambda D_2^{\gamma 2} D_\epsilon^{\gamma 2} ReC\||u|\|_{4,k+1}^4 \\
&+ \sum_{n=0}^{M-1}\Big[C_{PF}^2 Ri^2 RePrD_E^{\gamma 2} + 20^2 3Re^3\sigma_2^4 D_E^{\lambda 2} D_\epsilon^{\lambda 2} D_\epsilon^{\gamma 4} D_2^{\gamma 4}(2\|\nabla u^{n+\frac{1}{2}}\|^4 + \|\nabla u^{n+\frac{3}{2}}\|^4)\Big]\|e_h^{n+\frac{1}{2}}\|_{E^\gamma,N}^2 \\
&+ h^{2k+2}40^2 3Re^3\sigma_2^4 D_E^{\lambda 2} D_\epsilon^{\lambda 2} D_\epsilon^{\gamma 4} D_2^{\gamma 4} Cc_{E^\gamma,N}^{-2}(2\|\nabla u^{\frac{1}{2}}\|^4 + \|\nabla u^{\frac{3}{2}}\|^4)\|u(0)\|_{k+1}^2,
\end{aligned}
\tag{5.43}
$$

where we have used that

$$
\begin{aligned}
\sum_{n=0}^{M-1}\|\nabla u^{n+\frac{1}{2}}\|^4\|\xi(e_h^{n+\frac{1}{2}})\|_{E^\gamma,N}^2 \leq& \sum_{n=0}^{M-1}\|e_h^{n+\frac{1}{2}}\|_{E^\gamma,N}^2(2\|\nabla u^{n+\frac{1}{2}}\|^4 + \|\nabla u^{n+\frac{3}{2}}\|^4) \\
&+ h^{2k+2}4Cc_{E^\gamma,N}^{-2}(2\|\nabla u^{\frac{1}{2}}\|^4 + \|\nabla u^{\frac{3}{2}}\|^4)\|u(0)\|_{k+1}^2
\end{aligned}
$$

Also

$$\begin{aligned}\Delta t \sum_{n=0}^{M-1} \|q_h - p^{n+\frac{1}{2}}\|^2 &\leq \Delta t \sum_{n=0}^{M-1} \Big[\|p^{n+\frac{1}{2}} - p(t^{n+\frac{1}{2}})\|^2 + \|p^{n+\frac{1}{2}} - q_h\|^2\Big] \\ &\leq \frac{\Delta t^4}{48}\|p_{tt}\|^2_{2,0} + h^{2s+2}C\|p^{1/2}\|^2_{2,s+1}. \end{aligned} \tag{5.44}$$

Finally, we have to evaluate the Intp term in (5.35). Here we perform the standard analysis (see e. g. [76]) with only a small modification to consider the temperature term which gives

$$\Big\langle \big(T^{n+\frac{1}{2}} - T(t^{n+\frac{1}{2}})\big)\hat{k}, H_\gamma^N e_h^{n+\frac{1}{2}} \Big\rangle \leq \Delta t^3 \tfrac{Ri^{-1}}{96} \int_{t^n}^{t^{n+1}} \|T_{tt}\|^2 dt + \tfrac{Ri}{2}\|e_h^{n+\frac{1}{2}}\|^2_{E^\gamma,N}.$$

and the extrapolation term

$$\begin{aligned}&a_\beta\big(\xi(u^{n+\frac{1}{2}}) - u^{n+\frac{1}{2}}, u(t^{n+\frac{1}{2}}), H_\gamma^N e_h^{n+\frac{1}{2}}\big) \\ &\quad \leq \frac{Re^{-1}}{16}\|e_h^{n+\frac{1}{2}}\|^2_{\epsilon^\gamma,N} + \Delta t^3 2\sigma_1 Re D_\epsilon^{\gamma 2}\Big(\|\nabla u(t^{n+\frac{1}{2}})\|^4 dt + \int_{t^{n-1}}^{t^{n+1}} \|\nabla u_{tt}\|^4 dt\Big),\end{aligned}$$

which gives

$$\begin{aligned}\Delta t \sum_{n=0}^{M-1} |Intp_2| &\leq \tfrac{Re^{-1}}{4}\Delta t \sum_{n=0}^{M-1} \|e_h^{n+\frac{1}{2}}\|^2_{\epsilon^\gamma,N} + \Delta t \sum_{n=0}^{M-1} \left(\tfrac{1+Ri^2}{2}\right)\|e_h^{n+\frac{1}{2}}\|^2_{E^\gamma,N} + \Delta t^4 \tfrac{1}{2560} D_E^{\gamma 2}\|u_{ttt}\|^2_{2,0} \\ &+ \Delta t^4 \tfrac{1}{6} Re D_\epsilon^{\gamma 2} C_{PF}^2 \|p_{tt}\|^2_{2,0} + \Delta t^4 \tfrac{1}{6} Re^{-1} D_\epsilon^{\gamma 2}\|\nabla u_{tt}\|^2_{2,0} + \Delta t^4 \tfrac{1}{96} D_E^{\gamma 2}\|T_{tt}\|^2_{2,0} \\ &+ \Delta t^4 \tfrac{1}{12}\sigma_1^2 Re D_\epsilon^{\gamma 2}\|\nabla u_{tt}\|^4_{4,0} + \Delta t^4 2\sigma_1^2 Re D_\epsilon^{\gamma 2}\|\nabla \xi(u^{1/2})\|^4_{4,0} + \Delta t^4 4\sigma_1^2 Re D_\epsilon^{\gamma 2}\|\nabla u\|^4_{4,0} \\ &+ \Delta t^4 \tfrac{49}{6}\sigma_1^2 Re D_\epsilon^{\gamma 2}\|\nabla u_{tt}\|^4_{4,0} + \gamma^2(\alpha^{4N+4} + \alpha^2 h^{2k} + h^{2k+2}) 4ReCD_\epsilon^{\gamma 2} \sum_{i=1}^{N} |||F^{i+1}u^{1/2}|||^2_{2,k+1} \\ &+ \lambda^2(\alpha^{4N+4} + \alpha^2 h^{2k} + h^{2k+2}) 4ReCD_\epsilon^{\lambda 2} \sum_{i=1}^{N} \Big(|||F^{i+1}u^{-1/2}|||^2_{2,k+1} + |||F^{i+1}u^{-3/2}|||^2_{2,k+1}\Big).\end{aligned} \tag{5.45}$$

Now, using (5.44) and (5.45) in (5.43) and adding (5.33)

$$
\begin{aligned}
&(\|E_h^M\|^2 + \|e_h^M\|^2_{E^\gamma,N}) - (\|E_h^0\|^2 + \|e_h^0\|^2_{E^\gamma,N}) + \Delta t Re^{-1} \sum_{n=0}^{M-1} (\|e_h^{n+\frac{1}{2}}\|^2_{\epsilon^\gamma,N} + Pr^{-1}\|\nabla E_h^{n+\frac{1}{2}}\|^2) \\
&\le h^{2k} 16 (RePr)^{-1} C |||T^{1/2}|||^2_{2,k+1} + h^{2k} 8A_1^2 RePrC |||\xi(u^{1/2})|||^4_{4,k+1} + h^{2k} 8A_1^2 RePrC |||\nabla T^{1/2}|||^4_{4,0} \\
&+ h^{2k} 8A_2^2 RePrC |||\nabla \xi(u_h^{1/2})|||^2_{2,0} + h^{2k} 8A_2^2 RePrC |||T^{1/2}|||^4_{4,k+1} + \Delta t^4 \tfrac{RePrC_{PF}^2}{80} \|T_{ttt}\|^2_{2,0} \\
&+ \Delta t^4 \tfrac{(RePr)^{-1}}{3} \|\nabla T_{tt}\|^2_{2,0} + \Delta t^4 \tfrac{A_1^2 RePr}{6} |||\nabla \xi(u^{1/2})|||^4_{4,0} + \Delta t^4 \tfrac{A_1^2 RePr}{6} \|\nabla T_{tt}\|^4_{4,0} + \Delta t^4 \tfrac{49A_1^2 RePr}{3} \|\nabla T^{1/2}\|^4_{4,0} \\
&+ \Delta t^4 \tfrac{49A_1^2 RePr}{3} \|\nabla u_{tt}\|^4_{4,0} + \Delta t^4 \tfrac{5}{12} ReD_\epsilon^{\gamma 2} \|p_{tt}\|^2_{2,0} + h^{2s+2} 20ReCD_\epsilon^{\gamma 2} \|p^{1/2}\|^2_{2,s+1} \\
&+ h^{2k} 20Re^{-1}(1+\kappa Re)^2 CD_\epsilon^{\gamma 2} |||u|||^2_{2,k+1} + h^{2k} 10Re\sigma_1^2 D_2^{\lambda 2} D_\epsilon^{\gamma 2} D_2^{\gamma 2} C |||u^{-1/2}|||^4_{4,k+1} \\
&+ h^{2k} 10Re\sigma_1^2 D_2^{\lambda 2} D_\epsilon^{\gamma 2} D_2^{\gamma 2} C |||u^{-3/2}|||^4_{4,k+1} + h^{2k} 10Re\sigma_1^2 D_2^{\lambda 2} D_2^{\gamma 2} D_\epsilon^{\gamma 2} C |||\nabla u|||^4_{4,0} \\
&+ h^{2k} 10\sigma_2^2 ReD_E^\lambda D_\epsilon^\lambda D_2^{\gamma 2} D_\epsilon^{\gamma 2} C \|\nabla \xi(u_h)\|^2_{2,0} + h^{2k} 10Re\sigma_2^2 D_E^\lambda D_\epsilon^\lambda D_2^{\gamma 2} D_\epsilon^{\gamma 2} C |||u|||^4_{4,k+1} \\
&+ \Delta t^4 \tfrac{1}{1280} D_E^{\gamma 2} \|u_{ttt}\|^2_{2,0} + \Delta t^4 \tfrac{1}{3} D_\epsilon^{\gamma 2} C_{PF}^2 \|p_{tt}\|^2_{2,0} + \Delta t^4 \tfrac{Re^{-1}}{3} D_\epsilon^{\gamma 2} \|\nabla u_{tt}\|^2_{2,0} + \Delta t^4 \tfrac{1}{48} D_E^{\gamma 2} \|T_{tt}\|^2_{2,0} \\
&+ \Delta t^4 \tfrac{1}{6} \sigma_1^2 ReD_\epsilon^{\gamma 2} \|\nabla u_{tt}\|^4_{4,0} + \Delta t^4 4\sigma_1^2 ReD_\epsilon^{\gamma 2} |||\nabla \xi(u^{1/2})|||^4_{4,0} + \Delta t^4 8\sigma_1^2 ReD_\epsilon^{\gamma 2} \|\nabla u\|^4_{4,0} \\
&+ \Delta t^4 \tfrac{49}{3} \sigma_1^2 ReD_\epsilon^{\gamma 2} \|\nabla u_{tt}\|^4_{4,0} + \gamma^2 (\alpha^{4N+4} + \alpha^2 h^{2k} + h^{2k+2}) 8ReCD_\epsilon^{\gamma 2} \sum_{i=1}^{N} |||F^{i+1} u^{1/2}|||^2_{2,k+1} \\
&+ \lambda^2 (\alpha^{4N+4} + \alpha^2 h^{2k} + h^{2k+2}) 8ReCD_\epsilon^{\lambda 2} \sum_{i=1}^{N} \Big(|||F^{i+1} u^{-1/2}|||^2_{2,k+1} + |||F^{i+1} u^{-3/2}|||^2_{2,k+1} \Big) \\
&+ \Delta t \sum_{n=0}^{M-1} \Big[1 + Ri^2 + 2C_{PF}^2 Ri^2 RePrD_E^{\gamma 2} + 2^9 3A_2^4 Re^3 Pr^2 C^2_{E^\gamma,N} C^2_{\epsilon^\gamma,N} (2\|\nabla T^{n+\frac{1}{2}}\|^4 + \|\nabla T^{n+\frac{3}{2}}\|^4) \\
&+ 20^2 6Re^3 \sigma_2^4 D_E^{\lambda 2} D_\epsilon^{\lambda 2} D_\epsilon^{\gamma 4} D_2^{\gamma 4} (2\|\nabla u^{n+\frac{1}{2}}\|^4 + \|\nabla u^{n+\frac{3}{2}}\|^4) \Big] \|e_h^{n+\frac{1}{2}}\|^2_{E^\gamma,N} + h^{2k} \tfrac{1}{3} c^{-2}_{\epsilon^\gamma,N} Re^{-1} \|u(0)\|^2_{k+1} \\
&+ h^{2k+2} 2^{11} 3A_2^4 Re^3 Pr^2 C^2_{E^\gamma,N} C^2_{\epsilon^\gamma,N} Cc^{-2}_{E^\gamma,N} (2\|\nabla T^{\frac{1}{2}}\|^4 + \|\nabla T^{\frac{3}{2}}\|^4) \|u(0)\|^2_{k+1} \\
&+ h^{2k+2} 20^2 6Re^3 \sigma_2^4 D_E^{\lambda 2} D_\epsilon^{\lambda 2} D_\epsilon^{\gamma 4} D_2^{\gamma 4} Cc^{-2}_{E^\gamma,N} (2\|\nabla u^{\frac{1}{2}}\|^4 + \|\nabla u^{\frac{3}{2}}\|^4) \|u(0)\|^2_{k+1},
\end{aligned}
$$

where we have used that

$$
\sum_{n=0}^{M-1} \|\xi(e_h^{n+\frac{1}{2}})\|^2_{\epsilon^\gamma,N} \le 3 \sum_{n=1}^{M-1} \|e_h^{n+\frac{1}{2}}\|^2_{\epsilon^\gamma,N} + h^{2k} 4Cc^{-2}_{\epsilon^\gamma,N} \|u(0)\|^2_{k+1}.
$$

Now, let

$$
\begin{aligned}
W :=\ & 1 + Ri^2 + 2C_{PF}^2 Ri^2 RePrD_E^{\gamma 2} + 2^9 3A_2^4 Re^3 Pr^2 C^2_{E^\gamma,N} C^2_{\epsilon^\gamma,N} (\|\nabla T^{n+\frac{1}{2}}\|^4 + \|\nabla T^{n+\frac{3}{2}}\|^4) \\
& + 20^2 6Re^3 \sigma_2^4 D_E^{\lambda 2} D_\epsilon^{\lambda 2} D_\epsilon^{\gamma 4} D_2^{\gamma 4} (\|\nabla u^{n+\frac{1}{2}}\|^4 + \|\nabla u^{n+\frac{3}{2}}\|^4), \qquad (5.46)
\end{aligned}
$$

and considering $\Delta t < W^{-1}$ (in order to apply the Gronwall's inequality) we have

$$
\begin{aligned}
&(\|E_h^M\|^2 + \|e_h^M\|^2_{E^\gamma,N}) - (\|E_h^0\|^2 + \|e_h^0\|^2_{E^\gamma,N}) + \Delta t Re^{-1} \sum_{n=0}^{M-1} (\|e_h^{n+\frac{1}{2}}\|^2_{\epsilon^\gamma,N} + Pr^{-1}\|\nabla E_h^{n+\frac{1}{2}}\|^2)\\
&\leq C^*\Big\{ h^{2k}16(RePr)^{-1}C\vert\!\vert\!\vert T^{1/2}\vert\!\vert\!\vert^2_{2,k+1} + h^{2k}8A_1^2RePrC\vert\!\vert\!\vert\xi(u^{1/2})\vert\!\vert\!\vert^4_{4,k+1} + h^{2k}8A_1^2RePrC\vert\!\vert\!\vert\nabla T^{1/2}\vert\!\vert\!\vert^4_{4,0}\\
&+ h^{2k}8A_2^2RePrC\vert\!\vert\!\vert\nabla\xi(u_h^{1/2})\vert\!\vert\!\vert^2_{2,0} + h^{2k}8A_2^2RePrC\vert\!\vert\!\vert T^{1/2}\vert\!\vert\!\vert^4_{4,k+1} + \Delta t^4\tfrac{RePrC_{PF}^2}{80}\|T_{ttt}\|^2_{2,0}\\
&+ \Delta t^4\tfrac{(RePr)^{-1}}{3}\|\nabla T_{tt}\|^2_{2,0} + \Delta t^4\tfrac{A_1^2RePr}{6}\vert\!\vert\!\vert\nabla\xi(u^{1/2})\vert\!\vert\!\vert^4_{4,0} + \Delta t^4\tfrac{A_1^2RePr}{6}\|\nabla T_{tt}\|^4_{4,0} + \Delta t^4\tfrac{49A_1^2RePr}{3}\|\nabla T^{1/2}\|^4_{4,0}\\
&+ \Delta t^4\tfrac{49A_1^2RePr}{3}\|\nabla u_{tt}\|^4_{4,0} + \Delta t^4\tfrac{5}{12}ReD_\epsilon^{\gamma 2}\|p_{tt}\|^2_{2,0} + h^{2s+2}20ReCD_\epsilon^{\gamma 2}\|p^{1/2}\|^2_{2,s+1}\\
&+ h^{2k}20Re^{-1}(1+\kappa Re)^2CD_\epsilon^{\gamma 2}\vert\!\vert\!\vert u\vert\!\vert\!\vert^2_{2,k+1} + h^{2k}10Re\sigma_1^2D_2^{\lambda 2}D_\epsilon^{\gamma 2}D_2^{\gamma 2}C\vert\!\vert\!\vert u^{-1/2}\vert\!\vert\!\vert^4_{4,k+1}\\
&+ h^{2k}10Re\sigma_1^2D_2^{\lambda 2}D_\epsilon^{\gamma 2}D_2^{\gamma 2}C\vert\!\vert\!\vert u^{-3/2}\vert\!\vert\!\vert^4_{4,k+1} + h^{2k}10Re\sigma_1^2D_2^{\lambda 2}D_2^{\gamma 2}D_\epsilon^{\gamma 2}C\vert\!\vert\!\vert\nabla u\vert\!\vert\!\vert^4_{4,0}\\
&+ h^{2k}10\sigma_2^2ReD_E^{\lambda}D_\epsilon^{\lambda}D_2^{\gamma 2}D_\epsilon^{\gamma 2}C\|\nabla\xi(u_h)\|^2_{2,0} + h^{2k}10Re\sigma_2^2D_E^{\lambda}D_\epsilon^{\lambda}D_2^{\gamma 2}D_\epsilon^{\gamma 2}C\vert\!\vert\!\vert u\vert\!\vert\!\vert^4_{4,k+1}\\
&+ \Delta t^4\tfrac{1}{1280}D_E^{\gamma 2}\|u_{ttt}\|^2_{2,0} + \Delta t^4\tfrac{1}{3}D_\epsilon^{\gamma 2}C_{PF}^2\|p_{tt}\|^2_{2,0} + \Delta t^4\tfrac{Re^{-1}}{3}D_\epsilon^{\gamma 2}\|\nabla u_{tt}\|^2_{2,0} + \Delta t^4\tfrac{1}{48}D_E^{\gamma 2}\|T_{tt}\|^2_{2,0}\\
&+ \Delta t^4\tfrac{1}{6}\sigma_1^2ReD_\epsilon^{\gamma 2}\|\nabla u_{tt}\|^4_{4,0} + \Delta t^4 4\sigma_1^2ReD_\epsilon^{\gamma 2}\|\nabla\xi(u^{1/2})\|^4_{4,0} + \Delta t^4 8\sigma_1^2ReD_\epsilon^{\gamma 2}\|\nabla u\|^4_{4,0}\\
&+ \Delta t^4\tfrac{49}{3}\sigma_1^2ReD_\epsilon^{\gamma 2}\|\nabla u_{tt}\|^4_{4,0} + \gamma^2(\alpha^{4N+4} + \alpha^2h^{2k} + h^{2k+2})8ReCD_\epsilon^{\gamma 2}\sum_{i=1}^{N}\vert\!\vert\!\vert F^{i+1}u^{1/2}\vert\!\vert\!\vert^2_{2,k+1}\\
&+ \lambda^2(\alpha^{4N+4} + \alpha^2h^{2k} + h^{2k+2})8ReCD_\epsilon^{\lambda 2}\sum_{i=1}^{N}\Big(\vert\!\vert\!\vert F^{i+1}u^{-1/2}\vert\!\vert\!\vert^2_{2,k+1} + \vert\!\vert\!\vert F^{i+1}u^{-3/2}\vert\!\vert\!\vert^2_{2,k+1}\Big)\\
&+ h^{2k}\tfrac{1}{3}c_{\epsilon^\gamma,N}^{-2}Re^{-1}\|u(0)\|^2_{k+1} + h^{2k+2}2^{11}3A_2^4Re^3Pr^2C_{E^\gamma,N}^2C_{\epsilon^\gamma,N}^2Cc_{E^\gamma,N}^{-2}(2\|\nabla T^{\frac{1}{2}}\|^4 + \|\nabla T^{\frac{3}{2}}\|^4)\|u(0)\|^2_{k+1}\\
&+ h^{2k+2}20^2 6Re^3\sigma_2^4D_E^{\lambda 2}D_\epsilon^{\lambda 2}D_\epsilon^{\gamma 4}D_2^{\gamma 4}Cc_{E^\gamma,N}^{-2}(2\|\nabla u^{\frac{1}{2}}\|^4 + \|\nabla u^{\frac{3}{2}}\|^4)\|u(0)\|^2_{k+1}\Big\}.
\end{aligned}
\tag{5.47}
$$

where

$$C^* := exp\Big\{\Delta t\sum_{n=0}^{M-1}\tfrac{W}{1-\Delta tW}\Big\}.$$

Estimates (5.16) - (5.19) follow from (5.47) and the triangle inequality.

□

5.4 Numerical experiments

In this section we provide two examples to confirm the convergence theory and compare the solutions obtained with the diferent regularized Boussinesq model. In the first we estimate convergence rates using an analytical solution based on the Taylor-Green solution for Navier-Stokes equations. In the second, the regularized models were evaluated in traditional the Marsigli's flow benchmark. Both experiments were made with the FreeFem++ software [40] using a multi-frontal Gauss LU factorization implemented in the package UMFPACK (provided with FreeFem++ software).

5.4.1 Convergence rates

In order to evaluate the computational implementation of the above mentioned algorithm and validate its convergence theory, in this section we estimate convergence rates for four regularized versions of the Boussinesq model. To perform this analysis, we adapt the traditional Taylor-Green solution used for Navier-Stokes equations as a means to construct a solution of the Boussinesq model. Considering the forcing $f = \Big(0, -Ri \exp\big[-\frac{2m^2\pi^2 t}{Re}\big]\cos(N\pi x)\cos(m\pi y)\Big)$ and the square domain $[0,1]\times[0,1]$ we obtain the following solution of Boussinesq model:

$$
\begin{aligned}
p &= -\tfrac{1}{4}\exp\left[-\tfrac{2m^2\pi^2 t}{Re}\right][\cos(2m\pi x)+\cos(2m\pi y)]\\
u_1 &= -\exp\left[-\tfrac{2m^2\pi^2 t}{Re}\right]\cos(m\pi x)\sin(m\pi y)\\
u_2 &= \exp\left[-\tfrac{2m^2\pi^2 t}{Re}\right]\sin(m\pi x)\cos(m\pi y)\\
T &= \exp\left[-\tfrac{2m^2\pi^2 t}{Re}\right]\cos(m\pi x)\cos(m\pi y).
\end{aligned}
$$

In this experiment we considered the temporal interval $[0,2]$, Taylor-Hood and $P_2/P_3/P_3$ elements and $m = 1$. We also considered regular meshes for $h = \frac{1}{8}$, $h = \frac{1}{16}$, $h = \frac{1}{32}$ and $h = \frac{1}{64}$ and $\alpha = h$. Then we carefully chose the timestep Δt in order to balance error sources from the convergence theorem. In Tables 5.2 - 5.9 we present convergence rates estimated for several regularized Boussinesq model (Boussinesq-α, Boussinesq-Leray, Boussinesq-ω and Modified-Boussinesq-Leray Models).

Examining the above mentioned tables, we observe that estimated convergence rates agree well with the convergence theory presented in the previous section. That is, the proposed algorithms are second order accurate when zeroth

Element	h^{-1}	$\|u - u_h\|_{2,1}$	Rate	$\|u - u_h\|_{\infty,0}$	Rate	$\|T - T_h\|_{2,1}$	Rate	$\|T - T_h\|_{\infty,0}$	rate
$P_1/P_2/P_2$	8	8.2406E-03		5.4350E-01		2.4673E-02		5.8004E-04	
$\Delta t = h$	16	1.6296E-03	2.34	1.4125E-01	1.94	6.2468E-03	1.98	7.1054E-05	3.03
	32	2.9362E-04	2.47	3.6040E-02	1.97	1.5694E-03	1.99	8.9673E-06	2.99
	64	5.8693E-05	2.32	9.0846E-03	1.99	3.9314E-04	2.00	1.2103E-06	2.89
$P_2/P_3/P_3$	8	1.0791E-03		2.3390E-05		8.6364E-04		4.1567E-05	
$\Delta t = h$	16	1.7465E-04	2.63	5.2190E-06	2.16	1.1353E-04	2.93	7.7097E-06	2.43
	32	2.6206E-05	2.74	1.3616E-06	1.94	1.7428E-05	2.70	2.0195E-06	1.93
	64	3.9838E-06	2.72	3.5066E-07	1.96	3.3903E-06	2.36	5.2456E-07	1.94

Table 5.2: Convergence rates for Boussinesq-α-D_0 for $Re = 10$, $Ri = 1$ and $Pr = 10$.

Element	h^{-1}	$\|u - u_h\|_{2,1}$	Rate	$\|u - u_h\|_{\infty,0}$	Rate	$\|T - T_h\|_{2,1}$	Rate	$\|T - T_h\|_{\infty,0}$	rate
$P_1/P_2/P_2$	8	8.4932E-03		2.5673E-04		2.4674E-02		5.8172E-04	
$\Delta t = h$	16	1.7018E-03	2.32	2.4209E-05	3.41	6.2468E-03	1.98	7.1158E-05	3.03
	32	3.0447E-04	2.48	2.4857E-06	3.28	1.5694E-03	1.99	8.9607E-06	2.99
	64	5.9807E-05	2.35	4.0743E-07	2.61	3.9314E-04	2.00	1.2071E-06	2.89
$P_2/P_3/P_3$	8	1.0250E-03		1.3447E-05		8.4919E-04		3.2884E-05	
$\Delta t = h^{3/2}$	16	1.1178E-04	3.20	9.1164E-07	3.88	1.0400E-04	3.03	2.0305E-06	4.02
	32	6.9374E-06	4.01	4.8437E-08	4.23	1.2861E-05	3.02	1.3077E-07	3.96
	64	4.8708E-07	3.83	5.7931E-09	3.06	1.5991E-06	3.01	1.0929E-08	3.58

Table 5.3: Convergence rates for Boussinesq-α-D_1 for $Re = 10$, $Ri = 1$ and $Pr = 10$.

order deconvolution ($N = 0$) is chosen and third order for first order deconvolution ($N = 1$). We do not test the second order deconvolution case because, even using P2/P3/P3 elements, the algorithm would still be second order accurate and no differences in terms of convergence rates are expected in this case in comparison to the $N = 1$ case. However, as will be shown in the next section, despite having no difference in terms of accuracy, even for P1/P2/P2 elements, increasing deconvolution order still improves significantly the obtained solutions.

5.4.2 Marsigli's experiment with $Re = 2000$

In a first test we evaluate the performance of the four above mentioned regularized versions of the Boussinesq model in the Marsigli flow experiment for $Re = 2000$. In the case of the Boussinesq-α and Modified-Boussinesq-Leray models, zeroth and first order deconvolution were tested and in the case of the Boussinesq-Leray and Boussinesq-ω regularizations, due to the decoupling between momentum and filter equations which reduces the computational cost, we also tested second

Element	h^{-1}	$\|u-u_h\|_{2,1}$	Rate	$\|u-u_h\|_{\infty,0}$	Rate	$\|T-T_h\|_{2,1}$	Rate	$\|T-T_h\|_{\infty,0}$	rate
$P_1/P_2/P_2$	8	8.4502E-03		2.5556E-04		2.4673E-02		5.8055E-04	
$\Delta t = h$	16	1.6485E-03	2.36	2.3927E-05	3.42	6.2467E-03	1.98	7.0929E-05	3.03
	32	2.9442E-04	2.49	2.4705E-06	3.28	1.5694E-03	1.99	8.9674E-06	2.98
	64	5.8688E-05	2.33	4.0781E-07	2.60	3.9314E-04	2.00	1.2109E-06	2.89
$P_2/P_3/P_3$	8	1.1322E-03		2.4034E-05		8.6363E-04		4.1510E-05	
$\Delta t = h$	16	1.8172E-04	2.64	5.2399E-06	2.20	1.1353E-04	2.93	7.7078E-06	2.43
	32	2.6917E-05	2.76	1.3620E-06	1.94	1.7432E-05	2.70	2.0200E-06	1.93
	64	4.0499E-06	2.73	3.5067E-07	1.96	3.3908E-06	2.36	5.2463E-07	1.94

Table 5.4: Convergence rates for Boussinesq-Leray-D_0 for $Re = 10$, $Ri = 1$ and $Pr = 10$.

Element	h^{-1}	$\|u-u_h\|_{2,1}$	Rate	$\|u-u_h\|_{\infty,0}$	Rate	$\|T-T_h\|_{2,1}$	Rate	$\|T-T_h\|_{\infty,0}$	rate
$P_1/P_2/P_2$	8	9.4437E-03		2.6755E-04		2.4675E-02		5.8331E-04	
$\Delta t = h$	16	1.8485E-03	2.35	2.5067E-05	3.42	6.2467E-03	1.98	7.0900E-05	3.04
	32	3.2144E-04	2.52	2.5350E-06	3.31	1.5694E-03	1.99	8.9648E-06	2.98
	64	6.1323E-05	2.39	4.0963E-07	2.63	3.9314E-04	2.00	1.2107E-06	2.89
$P_2/P_3/P_3$	8	1.1394E-03		1.7152E-05		8.4920E-04		3.2887E-05	
$\Delta t = h^{3/2}$	16	1.1847E-04	3.27	1.0554E-06	4.02	1.0400E-04	3.03	2.0327E-06	4.02
	32	6.9510E-06	4.09	4.8975E-08	4.43	1.2861E-05	3.02	1.3116E-07	3.95
	64	4.8441E-07	3.84	5.8058E-09	3.08	1.5991E-06	3.01	1.1029E-08	3.57

Table 5.5: Convergence rates for Boussinesq-Leray-D_1 for $Re = 10$, $Ri = 1$ and $Pr = 10$.

order deconvolution, in addition to zeroth and first order. Simulations were made in the $[0, 8] \times [0, 1]$ rectangle and they last from t=0 until t=8 with a time step of $\Delta t = 0.002$. In addition, P2 elements for velocity and temperature and P1 elements for pressure were employed in these simulations. In order to evaluate the regularized versions of the Boussinesq model, solutions obtained in a coarse mesh with the regularized and the original Boussinesq model (with and without artificial viscosity) are compared with a high resolution solution. The high resolution test was made using regular triangular elements with mesh-width $h = 0.01$ which corresponds to a grid of 800×100 squares. Solutions obtained for instants 2, 4, 6 and 8 with the Boussinesq model without regularization in the high resolution mesh are shown respectively in Figures 5.1(a), 5.2(a), 5.3(a) and 5.4(a). These figures show that the Boussinesq model was able to reproduce the expected behavior in this kind of flow, namely, the dense fluid moving in a lower current to the left and the light fluid moving in a upper current to the right. Moreover, as expected, a vortex sheet in the interface between the upper and lower part of fluid is formed due to the development of Kelvin-Helmholtz instabilities.

Element	h^{-1}	$\|u-u_h\|_{2,1}$	Rate	$\|u-u_h\|_{\infty,0}$	Rate	$\|T-T_h\|_{2,1}$	Rate	$\|T-T_h\|_{\infty,0}$	rate
$P_1/P_2/P_2$	8	9.0285E-03		2.6345E-04		2.4674E-02		5.7970E-04	
$\Delta t = h$	16	1.8171E-03	2.31	2.5396E-05	3.37	6.2491E-03	1.98	7.7991E-05	2.89
	32	3.2101E-04	2.50	2.8748E-06	3.14	1.5700E-03	1.99	1.2810E-05	2.61
	64	6.1481E-05	2.38	4.6921E-07	2.62	3.9322E-04	2.00	2.0650E-06	2.63
$P_2/P_3/P_3$	8	1.2850E-03		2.4843E-05		8.6559E-04		4.1838E-05	
$\Delta t = h$	16	2.2380E-04	2.52	5.3228E-06	2.22	1.1369E-04	2.93	7.7635E-06	2.43
	32	3.4019E-05	2.72	1.3653E-06	1.96	1.7456E-05	2.70	2.0267E-06	1.94
	64	4.9874E-06	2.77	3.5080E-07	1.96	3.3931E-06	2.36	5.2523E-07	1.95

Table 5.6: Convergence rates for Boussinesq-ω-D_0 for $Re = 10$, $Ri = 1$ and $Pr = 10$.

Element	h^{-1}	$\|u-u_h\|_{2,1}$	Rate	$\|u-u_h\|_{\infty,0}$	Rate	$\|T-T_h\|_{2,1}$	Rate	$\|T-T_h\|_{\infty,0}$	rate
$P_1/P_2/P_2$	8	1.1452E-02		2.9813E-04		2.4678E-02		5.8392E-04	
$\Delta t = h$	16	2.4189E-03	2.24	2.9144E-05	3.35	6.2503E-03	1.98	8.1489E-05	2.84
	32	4.1286E-04	2.55	2.9978E-06	3.28	1.5699E-03	1.99	1.1882E-05	2.78
	64	7.1533E-05	2.53	4.4424E-07	2.75	3.9318E-04	2.00	1.6335E-06	2.86
$P_2/P_3/P_3$	8	1.6575E-03		2.1259E-05		8.4985E-04		3.3620E-05	
$\Delta t = h^{3/2}$	16	1.6536E-04	3.33	1.4616E-06	3.86	1.0403E-04	3.03	2.0931E-06	4.01
	32	8.5377E-06	4.28	5.3917E-08	4.76	1.2862E-05	3.02	1.3469E-07	3.96
	64	5.4761E-07	3.96	5.8337E-09	3.21	1.5992E-06	3.01	1.1194E-08	3.59

Table 5.7: Convergence rates for Boussinesq-ω-D_1 for $Re = 10$, $Ri = 1$ and $Pr = 10$.

Now, we present the results obtained in the coarse mesh with the Boussinesq model without regularization. In this test we adopted regular triangular elements with $h = 0.034$, which corresponds to a grid with 240 × 30 squares. The obtained results are presented in Figures 5.1(b), 5.2(b), 5.3(b) and 5.4(b). We see that at $t = 2$ solution is very noisy and in the subsequent instants it degenerates.

After that, we test the commonly used technique of artificial viscosity in which the viscosity is artificially increased in order to stabilize the model. Solution obtained for $Re = 1000$ is presented in Figures 5.1(c), 5.2(c) and 5.3(c) and 5.4(c) and for $Re = 1500$ in Figures 5.1(d), 5.2(d), 5.3(d) and 5.4(d). For the case in which $Re = 1000$ we observe that the consistency error is large causing the solution to be smoother when compared to the fine solution. On the other hand, when $Re = 1500$ solution gradually becomes noisy and in the final instant $t = 8$ it degenerates.

Finally, we present the results obtained with regularized Boussinesq models using $\alpha = h$. Figures 5.1, 5.2, 5.3 and 5.4 (e) and (f) present the results produced with Boussinesq-α (D_0 and D_1, respectively), (g), (h) and (m) the results

Element	h^{-1}	$\Vert u-u_h\Vert_{2,1}$	Rate	$\Vert u-u_h\Vert_{\infty,0}$	Rate	$\Vert T-T_h\Vert_{2,1}$	Rate	$\Vert T-T_h\Vert_{\infty,0}$	rate
$P_1/P_2/P_2$	8	8.1597E-03		2.5235E-04		2.4674E-02		5.8082E-04	
$\Delta t = h$	16	1.5943E-03	2.36	2.4448E-05	3.37	6.2493E-03	1.98	7.8429E-05	2.89
	32	2.8740E-04	2.47	2.8313E-06	3.11	1.5700E-03	1.99	1.2814E-05	2.61
	64	5.8033E-05	2.31	4.6741E-07	2.60	3.9322E-04	2.00	2.0547E-06	2.64
$P_2/P_3/P_3$	8	1.0555E-03		2.3287E-05		8.6386E-04		4.1871E-05	
$\Delta t = h$	16	1.6475E-04	2.68	5.2081E-06	2.16	1.1367E-04	2.93	7.7594E-06	2.43
	32	2.4280E-05	2.76	1.3619E-06	1.94	1.7455E-05	2.70	2.0260E-06	1.94
	64	3.7226E-06	2.71	3.5072E-07	1.96	3.3930E-06	2.36	5.2516E-07	1.95

Table 5.8: Convergence rates for Modified-Boussinesq-Leray-D_0 for $Re = 10$, $Ri = 1$ and $Pr = 10$.

Element	h^{-1}	$\Vert u-u_h\Vert_{2,1}$	Rate	$\Vert u-u_h\Vert_{\infty,0}$	Rate	$\Vert T-T_h\Vert_{2,1}$	Rate	$\Vert T-T_h\Vert_{\infty,0}$	rate
$P_1/P_2/P_2$	8	8.2715E-03		2.5470E-04		2.4679E-02		5.8579E-04	
$\Delta t = h$	16	1.6244E-03	2.35	2.6019E-05	3.29	6.2530E-03	1.98	8.8815E-05	2.72
	32	2.9208E-04	2.48	3.3004E-06	2.98	1.5709E-03	1.99	1.6509E-05	2.43
	64	5.8521E-05	2.32	5.3450E-07	2.63	3.9332E-04	2.00	2.7328E-06	2.59
$P_2/P_3/P_3$	8	9.1121E-04		1.2501E-05		8.5000E-04		3.3897E-05	
$\Delta t = h^{3/2}$	16	1.0280E-04	3.15	8.2361E-07	3.92	1.0404E-04	3.03	2.1274E-06	3.99
	32	6.6840E-06	3.94	4.7824E-08	4.11	1.2863E-05	3.02	1.3720E-07	3.95
	64	4.7804E-07	3.81	5.8014E-09	3.04	1.5992E-06	3.01	1.1257E-08	3.61

Table 5.9: Convergence rates for Modified-Boussinesq-Leray-D_1 for $Re = 10$, $Ri = 1$ and $Pr = 10$.

with Boussinesq-Leray (D_0, D_1 and D_2, respectively), (i) and (j) the results with Modified-Boussinesq-Leray (D_0 and D_1, respectively) and (k), (l) and (n) the results with Boussinesq-ω (D_0, D_1 and D_2, respectively). In these figures we can see that Boussinesq-α and Boussinesq-Leray solutions are accurate and very similar to the high resolution solution. On the other hand, Boussinesq-ω and Modified-Boussinesq-Leray, despite being stable, produced very smoothed solutions in comparison with the fine solution. Moreover, at $t = 8$ only small discrepancies between Boussinesq-α-D_1 and Boussinesq-Leray-D_2 can be observed. The main difference is the central vortice which is better represented in the Boussinesq-Leray-D_2 solution. The L^2 error estimated using the fine solution as reference is presented in Table 5.10. In this table we also see that Boussinesq-Leray and Boussinesq-alpha produced the best approximations.

In Table 5.11 we also present the computional time for each model in this experiment. These simulations were made in a Intel® Core™ i7 3.70 GHz. It shows that Leray and omega regularizations presented the smaller computational due to the decoupling between the momentum and filter equations resulting from the Baker extrapolation.

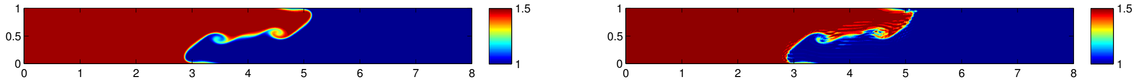

(a) DNS - High (b) DNS - Low

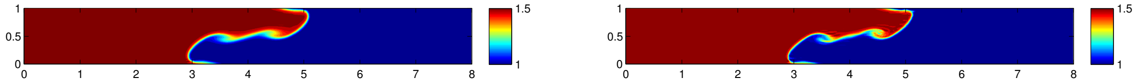

(c) Art.Visc.1 (Re=1000) - Low (d) Art.Visc.1 (Re=1500) - Low

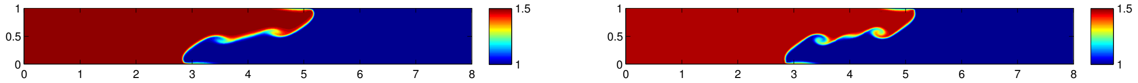

(e) Alpha - Low (f) Alpha-D_1 - Low

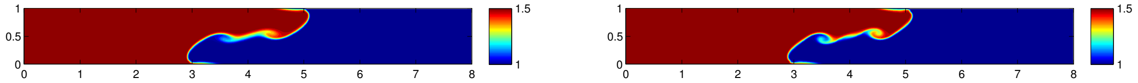

(g) Leray - Low (h) Leray-D_1 - Low

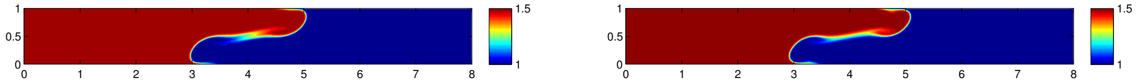

(i) Modified-Leray - Low (j) Modified-Leray-D_1 - Low

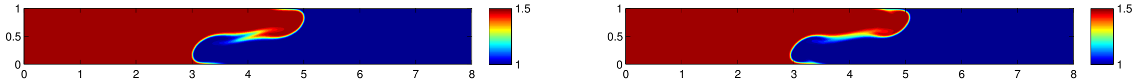

(k) Omega - Low (l) Omega-D_1 - Low

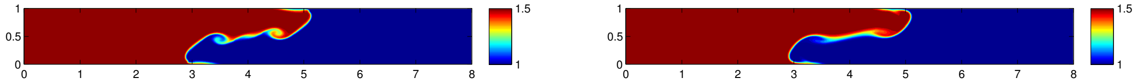

(m) Leray-D_2 - Low (n) Omega-D_2 - Low

Figure 5.1: Temperature field in the Marsigli's experiment with $Re = 2000$ for $t = 2$.

5.4.3 Marsigli's experiment with $Re = 5000$

In our last experiment, we evaluate solutions provided by the regularized versions of the Boussinesq model in the more challenging case in which $Re = 5000$. The reference high resolution solution for this experiment was obtained using a 800×100 regular triangular element mesh and a third order backward dif-

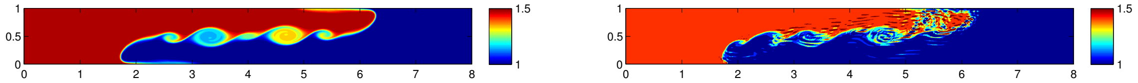

(a) DNS - High (b) DNS - Low

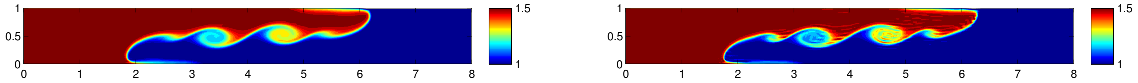

(c) Art.Visc.1 (Re=1000) - Low (d) Art.Visc.1 (Re=1500) - Low

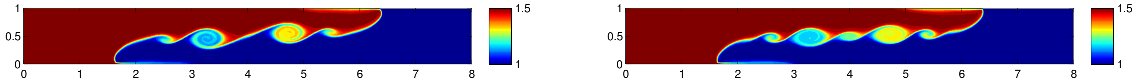

(e) Alpha - Low (f) Alpha-D1 - Low

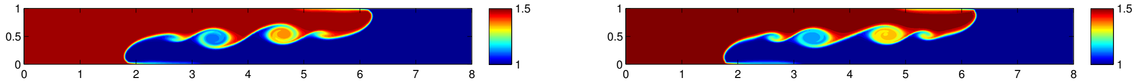

(g) Leray - Low (h) Leray-D_1 - Low

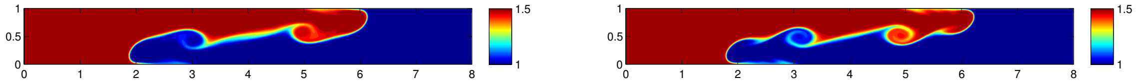

(i) Modified-Leray - Low (j) Modified-Leray-D_1 - Low

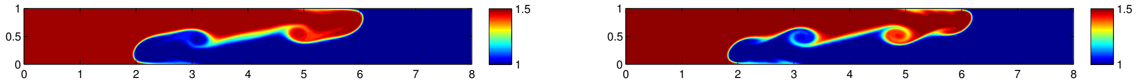

(k) Omega - Low (l) Omega-D_1 - Low

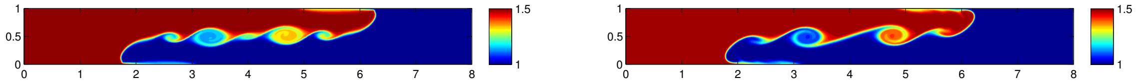

(m) Leray-D_2 - Low (n) Omega-D_2 - Low

Figure 5.2: Temperature field in the Marsigli's experiment with $Re = 2000$ for $t = 4$.

ference formulae (BDF3) time discretization scheme using $\Delta t = 0.001$. The BDF3 scheme used in the high resolution mesh was

Algorithm 5.2. *Given* u_h^0, u_h^1 *and* u_h^2 *and* T_h^0, T_h^1 *and* T_h^2, *set* $M = \frac{T}{\Delta t}$ *and for* $n = 2, ..., M-1$, *find* $u_h^{n+1} \in V_h$ *and* $T_h^{n+1} \in Y_h$ *satisfying* $\forall v_h \in V_h$ *and* $\forall s_h \in Y_h$,

$$\left\langle \frac{u_h^{n+1} - \frac{18}{11}u_h^n + \frac{9}{11}u_h^{n-1} - \frac{2}{11}u_h^{n-2}}{\Delta t}, v_h \right\rangle + \frac{6}{11}a_2\big(\xi(u_h^{n+1}), u_h^{n+1}, v_h\big) - \frac{6}{11}Re^{-1}\langle \tilde{\Delta}_h u_h^{n+\frac{1}{2}}, v_h\rangle$$

$$-\frac{6}{11}Ri\langle T_h^{n+1}\hat{k}, v_h\rangle = \frac{6}{11}\langle f^{n+1}, v_h\rangle$$

$$\left\langle \frac{T_h^{n+1} - \frac{18}{11}T_h^n + \frac{9}{11}T_h^{n-1} - \frac{2}{11}T_h^{n-2}}{\Delta t}, s_h \right\rangle + \frac{6}{11}a^*\big(\xi(u_h^{n+1}), T_h^{n+1}, s_h\big) + \frac{6}{11}(RePr)^{-1}\langle \nabla T_h^{n+1}, \nabla s_h\rangle = 0,$$

where ξ *is the extrapolation operator defined by* $\xi(u_h^{n+1}) = 3u_h^n - 3u_h^{n-1} + u_h^{n-2}$.

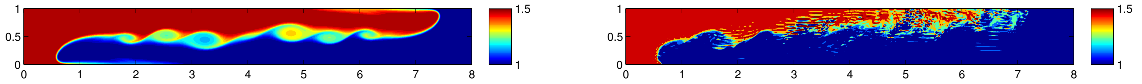

(a) DNS - High (b) DNS - Low

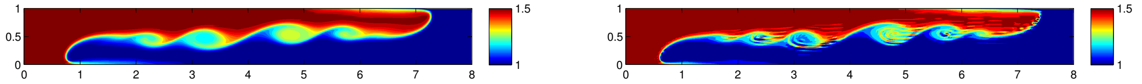

(c) Art.Visc.1 (Re=1000) - Low (d) Art.Visc.1 (Re=1500) - Low

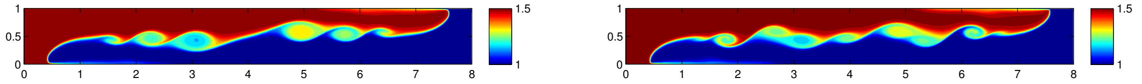

(e) Alpha - Low (f) Alpha-D1 - Low

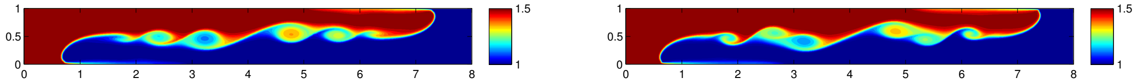

(g) Leray - Low (h) Leray-D_1 - Low

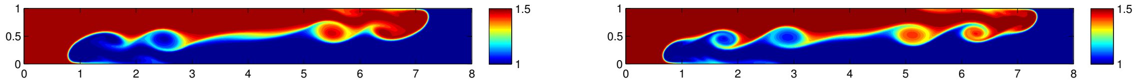

(i) Modified-Leray - Low (j) Modified-Leray-D_1 - Low

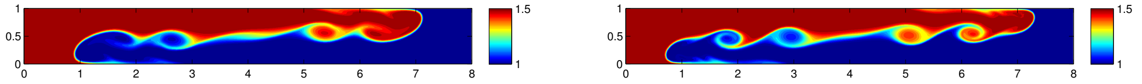

(k) Omega - Low (l) Omega-D_1 - Low

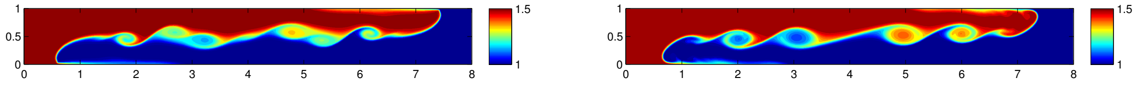

(m) Leray-D_2 - Low (n) Omega-D_2 - Low

Figure 5.3: Temperature field in the Marsigli's experiment with $Re = 2000$ for $t = 6$.

Remark 5.6. *We have used the BDF3 scheme because it is third order accurate which allowed more accuracy with less computational effort. However, it has the disadvantage of being conditionally stable.*

Remark 5.7. *The three initial condition* u_h^0, u_h^1 *and* u_h^2 *and* T_h^0, T_h^1 *and* T_h^2 *necessary for three step backward differentiation method should be provided by a single-step method as proposed in [2]. In our experiment the Crank-Nicolson single step method was used to provide* u_h^0, u_h^1 *and* u_h^2 *and* T_h^0, T_h^1 *and* T_h^2.

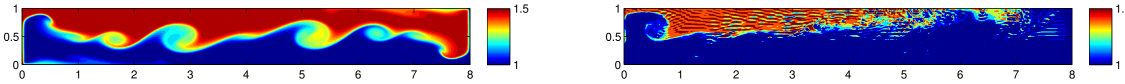

(a) DNS - High (b) DNS - Low

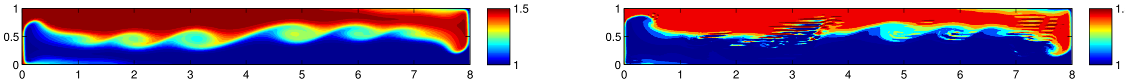

(c) Art.Visc.1 (Re=1000) - Low (d) Art.Visc.1 (Re=1500) - Low

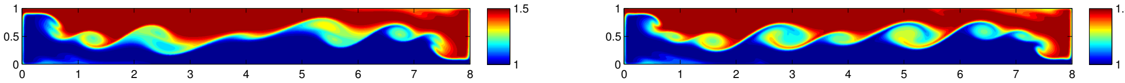

(e) Alpha - Low (f) Alpha-D1 - Low

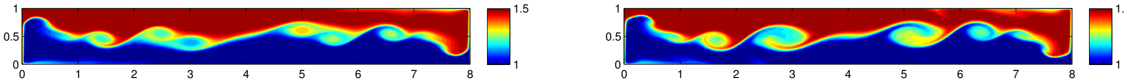

(g) Leray - Low (h) Leray-D_1 - Low

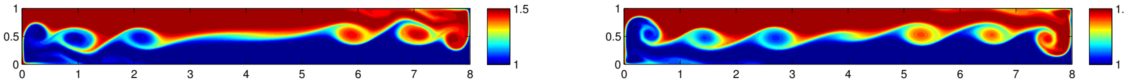

(i) Modified-Leray - Low (j) Modified-Leray-D_1 - Low

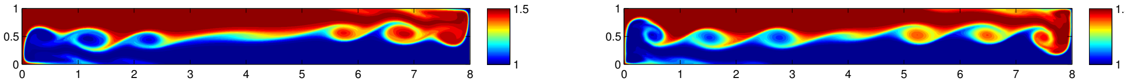

(k) Omega - Low (l) Omega-D_1 - Low

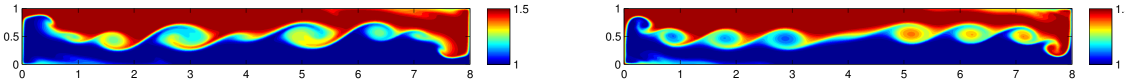

(m) Leray-D_2 - Low (n) Omega-D_2 - Low

Figure 5.4: Temperature field in the Marsigli's experiment with $Re = 2000$ for $t = 8$.

Results obtained in the high resolution mesh are presented in Figures 5.5(a), 5.6(a), 5.7(a) and 5.8(a). In these figures we can observe that the high resolution solution completely agree with the results presented in [69], where the same experiment was performed but with different spatial and temporal discretization techniques.

In order to evaluate the solutions obtained with regularized Boussinesq models for $Re = 5000$ when the mesh is coarse, we accomplished an experiment in a coarse mesh using regular triangular elements with $h = 0.02$, which corresponds to a grid with 400×50 squares. Solution produced with the Boussinesq model

	$\|T_h^{coarse} - T_h^{fine}\|_{2,0}^2$
Boussinesq	2.5974
Boussinesq+Art. Visc. 1000	0.21506
Boussinesq+Art. Visc. 1500	0.2377
Boussinesq-alpha	0.2218
Boussinesq-alpha-D_1	0.145034
Boussinesq-Modified-Leray	0.42708
Boussinesq-Modified-Leray-D_1	0.24884
Boussinesq-Leray	0.142466
Boussinesq-Leray-D_1	0.057094
Boussinesq-Leray-D_2	0.044276
Boussinesq-omega	0.4889
Boussinesq-omega-D_1	0.27158
Boussinesq-omega-D_2	0.2071

Table 5.10: $L^2(0,8;\Omega)$ error estimates in the coarse mesh temperature aproximations for $Re = 2000$.

Fine	Coarse	alpha		Leray			Leray-Mod		omega		
		D_0	D_1	D_0	D_1	D_2	D_0	D_1	D_0	D_1	D_2
2.65e6	1.08e5	1.09e5	1.09e5	3.6e4	4.8e4	6.2e4	8.8e4	2.8e5	3.2e4	4.52e4	6.0e4

Table 5.11: Computational time in seconds obtained in simulations with Boussinesq model and its regularizations for $Re = 2000$.

(without regularization) in the coarse mesh is presented in Figures 5.5(b), 5.6(b), 5.7(b) and 5.8(b). In these figures we can see that solution quickly degenerates using the Boussinesq model without regularization.

Also, we evaluate the Boussinesq model solution obtained in the coarse mesh when viscosity is increased in order to stabilize the model (artificial viscosity technique). In Figures 5.5(c), 5.6(c), 5.7(c) and 5.8(c) we present solutions produced using $Re = 1000$ and in Figures 5.5(d), 5.6(d), 5.7(d) and 5.8(d) using $Re = 1500$. In these figures we see that the solution becomes quite smoothed in both $Re = 1000$ and $Re = 1500$ cases due to the consistency error caused by increasing the viscosity coefficient.

Finally, we present the solutions obtained in the coarse mesh with regularized versions of the Boussinesq model. In this experiment we also adopted $\alpha = h$. Results for $t = 2$ are presented in Figure 5.5. In this instant we observe that solutions are generally good, except in the case of the Boussinesq-ω and Modified-

Boussinesq-Leray without deconvolution. However, solutions produced by the deconvolved versions of these models are also accurate at $t = 2$. At $t = 4$ (Figure 5.6) solutions provided by the regularized versions of Boussinesq model start to present significant differences between them. Although all deconvolved solutions are stable, we observe that the Boussinesq-α-D_1 and Boussinesq-Leray-D_2 were more similar to the high resolution solution at $t = 4s$. Moreover, we observe that in general all regularized models are improved when the deconvolution order is increased. A similar pattern is still observed in $t = 6$ (Figure 5.7). Nevertheless, the Boussinesq-α-D_1 solution lost its symmetry. Lastly, for $t = 8$ we observe that all deconvolved regularizations presented some degree of accuracy when compared to the high resolution solution. But, Boussinesq-Leray-D_2 clearly provides the best solution among the regularized models. The L^2 error estimated using the fine solution as reference for this experiment is presented in Table 5.12. In this table we see again that the Boussinesq-Leray produced the best approximations. It is important to remark that, clearly from Algorithm 5.1, the Boussinesq-Leray (as well as the Boussinesq-ω) also has strong computational advantages when compared to Boussinesq-α and Modified-Boussinesq-Leray models, due to the decoupling between the momentum and the filter equation, which reduces the computational cost and enables it to work with any deconvolution order without a significant increase in computational time.

	$\|T_h^{coarse} - T_h^{fine}\|_{2,0}^2$
Boussinesq	8.3356
Boussinesq+Art. Visc. 1000	0.5686
Boussinesq+Art. Visc. 1500	0.4523
Boussinesq-alpha	0.3333
Boussinesq-alpha-D_1	0.3103
Boussinesq-Modified-Leray	0.53634
Boussinesq-Modified-Leray-D_1	0.46846
Boussinesq-Leray	0.30634
Boussinesq-Leray-D_1	0.23848
Boussinesq-Leray-D_2	0.21676
Boussinesq-omega	0.57784
Boussinesq-omega-D_1	0.47344
Boussinesq-omega-D_2	0.36828

Table 5.12: $L^2(0, 8; \Omega)$ error estimates in the coarse mesh temperature aproximations for $Re = 5000$.

(a) DNS - High (b) DNS - Low

(c) Art.Visc.1 (Re=1000) - Low (d) Art.Visc.1 (Re=1500) - Low

(e) Alpha - Low (f) Alpha-D_1 - Low

(g) Leray - Low (h) Leray-D_1 - Low

(i) Modified-Leray - Low (j) Modified-Leray-D_1 - Low

(k) Omega - Low (l) Omega-D_1 - Low

(m) Leray-D_2 - Low (n) Omega-D_2 - Low

Figure 5.5: Temperature field in the Marsigli's experiment with $Re = 5000$ for $t = 2$.

5.5 Concluding remarks

In this chapter, we have studied four regularized versions of the Boussinesq model for density currents, namely, Boussinesq-α, Boussinesq-Leray, Boussinesq-ω and Modified-Boussinesq-Leray. We have proved stability and optimal convergence in which case we have shown that increasing deconvolution order increases the consistency error order of the regularized model. Then, we tested the proposed algorithm in computational simulations. Firstly, convergence rates were estimated in simulations and agreed well with the theoretical ones. Afterward, the regularized

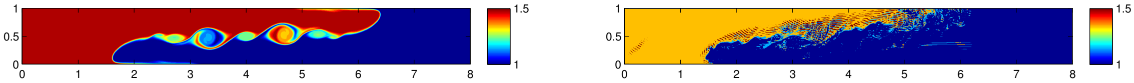

(a) DNS - High (b) DNS - Low

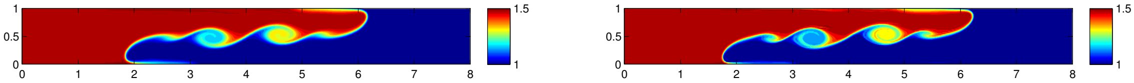

(c) Art.Visc.1 (Re=1000) - Low (d) Art.Visc.1 (Re=1500) - Low

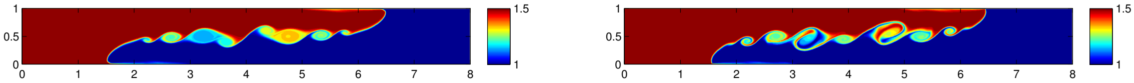

(e) Alpha - Low (f) Alpha-D_1 - Low

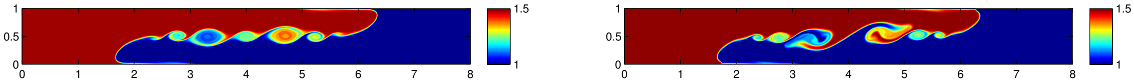

(g) Leray - Low (h) Leray-D_1 - Low

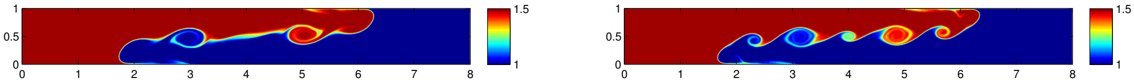

(i) Modified-Leray - Low (j) Modified-Leray-D_1 - Low

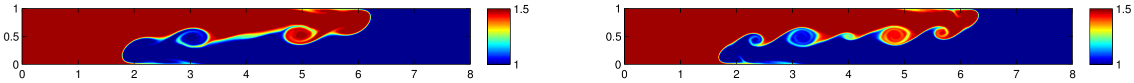

(k) Omega - Low (l) Omega-D_1 - Low

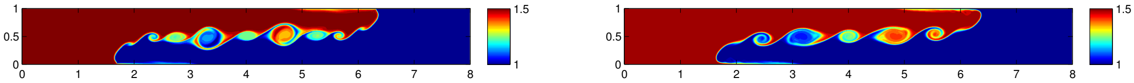

(m) Leray-D_2 - Low (n) Omega-D_2 - Low

Figure 5.6: Temperature field in the Marsigli's experiment with $Re = 5000$ for $t = 4$.

models were compared in the Marsigli's density flow experiment. In this experiment, we observed that for low Reynolds numbers, all tested regularized models provided accurate solutions, being more accurate for larger deconvolution order. However, the best solutions were obtained with the Boussinesq-α-D_1 and Boussinesq-Leray-D_2 models. On the other hand, in the case of high Reynolds number we found that, despite of all first order deconvolved models being better than the non-regularized Boussinesq model with and without artificial viscosity, Boussinesq-Leray with second order deconvolution provided the best solution. In addition to having performed better in these tests, Boussinesq-Leray also has large advantages from the compu-

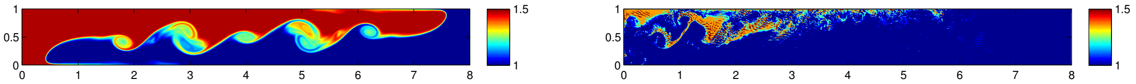

(a) DNS - High

(b) DNS - Low

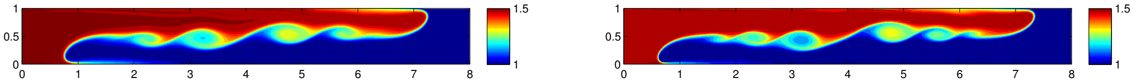

(c) Art.Visc.1 (Re=1000) - Low

(d) Art.Visc.1 (Re=1500) - Low

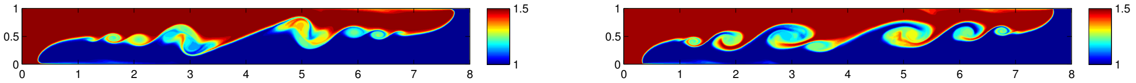

(e) Alpha - Low

(f) Alpha-D_1 - Low

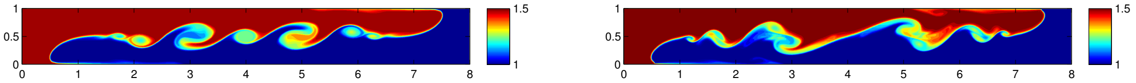

(g) Leray - Low

(h) Leray-D_1 - Low

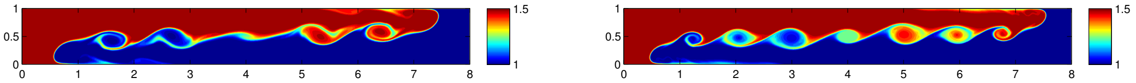

(i) Modified-Leray - Low

(j) Modified-Leray-D_1 - Low

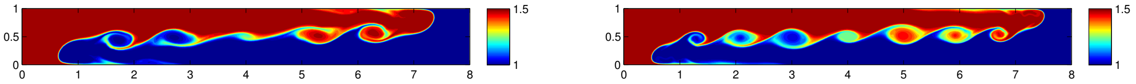

(k) Omega - Low

(l) Omega-D_1 - Low

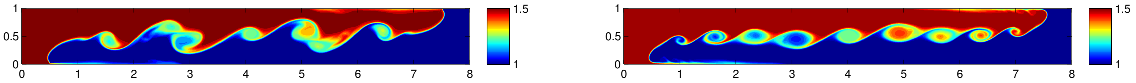

(m) Leray-D_2 - Low

(n) Omega-D_2 - Low

Figure 5.7: Temperature field in the Marsigli's experiment with $Re = 5000$ for $t = 6$.

tational viewpoint because its decoupling between momentum and filter equation reducing the model degrees of freedom and enabling it to work with any deconvolution order without a significant increase in computational time.

As for LES (see [87, 88, 49, 6], for instance), we believe the next step in a future work is to apply the regularized models in threedimensional simulations. In this kind of flow, other aspects resulting from the vortex stretching mechanism will emerge and could reveal other differences between the regularized Boussinesq models.

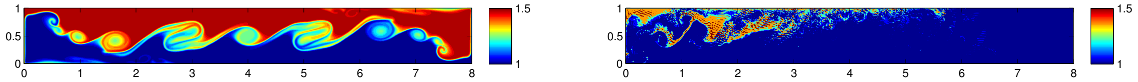

(a) DNS - High (b) DNS - Low

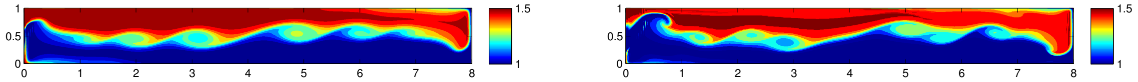

(c) Art.Visc.1 (Re=1000) - Low (d) Art.Visc.1 (Re=1500) - Low

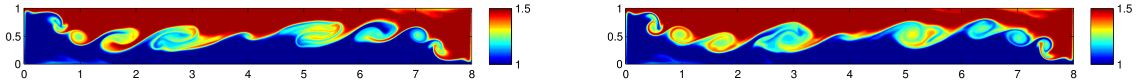

(e) Alpha - Low (f) Alpha-D_1 - Low

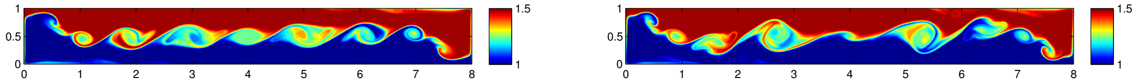

(g) Leray - Low (h) Leray-D_1 - Low

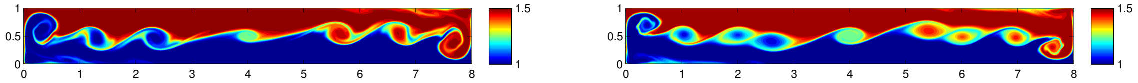

(i) Modified-Leray - Low (j) Modified-Leray-D_1 - Low

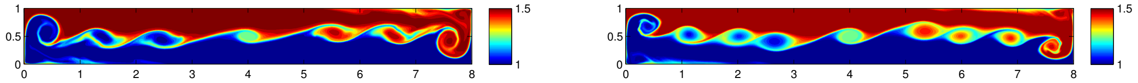

(k) Omega - Low (l) Omega-D_1 - Low

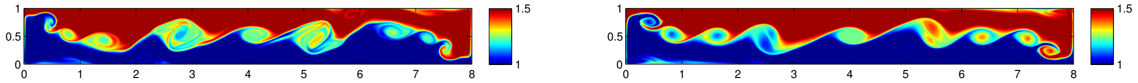

(m) Leray-D_2 - Low (n) Omega-D_2 - Low

Figure 5.8: Temperature field in the Marsigli's experiment with $Re = 5000$ for $t = 8$.

6 CONCLUSIONS

In the present Thesis, we have studied regularization techniques for geophysical models. As discussed in Chapter 1, geophysical flows are immensely important because of their plethora of applications in the atmospheric and oceanic sciences. Despite being one of the first applications of scientific computation and the great development of the computer power, realistic geophysical flow simulations are far from being fully resolved, largely due to the huge computational cost that would be necessary to reproduce all the necessary scales, but also because turbulence in this kind of flow is not totally understood. Thus, meteorologists and oceanographers very often have to resort to additional techniques in order to overcome these problems. Interestingly, despite the great importance of techniques to deal with turbulence in geophysical flows simulations, they are mainly projected and analysed in the engineering applications context. The main objective of this thesis is to apply and analyse these techniques, particularly the regularization models, in the geophysical framework. Our interest in regularization models is due to its sound mathematical and physical foundations and its ease to implement and low computational cost. Moreover, we are also motivated by some recent studies involving the application of alpha regularizations in the geophysical context which demonstrated some success in this kind of application.

Following the classical division adopted in Geophysical Fluid Dynamics in terms of barotropic and baroclinic flows, this thesis was divided into two parts in which regularizations technique was applied in the Barotropic Vorticity model in the first part and in the Boussinesq model for density currents in the second one.

In the first part, we started in Chapter 2 with the BV-Tikhonov model, which is a regularization of the Barotropic Vorticity model based on the Navier-Stokes-α model with the modified Tikhonov-Lavrentiev deconvolution. Then, we proposed a Crank-Nicolson algorithm for BV-Tikhonov model and showed it is stable and optimally convergent. Afterward, the BV-Tikhonov model was tested in the the traditional double gyre wind forcing benchmark in which it could recover the high resolution pattern when computing on a coarse mesh. However, these experiments also showed that the BV-Tikhonov solution can dramatically improve over the BV-α solution (obtained when $\mu = 1$ in the BV-Tikhonov model) by a careful choice of the μ parameter. That is, $\mu < 1$ has to be chosen in order to improve the solution by controlling the model consistency error and avoiding filtering in the resolved scales, but on the other hand it weakens the regularization.

Two natural improvements in the BV-Tikhonov model were 1) look for a less sensible regularization to this kind of problem and 2) apply the van Cittert approximate deconvolution method in the BV model, which, in the case of Navier-Stokes equations, is known to increase the model consistency error order. The former improve was studied in Chapter 3 and the latter in Chapter 4.

In Chapter 3, we tested, to the best of our knowledge for the first time, the Bardina regularization of the Barotropic Vorticity model, which was called BV-Bardina model. The BV-Bardina model is a regularization of the BV model which differs from the BV-α by the presence of a filtered vorticity in the nonlinear term having, consequently, more regularization. We proposed a Crank-Nicolson finite element scheme for BV-Bardina model and showed it is unconditionally stable and optimally convergent, which was also corroborated in numerical simulations. Finally, we evaluated the BV-Bardina solution in the double wind forcing benchmark against the artificial vorticity technique and the BV-α model, in which we show that the BV-Bardina model compares favourably to both.

In Chapter 4, we proposed and studied the BV-α-Deconvolution model. The BV-α-Deconvolution model was inspired in the Navier-Stokes-α-Deconvolution model in which, through the approximate deconvolution technique, increase arbitrarily the consistency error order in the model. Actually, the BV-α-Deconvolution is a family of models which generalizes the BV-α and improves accuracy. We studied a

Crank-Nicolson finite element scheme for BV-α-Deconvolution and prove its stability and optimal convergence. In particular, we showed that the BV-α-Deconvolution has an $O(\alpha^{2N+2})$ consistency error, where N is the deconvolution order, whereas BV-α is only $O(\alpha^2)$ accurate. In addition, we confirmed the convergence theory by estimating convergence rates through computational simulations. Finally, we demonstrated that the BV-α-Deconvolution model can accurately retrieve the high resolution solution without weakening the filtering, as in the BV-Tikhonov model. Instead, dramatic improvement is obtained only increasing the deconvolution order. Moreover, we showed both that i) even when the convergence error is dominated by the spatial error term, increasing deconvolution order still improve the model solution and ii) higher-order BV-α-Deconvolution model can retrieve very challenging solution structures which cannot be retrieved by decreasing the μ parameter in the BV-Tikhonov model.

The second part of this thesis was devoted to the baroclinic flows through the Boussinesq model. Then, based in the regularization theory for Navier-Stokes equations, in Chapter 5 we proposed a family of regularizations for the Boussinesq model, namely Boussinesq-α, Boussinesq-ω, Boussinesq-Leray and Modified-Boussinesq-Leray models, all of them using the approximate deconvolution technique. Initially, we propose and analyse a Crank-Nicolson finite element scheme for a general regularized Boussinesq model which conserves energy and is unconditionally stable and optimally convergent. Then, we showed through simulations that i) the convergence theory is supported by all of them, ii) they all perform well in the Marsigli flow's experiment and iii) increasing the deconvolution order improves the solution. However, in the more challenging situation in which the Reynolds number is large, we showed that the Boussinesq-Leray model was significantly better than the other regularized models. Moreover, the Boussinesq-Leray, because of its mathematical structure, allows the decoupling between the filter equation and the momentum equation enabling a much smaller computational cost regardless of the deconvolution order.

There are several directions in which this thesis can be extended, giving rise to future research. Firstly, in the case of BV model, there are some regularizations that need to be tested such as Voigt [55, 56, 68] and omega [65], and their respective approximate deconvolved versions (Van Cittert [75] and Tikhonov-Lavrentiev [105]). Another interesting recent approach is the iterated modified Tikhonov-Lavrentiev approximate deconvolution [53], which allows control of the convergence order and, in principle, can be applied in any regularization model. Moreover, another direction in which the studies with BV model can be extended is to consider the BV model for two layers. Recently, a LES version of the BV model based on the Approximate Deconvolution Model (ADM), was studied considering two layers [99], after being studied for one layer [100]. Thus, the first baroclinic mode can be considered in the model which would permit to evaluate the regularizations in a situation more similar with the true threedimensional ocean dynamic.

On the other hand, a natural next step for the study of density currents using the Boussinesq model is to extend the experiments for threedimensional situations. An interesting benchmark test is the 3D lock-exchange problem [87] in which some LES and parametrization models were recently tested [87, 88, 6, 16]. Also, even for 2D simulations, it would be very interesting to study Voigt and modified Tikhonov-Lavrentiev regularizations for the Boussinesq model. In our experiments with the Boussinesq model, we observed that small changes in the alpha parameter can significantly improve the solution, which is probably related to a better adjustment of the filter transfer function. The modified Tikhonok-Lavrentiev deconvolution [105] permits control of the regularization transfer function, what would allow a better tuning of the regularized model, or even better with higher order consistency error such as in [53].

An interesting open problem regarding regularization models is related to the kind of filter used. The Helmholtz filter used in regularization models is a kind of differential filter introduced by Germano [30, 29], which has several advantages from the implementation point of view. However, this filter has some drawbacks, e.g., 1) its transfer function never goes zero, what means that it does not completely remove the energy in subgrid wavenumbers; 2) it is too dissipative in the region close to grid cut-off wavenumber, meaning that it significantly affects the resolved scales. Thus, meaningful improvement in solutions provided by regularization models can be achieved by fixing this problem. An interesting approach is the nonlinear filtering [67, 8] which permits to filter locally the flow based in a given indicator function avoiding regions where the flow is resolvable. In addition to the physical based indicator functions [67, 8], recently a mathematical based indicator function given by $\left\| u_h - D_N^h u_h \right\|$ [10] permits, as well to select filtered regions, to increase the consistency error in the regularization model. Another interesting approach is to investigate and apply other filters with a sharper transfer function decay which save the low to moderate scales and completely remove the subgrid scales (see [101, 83, 80]).

Bibliography

[1] Adams, N., and Stolz, S. Deconvolution methods for subgrid-scale approximation in large eddy simulation. *Modern Simulation Strategies for Turbulent Flow* (2001), 21–41.

[2] Baker, G. A., Dougalis, V. A., and Karakashian, O. A. On a higher order accurate fully discrete galerkin approximation to the navier-stokes equations. *mathematics of computation 39*, 160 (1982), 339–375.

[3] Bardina, J., Ferziger, J., and Reynolds, W. Improved subgrid-scale models for large-eddy simulation. In *13th Fluid and PlasmaDynamics Conference* (1980), American Institute of Aeronautics and Astronautics (AIAA).

[4] Bernsen, E., Bokhove, O., and van der Vegt, J. J. A (Dis) continuous finite element model for generalized 2D vorticity dynamics. *Journal of Computational Physics 211*, 2 (2006), 719–747.

[5] Berselli, L., Iliescu, T., and Layton, W. *Mathematics of Large Eddy simulation of Turbulent Flows.* Scientific Computation. Springer, New York, 2006.

[6] Berselli, L. C., Fischer, P. F., Iliescu, T., and Özgökmen, T. M. Horizontal Large Eddy Simulation of Stratified Mixing in a Lock-Exchange System. *Journal of Scientific Computing* (2011).

[7] Bongolan-Walsh, V. P., Duan, J., Fischer, P., Özgökmen, T., and Iliescu, T. Impact of boundary conditions on entrainment and transport in gravity currents. *Applied Mathematical Modelling 31*, 7 (2007), 1338–1350.

[8] Bowers, A., Rebholz, L., Takhirov, A., and Trenchea, C. Improved accuracy in regularization models of incompressible flow via adaptive nonlinear filtering. *International Journal for Numerical Methods in Fluids 70*, 7 (2012), 805–828.

[9] Bowers, A. L., and Rebholz, L. G. Increasing accuracy and efficiency in FE computations of the Leray-Deconvolution model. *Numerical Methods for Partial Differential Equations 28*, 2 (2012), 720–736.

[10] Bowers, A. L., and Rebholz, L. G. Numerical study of a regularization model for incompressible flow with deconvolution-based adaptive nonlinear filtering. *Computer Methods in Applied Mechanics and Engineering 258* (2013), 1–12.

[11] Brenner, S. C., and Scott, L. R. *The Mathematical Theory of Finite Element Methods*, vol. 15. Springer, 2008.

[12] Bresch, D., and Gérard-Varet, D. Roughness-Induced Effects on the Quasi-Geostrophic Model. *Communications in Mathematical Physics 253*, 1 (2005), 81–119.

[13] Cantero, M. I., Balachandar, S., and Garcia, M. H. High-resolution simulations of cylindrical density currents. *Journal of Fluid Mechanics 590* (2007), 437–469.

[14] Cao, C., and Titi, E. S. Global well-posedness of the three-dimensional viscous primitive equations of large scale ocean and atmosphere dynamics. *Annals of Mathematics* (2007), 245–267.

[15] Cao, Y., Lunasin, E., and Titi, E. Global well-posedness of the three-dimensional viscous and inviscid simplified Bardina turbulence models. *Communications in Mathematical Sciences 4* (2006), 823–848.

[16] Chang, Y. S., Xu, X., Özgökmen, T. M., Chassignet, E. P., Peters, H., and Fischer, P. F. Comparison of gravity current mixing parameterizations and calibration using a high-resolution 3d nonhydrostatic spectral element model. *Ocean Modelling 10*, 3 (2005), 342–368.

[17] Charney, J. G., Fjörtoft, R., and Von Neumann, J. Numerical Integration of the Barotropic Vorticity Equation. *Tellus 2*, 4 (1950), 237–254.

[18] Ciarlet, P. G. *The Finite Element Method for Elliptic Problems.* Cambridge University Press, 1978.

[19] Connors, J. Convergence analysis and computational testing of the finite element discretization of the Navier–Stokes alpha model. *Numerical Methods for Partial Differential Equations 26*, 6 (2010), 1328–1350.

[20] Domaradzki, J., and Holm, D. D. Navier-Stokes-alpha model: LES equations with nonlinear dispersion. *arXiv preprint nlin/0103036* (2001).

[21] Evensen, G. Sequential data assimilation with a nonlinear Quasi-Geostrophic model using Monte Carlo methods to forecast error statistics. *Journal of Geophysical Research 99* (1994), 10–10.

[22] Fabijonas, B. R., and Holm, D. D. Elliptic instability in the Lagrangian-averaged Euler-Boussinesq-α equations. *Physics of Fluids 17*, 5 (2005), 054113.

[23] Fix, G. Finite Element Models for Ocean Circulation Problems. *SIAM Journal on Applied Mathematics 29*, 3 (1975), 371–387.

[24] Foias, C., Holm, D., and Titi, E. The three dimensional viscous Camassa–Holm equations, and their relation to the Navier–Stokes equations and turbulence theory. *Journal of Dynamics and Differential Equations 14*, 1 (2002), 1–35.

[25] Foias, C., Holm, D. D., and Titi, E. S. The Navier–Stokes-alpha model of fluid turbulence. *Physica D: Nonlinear Phenomena 152* (2001), 505–519.

[26] Foster, E., Iliescu, T., and Wang, Z. A Finite Element Discretization of the Streamfunction Formulation of the Stationary Quasi-Geostrophic Equations of the Ocean. *Comput. Meth. Appl. Mech. Eng. 261-262* (2013), 105–117.

[27] Foster, E., Iliescu, T., and Wells, D. A Two-Level Finite Element Discretization of the Streamfunction Formulation of the Stationary Quasi-Geostrophic Equations of the Ocean. *Comput. Math. Appl. 66* (2013), 1261–1271.

[28] Fox-Kemper, B., and Menemenlis, D. Can Large Eddy Simulation Techniques Improve Mesoscale Rich Ocean Models? In *AGU Monographs Series*, M. Hecht and H. Hasumi, Eds. AGU, 2008.

[29] Germano, M. Differential filters for the large eddy numerical simulation of turbulent flows. *Physics of Fluids (1958-1988) 29*, 6 (1986), 1755–1757.

[30] Germano, M. Differential filters of elliptic type. *Physics of Fluids (1958-1988) 29*, 6 (1986), 1757–1758.

[31] Geurts, B. J., and Holm, D. D. Alpha-modeling strategy for LES of turbulent mixing. In *Turbulent flow computation*. Springer, 2002, pp. 237–278.

[32] Geurts, B. J., and Holm, D. D. Regularization modeling for large-eddy simulation. *Physics of Fluids (1994-present) 15*, 1 (2003), L13–L16.

[33] Geurts, B. J., and Holm, D. D. Leray and LANS-α modelling of turbulent mixing. *Journal of Turbulence*, 7 (2006).

[34] Geurts, B. J., Kuczaj, A. K., and Titi, E. S. Regularization modeling for large-eddy simulation of homogeneous isotropic decaying turbulence. *Journal of Physics A: Mathematical and Theoretical 41*, 34 (2008), 344008.

[35] Girault, V., and Raviart, P.-A. *Finite Element Methods for Navier-Stokes equations.* Springer-Verlag, 1986.

[36] Goosse, H., Renssen, H., Timmermann, A., and Bradley, R. S. Internal and forced climate variability during the last millennium: A model-data comparison using ensemble simulations. *Quaternary Science Reviews 24*, 12 (2005), 1345–1360.

[37] Greatbatch, R. J., and Nadiga, B. Four-Gyre Circulation in a Barotropic Model with Double-Gyre Wind Forcing. *Journal of Physical Oceanography 30*, 6 (2000), 1461–1471.

[38] Guermond, J., Oden, J., and Prudhomme, S. An interpretation of the Navier–Stokes-alpha model as a frame-indifferent Leray regularization. *Physica D: Nonlinear Phenomena 177*, 1-4 (2003), 23.

[39] Gunzburger, M. *Finite Elment Methods For Viscous incompressible flows. A guide to theory, practice, and algorithms.* Academic Press, 1989.

[40] Hecht, F. New development in freefem++. *J. Numer. Math. 20*, 3-4 (2012), 251–265.

[41] Hecht, M., Holm, D., Petersen, M., and Wingate, B. Implementation of the LANS-α turbulence model in a primitive equation ocean model. *Journal of Computational Physics 227*, 11 (2008), 5691.

[42] Hecht, M., Holm, D., Petersen, M., and Wingate, B. The LANS-α and Leray turbulence parameterizations in primitive equation

ocean modeling. *Journal of Physics A: Mathematical and Theoretical 41*, 34 (2008), 344009.

[43] Heggelund, Y., Vikebø, F., Berntsen, J., and Furnes, G. Hydrostatic and non-hydrostatic studies of gravitational adjustment over a slope. *Continental Shelf Research 24*, 18 (2004), 2133–2148.

[44] Heywood, J., and Rannacher, R. Finite element approximation of the nonstationary Navier-Stokes problem. Part IV: Error analysis for the second order time discretization. *SIAM J. Numer. Anal. 2* (1990), 353–384.

[45] Heywood, J. G., and Rannacher, R. Finite element approximation of the nonstationary Navier-Stokes problem. I. regularity of solutions and second-order error estimates for spatial discretization. *SIAM Journal on Numerical Analysis 19*, 2 (1982), 275–311.

[46] Hiester, H., Piggott, M., Farrell, P., and Allison, P. Assessment of spurious mixing in adaptive mesh simulations of the two-dimensional lock-exchange. *Ocean Modelling 73* (2014), 30–44.

[47] Holm, D. D., and Nadiga, B. T. Modeling Mesoscale Turbulence in the Barotropic Double-Gyre Circulation. *Journal of Physical Oceanography 33*, 11 (2003), 2355.

[48] Ilicak, M., Legg, S., Adcroft, A., and Hallberg, R. Dynamics of a dense gravity current flowing over a corrugation. *Ocean Modelling 38*, 1 (2011), 71–84.

[49] Ilicak, M., Özgökmen, T. M., Özsoy, E., and Fischer, P. F. Non-hydrostatic modeling of exchange flows across complex geometries. *Ocean Modelling 29*, 3 (2009), 159–175.

[50] Ilicak, M., Özgökmen, T. M., Peters, H., Baumert, H. Z., and Iskandarani, M. Performance of two-equation turbulence closures in three-dimensional simulations of the Red Sea overflow. *Ocean Modelling 24*, 3 (2008), 122–139.

[51] Ilyin, A. A., Lunasin, E. M., and Titi, E. S. A modified-Leray-α subgrid scale model of turbulence. *Nonlinearity 19*, 4 (2006), 879.

[52] Ingram, R. A new linearly extrapolated Crank-Nicolson time-stepping scheme for the Navier-Stokes equations. *Mathematics of Computation 82*, 284 (2013), 1953–1973.

[53] Ingram, R., Manica, C., Mays, N., and Stanculescu, I. Convergence Analysis of a Fully Discrete Family of Iterated Deconvolution Methods for Turbulence Modeling with Time Relaxation. *Advances in Numerical Analysis 2012* (2012).

[54] Jochum, M., Danabasoglu, G., Holland, M., Kwon, Y.-O., and Large, W. G. Ocean viscosity and climate. *Journal of Geophysical Research 113*, C6 (2008).

[55] Kalantarov, V., Levant, B., and Titi, E. Gevrey Regularity for the Attractor of the 3D Navier–Stokes–Voight Equations. *Journal of Nonlinear Science 19* (2008), 133–152.

[56] Kalantarov, V., and Titi, E. Global attractors and determining modes for the 3d Navier-Stokes-Voigt equations. *Chinese Annals of Mathematics, Series B 30*, 6 (2009), 697–714.

[57] Kalnay, E. *Atmospheric modeling, data assimilation and predictability.* Cambridge University Press, United Kingdom, 2003.

[58] Katavouta, A., and Thompson, K. Downscaling ocean conditions: Experiments with a quasi-geostrophic model . *Ocean Modelling 72*, 0 (2013), 231 – 241.

[59] Khouider, B., and Titi, E. An Inviscid Regularization for the Surface Quasi-Geostrophic Equation. *Communications on Pure and Applied Mathematics 61*, 10 (2008), 1331–1346.

[60] Layton, W. *An Introduction to the Numerical Analysis of Viscous Incompressible Flows.* SIAM, Philadelphia, 2008.

[61] Layton, W. Existence of smooth attractors for the Navier-Stokes-omega model of turbulence. *Journal of Mathematical Analysis and Applications 366*, 1 (2010), 81.

[62] Layton, W., and Lewandowski, R. On a well-posed turbulence model. *Discrete and Continuous Dynamical Systems Series B 6*, 1 (2006), 111–128.

[63] Layton, W., Manica, C. C., Neda, M., Olshanskii, M., and Rebholz, L. G. On the accuracy of the rotation form in simulations of the Navier–Stokes equations. *Journal of Computational Physics 228*, 9 (2009), 3433–3447.

[64] Layton, W., Manica, C. C., Neda, M., and Rebholz, L. G. Numerical analysis and computational testing of a high accuracy Leray-deconvolution model of turbulence. *Numerical Methods for Partial Differential Equations 24*, 2 (2008), 555–582.

[65] Layton, W., Manica, C. C., Neda, M., and Rebholz, L. G. Numerical analysis and computational comparisons of the NS-alpha and NS-omega regularizations. *Computer Methods in Applied Mechanics and Engineering 199*, 13-16 (2010), 916.

[66] Layton, W., and Rebholz, L. *Approximate deconvolution models of turbulence: analysis, phenomenology, and numerical analysis.* Springer-Verlag, 2012.

[67] Layton, W., Rebholz, L. G., and Trenchea, C. Modular nonlinear filter stabilization of methods for higher reynolds numbers flow. *Journal of Mathematical Fluid Mechanics 14*, 2 (2012), 325–354.

[68] Levant, B., Ramos, F., and Titi, E. On the statistical properties of the 3d incompressible Navier-Stokes-Voigt model. *Communications in Mathematical Sciences 8*, 1 (2010), 277–293.

[69] Liu, J.-G., Wang, C., and Johnston, H. A fourth order scheme for incompressible Boussinesq equations. *Journal of Scientific Computing 18*, 2 (2003), 253–285.

[70] Luo, Z. Proper orthogonal decomposition-based reduced-order stabilized mixed finite volume element extrapolating model for the nonstationary incompressible Boussinesq equations. *Journal of Mathematical Analysis and Applications 425*, 1 (2015), 259–280.

[71] Lynch, P. The origins of computer weather prediction and climate modeling. *Journal of Computational Physics 227*, 7 (2008), 3431–3444.

[72] Lynch, P. The ENIAC forecasts: A re-creation. *Bulletin of the American Meteorological Society 89*, 1 (2008), 45–55.

[73] Majda, A. J., Franzke, C., and Crommelin, D. Normal forms for reduced stochastic climate models. *Proceedings of the National Academy of Sciences 106*, 10 (2009), 3649–3653.

[74] Manica, C., and Merdan, S. Finite element analysis of a zeroth order approximate deconvolution model based on a mixed formulation. *Journal of Mathematical Analysis and Applications 331*, 1 (2007), 669–685.

[75] Manica, C., Neda, M., Olshanskii, M., Rebholz, L., and Wilson, N. On an Efficient Finite Element Method for Navier-Stokes-ω with Strong Mass Conservation. *Computational Methods in Applied Mathematics 11*, 1 (2011), 3–22.

[76] Manica, C. C., Neda, M., Olshanskii, M., and Rebholz, L. G. Enabling numerical accuracy of Navier-Stokes-α through deconvolution and enhanced stability. *ESAIM: Mathematical Modelling and Numerical Analysis 45*, 2 (2011), 277–307.

[77] Marsden, J. E., and Shkoller, S. Global well–posedness for the Lagrangian averaged Navier–Stokes (LANS–α) equations on bounded domains. *Philosophical Transactions of the Royal Society of London A: Mathematical, Physical and Engineering Sciences 359*, 1784 (2001), 1449–1468.

[78] Medjo, T. T. Numerical Simulations of a Two-layer Quasi-Geostrophic equation of the Ocean. *SIAM Journal on Numerical Analysis 37*, 6 (2000), 2005–2022.

[79] Miles, W., and Rebholz, L. An Enhanced-Physics-Based Scheme for the NS-α Turbulence Model. *Numerical Methods for Partial Differential Equations 26*, 6 (2010), 1530–1555.

[80] Mullen, J. S., and Fischer, P. F. Filtering techniques for complex geometry fluid flows. *Communications in numerical methods in engineering 15*, 1 (1999), 9–18.

[81] Nadiga, B. T., and Margolin, L. G. Dispersive-dissipative eddy parameterization in a barotropic model. *Journal of Physical Oceanography 31*, 8 (2001), 2525–2531.

[82] Nadiga, B. T., and Shkoller, S. Enhancement of the inverse-cascade of energy in the two-dimensional Lagrangian averaged Navier-Stokes equations. *Physics of Fluids 13*, 5 (2001), 1528–1531.

[83] Najafi-Yazdi, A., Najafi-Yazdi, M., and Mongeau, L. A high resolution differential filter for large eddy simulation: Toward explicit filtering on unstructured grids. *Journal of Computational Physics 292* (2015), 272–286.

[84] Özgökmen, T. M., and Chassignet, E. P. Dynamics of two-dimensional turbulent bottom gravity currents. *Journal of Physical Oceanography 32*, 5 (2002), 1460–1478.

[85] Özgökmen, T. M., Fischer, P. F., Duan, J., and Iliescu, T. Entrainment in bottom gravity currents over complex topography from three-dimensional nonhydrostatic simulations. *Geophysical Research Letters 31*, 13 (2004).

[86] Özgökmen, T. M., Fischer, P. F., Duan, J., and Iliescu, T. Three-dimensional turbulent bottom density currents from a high-order nonhydrostatic spectral element model. *Journal of Physical Oceanography 34*, 9 (2004), 2006–2026.

[87] Özgökmen, T. M., Iliescu, T., and Fischer, P. F. Large eddy simulation of stratified mixing in a three-dimensional lock-exchange system. *Ocean Modelling 26*, 3 (2009), 134–155.

[88] Özgökmen, T. M., Iliescu, T., and Fischer, P. F. Reynolds number dependence of mixing in a lock-exchange system from direct numerical and large eddy simulations. *Ocean Modelling 30*, 2 (2009), 190–206.

[89] Özgökmen, T. M., Iliescu, T., Fischer, P. F., Srinivasan, A., and Duan, J. Large eddy simulation of stratified mixing in two-

dimensional dam-break problem in a rectangular enclosed domain. *Ocean Modelling 16*, 1 (2007), 106–140.

[90] Özgökmen, T. M., Johns, W. E., Peters, H., and Matt, S. Turbulent mixing in the red sea outflow plume from a high-resolution nonhydrostatic model. *Journal of Physical Oceanography 33*, 8 (2003), 1846–1869.

[91] Pedlosky, J. *Geophysical Fluid Dynamics*, 2nd ed. ed. Springer-Verlag, New York, 1987.

[92] Pope, S. *Turbulent flows.* Cambridge University Press, 2000.

[93] Rebholz, L. G. A family of new, high order NS-α models arising from helicity correction in Leray turbulence models. *Journal of Mathematical Analysis and Applications 342*, 1 (2008), 246–254.

[94] Rebholz, L. G., and Sussman, M. M. On the high accuracy NS-alpha-deconvolution turbulence model. *Mathematical Models and Methods in Applied Sciences 20*, 04 (2010), 611–633.

[95] Renssen, H., Brovkin, V., Fichefet, T., and Goosse, H. Simulation of the Holocene climate evolution in Northern Africa: the termination of the African Humid Period. *Quaternary International 150*, 1 (2006), 95–102.

[96] Rivière, G., Arbogast, P., and Joly, A. Eddy kinetic energy redistribution within idealized extratropical cyclones using a two-layer quasi-geostrophic model. *Quarterly Journal of the Royal Meteorological Society* (2014), 1–18.

[97] Sagaut, P. *Large eddy simulation for incompressible flows: an introduction.* Springer Science & Business Media, 2006.

[98] San, O., and Borggaard, J. Principal interval decomposition framework for POD reduced-order modeling of convective Boussinesq flows. *International Journal for Numerical Methods in Fluids* (2015), 37–52.

[99] San, O., Staples, A., and Iliescu, T. Approximate deconvolution large eddy simulation of a stratified two-layer quasigeostrophic ocean model. *Ocean Modeling 63* (2013), 1 – 20.

[100] San, O., Staples, A., Wang, Z., and Iliescu, T. Approximate Deconvolution Large Eddy Simulation of a Barotropic Ocean Circulation Model. *Ocean Modeling 40*, 2 (2011), 120 – 132.

[101] San, O., Staples, A. E., and Iliescu, T. A posteriori analysis of low-pass spatial filters for approximate deconvolution large eddy simulations of homogeneous incompressible flows. *International Journal of Computational Fluid Dynamics*, ahead-of-print (2014), 1–27.

[102] Scott, R. B., and Arbic, B. K. Spectral Energy Fluxes in Geostrophic Turbulence: Implications for Ocean Energetics. *Journal of Physical Oceanography 37*, 3 (2007), 673–688.

[103] Scott, R. B., and Wang, F. Direct Evidence of an Oceanic Inverse Kinetic Energy Cascade from Satellite Altimetry. *Journal of Physical Oceanography 35*, 9 (2005), 1650–1666.

[104] Smagorinsky, J. General Circulation Experiments With The Primitive Equations: I. The basic experiment. *Monthly Weather Review 91*, 3 (1963), 99–164.

[105] Stanculescu, I., and Manica, C. C. Numerical analysis of Leray–Tikhonov deconvolution models of fluid motion. *Computers & Mathematics with Applications 60*, 5 (2010), 1440–1456.

[106] Stolz, S., Adams, N., and Kleiser, L. An approximate deconvolution model for large-eddy simulation with application to incompressible wall-bounded flows. *Physics of Fluids 13*, 4 (2001), 997–1015.

[107] Stolz, S., and Adams, N. A. An approximate deconvolution procedure for large-eddy simulation. *Physics of Fluids 11*, 7 (1999), 1699.

[108] Sutyrin, G., and Carton, X. Vortex interaction with a zonal Rossby wave in a Quasi-Geostrophic model. *Dynamics of Atmospheres and Oceans 41*, 2 (2006), 85–102.

[109] Thomée, V. *Galerkin finite element methods for parabolic problems*, second ed. Springer, Berlin, 2010.

[110] Vallis, G. K. *Atmospheric and oceanic fluid dynamics: fundamentals and large-scale circulation.* Cambridge University Press, 2006.

[111] Williams, P. D. The RAW filter: An improvement to the Robert-Asselin filter in semi-implicit integrations. *Monthly Weather Review 139*, 6 (2011), 1996–2007.

[112] Wingate, B. A. The Maximum Allowable Time Step for the Shallow Water-α Model and Its Relation to Time-Implicit Differencing. *Monthly Weather Review 132*, 12 (2004), 2719–2731.

[113] Yang, S. C., Corazza, M., Carrassi, A., Kalnay, E., and Miyoshi, T. Comparison of ensemble-based and variational-based data assimilation schemes in a Quasi-Geostrophic model. In *AMS 10th Symposium on Integrated Observing and Assimilation Systems for the Atmosphere, Oceans, and Land Surface* (2007).